RUHR
UNIVERSITÄT
BOCHUM

RUB

Plasma chemistry of H_2O_2 generation in atmospheric pressure plasma jets: from gas to liquid phase

Dissertation

zur
Erlangung des Grades
„Doktor der Naturwissenschaften“

an der Fakultät für Physik und Astronomie
der Ruhr-Universität Bochum

von
Steffen Burkhard Schüttler
aus Gelsenkirchen

Bochum 2024

1. Gutachterin:	Jun.-Prof. Judith Golda
2. Gutachter:	Prof. Achim von Keudell

Datum der Einreichung:	10.12.2024
Datum der Disputation:	to be announced

This work was founded by the Deutsche Forschungsgemeinschaft (DFG) within the collaborative research centre CRC 1316 entitled "Transient Atmospheric Plasmas: From Plasmas to Liquids To Solids" (project number 327886311) in the subproject B11.

Abbreviations

APPJ atmospheric pressure plasma jet

BCS back current shunt

CL chemiluminescence

DBD dielectric barrier discharge

FTIR fourier-transform infrared

FWHM full width half maximum

iCCD intensified charge coupled device

LIF laser-induced fluorescence

ODE ordinary differential equation

OES optical emission spectroscopy

PIV particle imaging velocimetry

PROES phase-resolved optical emission spectroscopy

PTL plasma-treated liquid

RONS reactive oxygen and nitrogen species

TA terephthalic acid

UPO unspecific peroxygenase

VET vibrational energy transfer

Contents

1 Introduction **1**

1.1 Motivation . . . 1
1.2 H_2O_2 production by plasmas . . . 2
1.3 Research focus . . . 4
1.4 Research questions . . . 5
1.5 Thesis outline . . . 6

2 Fundamentals **9**

2.1 Non-equilibrium atmospheric pressure plasmas . . . 9
2.1.1 Electrical breakdown . . . 11
2.1.2 Streamer . . . 13
2.1.3 Capillary plasma jet . . . 15
2.2 Humidified plasma chemistry . . . 19
2.3 Plasma-liquid interactions . . . 20
2.3.1 Solubility of species . . . 22
2.3.2 Transport phenomena in liquids . . . 23
2.3.3 Source of H_2O_2 production . . . 24
2.4 Optical emission spectroscopy . . . 25
2.5 Absorption spectroscopy . . . 27

3 Experimental procedure and modelling **29**

3.1 Capillary plasma jet . . . 29
3.1.1 Pulse modulation . . . 32
3.2 Gas phase diagnostics . . . 33
3.2.1 Temperature measurements . . . 33
3.2.2 Laser-induced fluorescence . . . 35
3.2.3 Fourier-transform infrared spectroscopy . . . 40
3.2.4 Mass spectrometry . . . 42
3.2.5 Phase-resolved optical emission spectroscopy . . . 44
3.3 Liquid diagnostics . . . 46
3.3.1 UV absorption for H_2O_2 detection . . . 46
3.3.2 Spectrophotometry for H_2O_2 detection . . . 48
3.3.3 Electrochemical sensing for H_2O_2 detection . . . 50
3.3.4 Terephthalic acid dosimeter for OH detection . . . 51
3.3.5 Chemiluminescence for OH detection . . . 54

3.3.6 Particle imaging velocimetry . . . 55
3.4 Chemical model . . . 55
3.5 Transport model in PTL . . . 56

4 Gas phase dynamics and chemistry 59
4.1 Plasma power and electron density . . . 59
4.2 Gas temperature . . . 62
4.3 Electron dynamics . . . 64
4.4 Detection limit of LIF spectroscopy . . . 70
4.5 Air entrainment . . . 72
4.6 Absolute species densities . . . 74
4.6.1 Consumed water . . . 74
4.6.2 Humidity and plasma power variation . . . 76
4.6.3 Chemistry model and species evolution . . . 80
4.6.4 Species densities under pulse modulation . . . 85
4.7 Summary gas phase dynamics and chemistry . . . 90

5 Liquid phase dynamics and chemistry 91
5.1 H_2O_2 production . . . 91
5.2 OH distribution . . . 93
5.3 Impact of treatment parameters . . . 96
5.4 Species concentration under pulse modulation . . . 98
5.5 Distribution of liquid H_2O_2 . . . 100
5.6 H_2O_2 distribution in buffered solution . . . 108
5.7 Comparing liquid phase to gas phase . . . 110
5.8 Summary liquid phase dynamics and chemistry . . . 113

6 Scale-up 115
6.1 Plasma volume . . . 115
6.2 Ar as feed gas . . . 118
6.3 Summary scale-up . . . 122

7 Tuning plasma chemistry 123
7.1 Nitrogen fixation . . . 124
7.2 Various excitation mechanisms . . . 136
7.3 Summary tuning plasma chemistry . . . 151

8 Conclusion and outlook 153
8.1 Outlook . . . 156
8.2 Publication list . . . 158

Bibliography **159**

A Appendix **181**

A.1 Humidity admixture 181
A.2 Temperature measurements 182
A.3 Images of the CL of luminol for correction 183
A.4 Images of luminol under humidity variation at 6 W 184
A.5 Images of luminol under distance variation 184
A.6 Log scale of modelled H_2O_2 concentration profiles 185
A.7 Temporal behaviour of absorbance 185
A.8 Determination of plasma volume 186
A.9 Correction of power measurements under ns operation 187

1. Introduction

1.1 Motivation

Conventional "thermal" catalysis of many chemicals relies on catalytic reactions of metal catalysts at high pressures and temperatures. This is accompanied by harsh reaction conditions and high energy consumption and produces a large amount of heavy waste metals. In addition, conventional catalysis faces the challenges of electrification by renewable energy sources leading to net-zero emissions of greenhouse gases [1]. Plasma catalysis is one alternative to face the challenges of conventional catalysis, establishing a green and more sustainable alternative [2]. In the field of plasma catalysis, plasma-driven biocatalysis was introduced [3, 4].

In biocatalysis, biological enzymes act as natural sustainable catalysts performing catalytic reactions [5]. Enzymes are highly selective to specific reactions converting precursor substances (substrates) into valuable products using reactants. The high selectivity reduces the formation of unwanted side products, often produced in conventional catalysis utilising metal catalysts. Thus, biocatalysis can be seen as a green and sustainable alternative to conventional catalysis. However, the enzymes require mild and stable operating conditions: Too high supplies of substrates or reactants can lead to the inactivation of the enzymes, and tuning the biocatalysis with the optimum amounts is crucial. In plasma-driven biocatalysis, the species production of atmospheric pressure plasmas and catalytic reactions of biological enzymes utilising the plasma-generated species are connected. In this approach, the plasma produces the reactants of the reaction and the enzymes can transform a substrate into a valuable product. This idea was previously investigated by the chair of Applied Microbiology at Ruhr University Bochum in Germany [3, 6] and a research group at North Carolina State University in the USA [4].

Yayci et al. from the Ruhr University Bochum used the model enzyme unspecific peroxygenase from Agrocybe aegerita (rAaeUPO), a promising enzyme for peroxide-dependent oxyfunctionalisation chemistry [7–9]. It transforms ethylbenzene (substrate) to (R)-1-phenylethanol (product) by consuming H_2O_2 (reactant). The main advantage of this biocatalytic reaction is to produce (R)-1-phenylethanol with high stereoselectivity [10]. The product (R)-1-phenylethanol is a valuable chemical used in the pharmaceutical, cosmetic, and chemical industries [11, 12].

The supply of H_2O_2 is crucial for the performance of the enzymatic reactions.

However, the on-demand delivery of H_2O_2 under biocatalysis by various technologies, such as enzyme cascades, electrochemistry or photocatalytic reactions are problematic as these technologies require the addition of components like electrodes or chemicals to the liquid which might negatively influence the enzymes [3]. Furthermore, the supply of H_2O_2 from stock solutions can lead to the inactivation of the enzymes by a too high concentration of H_2O_2 or would lead to a strong dilution of the reaction solution [3]. An alternative can be provided by atmospheric plasmas [3]. These do not require additions to the liquid and only the reactive species produced by the plasma interact with the liquid. However, the species composition is important as only H_2O_2 is necessary for the enzymes and other reactive can even be harmful to the enzymes. In the first work of the research group at Ruhr University Bochum regarding plasma-driven biocatalysis, Yayci et al. used a dielectric barrier discharge (DBD) in contact with a liquid to study the proof of principle of plasma-driven biocatalysis [3]. Under treatment of the DBD, H_2O_2 was produced and available for the enzymes to perform the catalytic reaction [3]. This was the proof in principle that plasma is a suitable source of H_2O_2 for biocatalysis. In a subsequent work, they used a micro-scale atmospheric pressure plasma jet, namely the COST reference plasma jet [13], successfully for the plasma-driven biocatalysis with enhanced performance compared to the DBD plasma [6]. This work formed the basis for the B11 project of the second funding period of the CRC 1316 entitled "Rational tuning of plasma and liquid chemistry for biocatalysis" [14], under which this dissertation was conducted.

Here, the COST reference plasma jet has been replaced by a capillary plasma jet with similar characteristics to the COST reference plasma jet [15]. Due to the capillary introduced in the plasma jet, higher plasma powers and reactive admixture can be used compared to the COST reference plasma jet. In addition, the plasma volume can be easily adjusted by widening the capillary. This could open up a broader application window for plasma-driven biocatalysis. The biocatalysis process is studied by colleagues from the chair of Applied Microbiology at Ruhr University Bochum. The research focus of this thesis is to understand and improve the H_2O_2 generation of the capillary plasma jet and its delivery to a liquid sample.

1.2 H_2O_2 production by plasmas

In general, H_2O_2 is widely used in chemical processes as an environmentally friendly and sustainable oxidising agent and it is stated as "a key chemical for today's sustainable development" [16]. It is involved in processes such as chemical synthesis, wastewater treatment, paper bleaching, and medical disinfection [16–18]. Its pro-

duction on a large scale is mainly performed via the anthraquinone oxidation process (AOP) or Riedl-Pfleiderer process [17, 19]. The process uses catalysts to convert H_2 and O_2 into H_2O_2 and has the drawback of complex and centralized plants as well as risk in transportation [17, 20, 21]. Its energy costs are given to 17.6 kWh/kg (57 g kWh^{-1}) [22]. Alternatives to AOP, especially with regard to the simple production of H_2O_2 at the point of use, have been widely discussed [20, 21], including photocatalytic [18] and electrocatalytic processes [23] as well as plasma technology [19]. In the case of plasma technology, the direct synthesis of H_2O_2 from H_2 and O_2 can be achieved in DBD plasmas without the use of a solvent or catalyst [19]. However, due to the gas mixture of H_2 and O_2, safety issues are present as an explosive gas mixture can be created at high O_2 admixtures [19]. Furthermore, various discharge setups involving water have been developed, including discharges in liquids, in bubbles and discharges above liquids [24]. Energy yields of H_2O_2 production from plasmas interacting with liquids were found in the range from 4×10^{-2} g kWh^{-1} to 80 g kWh^{-1} [24].

As a safe and on-demand technology for the production of H_2O_2, atmospheric pressure plasma jets (APPJs) operated with noble gases as feed gas and humidity admixture can be used. These sources have been intensively characterised in terms of H_2O_2 production, often in the combination with treated liquids [25–35]. In the gas phase, H_2O_2 densities in the order of up to 2×10^{14} cm^{-3} were found [29, 33–35]. Due to the high solubility of H_2O_2 and its impact on biological and medical applications, H_2O_2 from APPJ can be dissolved in liquids for various applications. Concentrations of H_2O_2 in liquids varied over a broad range from micromolar to millimolar [25–28, 30–32]. However, these values have to be taken with care since in liquid treatments the volume of the treated liquid and the treatment time determine the amount of H_2O_2 dissolved in the liquid and its concentration.

Furthermore, the combination of a plasma jet treating a liquid is a useful tool for separating plasma and liquid chemistry. However, when species are detected in the liquid after or during plasma treatment, the source of their formation remains unclear. It is uncertain whether these species are generated in the plasma and subsequently dissolve in the liquid, or if they are formed directly within the liquid itself. To study this aspect, isotope tracing was used to distinguish between H_2O_2 produced in the gas or liquid phase. Gorbanev et al. have shown that in the setup of a humidified APPJ treating a liquid sample, the H_2O_2 is produced in the gas phase and dissolved in the liquid [31]. Thus, the source of H_2O_2 consists of the H_2O molecules in the gas phase, when H_2O is added to the feed gas. In this way, the species composition in the liquid can be tuned by varying the gas composition.

1.3 Research focus

A sketch of the plasma-liquid system investigated in this thesis is shown in figure 1.1. The capillary plasma jet is operated in humidified He at a certain gas flow rate. The electrode arrangement is plan-parallel and a cross-field plasma jet is created. Excitation of the capillary plasma jet is performed via RF signals with sinusoidal waveforms at a frequency of 13.56 MHz and peak-to-peak voltages up to 2 kV. Within the plasma, dissociation processes occur and H_2O will be dissociated producing reactive species such as H and OH [24, 27, 36, 37]. OH radicals recombine to form H_2O_2 in the plasma phase and further species like HO_2, H_2 and O_2 are generated [24, 27, 36, 37]. The generated species are transported via the effluent of the plasma jet to the surface of the liquid sample. There, the gas flow interacts with the surface and the species will be dissolved in the liquid. Interactions of the gas flow with the liquid surface are crucial [38–40]. The gas flow in the system investigated is laminar, similar to the COST reference plasma jet [41] minimising disturbances at the liquid interface. Nevertheless, vortices will be created in the liquid due to the interaction of the gas and the liquid [42–44]. In the liquid, transport processes take place that lead to the distribution of the dissolved species.

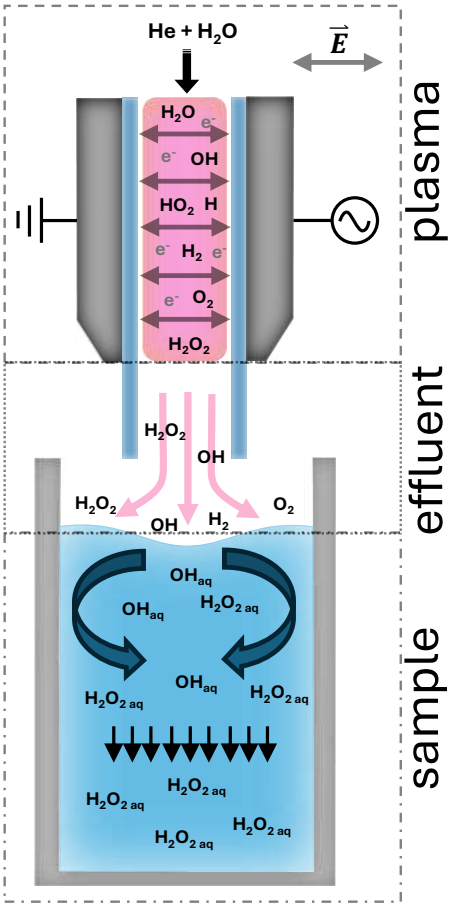

Figure 1.1: Sketch of the liquid treatment by the capillary plasma jet operated in humidified He.

The understanding of the mechanisms to generate H_2O_2 by the capillary plasma jet is used to improve its H_2O_2 generation and to enhance the performance and efficiency of plasma-driven biocatalysis. To achieve this goal, a close collaboration with the chair of Applied Microbiology at Ruhr University Bochum was maintained throughout the period of this PhD thesis. This also included the construction and maintenance of the same plasma source with gas and power supply for the Chair of Applied Microbiology. The findings on H_2O_2 generation of the capillary plasma jet gained in this thesis could be directly implemented in plasma-driven biocatalysis. However, the results of the plasma-driven biocatalysis will not be presented in this

thesis as the thesis focuses on the plasma physics and chemistry of the humidified capillary plasma jet. In addition, modelling studies of the plasma-liquid system were carried out in collaboration with the Chair of Applied Electrodynamics and Plasma Technology at the Ruhr University Bochum. The modelling results of the gas phase have been published in a joint publication and will be shown in this thesis.

In addition, a large number of enzymes are available for the biocatalysis of various chemical reactions, in addition to peroxide-dependent oxyfunctionalisation chemistry with H_2O_2. One example is TxTE, which utilises nitric oxide NO for nitration processes, e.g. of L-tryptophan [45–47]. Atmospheric pressure plasmas can produce nitrogen-containing species when N_2 is added to the feed gas [48, 49] or when directly driven in N_2 [50, 51]. In this case, N_2 is transformed into NOx species by the addition of O_2 or into ammonia NH_3 by the addition of H_2 or H_2O. The process of transformation of N_2 into NOx or NH_3 is known as nitrogen fixation [52]. Thus, by changing the gas composition from He+H_2O to a gas composition including N_2 admixtures, reactive nitrogen species can be produced by the capillary plasma jet. This might broaden the application window of plasma-driven biocatalysis. In addition, the cooperation with the B13 project of the CRC 1316 required a gas mixture of He+H_2O+N_2 to produce NH-containing species to generate nanoparticles by the use of micelles in the plasma-treated liquid (PTL) [14]. Thus, the information on the species production of the capillary plasma jet operated in He+H_2O+N_2 is important for the progress of the B13 project.

1.4 Research questions

The following research questions have been formulated to be addressed by the investigation conducted in this thesis:

1. Can H_2O_2 be generated by the capillary plasma jet? What are the main production and consumption mechanisms of H_2O_2 and what other species are involved in the plasma chemistry? How do plasma parameters such as gas composition and plasma power influence the plasma chemistry?
2. How is the transfer of gaseous OH and H_2O_2 to the liquid achieved? What are the physical and chemical processes, and how is the species transport conducted within the liquid?
3. How can pulse modulation of the RF signal be utilised to tune the plasma chemistry? How is pulse modulation affecting the generation of short-lived species like OH and of long-lived species like H_2O_2?

4. How can an increased plasma volume be used for scaling up the H_2O_2 generation? In addition, does the plasma chemistry of H_2O_2 generation and the transfer of the gaseous species into the liquid change when Ar is used as an alternative to He as feed gas?

5. How is nitrogen fixation in the capillary plasma jet achieved when operating in gas mixtures of He+H_2O+N_2+O_2? And what is the efficiency of H_2O_2 generation when the capillary plasma jet is operated with µs or ns pulses instead of RF operation?

1.5 Thesis outline

The thesis is structured as follows. Chapter 2 provides a theoretical foundation for the most important physical concepts regarding this thesis. An overview of the characteristics of non-equilibrium plasmas at atmospheric pressure is given, followed by the essential aspects of the capillary plasma jet. Then the chemistry of a humidified He plasma and the main plasma-liquid interactions are discussed. Finally, the chapter concludes with fundamentals on optical emission and absorption spectroscopy.

In Chapter 3, the experimental setup for the plasma source and the diagnostics utilised are explained. The chapter begins with a description of the plasma jet, followed by an explanation of power measurements and the implementation of pulse modulation of the RF signal. Next, gas phase diagnostics are discussed, along with the procedures for liquid treatments involving various liquid diagnostics. The chapter concludes with a description of a chemical model of the gaseous species and a transport model for H_2O_2 in the liquid phase.

Gas phase results of the capillary plasma jet are presented in chapter 4. First, the performance of the plasma jet under humidity admixture is discussed, focusing on plasma power, electron density, and gas temperature. The excitation of various species using phase-resolved optical emission spectroscopy (PROES) measurements are visualised. Then gas phase densities of the most important species are discussed and the impact of humidity admixture and plasma power on their production is investigated. This chapter closes with model results on species productions and the impact of pulse modulation on species densities.

The delivery of OH and H_2O_2 from the gas phase into the treated liquid is analysed in chapter 5. It focuses on measuring the concentrations of H_2O_2 and OH in the liquid and their distribution in the liquid. The distribution of H_2O_2 is further modelled by solving the convection-diffusion equation. At the end of the chapter, a comparison between the liquid concentrations and the gaseous densities is made.

The upscaling of the H_2O_2 generation by a larger plasma volume is investigated in chapter 6. The setup and the results of a larger plasma volume are described and discussed in the first section of the chapter. In addition, the use of Ar as feed gas was tested and the plasma performance and the results of the H_2O_2 production when the capillary plasma jet is operated in Ar are discussed in the second part.

Chapter 7 deals with two extended applications of the capillary plasma jet in its species generation. First, the effect of additional reactive components such as N_2 and O_2 to the humidified He plasma on the production of reactive species and their delivery into a liquid was investigated. Second, the H_2O_2 production of the capillary plasma jet operated with high-voltage pulses with rise times in the order of µs or ns is analysed. The experimental adaptions for both investigations are described first individually and then the results regarding the species production and measurements in the liquid are given.

Finally, chapter 8 summarises all findings of the thesis and provides answers to the main research questions.

2. Fundamentals

This chapter provides a theoretical foundation for the physical concepts discussed in this thesis. It begins with an overview of the characteristics of non-equilibrium plasmas at atmospheric pressure. Next, it describes the process of electrical breakdown (ignition) and introduces the theory of streamers. The chapter then describes the essential aspects of the capillary plasma jet, which operates as an RF-driven non-equilibrium atmospheric pressure plasma jet. Key topics include the operating modes under RF conditions and the principles of electrical modelling. Following this, the second section explores the chemistry of a humidified helium plasma to produce H_2O_2, while the third section focuses on plasma-liquid interactions. Finally, the chapter concludes with fundamental concepts related to optical emission spectroscopy (OES) and absorption spectroscopy.

2.1 Non-equilibrium atmospheric pressure plasmas

Low-temperature plasmas had an enormous impact on our society in recent decades, e.g. in the microelectronics industry [53]. These plasmas can be created by depositing energy into a gas, e.g. by applying an external electric field. If the field strength is high enough, ionisation occurs and a plasma is formed, which consists of electrons, ions and neutrons. However, not all ionised gases can be called plasmas. The definition of plasma can be given by [54]:

"A plasma is a quasineutral gas of charged and neutral particles
which exhibits collective behavior."

Thus, besides the presence of charged particles, the quasineutrality and the collective behaviour of the species are important requirements for a plasma. In the plasma, the charged particles (electrons and ions) do not move independently due to the Coulomb force between them. The charged particles shield the potential of each other and on larger scales, the plasma is in a neutral state. However, on small scales, local differences can exist. The deviation from neutrality on small scales is called quasineutrality and the characteristic length scale is the *Debye length* λ_D:

$$\lambda_D = \left(\frac{\epsilon_0 \, k_B T_e}{n_e \, e^2} \right)^{\frac{1}{2}}, \tag{2.1}$$

which depends on the electron temperature T_e and the electron density n_e. To achieve quasineutrality, the dimension of the plasma L has to be much larger than the Debye length: $L \gg \lambda_D$. The collective behaviour means that the motions of the particles depend not only on local conditions but on the whole plasma state. This is valid when the number of particles within a sphere of the Debye length is much larger than unity: $N_D = \frac{4}{3} n \pi \lambda_D^3 \gg 1$.

Another important characteristic of a plasma is its response to alternating external electric fields. This aspect is described by the *plasma frequency* ω_p:

$$\omega_p = \left(\frac{n\, e^2}{\epsilon_0\, m} \right)^{\frac{1}{2}} . \tag{2.2}$$

This frequency depends on the density n and mass m and can be calculated for both electrons and ions, describing the oscillation of particles within plasmas. The frequency of these oscillations determines whether charged particles can effectively follow an external electric field. Regarding the requirements of a plasma, the product of plasma frequency and the mean time between collisions of charged particles with neutral atoms τ has to be larger than unity to achieve electrostatic forces dominate over conventional gas kinetics by collisions: $\omega_p \tau > 1$.

For typical electron densities of APPJs operated in He in the order of $n_e \approx 1 \times 10^{11}\,\mathrm{cm}^{-3}$ [55] and electron temperatures of about $T_e \approx 2\,\mathrm{eV}$ [56, 57], the Debye length and the plasma frequencies of electrons and ions are about $\lambda_D \approx 105\,\mu\mathrm{m}$, $\omega_{p,e} \approx 6 \times 10^9\,\mathrm{Hz}$ and $\omega_{p,i} \approx 7 \times 10^7\,\mathrm{Hz}$, respectively. Considering the dimension of the plasma in the order of millimetres, the dimension is larger than the Debye length and the number of particles within this sphere is greater than unity. Considering the high collision frequency of electrons with the neutral background gas at atmospheric pressure in the order of $10^{12}\,\mathrm{Hz}$ [58] (three orders of magnitude higher than the electron plasma frequency), the product $\omega_p \tau$ is smaller than unity. Thus, gas kinetics dominate over Coulomb interactions and APPJs can be referred to as collisional dominated discharges rather than classical plasmas.

Plasmas and discharges can be created at low pressures in vacuum chambers or higher pressures, for example at atmospheric pressure where high collision rates affect the overall discharge performance. External electric fields are most commonly used to heat the electrons in the plasma. The electric fields can be constant (DC), pulsed at low frequencies in the range of kHz (AC), radio frequency (RF) and electromagnetic waves at GHz frequencies (microwaves) [59]. Using the pulsed or AC excitation mechanisms, thermalisation between the heated electrons and the surrounding ions can be avoided. This is the main feature of low temperature or *non-equilibrium plasmas* [60]. The hot (highly energetic) electrons can trigger chem-

ical reactions while the overall gas temperature, given by ions and neutrals, remains close to room temperature. This is of major importance for applications where heat-sensitive samples are treated as is the case in this thesis where an atmospheric pressure plasma treats liquid samples.

2.1.1 Electrical breakdown

The breakdown of plasmas is characterised by the breakdown voltage from which the production of electrons exceeds the loss of electrons and ionisation of the carrier gas. Then, one electron results in an exponential multiplication of electrons and ions by direct ionisation of the carrier gas and an electron avalanche is created. This simple mechanism is called Townsend breakdown. There, the electron avalanche is described by the *first Townsend coefficient* α, or called Townsend ionisation coefficient, describing the electron production $n_e(x)$ over a length x from an initial density n_0:

$$n_e(x) = n_0 \, e^{\alpha \, x}. \tag{2.3}$$

The dependence of the Townsend ionisation coefficient, normalised to the pressure, on the reduced electric field E/p is described by

$$\frac{\alpha}{p} = A \, e^{-B \, (E/p)^{-1}} \tag{2.4}$$

with empirical gas-dependent constants A and B, pressure p and electric field E. With increasing electric field the Townsend ionisation coefficient increases and breakdown can occur.

The overall breakdown process is described in low-pressure DC plasmas by the *Paschen law*. It provides a relation between the breakdown voltage V_{bd} and the gas, its pressure p and the discharge gap d and is given by [61]:

$$V_{bd} = \frac{B \, pd}{ln(A \, pd) - ln(ln(\frac{1}{\gamma} + 1))}. \tag{2.5}$$

γ accounts for secondary processes that produce electrons such as surface reactions, ion impact production, photoeffect and metastables. An example of a Paschen curve for the breakdown in the DC case is shown in figure 2.1 (a). A minimum of required breakdown voltage exists at a certain product of pressure and distance pd. At low values of pd, the electrons reach the anode fast and cannot generate further electrons on their way and higher breakdown voltages are required to enhance the ionisation. At higher values of pd, the breakdown voltage increases linearly since the probability of the electrons colliding with neutrals increases as the pressure or the distance increases. Then, the electrons lose energy before they ionise and higher

breakdown voltages are required.

In the RF case, the breakdown process differs from the DC case. The electrons follow the alternating electric field and oscillate around their rest position and the net energy gain of the electrons would be zero. However, due to elastic collisions with neutrals, the electrons move out of phase with the alternating electric field and a net energy gain by the electrons is achieved. Over many oscillations, the electrons can gain high energies and the overall breakdown voltage in RF plasmas is lower than in DC plasmas at the same *pd* value. The shape of the Paschen curve for RF looks similar to the DC case as shown in figure 2.1 (b). At low-pressure values, the electrons are lost to the walls before they can be kicked out of phase and higher breakdown voltages are required. At high pressure values, similar to the DC case too many collisions with neutrals occur and the energy of the electrons is not high enough to perform ionisation. When designing atmospheric pressure plasmas, the pressure is fixed and significantly high. Thus, to obtain achievable breakdown voltages the gap distance has to be lowered. Since the value is in the order of micro- to millimetres, the name of *micro-scale atmospheric pressure plasmas* has been proposed [62].

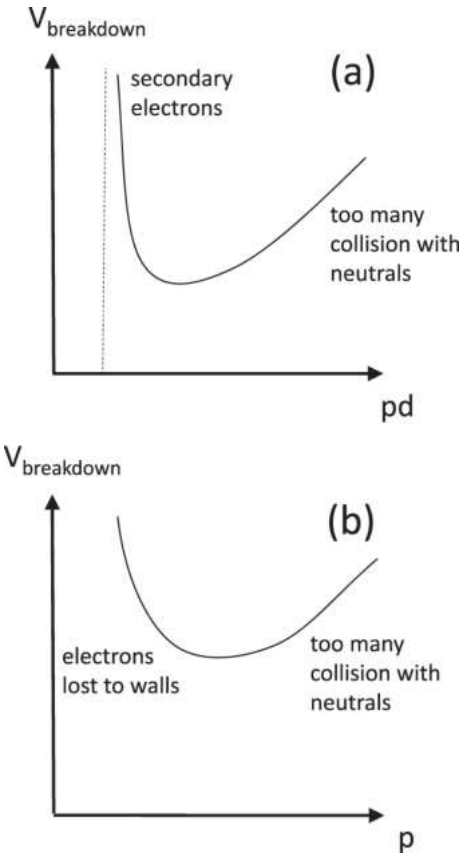

Figure 2.1: Examples of Paschen curves in **(a)** DC electric field and **(b)** in RF electric field. Taken from [60].

Besides the pressure and the electrode distance, the feed gas also affects the ignition and maintenance of the plasma as the ionisation properties are different for different gases. The noble gases Ar and He are widely used for atmospheric pressure plasmas as the ignition in noble gases is easier because no dissociation of these atoms occurs. He and Ar differ in their gas-dependent constants A and B, as well as in their ionisation energies and thermal conductivities. The parameters for He and Ar are listed in table 2.1. He requires a higher ionisation energy than Ar and has a higher thermal conductivity. This prevents the He plasma from thermal instabilities (see the discussion below). The gas parameters A and B are lower for He, which results in a higher first Townsend coefficient for He. Thus, although ionisation requires more energy for Ar, the volumetric ionisation rate is higher for He than that for Ar

and the ignition of Ar is more difficult. Therefore, the COST reference plasma jet for example is normally operated in He rather than Ar [13, 63].

The ignition in N_2 or air is even more difficult than in Ar. The parameters A and B for N_2 and air are also listed in table 2.1. The resulting first Townsend coefficients at an applied voltage of 2 kV and 5 kV were also calculated for N_2 and air. The first Townsend coefficients of N_2 and air are one and two orders of magnitude lower than the first Townsend coefficient of Ar. Thus, even higher voltages are required to ignite a plasma in N_2 or air at the same pressure and gap distance.

Table 2.1: Characteristic gas parameters of He, Ar, N_2 and air. Values for ionisation, thermal conductivity and heat capacity were taken from [64], parameters A and B from [61, 65]. α was calculated by using the A and B values for applied voltages V of 2 kV and 5 kV at a gap distance d of 0.1 cm at a pressure of 760 Torr (atmospheric pressure) with $V = E\,d$.

Parameter	**He**	**Ar**	**N_2**	**Air**
Ionisation energy [eV]	24.59	15.76	15.58	-
Thermal conductivity at 300 K [$\mathrm{mW\,m^{-1}\,K^{-1}}$]	156.7	17.9	26.0	26.2
Heat capacity [$\mathrm{J\,g^{-1}\,K^{-1}}$]	5.2	0.52	1.04	0.92
A [$\mathrm{Torr^{-1}\,cm^{-1}}$]	2.8	13.6	5.5	14.6
B [$\mathrm{V\,Torr^{-1}\,cm^{-1}}$]	34	235	273	365
$\alpha_{2\,\mathrm{kV}}$ [ion pairs $\mathrm{Torr^{-1}\,cm^{-1}}$]	0.769	0.002	1.7×10^{-4}	1.4×10^{-5}
$\alpha_{5\,\mathrm{kV}}$ [ion pairs $\mathrm{Torr^{-1}\,cm^{-1}}$]	1.670	0.382	0.087	0.057

2.1.2 Streamer

After the breakdown of atmospheric pressure plasmas, the electrons can follow the external electric field and in DC or low-frequency pulsed plasmas so-called negative streamers develop [66]. The streamer consists of a streamer head and a streamer channel. The negative streamer head is dominated by electrons and the slow-moving ions remain in the streamer channel. The streamer channel is slowly neutralised by electrons diffusing from the outside into the channel. Furthermore, there are positive streamers that distribute towards the cathode if photoionisation is a dominant process. The avalanche of electrons produces strong photon emission that ionises the gas in the direction of the cathode. These electrons travel to the anode, neutralise the streamer channel and leave another ion cloud behind them, which is shifted towards the cathode. Once the streamer has fully developed between the electrodes, a conductive short-circuit is formed and an arc between the two electrodes will occur

when the voltage is high enough [54]. This arc may damage the electrodes, requiring the plasma to be turned off or the voltage lowered. The development of streamers and sparks is mainly present when the plasma is operated with DC voltages or under low-frequency pulsing with µs or ns pulses and is avoided in RF discharges.

However, spark formation can also occur in RF operation due to instabilities within the plasma, one of which is thermal instability. When the electron density experiences a local disturbance that increases its value, the power deposited at that location is enhanced. With more power being delivered, the gas temperature rises. Since the pressure remains constant and is proportional to the product of gas density and temperature, the background gas density decreases. This reduction leads to an increased reduced electric field, which in turn raises the electron temperature. As a result, the ionisation rate increases, creating more electrons and further raising the electron density. This sets off a positive feedback loop, resulting in thermal instability. Such instabilities can also lead to spark formation in atmospheric pressure plasmas.

To prevent spark formation in atmospheric pressure plasmas, various technical developments can be employed. One effective method is to place a dielectric material in front of the electrodes, which helps to avoid the formation of conductive short circuits. When the electrons from the streamer head reach the anode covered by the dielectric, they accumulate on the dielectric surface, resulting in its charging. This charging shields the external electric field and the plasma will be distinguished. To effectively remove the charges in front of the anode and reignite the plasma, alternating voltages must be applied. Alternatively, short pulses can be used instead of a constant DC voltage. Fast alternating voltage pulses with RF frequencies can also help prevent spark formation, even in the absence of dielectrics on the electrodes. In this case, the rapid change in the polarity of the electric field prevents the electrons from reaching the anode. Additionally, using He can help avoid thermal instabilities in the plasma due to its high thermal conductivity and heat capacity.

When fast voltage pulses or alternating voltage in the RF range are applied, only electrons can respond to the electric field, while ions remain largely unaffected. This results in a non-equilibrium state between the electrons and ions. The external electric field heats the electrons to several electronvolts, while the ions and neutral particles stay at room temperature. This difference creates a non-equilibrium atmospheric pressure plasma.

2.1.3 Capillary plasma jet

Atmospheric pressure plasma jets are widely used for applications [63, 67–70] with the advantage of decentralized production of reactive species at local facilities [2]. In this thesis, an APPJ utilising a capillary and mainly operated at 13.56 MHz (RF) in He is used. The capillary plasma jet is a further development of the COST reference plasma jet [13, 15]. The electrodes are arranged in a parallel arrangement and the capillary is placed between the electrodes with the gas flowing through the capillary as illustrated in figure 2.2.

This configuration is commonly known as a capacitively coupled plasma, similar to a capacitor. Furthermore, the electric field in this arrangement is perpendicular to the gas flow. Thus, the plasma is confined between the two electrodes, forming an active plasma channel with the cross-section of the capillary and the length of the electrodes. This jet arrangement is referred to as a cross-field plasma jet. In the active plasma channel, ionisation, dissociation, and excitation driven by electrons occur as well as gas chemistry. Downstream the active plasma channel, the so-called effluent is present. The effluent is characterised by reactive species carried by the feed gas. Due to the absence of an electric field, electrons are not present in the effluent and only neutral gas chemistry occurs. The reactive species from the plasma are then transported to a sample, in the presented thesis a liquid sample. At the interface of the effluent and the sample, the reactive species produced by the plasma can interact with the sample. This arrangement ensures that only reactive species interact with the sample, neither electrons nor the electric field itself. This is the main advantage of sample treatment by cross-field atmospheric pressure plasma jet as performed in this thesis.

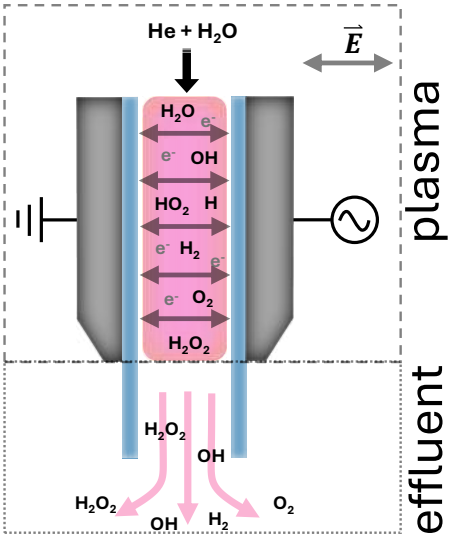

Figure 2.2: Sketch of the setup of the capillary plasma jet operated in humidified He.

However, highly energetic photons in the vacuum ultraviolet regime (VUV) below wavelengths of 150 nm and with energies up to 10 eV produced in plasmas can also interact with samples treated by cross-field plasma jets [71–75]. In the case of the COST reference plasma jet, these are measurable a few millimetres downstream of the plasma channel through the effluent [74]. It is likely that the capillary plasma jet also produces VUV photons, especially at higher plasma powers. The VUV photons can interact with the samples at short distances (in the millimetre range) and due

to their high energy, the VUV photons can trigger certain reaction processes at the surface of the sample.

Furthermore, the capillary acts as the dielectric to prevent the APPJ from sparking. Thus, high voltage up to 9 kV can be applied and plasmas can be generated by the capillary plasma jet with low-frequency pulses. This enables the operation of the capillary plasma jet using both RF excitation and low-frequency pulses with rise times in the order of µs or ns. Therefore, the capillary plasma jet provides a flexible plasma source for operation at atmospheric pressure.

Modes in RF operation

RF-driven APPJs operate in different modes depending on the applied voltage. This was investigated previously by PROES measurements [76], for example on the COST reference plasma jet [57, 77] and by simulations [78]. The finding also applies to the capillary plasma jet under RF operation [15]. At low applied voltages, close to the breakdown voltage, and correspondingly low plasma powers, the plasma is operated in the Ω-mode where the electrons are heated due to sheath expansion. Ionisation occurs at the sheath edges where a high bulk electric field is present. Further, not all electrons can follow the retreating sheath on the opposite side due to collisions at high pressure and a region of negative space charge is created. By this, an electric field is established accelerating the electrons towards the electrode. These two heating processes occur when the current reaches its maximum and leads to the presence of highly energetic electrons on both sides, visualised by two emission maxima in the plasma bulk at both sheath edges [57]. At higher voltages and higher plasma powers, a third emission maximum occurs. This can be attributed over time to the maxima of the applied voltage, where the electric field is largest at the cathode. In this case, predominately secondary effects in the sheath play a key role and high energetic electrons are present there leading to emission maxima in the sheath region. These secondary effects are Penning ionisation, charge transfer, electron reflection, photoionisation and surface reactions. Due to the impact of metastable species at atmospheric pressure by Penning ionisation, the second mode is called Penning mode [57].

Electric model

The capillary plasma jet can be seen as a capacitively coupled plasma jet. It can be electronically described as a capacitor and the impedance of the plasma jet can be analysed using an electrical equivalent circuit model. Here, the model described in [57, 79, 80] was used. This model was previously applied to the COST reference plasma jet [80] and was extended by the impact of the dielectric character of the

capillary used in this work. The circuit models in plasma-on and plasma-off cases are shown in figure 2.3. It consists of an RLC network with different components.

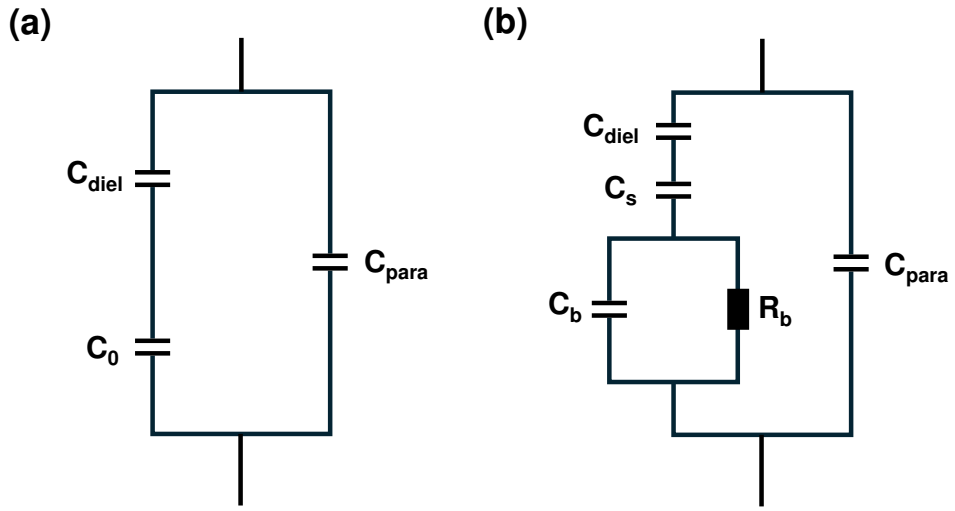

Figure 2.3: Electrical equivalent circuits of the capillary plasma jet with **a)** plasma off and **b)** plasma on. Taken from [80] and extended by the impact of the capillary C_{diel}.

The plasma impedance is divided into the bulk impedance of resistance R_b and bulk reactance X_b as well as the sheath reactance X_s. The electrode arrangement can be seen as a capacitor and without plasma, its capacitance C_{jet} can be calculated. Golda et al. have shown that in the plasma-off case, the capacitance C calculated from the measured impedance of the system deviates significantly from the theoretical value for the COST reference plasma jet [80]. This is partly due to the shielding of the electrodes affecting the capacitance of the plasma jet. By introducing a parasitic capacitance C_{para} in parallel to the jet capacitance, this aspect is considered [80]. In this work, a dielectric was introduced into the plasma jet leading to another capacitance contribution C_{diel} in series to the capacitance of the gas C_{gas}. Thus, the total capacitance of the system C is given by

$$C = C_{jet} + C_{para} \tag{2.6}$$

$$\frac{1}{C_{jet}} = \frac{1}{C_{gas}} + \frac{2}{C_{diel}} \tag{2.7}$$

The capacitance of the gas and dielectric can be calculated from

$$C_{gas} = \epsilon_0 \epsilon_{gas} \frac{A}{d_{gas}} \quad , \quad C_{diel} = \epsilon_0 \epsilon_{diel} \frac{A}{d_{diel}} \tag{2.8}$$

with the electrode surface area A (same surface area of the capillary), the width of the gas channel d_{gas} given by the inner diameter of the capillary, the width of the

capillary d_{diel} given by the wall thickness of the capillary and the permittivity of the gas $\epsilon_{gas,He} = 1.1\,\epsilon_0$ and dielectric $\epsilon_{diel} = 3.5\,\epsilon_0$.

The plasma impedance Z_P is given by the plasma resistance R_P, the plasma reactance X_P and reactance of the dielectric X_{diel}, while the parasitic impedance Z_{para} is only given by its reactance X_{para}:

$$Z_P = R_P + iX_P + iX_{diel}, \tag{2.9}$$

$$Z_{para} = iX_{para}. \tag{2.10}$$

The absolute value of the total impedance of the system Z is experimentally obtained by dividing the applied voltage U by the measured current I

$$|Z| = \frac{U}{I}. \tag{2.11}$$

Thus, the impedance can be determined by measuring voltage and current. Furthermore, the impedance is theoretically represented in the electronic equivalent circuit diagram as follows:

$$\frac{1}{Z} = \frac{1}{Z_P} + \frac{1}{Z_{para}}, \tag{2.12}$$

$$\frac{1}{R + iX} = \frac{1}{R_P + iX_P + iX_{diel}} + \frac{1}{iX_{para}}. \tag{2.13}$$

From the solution of the equations, the resistance R and reactance X of the system are obtained and the bulk resistance and reactance can be obtained:

$$R_P = \frac{RX_{papa}^2}{R^2 + (X - X_{para})^2} \tag{2.14}$$

$$X_P = -\frac{R^2(X_{diel} + X_{para}) + (X - X_{para})(-X_{diel}X_{para} + X(X_{diel} + X_{para}))}{R^2 + (X - X_{para})^2} \tag{2.15}$$

The sheath impedance is given by $X_s = X_0 - X_P$ and via the sheath impedance, the time-averaged sheath width $< s >$ can be estimated [79, 80]:

$$< s >= 0.5 \cdot \epsilon_0 \cdot A \cdot \omega \cdot |X_s| \tag{2.16}$$

with the RF angular excitation frequency $\omega = 2\pi\, f_{RF}$ and the cross-section area of the plasma A. Furthermore, the electron density n_e can be derived from the resistance of the bulk and the sheath thickness s via [79]:

$$n_e = \frac{d_{gas} - 2s}{A\,R_b}\frac{\nu_m\, m_e}{e^3} \tag{2.17}$$

with the electron-neutral collision frequency ν_m with a value of $1.52 \times 10^{12}\,\mathrm{s}^{-1}$ for

He [58]. The set of equations regarding the calculations of the impedance and the estimation of sheath thickness as well as electron density are used in chapter 4 to obtain the values of the sheath thickness and electron density from voltage and currents measurements of the capillary plasma jet operated in He+H_2O.

2.2 Humidified plasma chemistry

Within the plasma, various physical and chemical reactions can occur. These can involve the impact of electrons to create radicals A and B from molecule AB or only reactions of radicals and neutrals to transform species A and B into C and D [61]:

$$e^- + AB \longrightarrow e^- + A + B,$$

$$A + B \longrightarrow C + D\,.$$

The rate coefficients of the reactions depend on the electron temperature if electrons are involved or the gas temperature if chemical reactions take place in the gas phase. Due to the non-equilibrium character of atmospheric pressure plasmas, these rate coefficients and the overall chemistry differ significantly from thermal chemistry. The evolution of the species can be described by differential equations with the rate coefficients as proportionality constant [61] and the sets of differential equations are often solved numerically by global models [81].

The plasma chemistry of a He+H_2O plasma is quite complex, as a large number of species are involved, which are coupled by various reactions in the active plasma phase and the effluent. Several modelling groups have investigated the most important reactions that take place in a humidified atmospheric pressure plasma [36, 37]. Schröter et al. have investigated the most important production and consumption reactions of OH in the case of the COST reference plasma jet at various humidity admixtures [37]. The chemistry starts with the electron impact dissociation of H_2O in the plasma, producing OH and H

$$e^- + H_2O \longrightarrow OH + H + e^-\,. \qquad \text{(R 2.1)}$$

This reaction is responsible for more than 60 % of the production of OH at humidity admixtures higher than 100 ppm [37]. An energy delivered by the electrons of about 5.15 eV is necessary to perform this reaction [82]. OH radicals then recombine to produce H_2O_2, which accounts for nearly 50 % of the loss of OH [37]

$$OH + OH + M \longrightarrow H_2O_2 + M\,. \qquad \text{(R 2.2)}$$

Furthermore, OH is also involved in the consumption of H_2O_2 via

$$OH + H_2O_2 \longrightarrow H_2O + HO_2 \cdot \quad \text{(R 2.3)}$$

At an enhanced OH production, the production of H_2O_2 is enhanced but also the consumption of H_2O_2. Thus, an equilibrium between the production of H_2O_2 and its consumption by OH is established. From the consumption reaction of OH and H_2O_2, the HO_2 radical is produced.

Besides the formation of OH, H_2O_2 and HO_2, a significant amount of atomic species such as H and O are produced in humidified plasmas [83]. H is mainly produced during the electron impact dissociation of H_2O given in equation R 2.1 and O from electron impact dissociation of O_2 and the recombination of OH radicals [83]

$$e^- + O_2 \longrightarrow 2\,O + e^-, \quad \text{(R 2.4)}$$

$$2\,OH \longrightarrow H_2O + O \cdot \quad \text{(R 2.5)}$$

The atomic species are further converted to their molecular pendants by several mechanisms. The most important ones are recombination of H at the walls and reaction of H with HO_2 as well as O with OH [83]:

$$H \longrightarrow \frac{1}{2}\,H_2 \quad \text{(at wall)}, \quad \text{(R 2.6)}$$

$$H + HO_2 \longrightarrow H_2 + O_2, \quad \text{(R 2.7)}$$

$$O + OH \longrightarrow O_2 + H \cdot \quad \text{(R 2.8)}$$

All in all, the main species involved in the chemistry of a humidified atmospheric pressure plasma are the radicals OH, H, O and HO_2 and the long-lived species H_2O_2, O_2 and H_2. To gain information about the system and its performance in terms of H_2O_2 production, these species must be measured and taken into account in the modelling.

2.3 Plasma-liquid interactions

In plasma-driven biocatalysis, enzymes are located in a liquid environment. To deliver the plasma-generated H_2O_2 to the enzymes, it must be dissolved in a liquid. Thus, a combined plasma-liquid system is used in this work. Detailed reviews of plasma-liquid interactions can be found in the literature [38–40, 84–89]. When the plasma is in contact with a liquid sample, various processes at the plasma-liquid interface occur as presented in figure 2.4. In general, impinging ions from the plasma

can lead to sputtering of H_2O, its fragments or electrons from the liquid interface. These can enter the plasma and lead to further chemical reactions. Other plasma-generated species like radicals and neutrals can enter the liquid and diffuse through the liquid interface. Furthermore, evaporation might occur leading to the release of H_2O molecules from the liquid interface into the plasma. UV photons from the plasma can lead to the dissociation of H_2O at the liquid interface and electrolysis might also occur and H_2 as well as O_2 might be produced. The dissolved or produced radical species in the liquid interface will further react to form long-lived aqueous species like H_2O_2, NO_2^- or O_3 that are present in the liquid bulk.

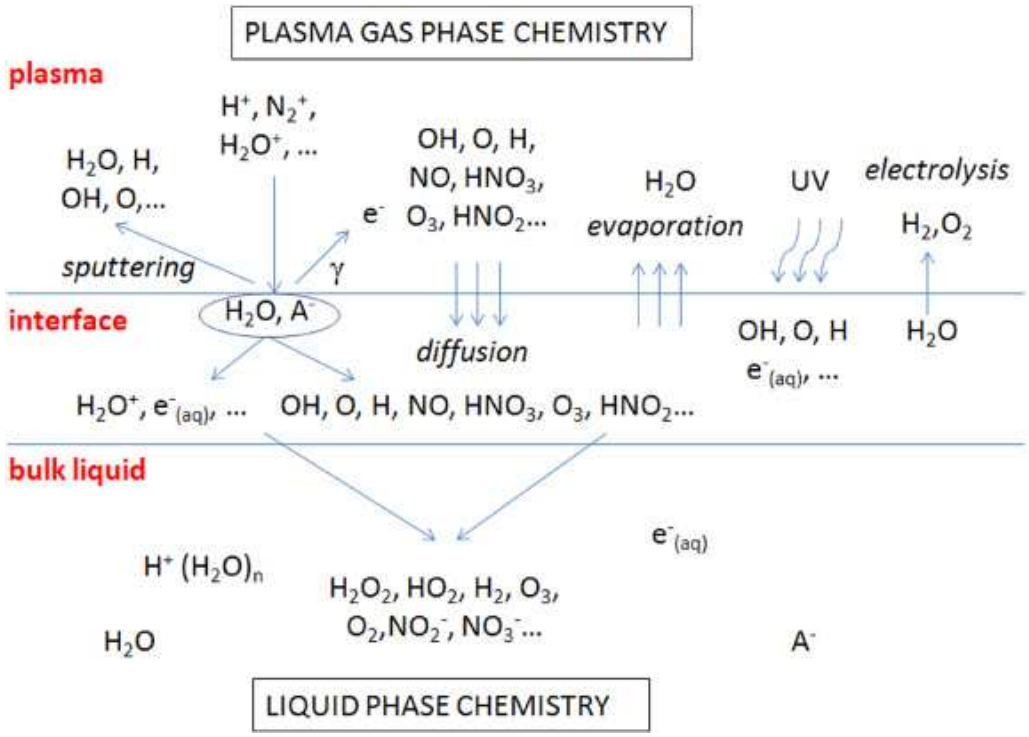

Figure 2.4: Overview of the most important plasma-liquid interactions. Taken from [90].

Not all of the processes described will appear in the plasma-liquid system used in this work. Since the plasma is confined between the two electrodes of the capillary plasma jet and the distance between plasma and liquid surface is large (more than 20 mm), sputtering by ions and electrolysis are not present. The impact of UV or even VUV photons might also be negligible due to the long distance and their interaction in the effluent. H_2O evaporation is also negligible as it does not enter the plasma due to the gas flow and is intentionally added to the gas flow. Thus, only the interaction of plasma-generated neutral and radical species at the liquid interface occurs. This is also the argument for choosing the plasma-liquid system used for the plasma-driven biocatalysis as it provides a stable and controllable system of species generation and delivery to a liquid sample.

Once the species are generated in the plasma, they are transported to the liquid surface via the effluent. The species dissolve in the liquid due to their solubility, and transportation mechanisms along with chemical reactions influence their distribution within the liquid. The solubility of the species and their transportation behaviour in the liquid are described in the following.

2.3.1 Solubility of species

The solubility of gaseous species into liquid phase is described by Henry's law, first described by Henry in 1803 [91]: the amount of dissolved gas of a species is proportional to the partial pressure of the species in the gas phase. The proportionality factor is the so-called "Henry's law constant". This factor is often referred to in literature, however, the volatility of aqueous species into the gas phase is also described via Henry's law with its constant. Therefore, the name " Henry's law solubility constant" should be used when referring to the dissolution of substances from the gas phase into the liquid phase, or conversely "Henry's law volatility constant" [92, 93]. The Henry's law solubility constants of various important plasma-generated species are listed in tables 2.2. The constant is specified there in the following form [92, 93]

$$H_s^{cp} = \frac{c_i}{p} \tag{2.18}$$

with the concentration c_i of a species i in the liquid phase and the partial pressure p of the species in the gas phase. The highest constant can be attributed to H_2O_2 and thus, it is the most soluble species in aqueous solutions. This is of advantage for the plasma-liquid system investigated as H_2O_2 is the desired species for the plasma-driven biocatalysis processes and the main focus is to maximise the H_2O_2 concentration in the PTL. Two orders of magnitude lower constants are found for HO_2, OH as well as H and the molecules H_2 and O_2 have even lower Henry's law solubility constants. In addition, O_3 also has a low Henry's law solubility constant. These species are less soluble. When the gas stream of the effluent hits the liquid surface, the species are differently dissolved in the liquid.

In the case of nitrogen species, NH_3 and HNO_2 have similar Henry's law solubility constants like OH, while NO_2 has a lower constant similar to O_2. Thus, also these species are less soluble in liquids. The concentration of species in the liquid is often given in the unit of molar describing the amount of a species (in mol) concentrated in one litre of a liquid:

$$1\,\mathrm{M} = 1\,\frac{mol}{L}. \tag{2.19}$$

Table 2.2: Henry's law solubility constants for various species in aqueous solutions. An overview can be found in [92].

Species	H_s^{cp} / $\frac{\mathbf{mol}}{\mathbf{m^3\,Pa}}$	**Ref**
H_2O_2	8.2×10^2	[94]
HO_2	6.8	[95]
OH	0.6	[96]
H	2.6×10^{-6}	[95]
H_2	7.8×10^{-6}	[95]
O_2	1.3×10^{-5}	[95]
O_3	1×10^{-4}	[95]
NH_3	0.3	[97]
HNO_2	0.6	[98]
NO_2	1.4×10^{-4}	[99]

2.3.2 Transport phenomena in liquids

Once the species are dissolved in the liquid, transport processes in the liquid take place. In several studies, transport processes in plasma-liquid systems, as used in this work, were investigated using modelling approaches [43, 44, 100, 101]. However, experimental studies are rare. The gas stream leaving the plasma moves in the direction of the liquid surface. It hits the liquid surface, moves radially across the surface and is finally blocked by the wall of the liquid vessel. By this, a tangential velocity at the liquid interface is created that induces a shear stress in the liquid from the gas stream. Vortices are created with the downward stream at the vessel sides and the upward stream in the centre where the gas hits the surface [28, 42–44, 101]. Furthermore, the interaction of the gas stream with the liquid surface results in a depletion of the liquid surface at the point of hitting. The higher the gas velocity, the deeper the depth of the depletion [43, 101].

The transport processes of the species in the liquid can be either by convection due to the flow patterns in the liquid or by diffusion due to concentration gradients. The transport of species in the liquid can be described by the convection-diffusion equation

$$\frac{\partial c}{\partial t} + \nabla \cdot (\mathbf{u}\, c) = \nabla \cdot (D\, \nabla c) - R_i. \tag{2.20}$$

There, c is the concentration of the species in the liquid, $\mathbf{u}$ the velocity in the liquid, D the diffusion coefficient and R_i is a source and loss term. The diffusion of species (first term on the right-hand side) is driven by gradients in the concentration present

in the liquid. Since the species are dissolved at the liquid surface, the concentration gradient at the liquid surface is strong and leads to the distribution of the species into the liquid bulk. Due to the interaction of the gas stream with the liquid surface and the resulting vortex patterns in the liquid, a convective mixing occurs in the liquid (second term on the left side).

Furthermore, chemical reactions in the liquid affect the distribution of the species, described by the source and loss term R_i in the convection-diffusion equation. Particularly reactive species are likely to react at the liquid interface and do not reach deep into the liquid bulk. In general, with increasing treatment time the penetration depths of the species increase. Long-lived species like H_2O_2, NO_2^- or NO_3^- can reach up to millimetres into the liquid and show a parabolic decay, while radicals like OH, O or HO_2 strongly decay at the liquid interface and barely exceed depths of 100 µm [102–106]. Furthermore, the pH value of a liquid significantly influences the chemistry of the liquid species present. For instance, under acidic conditions, both H_2O_2 and NO_2^- are unstable and will react to form NO_3^-, as demonstrated in the post-discharge evolution of species in a PTL [107]. In acidic environments, NO_2^- and H_2O_2 react with the abundant H^+ ions to generate peroxynitrous acid (HNO_3), which is subsequently converted into NO_3^- [86, 107]. Therefore, it is important to consider these liquid reactions when discussing the measured concentrations of species in the PTL. In most experiments conducted in this thesis, a phosphate buffer (KPi) at pH 7 was utilised, resulting in liquid chemistry occurring at a neutral pH, with equal amounts of H^+ and OH^- ions. This buffer maintains the pH value during plasma treatment.

Similar to the difference in plasma characteristics of He and Ar plasmas, the plasma-liquid interactions of He and Ar gas are very different. This was modelled for an APPJ at 1 slm gas flow rate and a distance of 14 mm between the nozzle and the liquid surface [108]. Due to the higher mass of Ar, the Ar gas stream conserves the velocity on its way to the liquid surface. The He gas stream shows a reduced gas velocity in the effluent. Thus, the interaction of the Ar gas stream with the liquid surface is stronger and the Ar gas shows a stronger depletion of the liquid surface and stronger vortices in the liquid [108]. This leads to different spatial distribution profiles of the species in the liquid when treating the liquid with Ar or He plasmas.

2.3.3 Source of H_2O_2 production

When species are detected in the PTL, the source of their creation is not clearly defined. It's uncertain whether these species are produced in the plasma and then dissolved in the liquid, or if they are formed in the liquid as a result of the plasma's impact. To investigate the source of the H_2O_2 production of the COST reference

plasma jet and measured in a PTL, Gorbanev et al. performed isotope tracing by using D_2O in the gas phase or the liquid phase [31]. They measured the formation of H or D radicals in the liquid by PBN spin trapping. When H_2O was added to the feed gas and D_2O was present in the liquid phase, H radicals were produced and when D_2O was present in the gas phase and H_2O in the liquid phase, D radicals were produced. From these results, they concluded that the H_2O_2 formation mostly happens in the gas phase of the plasma rather than in the liquid phase and only a minor production occurs in the effluent region [31].

This is an important finding for the plasma-liquid system investigated in this work. Since the species are mainly produced in the gas phase, controlling the gas phase chemistry in the plasma defines the species mixture in the liquid. Therefore, understanding the gas phase densities of the species produced by the capillary plasma jet is crucial for controlling the liquid species.

2.4 Optical emission spectroscopy

The energetic electrons present in the plasma can excite atoms and molecules. These excited states de-excite by spontaneous emission with radiation at a fixed wavelength λ given by the energy difference between the upper k and lower i level of the transition ΔE occurs:

$$\lambda = \frac{h\,c}{\Delta E} = \frac{h\,c}{E_k - E_i}. \tag{2.21}$$

E_k is the energy of the upper level k, E_i is the energy of the lower level i, h is the Planck constant and c is the speed of light. This leads to the characteristic light emission of plasmas and by detecting the radiation with a spectrometer, information about the plasma can be gained. Optical emission spectroscopy (OES) has the main advantage of being non-invasive and allows for real-time monitoring of the plasma. However, only information on excited states can be gained. Thus, if lines of an atom or molecule are not present in OES spectra, they can still be in the plasma but are not excited, not visible or reabsorbed. However, if some lines or band emissions are present in the OES spectra, the energy and wavelength of the emission can be attributed to the respective atoms or molecules. Thus, OES provides a powerful spectroscopic tool to investigate the species' behaviour in the plasma [109–111].

When the emission lines of the plasma and their temporal behaviour are observed during the excitation within the RF cycle, insights into the electron dynamics can be gained. This aspect is used during phase-resolved optical emission spectroscopy (PROES) analysis of the plasma [76]. Some emission lines present in OES spectra of a He+H_2O plasma used for PROES analysis are listed in table 2.3 with the excitation energy of the upper state of the transition. The He-706 line has the

highest excitation energy of 22.72 eV. Thus, by analysing this line, the impact of highly energetic electrons can be investigated. On the other hand, the OH band emission around 308 nm has a lower excitation energy of 4.17 eV and electrons with lower energies can excite the band emission of the OH radical.

Table 2.3: Transitions investigated by PROES with corresponding excitation energy. Values were taken from [112, 113].

Species	Transition	Wavelength / nm	Excitation energy / eV
He	$3s^3S^1 \rightarrow 2p^3P^0$	706.5	22.72
OH	$A^2\Sigma \rightarrow X^2\Pi$	308	4.17
H	$3d \rightarrow 2p$	656.3	12.09
O	$3p^5P \rightarrow 3s^5S^0$	777.5	10.74
O	$3p^3P \rightarrow 3s^3S^0$	844.6	10.99

The band emission of molecules can be either rotationally or vibrationally excited. By analysing the spectra, the contribution of both can be investigated and rotational as well as vibrational temperatures of the species can be determined. The temperatures can be gained by creating a Boltzmann plot or comparing the measured with simulated spectra [109]. From the rotational temperature, information about the gas temperature can be gained. Under the assumption of the Franck–Condon principle, the rotational quantum number is conserved by the electron impact excitation and the rotational temperature in the excited state represents the rotational temperature in the ground state. Furthermore, the rotational levels of the ground state must be populated by heavy particle collisions. Then, the rotational temperature resembles the gas temperature [109].

The determination of the gas temperature from the rotational temperature is often used and broadly investigated and details can be found in review and theory papers [109, 114, 115]. In equilibrium, the distribution of the rotational temperature follows a Boltzmann distribution and a linear relationship can be found in the Boltzmann plot. However, in non-thermal plasmas, deviations of the Boltzmann distribution are often present and deviations from the linear relationship in the Boltzmann plots are an indicator of the non-Boltzmann distribution [116]. In this case, a two-temperature Boltzmann distribution can be used to fit the data and the rotational temperature is obtained from the lower rotational states as the higher states are overpopulated [116].

The rotational temperature of OH(A – X) is often used to determine the gas temperature in plasma as the OH band emission is present in spectra from many plasmas due to water impurities in the feed gas [116–120]. This method was also applied

in this work as a He+H_2O plasma was investigated and fitting of the OH(A–X) spectra was performed based on the LIFBASE database [121]. However, at high humidity admixture, the rotational levels of OH are overpopulated due to the large collisional quenching rate of OH(A) by H_2O [114, 122]. The distribution of the rotational temperature then varies from the single-temperature Boltzmann distribution to a two-temperature distribution. In He+H_2O plasmas, a single-temperature Boltzmann distribution of OH(A–X) was found to be valid at humidity concentrations below 1000 ppm [122]. Furthermore, an overlap of the N_2(C–B) emission into the OH(A–X) band emission can lead to distortion when determining the rotational temperature of OH(A–X) [123].

The measured spectral lines have a certain spectral width, induced by different broadening mechanisms. This includes natural broadening, Doppler broadening, Stark broadening, van der Waals broadening or resonance broadening (pressure broadening) and instrumental broadening. For evaluating data obtained by OES, the underlying line-broadening mechanisms have to be considered and evaluated [109]. Details on the different broadening mechanisms can be found in the literature [109, 114, 115].

Besides the observation of spontaneous emission from the plasma, resonant fluorescence can be intentionally used to gain information about the density of species in the plasma. This is used in the laser-induced fluorescence (LIF) spectroscopy, where a lower level of an atom or a molecule is excited by a beam of laser radiation and the subsequent emission of radiation of the upper state is detected [124]. Here, LIF was applied to measure the density of OH as it was performed in various studies [125–127]. The experimental setup and the analysis of the data of the (LIF) diagnostics are explained in chapter 3.

2.5 Absorption spectroscopy

The absorption of light by atoms and molecules is a method to determine the densities of species in plasmas or other mediums. Absorption spectroscopy is a simple, in-situ and non-intrusive diagnostic technique [128]. The wavelength-dependent absorption of light by a medium is described by the Beer-Lambert law

$$I(\lambda) = I_0\, e^{-N\,\sigma(\lambda)\,L}, \tag{2.22}$$

with the transmitted radiation intensity $I(\lambda)$, the incident intensity I_0, the density N of the species, the absorption cross-section $\sigma(\lambda)$ and the absorption length L. Thus, the absorption increases exponentially with the density of the species and

the absorption length. If low densities of species should be measured, it might be helpful to increase the absorption length. Experimentally, the absorbance is often measured, which is given by

$$Absorbance(\lambda) = -ln\left(\frac{I}{I_0}\right) = -N\,\sigma(\lambda)\,L. \tag{2.23}$$

In this work, fourier-transform infrared (FTIR) spectroscopy was utilised to measure the H_2O_2 density in the gas phase. Additionally, UV absorption spectroscopy was employed to visualise the distribution of H_2O_2 in the liquid, while spectrophotometry was used to measure the H_2O_2 concentration in the liquid. In the UV absorption spectroscopy of H_2O_2, only relative absorbance was measured instead of absolute concentrations. The methods are explained in detail in chapter 3.

3. Experimental procedure and modelling

In this chapter, the experimental details of the plasma source and the diagnostics are described. First, the plasma jet with its gas and power supply is explained followed by a description of the plasma power measurements and the details of power modulation of the RF plasma. Afterwards, gas phase diagnostics are explained in the order of temperature measurements, laser-induced fluorescence (LIF) spectroscopy, fourier-transform infrared (FTIR) spectroscopy, mass spectrometry and phase-resolved optical emission spectroscopy (PROES). Subsequently, the procedure of liquid treatments with the various liquids diagnostics such as UV absorption spectroscopy, spectrophotometry and electrochemical sensing of H_2O_2 as well as terephthalic acid (TA) dosimeter and chemiluminescence (CL) of luminol for the detection of OH are explained. At the end of this chapter, a chemical model of the gaseous species and a transport model of H_2O_2 in the liquid are presented.

3.1 Capillary plasma jet

A micro-scale atmospheric pressure plasma jet (µAPPJ) was used in this work. The experimental setup is shown in figure 3.1 with the gas and power supply in part (a) and a front view of the cross-section of the plasma jet in part (b). The design of the plasma jet used was based on the well-known COST reference plasma jet [13], but was extended by a capillary acting as a dielectric between the two electrodes. The name of the plasma jet is therefore simply capillary plasma jet. Using the capillary as dielectric allows a greater variability of the plasma volume and operating parameters as arcing is avoided. The capillary plasma jet was developed at Kiel University and was described in an earlier publication [15]. It consisted of two stainless-steel electrodes and a Borosilicate glass capillary (CM Scientific Ryefield (EU) Ltd) through which the operating gas flows. The capillary had a cross-section of 1 mm × 1 mm and a wall thickness of 0.2 mm (see figure 3.1 b). The electrodes were 40 mm long resulting in a plasma volume of 165.6 mm^3. Please note that a wider capillary was used in chapter 6 to investigate the scaling possibilities of the plasma volume. The experimental setup for the wider capillary is explained there.

The gas supply consisted of two mass flow controllers (Analyt MTC, up to 2 slm) and an ice-cooled bubbler system. Helium (purity 5.0) was used as the carrier gas

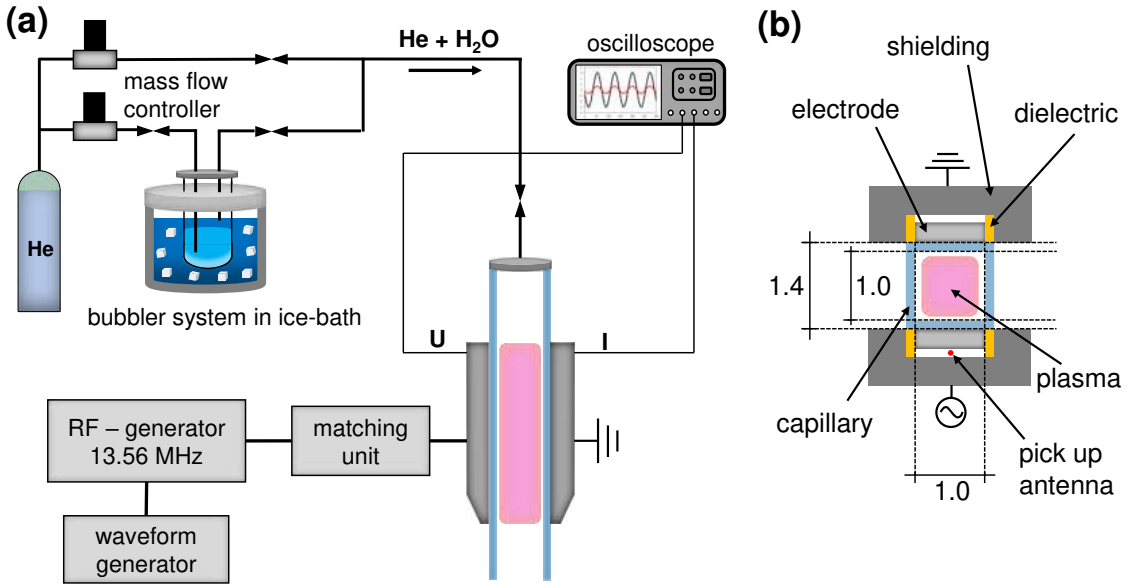

Figure 3.1: Sketch of the experimental setup of the plasma jet: **(a)** Gas and power supply and connections to the plasma jet. **(b)** Front view of the plasma jet with dimensions of the electrodes and the capillary in mm.

and a bubbler system was used to enrich the operating gas with water. The bubbler consisted of a glass vessel filled with 75 ml of pure distilled water (Fisher Scientific). An ice bath filled with 0.9 L ice cubes and 0.4 L fridge-cooled water at about 8 °C cooled the vessel during the operation to keep the temperature constant. The cooling process was started 1 h before the measurements to ensure thermal equilibrium of the water in the bubbler. The temperature of the water in the bubbler was measured by using a NiCr-Ni thermocouple type K (B+B Thermo-Technik, ranging from -50°C to 260°C) connected to a two-channel thermometer (Voltcraft). The thermocouple was inserted into the bubbler by one gas pipe and the water temperature in the cooled bubbler was measured to (1.4 ± 0.5) °C. The humidified He was mixed with dry He and fed to the plasma source to set a specific humidity concentration of the feed gas. The humidity concentration can be calculated by water vapour theory as explained in the appendix A.1 and shown by mass spectrometry measurements of the COST reference plasma jet equipped with an ice-cooled bubbler system [29]. Concentrations of up to (6400 ± 250) ppm could be achieved depending on the fraction of feed gas guided through the bubbler and the humidity admixtures used are listed in table 3.1. The capillary was connected to the stainless steel tubes of the gas supply via a Viton tube (Keller Elastomere GmbH, inner diameter 1 mm x 1 mm), which was bonded to the capillary with a ceramic adhesive (T-E-Klebetechnik Ceramabond 668, 671 or 835).

If not differently noted, the total gas flow was 1 slm. The residence time $t_{residence}$ of the gas in the discharge channel can be calculated by the length of the discharge

Table 3.1: Humidity admixture to the feed gas for various fractions of the feed gas guided through the bubbler as calculated from water vapour theory using a temperature of $(1.4 \pm 0.5)\,°C$.

$\Phi_{bubbler}$ / slm	fraction / %	c_{H_2O} / ppm	Δc_{H_2O} / ppm
0.0	0	0	0
0.1	10	640	24
0.2	20	1300	48
0.3	30	1900	72
0.4	40	2500	96
0.5	50	3200	120
1.0	100	6400	240

channel $L_{discharge}$ and the gas velocity v given by the total gas flow Φ_{total} over the cross-section of the discharge channel $A = 1\,mm^2$

$$t_{residence} = \frac{L_{discharge}}{v} = \frac{L_{discharge} \cdot A}{\Phi_{total}}. \tag{3.1}$$

The residence time at a gas flow rate of 1 slm is 2.4 ms.

As power supply an RF generator (Coaxial Power Systems RFG 150) with a frequency of 13.56 MHz was connected via a matching unit (Coaxial Power Systems MMN 150) to the powered electrode while the other electrode was grounded. The matching unit was used to minimise reflected power and to ensure a good coupling of the plasma impedance to the generator's impedance. The applied voltage was a sinusoidal waveform with a frequency of $f = 13.56\,MHz$ and a corresponding time period of $T = 74.75\,ns$. Measurements of the dissipated plasma power were performed as described by Golda et al. [80]. The induced voltage was measured using a homemade pick up antenna (1 mm wire) placed parallel behind the powered electrode. A high-voltage probe (Tektronix P5100A) was used to determine the calibration factor of the pick-up antenna. The calibration factor changed for different electrode adjustments and was between 100 and 200. Thus, the voltage applied to the electrode was derived by correcting the measured voltage of the pick-up antenna. To measure the current, a resistor $R_m = 4.7\,\Omega$ was connected to the grounded electrode and by measuring the voltage drop across the resistor U_R the current can be derived by Ohm's law. An oscilloscope (Teledyne LeCroy HDO6104B, 1 GHz, 10 GS/s) was used to measure the voltage and current and terminations of $R_t = 50\,\Omega$ were used at both channels. Furthermore, current and voltage had a certain phase shift Φ, and a reference phase Φ_0 of the system had to be recorded

before the measurements. This reference phase was recorded with the power on and no gas flow applied. The plasma power can then be calculated by:

$$P = U \cdot I \cdot cos(\Phi - \Phi_0) \tag{3.2}$$

with applied voltage U and measured current $I = U_R \cdot (R_m + R_t)/(R_m R_t)$.

3.1.1 Pulse modulation

The described RF excitation is mainly performed continuously. However, a low-frequency pulsing of the RF generator and thus of the plasma was possible. A waveform generator (Tektronix AFG 3011) was used for triggering and generating square waveforms at a specific frequency and a duty cycle.

An example of a modulated RF excitation waveform is shown in figure 3.2. At 0 µs the modulation signal starts and it takes about 8 µs for the full establishment of the applied sinusoidal voltage waveform of the RF signal. At this short modulation period of only 10 µs, given by the frequency of 10 kHz and the duty cycle of 10 %, the RF pulse is only applied to the discharge for a very short period. To maintain a stable operation of the RF plasma under pulse modulation, the plasma-on time should exceed 8 µs and be at least 100 µs. Therefore, lower frequencies were used to modulate the RF plasma. The frequencies f_{mod} and duty cycles F_{DC} used and corresponding plasma-on and plasma-off times as well as the number of pulses per residence time N_{pulses}, given by

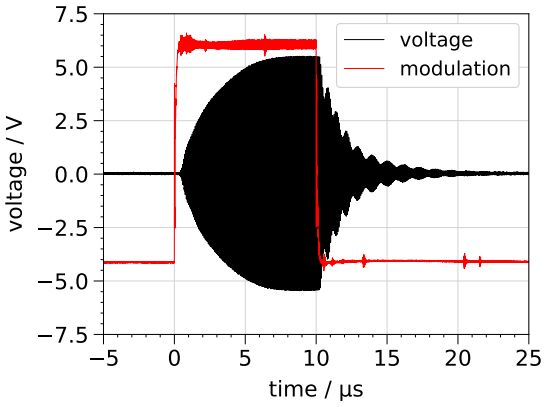

Figure 3.2: Example of voltage waveform (internal voltage) under pulse modulation. The RF signal was modulated with 10 kHz at 10 % duty cycle.

$$N_{pulses} = f_{mod} \cdot t_{residence}, \tag{3.3}$$

are listed in table 3.2. Numbers of pulses below 1 are possible. This means that a certain portion of the gas does not experience plasma at all. This must be taken into account when discussing the results or when carrying out simulations of the RF plasma under pulse modulation. Several thousand RF cycles occur within a pulse signal. For example, with a duty cycle of 10 % and a frequency of 100 Hz, 13.000 RF cycles are applied to the plasma.

Table 3.2: Parameters of the power modulation of the RF jet. The corresponding plasma-on t_{on} and plasma-off t_{off} times with the number of pulses per residence N_{pulses} for the different modulation frequencies f_{mod} at the two duty cycles F_{DC} are given.

F_{DC} / %	f_{mod} / Hz	t_{on} / ms	t_{off} / ms	N_{pulses}
10	42	2.4	21.4	0.1
	67	1.5	13.4	0.2
	100	1.0	9.0	0.2
	200	0.5	4.5	0.5
	400	0.3	2.3	1
	833	0.1	1.1	2
	1250	0.1	0.7	3
50	208	2.4	2.4	0.5
	333	1.5	1.5	0.8
	500	1.0	1.0	1.2
	1000	0.5	0.5	2.4
	2000	0.3	0.3	4.8

3.2 Gas phase diagnostics

3.2.1 Temperature measurements

Two methods have been implemented to measure the gas temperature of the discharge and its effluent. Both methods are shown in figure 3.3. At first, a NiCr-Ni thermocouple type K (B+B Thermo-Technik, ranging from -50°C to 260°C) was positioned directly under the capillary, centrally aligned and connected to a two-channel thermometer (Voltcraft). After the ignition of the plasma, the effluent temperature was recorded over 15 min to ensure the thermal equilibrium of the thermocouple. The distance from the end of the discharge to the thermocouple was 10 mm, so the measured temperature is lower than the discharge temperature due to cooling in the effluent. However, a calibration can be conducted to obtain the discharge temperature by measuring the temperature decrease at various distances [15]. With increasing distance, the temperature decreases and by fitting the linear slope, the temperature at the end of the discharge channel can be extrapolated. The calibration was done at plasma powers of 1 W, 6 W and 12 W and the calibration curves are shown in the appendix A.2. The uncertainty of the measured tempera-

ture is mainly determined by the positioning of the thermocouple, as it was aligned in the gas flow according to the position of the maximum temperature. This results in uncertainties of 3 °C and 5 °C for plasma powers of less than 6 W and equal to or greater than 6 W, respectively. The uncertainties of the determined discharge temperatures take into account the uncertainty of the linear fit, which leads to relative uncertainties between 8 % to 10 %.

Further, gas temperature measurements of the discharge were performed by optical emission spectroscopy to validate the extrapolation of the measured gas temperatures from the thermocouple measurements. For this purpose, the OH band emission at 308 nm was chosen to investigate the rotational temperature of OH to obtain the gas temperature of the discharge. As discussed in chapter 2, this is a valid method for gas temperature determination in plasmas with humidity admixtures below 1000 ppm [122]. The limited application of the temperature determination from the OH band emission at high humidity admixtures must be taken into account when applying this method and discussing the results. The plasma emission of the discharge was collected from the centre of the channel by a collimator and an optical fibre (both from Ocean Insight) as shown in figure 3.3. The optical fibre was connected via a second fibre (Ceram Otec) to a spectrograph (Acton: Research Spectra Pro 750) and the spectrum was measured by a camera (Princeton Instruments: PI-MAX). The spectrometer was equipped with a 1800 grooves/mm grating and the resolution of the system was (184 ± 5) pm. The setup was intensity-calibrated using a Deuterium Tungsten-Halogen Calibration Light Source (Ocean Optics: DH-3 plus). Fitting of the spectra was performed by using the software massiveOES [123, 129, 130] and an example of a fitted spectrum is shown in the appendix A.2. By shifting the measured spectrum to the line positions of the modelled spectrum, a wavelength calibration of the setup was performed. The uncertainties of the fit were in the range of 2.5 °C to 11 °C. Fluctuations of the measured spectra were in the same range as was checked by taking 20 spectra and calculating the rotational temperature. Thus, the uncertainties of the fits were used as measurement uncertainties.

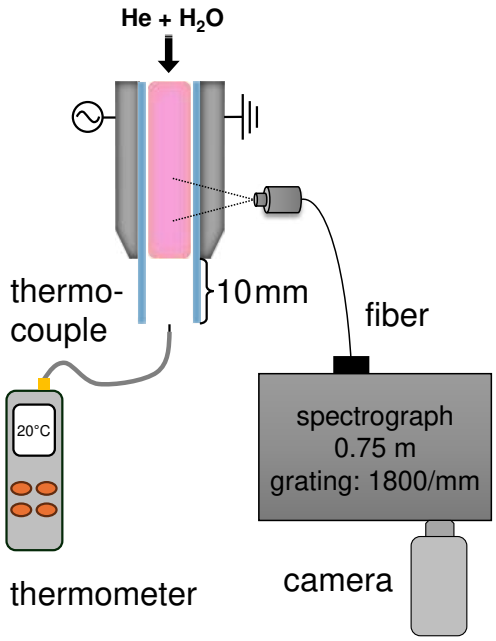

Figure 3.3: Sketch of the methods used to determine the gas temperature of the discharge.

3.2.2 Laser-induced fluorescence

As a detection method for OH radicals in the gas phase, laser-induced fluorescence (LIF) spectroscopy was applied. The fluorescence light of the $P_1(2)$ transition from OH was observed. It is given by the excitation from the $f_1(2)$ rotational level of OH X ($\nu'' = 0$) to the $f_1(1)$ rotational level of OH A ($\nu' = 1$) [125–127, 131–133]. The sketch of the LIF setup used is shown in figure 3.4. To produce the laser light in the UV range, a laser system consisting of a neodymium-doped yttrium aluminium garnet (Nd:YAG) laser (Continuum: Powerlite PL9010) and a dye laser (Radiant Dyes: Narrowscan) was used. The Nd:YAG laser operated at an energy of 140 mJ, repetition frequency of 20 Hz and pulse length of (11.5 ± 2.2) ns produced laser light at a wavelength of 1064 nm which was frequency-doubled to obtain laser light at 532 nm. That laser light pumped the dye laser which produced laser light at 565.2 nm. This laser light was again frequency-doubled to the desired wavelength of 282.6 nm which can be used to excite the investigated OH transition. After leaving the dye laser, the laser beam was cut by a 1 mm round pinhole and parallelised by a UV lens ($f = 200$ mm). A second pinhole with a diameter of 2 mm was used for reducing stray light. The laser system had to warm up three hours before the measurements.

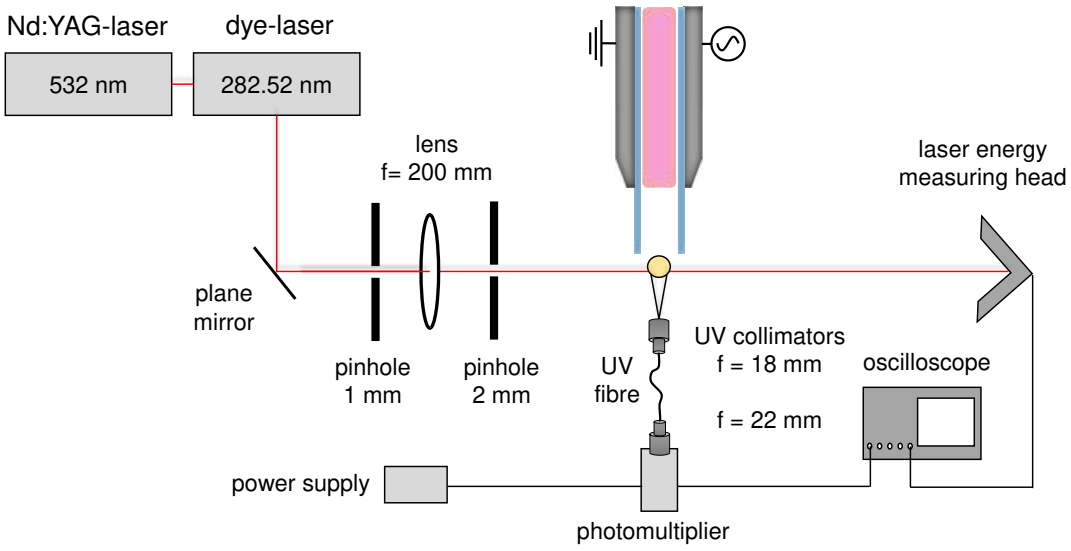

Figure 3.4: Sketch of the laser and optical system used for the LIF spectroscopy.

The laser energy was measured in the far field of the laser beam with a laser energy measuring head (Sensor- und Lasertechnik: PEM 11). During the experiments, the laser energy was continuously measured and kept between 4 µJ and 7 µJ. This allows the measurements to be performed in the linear regime where no saturation of the Rayleigh calibration occurs (see description of calibration process below) [124, 132]. The LIF signal was detected perpendicular to the light beam by a UV collimator

(Edmund Optics, $f = 18\,\text{mm}$) placed at the entry of a 200 µm optical fibre (Ocean Insight, UV-VIS). At the exit of the fibre, a second UV collimator (Ocean Insight, UV-VIS, $f = 20\,\text{mm}$) was installed. A photomultiplier was placed behind the second collimator to measure the light intensity and was powered at $-950\,\text{V}$ by a power supply (Hamamatsu: C3830). No bandpass filter was used to avoid additional corrections for transmission of filters [132].

The capillary plasma jet was mounted on digitally controllable stages (Zaber: X-LSM100A) to allow for precise adjustment of the position of the capillary plasma jet in all three dimensions. The alignment of the system was performed based on the observation of the LIF signal. The capillary plasma jet was adjusted to the maximum LIF signal in the xy-plane at $z = 4\,\text{mm}$ from the capillary end, which corresponded to the home position (0,0,4). The position of the maximum signal in the xy-plane should not vary by more than 0.1 mm from the centre at (0,0,z) with increasing distance. Otherwise, the capillary is tilted and has to be centrally aligned. This ensures a perpendicular alignment of the gas flow in the effluent to the laser beam.

Calibration

To obtain absolute densities of the ground state of OH in the effluent, intensity calibration of the setup by Rayleigh scattering was applied and the four-level collisional radiative model described by Verreycken et al. [132] was utilised to derive the ground state density from the measured signals. This approach has already been applied by Morabit et al. [127] and Cosimi et al. [133] to measure the OH ground state density of an APPJ with a similar setup used in this work. The calibration process is described in the following and a detailed description can be found in [132].

However, further information about the laser pulse, its interaction with the molecular transition of OH and the spatial detection volume is required first. The laser pulse behaviour over time is shown in figure 3.5 (a). It shows a Voigt profile and has a temporal full width half maximum (FWHM) of $(11.5 \pm 2.2)\,\text{ns}$. The bandwidth $\Delta\nu_L$ of the dye laser at 580 nm is $(0.06 \pm 0.02)\,\text{cm}^{-1}$ according to the manufacturer and the bandwidth after frequency-doubling is $(0.089 \pm 0.029)\,\text{cm}^{-1}$ with a linewidth of $(0.71 \pm 0.24)\,\text{pm}$. The spatial profile of the laser beam at the detection point (focal point of the LIF setup) was measured using a camera (Gentec: Beamage-4M) connected to a UV beam converter (Gentec: BSF23RS11.3N). Cross-sections of the laser beam profiles in y- and z-direction are shown in figure 3.5 (b). They reveal a Gaussian profile in both directions with a FWHM of (58.13 ± 0.28) µm and (62.4 ± 0.6) µm in y- and z-direction, respectively. For further calculations, a spatial FWHM of (60 ± 10) µm is used, considering the uncertainty of the camera

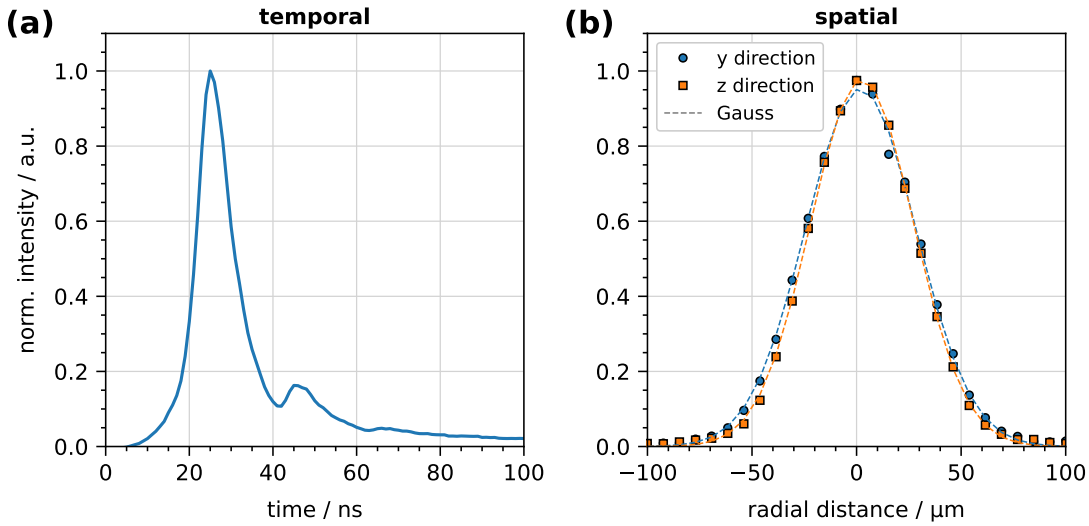

Figure 3.5: **(a)** Temporal laser profile. **(b)** Spatial laser profiles in y- and z-direction with corresponding fits of a Gaussian profile. The intensities of all profiles are normalised to their respective maximum.

measurements by several micrometres. The width of the detection volume is defined by the dimension of the optical fibre and is given by $(200 \pm 4)\,\mu m$.

To account for the interaction between the laser radiation and the molecular transition of the OH, the theory of the overlap integral has to be considered [134]. It is a measure of the overlap of the spectral profile of the laser beam $L_L(\nu)$ and the absorption profile $\Upsilon_A(\nu)$. The dimensionless overlap integral Γ is defined as [134]:

$$\Gamma = \Delta\nu_L \, g = \Delta\nu_L \int_{-\infty}^{\infty} \Upsilon_A(\nu) \, L_L(\nu) \, d\nu, \tag{3.4}$$

where both the spectral profile of the laser beam $L_L(\nu)$ and the absorption profile $\Upsilon_A(\nu)$ are normalised to unity. There, g is the dimensional overlap integral and $\Delta\nu_L$ is the bandwidth of the laser. The spectral profile of the absorption line is given by a Voigt profile determined by a Gaussian and a Lorentz profile. The widths of the two profiles are driven by Doppler broadening $\Delta\lambda_G$ (Gaussian profile) and van der Waals broadening $\Delta\lambda_L$ (Lorentz profile) and can be calculated by [135, 136]:

$$\Delta\lambda_G(pm) = 7.16 \times 10^{-7} \, \lambda \sqrt{\frac{T}{M}} \tag{3.5}$$

$$\Delta\lambda_L(pm) = 1.71 \times 10^{-3} \, \frac{\lambda^2}{c} \left(\frac{T}{M}\right)^{-0.7}. \tag{3.6}$$

The temperature T is given by temperature measurements (see section 4.2) and the atomic mass of OH is $M = 17\,\text{amu}$. Using these equations and parameters, the overlap integral is in the range of 0.17 to 0.18 for plasma powers between 1 W and

8 W since the plasma powers determine the gas temperature. The uncertainty of the overlap integral was determined to 24 %, which is mainly given by the uncertainty of the laser bandwidth. Thus, the small difference between 0.17 and 0.18 is within the uncertainty range and 0.17 was used for further calculations.

The Rayleigh calibration was performed with N_2 molecules as scatterers of the laser light. 1 slm of N_2 gas flow was set without any other admixture and flowed through the capillary to the detection area of the LIF setup. The signal of the light from Rayleigh scattering S_R can be described by:

$$S_R = \eta \cdot N_{N_2} \cdot \frac{\partial^{\beta=0}\sigma_0}{\partial\Omega} \cdot E_L \cdot \Delta x, \tag{3.7}$$

with the calibration factor η, the density of the scatterers N_{N_2}, differential cross-section for Rayleigh scattering of the surrounding gas $\frac{\partial^{\beta=0}\sigma_0}{\partial\Omega}$, the laser energy E_L and the length of the detection volume Δx. For the differential cross-section, the polarisation of the laser is important. The laser beam was polarised in the y-direction, parallel to the direction of the observation. This results in low signals of Rayleigh scattering, which is useful for the measurements as it reduces noise but makes the calibration more challenging. In addition, the differential cross-section for unpolarised Rayleigh signals proposed by Verreycken et al. was used [132]. To overcome this problem, the fibre collecting the signal was rotated by 90° into the z-direction. This was applicable during calibration with only N_2 gas but not during plasma measurements as the fibre would be in the effluent of the plasma jet. Thus, the calibration with the fibre in the y-direction was validated by the calibration of the fibre in the z-direction. It was found, that the calibration in the y-direction was a factor of 48 lower than in the z-direction. Thus, the calibration factor η was corrected by multiplying 48. In this way, polarisation was taken into account in the calibration and the differential cross-section proposed by Verreycken et al. of $8.8 \times 10^{-31}\,\mathrm{m^2 sr^{-1}}$ could be used [132].

Using the ideal gas law, a linear relationship between the Rayleigh signal and the product of pressure and energy can be obtained. The calibration factor η can then be derived from the slope α of the linear fit:

$$\eta = \alpha \cdot k_B T \cdot \left(\frac{\partial^{\beta=0}\sigma_0}{\partial\Omega} \Delta x \right). \tag{3.8}$$

Since the experiments were performed at atmospheric pressure, the laser energy was varied in the range from $(2.7 \pm 0.4)\,\mathrm{mJ}$ to $(44.8 \pm 1.8)\,\mathrm{mJ}$ to obtain the required calibration curve from Rayleigh scattering. The calibration curve is shown in figure 3.6. The mean slope considering day-to-day variation was $\alpha = (5.20 \pm 0.07) \times$

$10^{-10}\,\mathrm{Vs\,J^{-1}\,Pa^{-1}}$ (in y-direction) resulting in a calibration factor of $\eta_y = (12\,000 \pm 500)\,\mathrm{V\,sr\,J^{-1}}$. The final correction factor was then $\eta = (580 \pm 30) \times 10^3\,\mathrm{V\,sr\,J^{-1}}$.

The overall LIF signal S_{LIF} is then given by

$$S_{LIF} = \frac{1}{4\pi} \int \eta \frac{hc}{\lambda} n_{ecx}(x, y, z, t)\, A\, dx\, dy\, dz\, dt, \tag{3.9}$$

with the density of OH in the excited state $n_{exc}(x, y, z, t)$ at wavelength λ and Einstein coefficient of the observed transition A. This LIF signal is measured but is still dependent on the density of OH radicals in the excited state investigated.

To obtain the density of OH in the ground state, the four-level model described by Verreycken et al. was applied [132]. In the model, four levels are taken into account, namely the ground state and three laser-excited states. Each state is described by an ordinary differential equation (ODE) considering the gains and losses of the states by different mechanisms. Radiative excitation by the laser, quenching by air species (N_2, O_2 and H_2O), and vibrational energy transfer (VET) are taken into account. The ODEs are coupled to one system that has to be solved to get the density of OH in the ground state. Solving includes fitting the LIF signal modelled from the set of ODEs to the measured LIF signal. The photomultiplier records the decay time of the measured signal and proper fitting of the decay behaviour of the measured signal provides information on the density of the quenching partner. Further information, e.g. about the air input into the gas flow, can also be obtained from the modelling.

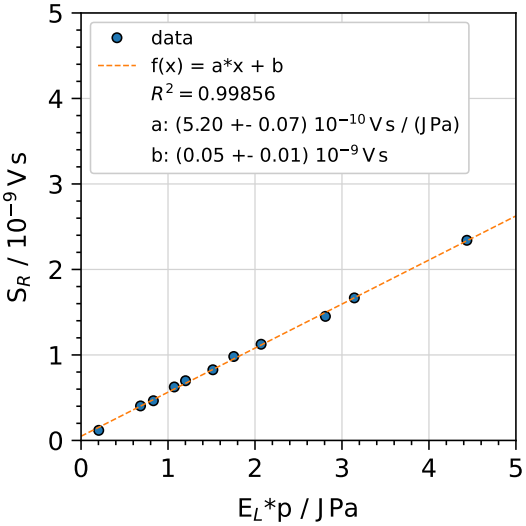

Figure 3.6: Calibration curve of the Rayleigh scattering with the fibre in y-direction. For details see text.

All parameters used for the LIF measurements and required for the model are listed in table 3.3. An uncertainty of 50 % was assumed for the absolute densities determined by LIF spectroscopy due to the uncertainties of the various parameters that were taken into account during the calibration process and the modelling.

Since the laser system is pulsed at a frequency of 20 Hz, an external trigger system had to be used when the plasma jet was driven under pulse modulation. To fit the frequency of the laser pulses, the frequencies used for the pulse modulation must be

Table 3.3: Parameters for the LIF measurements and modelling.

Parameter	Description	Value
λ_L	Laser wavelength	282.58 nm
$\Delta\lambda_L$	Linewidth of laser	(0.71 ± 0.24) pm
$\Delta\nu$	Bandwidth of laser	$(0.089 \pm 0.029)\,\mathrm{cm}^{-1}$
Γ	Overlap integral	0.17
A_L	Area of laser beam	$(11\,300 \pm 3800)\,\mu\mathrm{m}^2$
E_L	Laser energy	(7.4 ± 0.4) mJ
τ_L	Temporal FWHM of laser beam	(11.5 ± 2.2) ns
Δx	Length of detection volume	(200 ± 4) µm
Δy	Width of detection volume	(200 ± 4) µm
Δs	Spatial FWHM of laser beam	(60 ± 10) µm
η	LIF calibration factor	$(580 \pm 30) \times 10^3$ Vsr/J

multiples of 20 Hz. Thus, the frequencies of pulse modulation during the LIF measurements were slightly off compared to the ones listed in tables 3.2. To synchronise the pulse generator used for the pulse modulation of the RF signal, the delay generator was connected to an Arduino. The Arduino produced a signal at 20 Hz which is synchronised to the start time of the pulse from the pulse generator. This synchronised signal triggered the Nd:YAG laser and thus, the LIF measurements were synchronised to the pulsed plasma.

3.2.3 Fourier-transform infrared spectroscopy

To measure H_2O_2 ex-situ in the gas phase, two methods were used. FTIR absorption spectroscopy was applied and the setup is shown in figure 3.7 (a). The setup of the FTIR spectrometer (Bruker Vertex 70v) equipped with a multipass cell (Bruker, A136/2-LT) was previously implemented and used for the quantification of NH_3 and NO in the effluent of an atmospheric pressure plasma jet [137, 138]. In the presented work, the capillary end on the outlet side was connected to a Viton tube and via a connector to a stainless steel tube. In this way, the effluent of the capillary plasma jet was guided into the multipass cell. The multipass cell was used to enhance the sensitivity of the setup by increasing the absorption path length to 6.4 m. The multipass cell was heated up and controlled at a temperature of 60 °C to minimise adhesion and it was turned on one hour before the measurements started. The sample chamber in which the multipass cell was installed was flushed with an N_2

flow of 0.5 slm during the measurements to minimise water contamination in the beam path. An MCT detector was used to detect the IR light and the signal-to-noise ratio was improved by averaging over 300 samples.

The measured spectra were fitted using the HITRAN database [139], which contains transition energies, Einstein coefficients, broadening constants, and more. A detailed description of the fitting routine can be found elsewhere [140–142]. H_2O_2 appears in the spectrum at the region between 1100 - 1350 cm^{-1}. Since water absorption is also present in this region (1315 - 1350 cm), these lines were discarded from the spectrum when fitting the H_2O_2 lines. To do this, the position of water lines was obtained from a reference spectrum. If spectral lines in the transmission spectrum passed a threshold of 2 % of the line intensity of the reference spectrum, the data points in this region were discarded. Further, a baseline correction was performed. The fitting process yields the concentration c relative to 100 % of particles in the gas for an absorption length of 6.4 m. The density at room temperature is then calculated to:

$$n_{H_2O_2} = c \cdot 2.4 \times 10^{19}\,\mathrm{cm}^{-3}. \tag{3.10}$$

The uncertainty in the absolute density of H_2O_2 was estimated to be 30 % due to the potential adhesion of H_2O_2 to the walls and the length of the multipass cell, which can introduce additional uncertainty in the calculated absolute densities. The reproducibility of the measurements showed fluctuations of about 4 %.

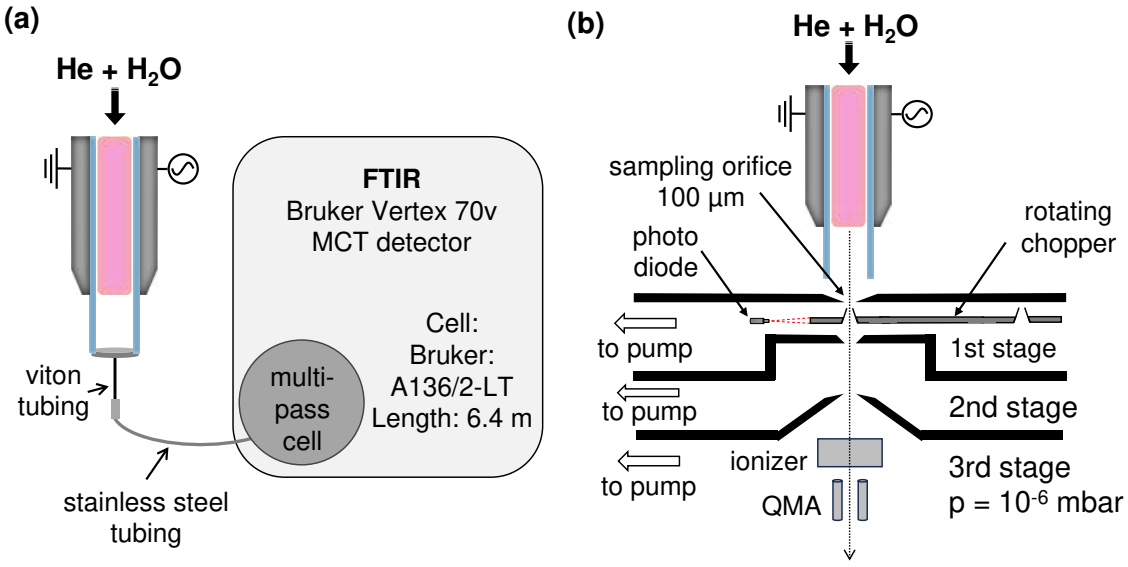

Figure 3.7: Schematic sketches of the gas phase H_2O_2 diagnostics. **(a)** FTIR spectroscopy using a multipass cell. **(b)** Setup of the mass spectrometer with the differential pumping system, adapted from [143, 144].

3.2.4 Mass spectrometry

Molecular beam mass spectrometry (MBMS) was used to measure the density of long-lived species important for the chemistry of a humid atmospheric pressure plasma: H_2O, H_2O_2, O_2 and H_2, as well as of the HO_2 radical. The system was the same as previously used for APPJs, including the COST reference plasma jet [29, 144–148] and a detailed description of the mass spectrometry of atmospheric pressure plasmas can be found elsewhere [143, 149]. The setup of the MBMS applied to the capillary plasma jet is shown in figure 3.7 (b). The mass spectrometer system consisted of an orifice with a diameter of 100 µm and a differential pumping system before the beam was guided into the mass spectrometer (Hiden Analytical - EPIC) equipped with an ioniser and a quadrupole mass analyser (QMA). The differential pumping system was used to overcome the big pressure difference from the atmosphere where the plasma was operated to the 10^{-6} mbar pressure range of the mass spectrometer. The capillary plasma jet was centrally aligned to the orifice of the mass spectrometer to guide the beam into the spectrometer and the distance between the capillary end and the orifice was (3 ± 1) mm. The alignment of the capillary was checked by turning on the He flow to 1 slm and minimising the pressure in the mass spectrometer as He has a lower density compared to air. Behind the orifice, a chopper with a rotating skimmer was placed. It was used to reduce the background and to reach a very high signal-to-noise ratio [150]. In addition, the signal can be corrected for background as the chopper determines when the actual sample beam enters the mass spectrometer.

Absolute densities were obtained by calibration of the system with known densities of gases inserted into the mass spectrometer. A specific calibration species was added to the He feed gas flow for each measured species. The mass and adiabatic index of the calibration species must be close to those of the analysed species. This is necessary to obtain the same mass-dependent transmission function $F(m_i, m_{cal})$ of the mass spectrometer for both species and to minimise the effects of the distortion of the gas composition when sampling and expanding in the vacuum. The density of the measured species n_i is then proportional to the ratio of measured intensities of the unknown species and the calibration species S_j (given in counts/s) and their ionisation cross-sections σ_j as well as the known density of the calibration species n_{cal} [29]:

$$n_i = F(m_i, m_{cal}) \, \frac{S_i \, \sigma_{cal}}{S_{cal} \, \sigma_i} \, n_{cal}. \tag{3.11}$$

An example of a calibration curve is shown in figure 3.8. There, an Ar calibration has been performed for the measurements of H_2O_2. A humidity of 3200 ppm was added in this case to check the effect of humidity on the calibration. No differences

in the calibration with or without humidity were observed (not shown here). The calibration shows a linear behaviour as the measured intensity increases linearly with increasing density of the calibration gas. This behaviour was found for all calibration species used. Since the mass-dependent transmission function was the same for all measured species and their respective calibration species ($F(m_i, m_{cal}) \approx 1$), equation 3.11 simplifies to:

$$n_i = \frac{\sigma_{cal}}{\sigma_i} \frac{S_i}{m} \tag{3.12}$$

with the slope of the linear relation of the calibration $m = S_{cal}/n_{cal}$. The energy of the ioniser was set to 70 eV and the ionisation cross-sections at this energy have to be used to get the absolute densities of the measured species.

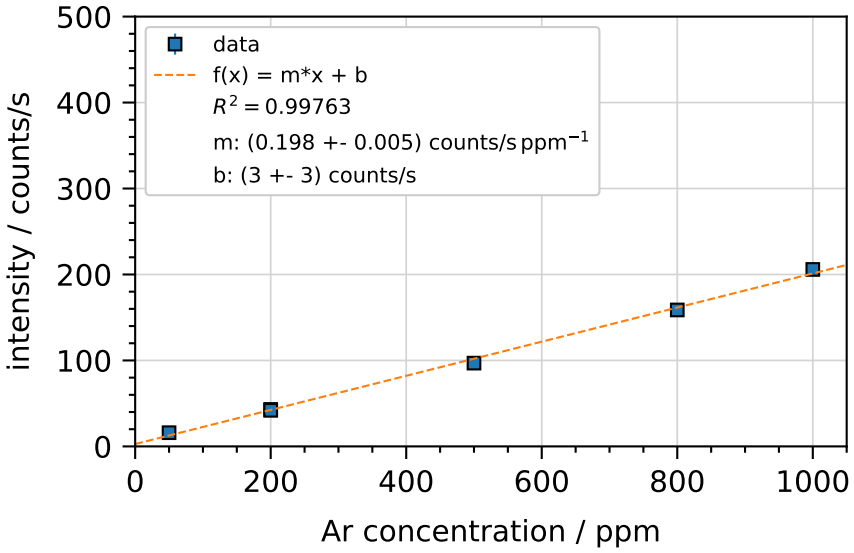

Figure 3.8: Example of an Ar calibration curve obtained for the mass spectrometry setup. A humidity of 3200 ppm was added to the 1 slm He gas flow.

As calibration gas for O_2 and HO_2, O_2 can be used [29]. In our work, O_2 was not applicable as calibration gas since no chamber protected the effluent and orifice from ambient air and fluctuations in the O_2 signals by the atmosphere were visible. Instead, Ar was used as calibration gas for O_2, HO_2 as well as for H_2O_2. The different measured species, their ionisation cross-sections and the respective calibration species are listed in table 3.4. A detailed analysis and discussion of the uncertainties of the mass spectrometry setup to measure species densities of atmospheric pressure plasma jets was given by Gert Willems in his dissertation [151]. Following this discussion an uncertainty of 40 % was used in this work.

Table 3.4: Measured species by mass spectrometry with their respective ionisation cross-section σ_I and the corresponding species used for the calibration. The ionisation cross-section of Ar is $2.55 \times 10^{-16}\,\mathrm{cm}^2$ [152, 153].

Species	σ_I / cm^2	Ref	Calibration
H_2O	1.27×10^{-16}	[154]	H_2O
H_2O_2	1.01×10^{-16}	[29]	Ar
HO_2	3.45×10^{-16}	[155]	Ar
O_2	1.49×10^{-16}	[154]	Ar
H_2	1.02×10^{-16}	[155]	H_2

3.2.5 Phase-resolved optical emission spectroscopy

The excitation of species in the plasma is the driving force of plasma chemistry and the knowledge about the excitation is essential to optimise the plasma chemistry. Phase-resolved optical emission spectroscopy (PROES) can be used to visualise the spatially and temporally resolved species emission during the RF cycle and with this the excitation of the species by electron impact [76]. This technique divides the RF cycle into intervals with about 1 ns length over which the emission is integrated. Each interval is measured over several RF cycles to increase the intensity of the measurements. By shifting the start time intervals, the total RF cycle can be scanned and at the end, a colourmap of the emission with spatial and temporal resolution can be obtained.

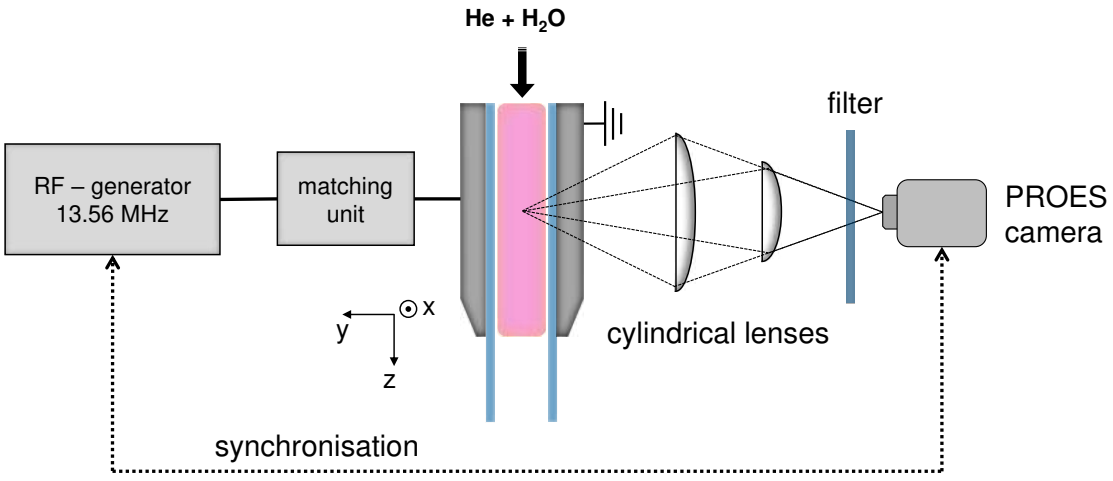

Figure 3.9: Schematic diagram of the PROES setup.

The setup used for the PROES measurements followed the experiments of a previous work using the COST reference plasma jet [57]. The setup is shown in figure 3.9 and described in the following.

The discharge emission of the capillary plasma jet was recorded by an intensified charge-coupled device (PicoStar HR 16, Lavision). The optical setup requires an anamorphic lens system to fit the different dimensions of the discharge and the camera chip. The discharge had a dimension of 40 mm × 1 mm, while the square chip had a dimension of 12.8 mm × 12.8 mm. For this purpose, two cylindrical lenses with focal lengths of 75 mm and 100 mm were positioned between the plasma source and the chip. The first lens reduced the discharge channel in the vertical plane (y-axis) and the second lens compressed the image in the horizontal plane (z-axis).

A calibration image of the discharge was taken in DC mode of the camera to calibrate the spatial dimensions of the system. To scan through the RF excitation cycle, synchronising of the camera system was required. For this purpose, a delay generator and a high-rate imager (HRI) were used to gate the camera. The gate delay was increased in 0.6 ns steps so that one RF cycle with a period of 74 ns was scanned by 123 individual images. The integration time was 1 s to 4 s depending on the emission intensity of the observed transition. In post-processing, from the 123 images, one image was obtained by integrating over the horizontal axis of the images (z-axis, direction of the gas flow) and concatenating the individual images. Thus, an image containing the emission over one RF cycle between the two electrodes (y-axis) was obtained. Since the emission originates from different excited states, certain optical filters (Quantum Design GmbH), listed in table 3.5, were inserted into the beam path to investigate the emission of the individual species separately.

Table 3.5: Optical filter used for PROES analysis of various species. Information on the transitions investigated and their energy thresholds can be found in table 2.3.

Species	**Central wavelength / nm**	**Width / nm**
He	700 +3/-0	10 ± 2
OH	307.1 +3/-1	10 ± 2
H	656.3 +0.2/-0	1 ± 0.2
O	770 +3/-0	10 ± 2
O	840 +3/-1	10 ± 2

3.3 Liquid diagnostics

The treatment of liquid samples was performed in UV cuvettes (Sarstedt polystyrene) placed beneath the capillary plasma jet. As liquid, distilled water or a 100 mM potassium phosphate (KPi) buffer was used. The buffer ensures a stable pH value of 7.0 during the plasma treatments and is used in the biology group when performing plasma-driven biocatalysis. Thus, by using the same buffer the results can be used to improve the plasma-driven biocatalysis process. In this work, 3 mL of liquid samples were filled in the cuvettes using a pipette (Eppendorf). To check that the same amount of liquid sample was filled in each cuvette, the weight of the filled cuvettes was measured. Ten weight measurements showed a standard deviation of only 1 %. Thus, it can be assumed that the amount of liquid sample was the same for each treatment.

The distance from the plasma end (end of the electrodes) to the liquid surface was (24 ± 2) mm. A gap of 10 mm was set between the end of the electrodes and the capillary end. Thus, the plasma effluent was guided for 10 mm through the capillary, protecting it from mixing with ambient air. On the last 14 mm the effluent passed through ambient air to the liquid surface. Unless otherwise stated, the treatment time for the measurements was set to 5 min. To measure the evaporation of the liquid during treatment, the weight of ten cuvettes was measured. The difference in weight was only 3.3 %, so that evaporation was negligible. During the treatment, the room temperature was recorded and ranged from 18 °C (winter) to 28 °C (summer). After the plasma treatment, the temperature of the liquid sample was only increased by a few °C. In the following, the liquid sample after plasma treatment is referred to as plasma-treated liquid (PTL).

3.3.1 UV absorption for H_2O_2 detection

A non-invasive method for the detection of H_2O_2 in liquids is the use of UV light for absorption spectroscopy since H_2O_2 absorbs light in the UV range from 180 nm to 300 nm [156, 157]. Some research groups have already used this technique to detect the concentration of H_2O_2 in PTLs [158–161]. The experimental setup of the UV absorption spectroscopy is shown in figure 3.10. Broadband emission (190 nm - 2500 nm) from a laser-driven light source (Energetiq EQ99X-FC) was passed through a UV lens and a slit into the UV cuvette filled with 3 mL distilled water. The light beam passed through the centre of the cuvette and had a width of 5 mm (compared to 10 mm of the cuvette) to avoid reflections at the sides of the cuvette. The height of the light beam was 20 mm and was set to 2 mm beneath the liquid surface to be undisturbed by interactions at the liquid surface. After passing through the cuvette,

two cylindrical lenses (100 mm focal length) were used to focus the light beam onto the dimensions of the entrance slit (2 mm x 10 mm) of a spectrometer. The use of cylindrical lenses enables a high spatial resolution and an improved signal-to-noise ratio. Thus, not only a volume-averaged concentration can be measured, but the spatial distribution of H_2O_2 can be visualised in the cuvette. This is a big advantage of the UV absorption technique, however, the optical setup is complex.

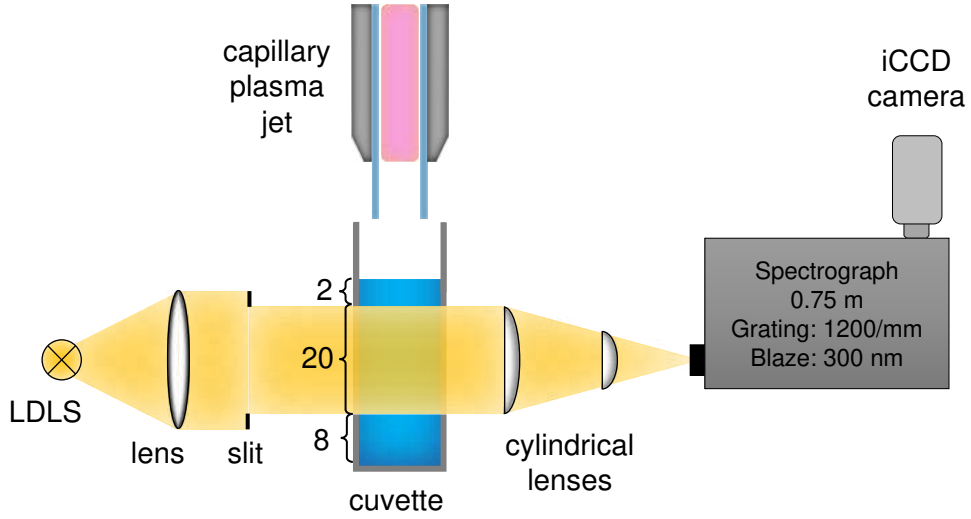

Figure 3.10: Sketch of the UV absorption setup for detection of H_2O_2 in PTL. The dimensions of the light beam in the cuvette are given in mm.

The spectrometer (Acton Research Corporation 300i, 0.3 m focal length) is an imaging spectrometer to maintain spatial resolution. It was equipped with a 1200 lines/mm grating at a blaze wavelength of 300 nm. An intensified charge coupled device (iCCD) camera (Andor iStar, DH334T-18U-E3) was used to capture the spectrum. The central wavelength was set to 250 nm for the absorption measurements. Calibration of the observable wavelength range was performed by a Ne-Penray lamp (LOT-Oriel LSP032) which provided several emission lines in the desired wavelength range. The resulting observable wavelength range of the system ranged from 237 nm to 271 nm. The camera was operated using a gain of 10 and an exposure time of 40 ms. The low gain was used to minimise disturbances from stray light. Long period measurements were performed by kinetic series with cycle times and number of images of 0.25 s and 1250 images or 1 s and 1800 images for treatment times of 5 min or 30 min, respectively. Thus, the temporal resolution of the measurements was 0.25 s or 1 s, respectively.

Examples of images taken for the UV absorption of H_2O_2 under plasma treatment are shown in figure 3.11. The total absorbance is shown as a colourmap for wavelengths from 237 - 271 nm and at depths from 2 mm to 22 mm within the liquid. At 1 min, the signal slowly starts at the top at 2 mm. After 10 min, the absorbance

penetrates deeper into the liquid to a depth of 14 mm and is strongly enhanced. This trend is even further pronounced after 20 min. Furthermore, the absorbance is stronger at lower wavelengths, which agrees with the expected H_2O_2 absorption profile in the UV range [156, 157].

Post-processing of the images had to be carried out to obtain depth profiles of the H_2O_2 absorption for further analysis. First, the absorbance signal was averaged over the investigated wavelength range to obtain the total absorbance. Second, depth profiles were created by obtaining the mean value of a 3 mm interval around specific depths. For example, the absorbance at a depth of 4.5 mm was averaged from 3 mm to 6 mm. In the end, a running mean of 30 time steps was used for all times examined to smooth the noise of the data due to temporal fluctuations of the signal.

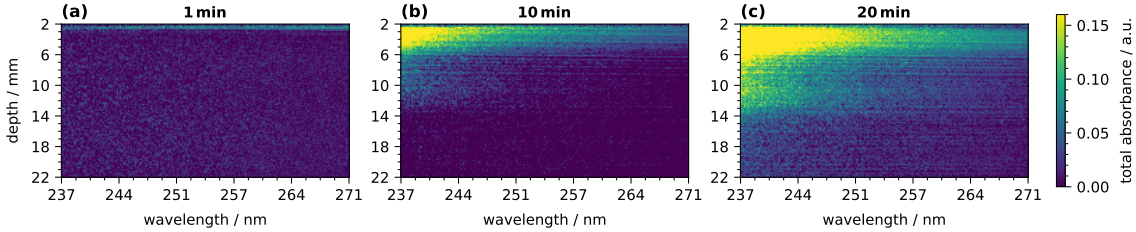

Figure 3.11: Examples of spectra obtained from UV absorption spectroscopy under plasma treatment after **(a)** 1 min, **(b)** 10 min and **(c)** 20 min treatment time. Plasma was operated with 0.25 slm total gas flow rate at a humidity of 6400 ppm and 6 W plasma power.

3.3.2 Spectrophotometry for H_2O_2 detection

To measure absolute H_2O_2 concentrations in the PTL, a second method for the detection of H_2O_2 was applied: a spectrophotometric approach utilising an ammonium metavanadate (NH_4VO_3) solution. In this method, light is absorbed at 450 nm and a less complicated optical setup was required compared to UV absorption. The ammonium metavanadate solution was prepared as described by Nogueira et al. and the lower detection limit of this spectrophotometric method was found to be 143 µM [162]. This method has already been used to measure the H_2O_2 concentration in plasma-treated liquids [27, 29]. To prepare the solution, 3.109 mL sulfuric acid (Fisher Chemical, $> 95\,\%$) was heated to 50 °C and 725.26 mg ammonium metavanadate (therma scientific, 99.5 %) was dissolved under stirring until a yellow solution was created. This solution was then diluted with distilled water and the final solution had a pH of less than 3.

The reaction of ammonium metavanadate with H_2O_2 results in a red-orange peroxovanadium cation solution with an absorption peak at 450 nm [162]. The setup

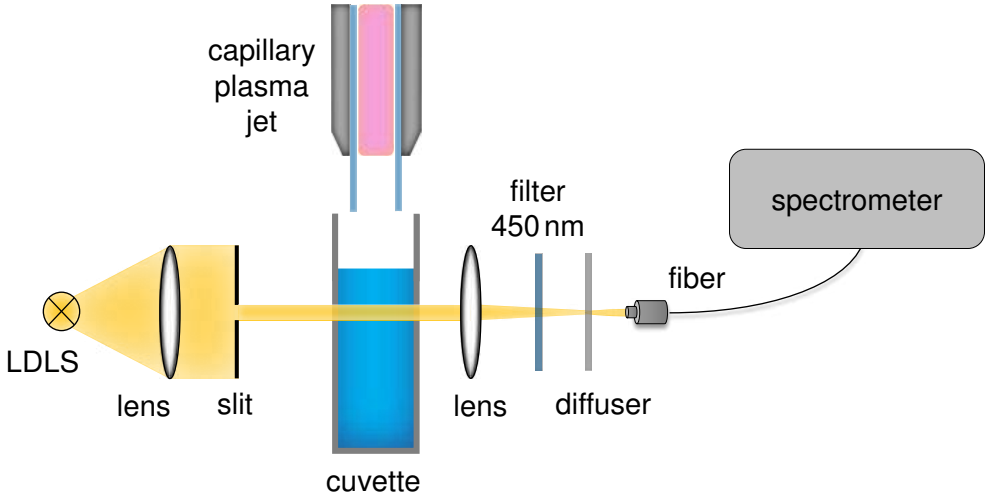

Figure 3.12: Sketch of the experimental setup of spectrophotometry.

of the absorption measurement is shown in figure 3.12. Light from a laser-stabilised broadband light source (Energetiq EQ-99 LDLS) was used, which passed through the plasma-treated liquid in the cuvette. The measurement depth was 8 mm beneath the liquid surface to avoid disturbances from the liquid surface. A lens was used for parallelising the light beam and a slit limited it to a width of 10 mm and a height of 1 mm. The final measurement was taken in a liquid volume of 1 mm x 10 mm x 10 mm. After passing the cuvette, a lens focused the light and a broadband filter at 450 nm was used to shrink the wavelength range to the region of interest around 450 nm. The light was guided through an optical fibre (Ocean Insight) to a spectrometer (Avantes Avaspec-ULS 2049x64 TEC-EVO) and a diffuser ensured homogeneous illumination of the fibre input. The spectra were recorded in-situ every 30 s during plasma treatment and the first spectrum was taken as a reference. Examples of spectra from plasma treatment can be seen in figure 3.13 (a) with the absorption maximum occurring at 450 nm and with increasing treatment time, the absorption increases linearly.

The absorption is proportional to the H_2O_2 concentration c and follows the Beer-Lambert Law $I = I_0 \exp(-\epsilon\, c\, d)$ with the intensity I, the reference intensity I_0, the absorptivity ϵ and the absorption length d. Calibration of the setup was performed using 30 % H_2O_2 stock solution (Fisher Chemical) and calibration solutions of H_2O_2 with concentrations up to 10 mM were used. The calibration curve is shown in figure 3.13 (b). Up to a concentration of 5 mM, linear behaviour of the absorption with increasing H_2O_2 concentration was found. At higher concentrations, saturation occurs and a deviation from the linear behaviour can be seen. Thus, for the measurements of the plasma-treated solution, it should be ensured that the concentration is less than 5 mM or appropriate dilution of the solution has to be applied.

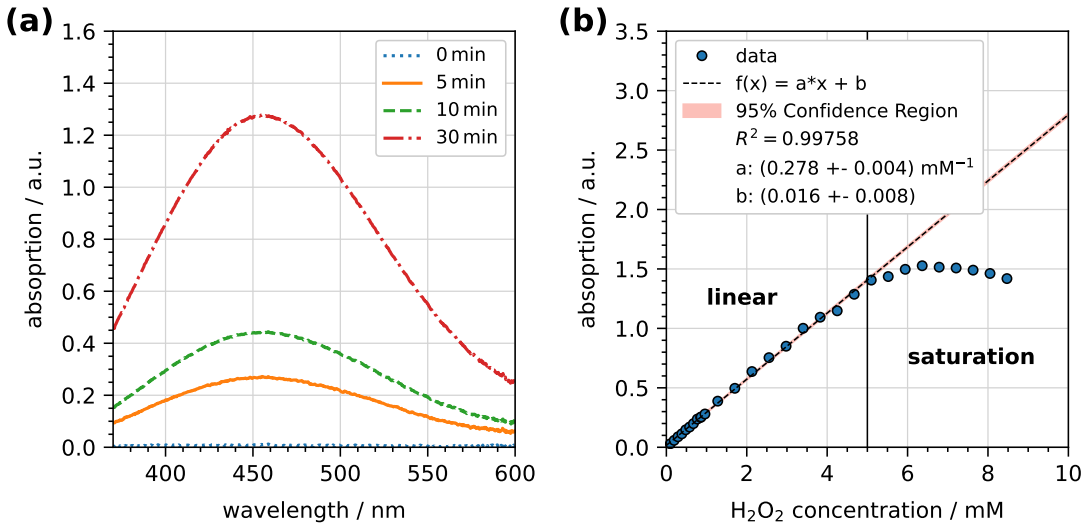

Figure 3.13: **(a)** Absorption spectra of the spectrophotometry recorded under plasma treatment. With increasing treatment time, the absorption increases linearly. **(b)** Calibration curve of the spectrophotometry. Up to a H_2O_2 concentration of 5 mM, the absorbance increases linearly.

3.3.3 Electrochemical sensing for H_2O_2 detection

Since the spectrophotometric approach was performed in an acid medium, differences in the H_2O_2 concentration compared to the buffer at pH 7, used for the treatments in plasma-driven biocatalysis, might be present. Therefore, to compare the liquids and to validate the values of the H_2O_2 measurements, electrochemical sensing of H_2O_2 was performed. The electrochemical sensors were produced by the chair of Analytical Chemistry II - Electrochemistry and Nano Materials at Ruhr University Bochum in collaboration with subproject B13 of the CRC 1316.

The electrochemical sensing of H_2O_2 was based on the use of Prussian blue carbon paste electrodes (PBcpe). Prussian blue and its analogues (PBA) are used in state-of-the-art H_2O_2 sensor systems [163, 164]. Sensing of the H_2O_2 concentration requires selectivity for the target molecule and stability in the medium of interest and materials like PBA can fulfil the requirements. The approach is based on either reduction or oxidation of H_2O_2 and the correlation of measured current I and initial concentration of the analyte c_j^0 is given by the Cottrell equation

$$I = \frac{nFAc_j^0\sqrt{D_j}}{\sqrt{\pi t}}, \tag{3.13}$$

with the number of electrons n, the Faraday constant $F = 96\,485\,\mathrm{Cmol}^{-1}$, the area of the electrode A, the diffusion coefficient D_j for species j and the time t. PBA catalyse the electrolysis of H_2O_2, so the measured current can be related to electrol-

ysis of H_2O_2 rather than possible side reactions with electrolytes, dissolved gases like oxygen, or water as the solvent itself. The PBcpe electrodes were manufactured by the chair of electrochemistry at Ruhr University Bochum and the production steps are explained in detail in our collaborative publication [165].

The measurements were performed as described in the following. Before the measurements started, the electrodes were polished with bond paper and electrochemically conditioned by cyclic voltammetry for 50 cycles with a scan rate of 50 mV/s in a range of 200 mV around the open-circuit potential in 0.1 M KCl solution (99 %, Sigma Aldrich). Then, the H_2O_2 measurements were conducted as chronoamperometry experiments with a reductive potential in a two-electrode setup. The current was recorded for 100 s and it increased with increasing time as can be seen in figure 3.14 (a) for all H_2O_2 concentrations added to the system. The final current after 100 s was used for calibration, as the current converges to its final value.

The calibration curve with H_2O_2 concentration series in the range of 0 - 1 mM is shown in figure 3.14 (b). The lower limit of the PBcpe was found to be 0.1 mM in this case as the current deviates noticeably from linear relation at these low concentrations. More complex PBAs can be used for lower detection limits, as described in the review by Matos-Peralta et al. [163]. However, for measurements of the plasma-treated liquid, higher values than 0.1 mM are expected and the sensitivity is sufficient.

Measurements of the H_2O_2 concentration in the PTL were performed ex-situ after 5 min of plasma treatment. In-situ measurements are not possible with the setup used since there was not enough space for entering the electrodes and simultaneously treating the liquid with the capillary plasma jet and the RF signal from the plasma could negatively influence the measurements.

3.3.4 Terephthalic acid dosimeter for OH detection

In a He+H_2O plasma, also OH is produced and a certain amount will reach the liquid surface. Thus, liquid measurements of OH have to be carried out for the system presented in this work. To measure the OH concentration in the PTL, the TA dosimeter was used [166, 167]. It is based on the hydroxylation of TA to 2-hydroxyterephthalic acid (HTA). The product HTA can be measured by illumination with UV light at 310 nm, resulting in a fluorescence signal of the molecule at 425 nm. A TA solution with a concentration of 2 mM was used by dissolving 332.26 mg TA (Aldrich Chemistry, 98 %) in 1 L KPi buffer. In other studies, NaOH helped to efficiently dissolve TA at pH values of about 10 [168, 169]. However, Charbouillot et al. used the TA dosimeter to investigate the photogeneration of OH in synthetic

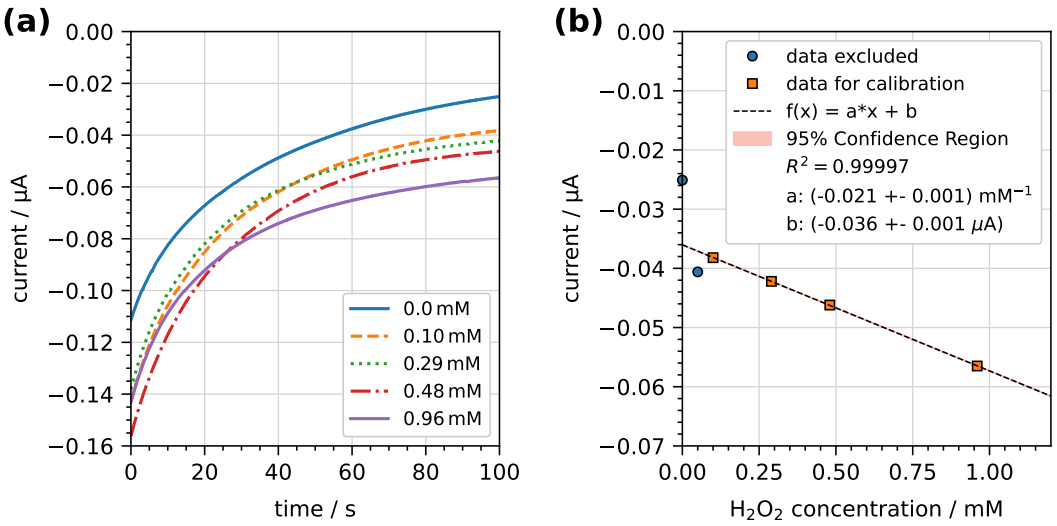

Figure 3.14: **(a)** Current characteristics of the electrochemical sensing for various additions of H_2O_2 to the buffer solution. **(b)** Calibration curve of the electrochemical sensing. The lower detection limit was found to be 0.1 mM.

waters and TA was dissolved in acid solutions with pH values between 3 and 7 [170]. Here, the KPi buffer at pH 7 was used and complete dissolution of TA in the buffer was found. The TA dosimeter has previously been used in plasma-liquid systems to measure OH concentrations. It was applied in liquids treated by streamer discharges [169, 171] and by plasma jets [168, 172].

The setup of the TA dosimeter is shown in figure 3.15 (a). UV light from the laser-driven light source (Energetiq EQ-99 LDLS) was used. A lens and a slit set the light beam to the same characteristics as used for the spectrophotometric approach. It passed through the cuvette at a depth of 8 mm with a width of 10 mm and a height of 1 mm, resulting in a measured volume of 1 mm x 10 mm x 10 mm. The fluorescence was measured by an iCCD camera (Andor iStar, DH334T-18U-E3) with a filter at 424 nm central wavelength (FWHM of 12 nm) in front of the camera. The camera was positioned at an angle of 90° to the light beam to observe only the fluorescence without being disturbed by the light beam. Images of the total cuvette were taken every 15 s under plasma treatment. A reference image was taken before every measurement using the pure buffer solution. The plasma was turned on and positioned as in the treatments to account for possible plasma emissions in the reference images.

Calibration of the system was performed using known HTA solutions. HTA (Aldrich Chemistry, 97 %) was dissolved in the buffer to concentrations up to 0.1 mM. A picture of the cuvette with 0.1 mM HTA under UV light irradiation is shown in figure 3.16 (a). The light beam passed through the cuvette at heights between

1.6 mm and 1.9 mm and the fluorescence of the HTA is visible in this region. The images contain the intensities for each pixel. In post-processing, the specific region of interest where the fluorescence signal occurred was selected and the sum over the intensity was calculated to obtain a volume-averaged intensity. The calibration curve of the system is shown in figure 3.16 (b). There, the volume-averaged intensity of the pictures shows a dependence on the HTA concentration according to a second-degree polynomial. This function can be used to calibrate the system. At low concentrations, the relationship between intensity and HTA concentration is linear (below 0.05 mM) but it deviates at higher concentrations. This indicates a saturation of the signal and an absorption of nearly 100 % of the light by the HTA. Thus, only HTA concentrations below 0.1 mM can be detected or appropriate dilution has to be performed.

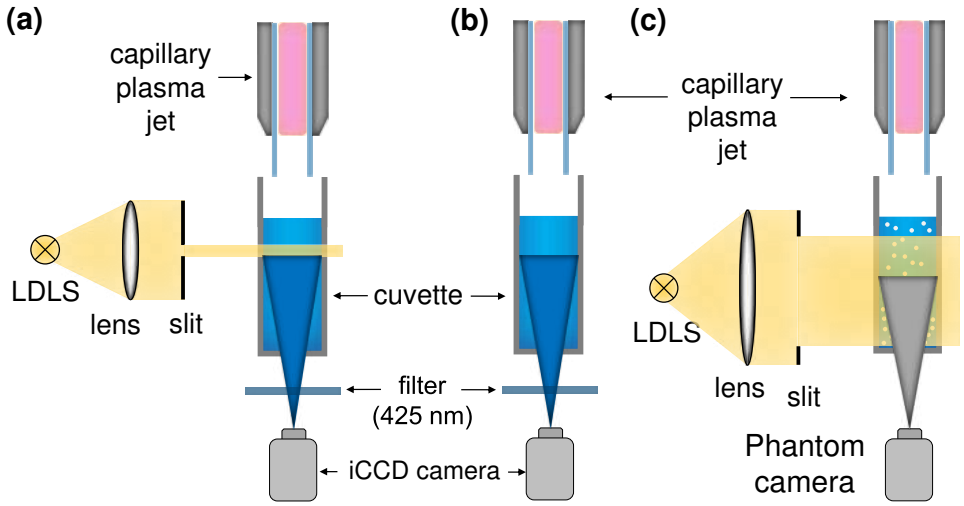

Figure 3.15: **(a)** Setup of the terephthalic acid dosimeter for detecting OH in the PTL. **(b)** Setup for the detection of the CL of luminol to visualise the distribution of OH in the PTL. **(c)** Setup of the PIV system to determine the flow patterns in the PTL.

Furthermore, the probability for OH capture by TA has to be considered to obtain the actual OH density. In oxygen-containing liquids, the probability for OH capture by TA was determined to be 35 % according to [173]. It was assumed that this value is valid for the buffer solution used. Thus, by measuring the fluorescence intensity I, the OH concentration c_{OH} is proportional to the corrected HTA concentration c_{HTA} by:

$$I \propto c_{OH} = \frac{c_{HTA}}{0.35}. \tag{3.14}$$

To highlight that the measured concentration is not the instantaneous OH concentration, the concentration is referred to as corrected HTA concentration proportional to the time-accumulated OH concentration.

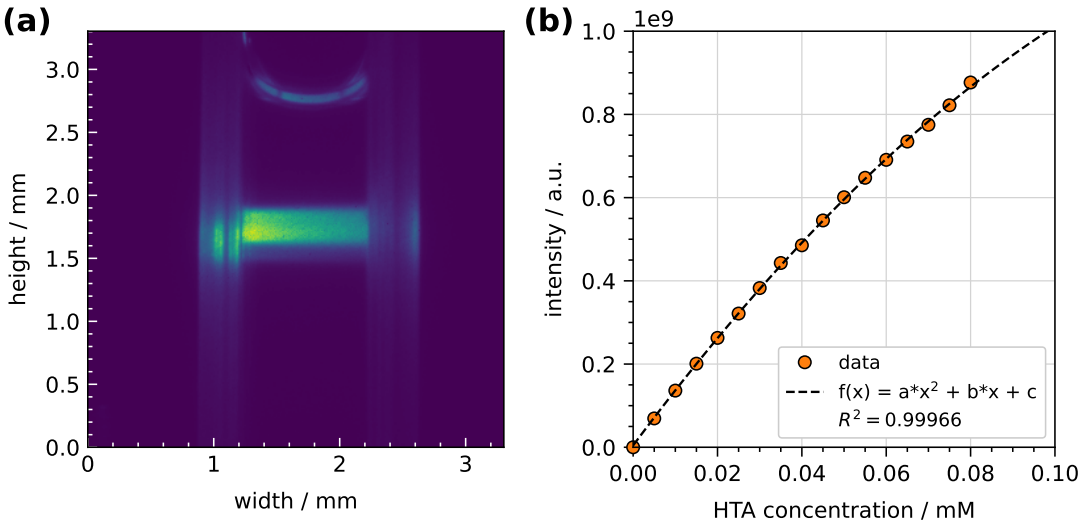

Figure 3.16: **(a)** Image of the fluorescence signal of the TA dosimeter containing 0.1 mM HTA. **(b)** Calibration curve of the TA dosimeter. A quadratic fit was applied to the data, indicating a saturation at higher concentrations.

3.3.5 Chemiluminescence for OH detection

As a second method to detect OH in the PTL, the chemiluminescence (CL) of luminol (3-aminophthal-hydrazide, $C_8H_7N_3O_2$) with an emission peak at 450 nm was used [174, 175]. Luminol can be excited by highly oxidative species such as OH or O_2^- and the CL signal occurs when the relaxation to the ground state takes place by photon emission. In the case of luminol, it was found that the superoxide radical O_2^- is the dominant exciter of luminol [174]. Shirai et al. used luminol in a setup of a glow discharge in contact with a liquid for observing its CL. In the first work, they found a correlation between the CL signal and the HTA signal [176], where HTA was formed from TA in reaction with OH as described in the previous section. In a following work, they investigated the decay of the CL signal and the decay of the LIF signal of OH and found the decay of the CL signal to follow the decay of the LIF signal [177]. Thus, the CL of luminol is a useful method for the detection of OH in liquids treated by plasmas [177].

In the presented work, a 5 mM luminol solution was prepared by dissolving 886 mg luminol (Serva Electrophoresis) in 1 L KPi buffer. The setup for detecting the CL signal is shown in figure 3.15 (b). The CL was measured using an iCCD camera (Andor iStar, DH334T-18U-E3) with a filter at 425 nm (FWHM of 12 nm) in front of the camera. The exposure time was set to 10 s to achieve a sufficient intensity. Thus, the CL signal was accumulated over 10 s of the plasma treatment. Two images were taken for each measurement. First, an image of the cuvette containing pure buffer under plasma treatment was taken as a reference image. Second, the measurement

was performed with the solution containing luminol. The final image was obtained by subtracting the reference buffer image from the luminol image. Examples of these images are shown in the appendix A.3.

3.3.6 Particle imaging velocimetry

The distribution of the species within the liquid is an important step for application purposes. Using particle imaging velocimetry (PIV) as a method to visualise flow patterns in gases or liquids can provide insights into the distribution of species. In this method, the motion of particles added to the gas or liquid is tracked. Thus, flow patterns can be visualised. In this work, the PIV method was applied to the PTL and the setup is shown in figure 3.15 (c). There, the laser-driven light source (Energetiq EQ99X-FC) was used to produce a narrow light sheet. A lens parallelised the light beam and a slit narrowed the light beam to a width of less than 1 mm in diameter. The height of the light beam was 30 mm to cover the entire depth of the liquid. Polyamide particles with a diameter of 55 µm (LaVision) were added to distilled water. The light from the light sheet is scattered by the polyamide particles and their movement can be tracked. A fast-imaging camera (Phantom VEO 410L) was positioned perpendicularly to the light sheet to observe the scattered light. 1000 images were recorded for every treatment and the camera was operated with an exposure time of 1900 µs and a sample rate of 500 fps.

Post-processing analysis of the images was performed using the open-source Python package OpenPIV [178]. There, the movement of the particles from one image to the next is tracked and the position of the particles is determined by the cross-correlation method. From the determined vector of particle movement and the time between the two images, the velocity vector of the particles is obtained [179]. PIV has been used in several studies to track the velocity patterns in plasma-treated liquids using DBD plasmas [180, 181], plasma in liquid configurations [182–184], kHz plasma jets [127, 185] and the COST reference plasma jet [28] with the last setup being comparable to the setup used in this work.

3.4 Chemical model

Insights into the reactions of the chemistry, species that were not measured in the frame of this thesis and the spatial and temporal evolution of the species within the plasma were gained by the **zero-dimensional plasma-chemical kinetics model** *GlobalKin* [186]. The adaption of the model to the system investigated in this thesis was performed by the chair of Applied Electrodynamics and Plasma Technology at the Ruhr University Bochum. The results of the investigations were published in

a collaborative publication and the results regarding the model are taken from the publication and are shown in this thesis [187]. The basic function of the model and the input parameters are briefly described in the following. A detailed explanation can be found elsewhere [186].

The power deposition in the plasma over time was taken as an input for the model calculations based on the applied power in the experiments. The model solves the mass continuity equation including gas phase and surface loss reactions of neutral and charged particles. The averaged electron energy and temperature were calculated using an electron energy conservation equation taking elastic and inelastic collisions into account. The electron energy distribution function (EEDF) was obtained using the two-term approximation of the Boltzmann equation. From this, the rate coefficient of electron impact processes and the electron transport coefficient were also obtained. To determine the gas temperature, the energy balance equation for neutral species is solved. As another input for the model, the wall temperature of the capillary was taken. The wall temperature was measured using the thermocouple also used to measure the gas temperature as described above. The thermocouple was placed on the outside of the capillary at the end of the discharge and the temperature was recorded during the plasma treatment. The gas temperature determined in the model was compared with the results presented in chapter 4 and good agreement was found.

To model the chemistry, an established set of reactions for He+H_2O chemistry was taken [37, 83, 188, 189]. The chemistry is quite complex as in total 46 neutral, charged and excited species in around 600 reactions were involved. The model was extended to a pseudo-1D plug flow model. Thus, the temporal evolution of the species is transformed into a spatial evolution along the gas flow by using the gas flow velocity.

3.5 Transport model in PTL

Besides the chemical model in the gas phase, a **transport model** was implemented to describe the transport of H_2O_2 in the PTL. This diffusion model was created within the frame of this thesis and the results have not been published yet. The transport of H_2O_2 in the PTL can be described by the convection-diffusion equation:

$$\frac{\partial c}{\partial t} + \nabla \cdot (\mathbf{u}\, c) = \nabla \cdot (D\, \nabla c) - R_i \tag{3.15}$$

with the concentration c, the velocity $\mathbf{u}$ and diffusion coefficient D. The second term on the right side R_i accounts for possible chemical loss reaction of H_2O_2 in

the liquid. In the model, the initial concentration at the liquid surface is given by the flux of H_2O_2 from the gas phase to the liquid surface. Due to the high Henry's law solubility constant of H_2O_2, all H_2O_2 molecules are assumed to enter the liquid as a simple approximation. The velocity was measured in the liquid by PIV and the diffusion coefficient was taken from the UV absorption measurements of H_2O_2 under plasma treatment as described in chapter 5.

The convection-diffusion equation was solved in 1D in the axial direction assuming radial symmetry to obtain depth profiles of the H_2O_2 transport. In spatial dimension, the dimension of the cuvette was characterised on a numerical grid with 220 points to cover the length of 22 mm as in the experiments. The temporal behaviour of the convection-diffusion equation was solved numerically by the forward Euler method. The time step was calculated to meet the Neumann stability criterion and resolve diffusion time scales with $dt \leq 0.5\,\mathrm{ms}$. The model provides the temporal and spatial transport of H_2O_2 in the PTL. These profiles can be compared to the experimental investigations of the UV absorption spectroscopy of H_2O_2 in the PTL under plasma treatment.

4. Gas phase dynamics and chemistry

This chapter analyses the performance of the capillary plasma jet and the production of gaseous species densities of the humidified capillary plasma jet. The results further provide insights into the excitation of species in the humidified He plasma and the production of H_2O_2. The chapter begins with a discussion of the performance of the plasma jet under humidity admixture, focusing on plasma power, electron density, and gas temperature. It then analyses the excitation of the most important species present in the He+H_2O plasma and the electron dynamics using PROES measurements. Additionally, it shows the gas phase density of the most important species of water chemistry, including H_2O_2 and OH and discusses the impact of humidity admixture and plasma power on their production. The chapter finishes with model results on species productions and the impact of pulse modulation on species density.

4.1 Plasma power and electron density

The following results on measurements of the electron density and sheath width using the electrical equivalent circuit model were developed in collaboration with Lara Boeddinghaus in the frame of her bachelor's thesis supervised in the course of this dissertation. Some parts of the following section have already been published in her bachelor thesis [190].

First, the plasma performance of the capillary plasma jet under the admixture of humidity is discussed. To this end, the dissipated plasma power into the capillary plasma jet as a function of the applied voltage for various humidity admixtures is shown in figure 4.1. The ignition of the plasma occurs between voltages of 180 V and 280 V for 0 ppm and 6400 ppm humidity concentrations, respectively. After ignition, a linear increase of plasma power with applied voltage can be recognised. This linear increase lasts up to a plasma power of 1 W until a change in the slope occurs. This change corresponds to a switch from the Ω-Mode at low plasma powers to Penning mode at higher plasma powers as discussed in chapter 2. In the Ω-Mode, the plasma is homogeneously distributed in the region between the electrodes and mainly emission from the bulk can be seen. On the other hand, in the Penning mode, the sheaths become more dominant with increasing voltage. The voltage of

the mode change, or equivalent the voltage at which 1 W is achieved, increases with increasing humidity concentrations from 330 V at 0 ppm to about 500 V at 6400 ppm humidity concentration. In the case of 0 ppm humidity admixture, another change in the slope of the curve can be recognised at about 6 W. At this point, the plasma volume and sheaths are fully developed and the coupling is less effective. This shows that, regardless of the humidity concentration, the plasma power at a voltage of 620 V is about 12 W in all cases.

It has to be noted that the voltages described above depend on the arrangement of the capillary plasma jet. Since the capillary and electrodes were not attached, they had to be parallelly aligned. If deviations in the electrode arrangement occurred, higher voltages were required for ignition and the voltages for mode change deviated. However, the trends described above were still the same. Thus, power measurements are more reliable than voltage measurements. The electrode arrangement was performed to achieve 6 W plasma power at a generator power between 20 W and 30 W with a homogeneous plasma distribution in the discharge channel.

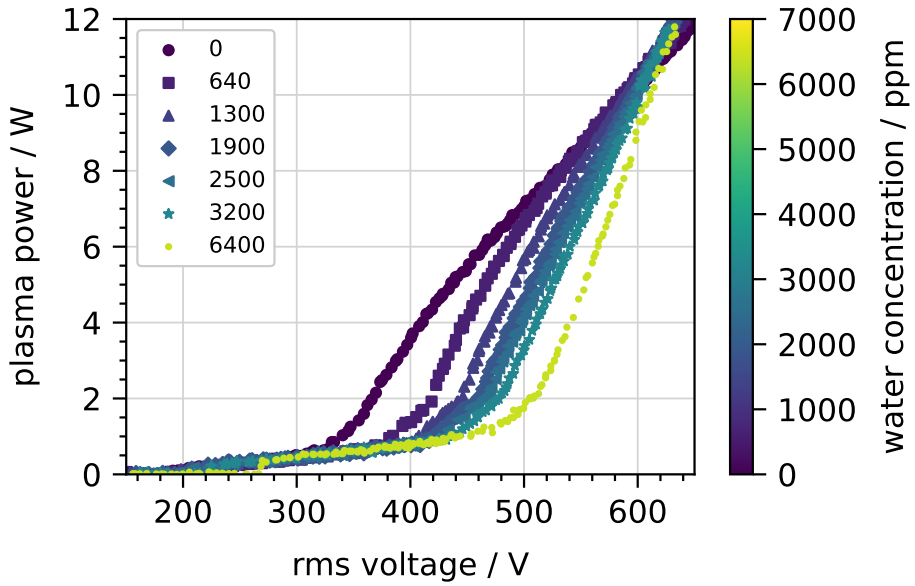

Figure 4.1: Power curves, defined as plasma power over applied voltage, of the capillary plasma jet for various humidity concentrations. The plasma was operated at 1 slm total gas flow rate.

The dissipated plasma power is important as it determines the energy coupled into the plasma. The coupled energy is transported into various processes via electron heating. The heated electrons will heat the gas via elastic collisions and inelastic collisions will lead to the excitation, dissociation and ionisation of atoms and molecules [15]. Thus, these processes can be enhanced by applying more power to the system. Compared to the COST reference plasma jet, the capillary plasma jet used in this

work is more powerful. The COST reference plasma jet is limited to plasma power of up to 2 W until constriction occurs [13]. As discussed above, a plasma power of 12 W can easily be applied to the capillary plasma jet. Even higher plasma powers were also possible, however, OES spectra have shown an unusual line in the spectra, namely the Na-D-line at 590 nm (discussion about the OES spectra is given later). This line might originate from Na released from the Borosilicate glass of the capillary at high temperatures (> 350 °C) that is excited in the plasma. Thus, the plasma power was set to a maximum of 12 W to avoid any contamination of the plasma by material from the capillary and destruction of the plasma jet.

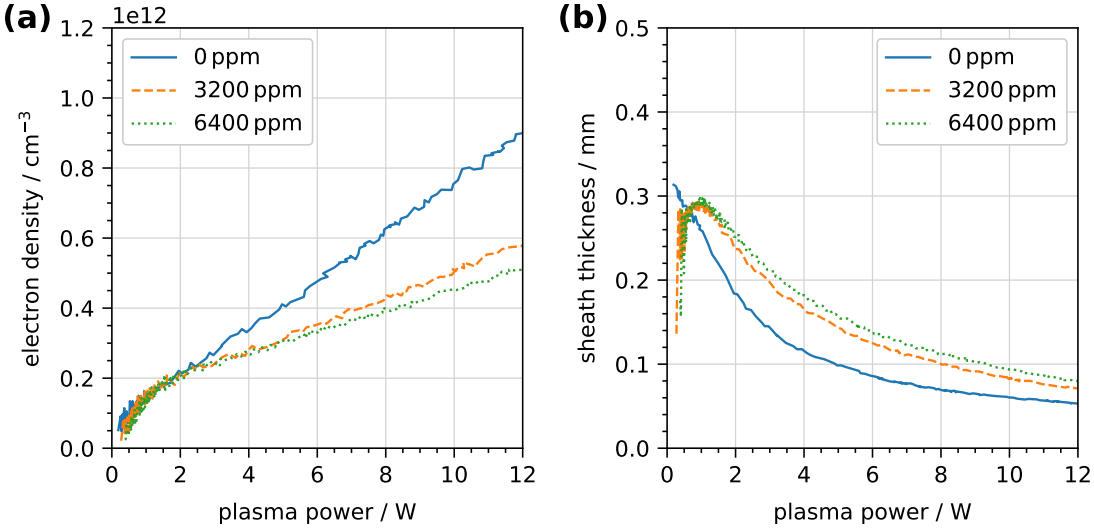

Figure 4.2: **(a)** Electron density obtained from electric circuit model as a function of plasma power for various humidity concentrations. **(b)** Sheath width from the model as a function plasma power for various humidity concentrations.

Electrons are responsible for driving processes of the plasma such as ionisation or dissociation. Therefore, the knowledge about the electron density is of major importance. The global electrical model described in chapter 2 was used to obtain the electron density from the power measurements described above. The electron density as a function of dissipated plasma power is shown in figure 4.2 (a) for various humidity concentrations. The electron density increases with increasing plasma power and reaches maximum values of about $0.9 \times 10^{12}\,\mathrm{cm}^{-3}$. The electron density at 0 ppm and 1 W is equal to the density obtained for the COST reference plasma jet [57] with the value of $1 \times 10^{11}\,\mathrm{cm}^{-3}$. At plasma powers below 2 W, the electron density is not strongly affected by humidity concentration in the He feed gas and increases linearly. However, at plasma powers higher than 2 W, the electron density is lower when humidity is added to the feed gas. In all cases, the electron density still increases and reaches values of $9 \times 10^{11}\,\mathrm{cm}^{-3}$ and $5 \times 10^{11}\,\mathrm{cm}^{-3}$ at 12 W plasma power for humidity concentrations of 0 ppm and 6400 ppm, respectively.

The global model also provides information on the sheath thickness of the plasma, which reflects the dynamics of the plasma and the results are shown in figure 4.2 (b). The sheath thickness steadily decreases with increasing plasma power for the case without humidity. This aligns with measurements performed with the COST reference plasma jet [80]. However, when humidity is present in the feed gas, the sheath thickness initially increases and reaches a plateau at 1 W, followed by a subsequent decrease at even higher plasma powers. There, the sheath thickness of the humidified He plasma is greater compared to the plasma without humidity. This agrees with the power curves discussed above as higher voltages are required with humidity admixture to achieve the same plasma power as the dry He plasma. The sheath thickness is affected by the electron temperature. Thus, the larger sheath thickness by applying humidity to the feed gas could indicate an increase in the electron temperature when H_2O is present in the plasma.

Simulation results of the He+H_2O chemistry for atmospheric pressure plasmas have shown that the electron temperature increases with increasing humidity concentration, due to enhanced energy losses of the electrons in inelastic collisions with H_2O molecules [37]. This increase in electron temperature goes hand in hand with a reduced electron density with increasing humidity. This agrees well with the experiments shown here, where the electron density is reduced and the sheath thickness is greater at higher humidity concentrations.

4.2 Gas temperature

The following results on gas temperature measurements were developed in collaboration with Maike Kai as part of her master's thesis supervised in the course of this dissertation. Some parts of the following section have already been published in her master thesis [191].

The gas temperature is an important characteristic of the plasma as the rate coefficients of neutral body reactions involved in the plasma chemistry are temperature dependent (see chapter 2) and high gas temperatures are destructive for application purposes. As described in chapter 3, two methods were used to determine the gas temperature of the discharge. In figure 4.3 (a), the two methods, namely OES and thermocouple measurements, are compared for three plasma powers and various humidity concentrations. At low humidity concentrations (0 ppm and 640 ppm), the gas temperature of the discharge obtained by both methods agrees very well. Temperatures of about 100 °C, 150 °C and 240 °C were measured at plasma powers of 3 W, 6 W and 12 W, respectively. The thermocouple measurements do not show any tendencies of the discharge temperature for various humidity concentrations (not

shown here). Therefore, the measured temperatures by this method are indicated as lines in the figure. However, the temperature obtained from OES measurements shows an increasing trend with increasing humidity concentrations.

This discrepancy is due to an overpopulation of rotationally excited states of OH, which misleadingly leads to an increased rotational temperature. Although a single-temperature distribution, which is normally applied to the fitted spectra, still provides a good fit at the expense of a higher rotational temperature, a two-temperature Boltzmann distribution should be used to avoid the overpopulation at high humidity concentrations [116]. The previously published study found the limit of applicability of OES to determine gas temperatures from rotational temperatures of OH at 308 nm to be below humidity concentrations of 1000 ppm [122]. This is in good agreement with our investigations as the gas temperature measurements from the thermocouple and OES deviate at humidity concentrations higher than 640 ppm. Since the gas temperature measurements from the thermocouple and OES are the same for low humidity concentrations, both methods are comparable and further results considering gas temperatures are shown for the thermocouple measurements.

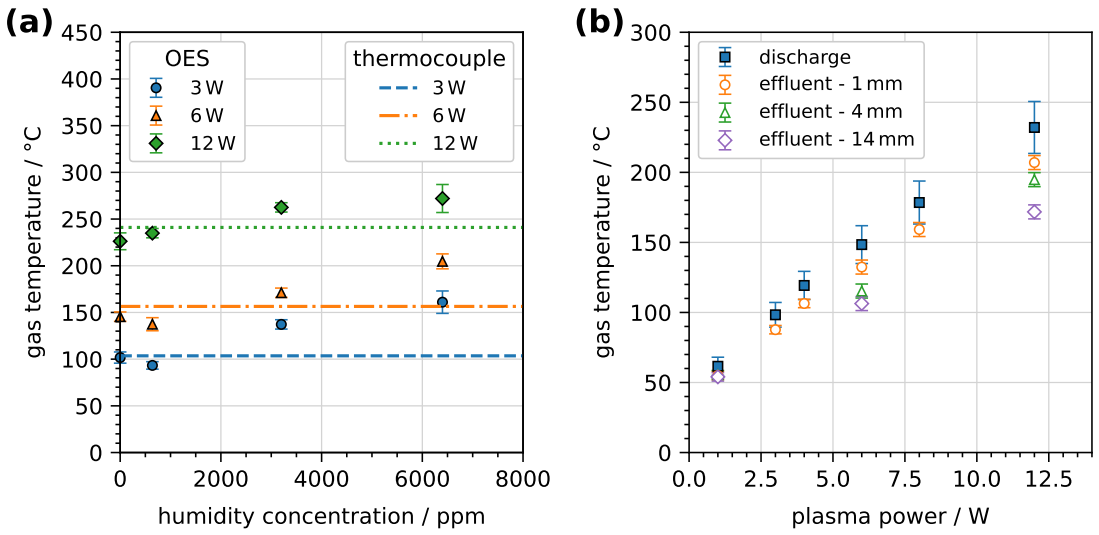

Figure 4.3: **(a)** Discharge temperature obtained from the rotational temperature of the OH band emission at 308 nm emission as a function of humidity concentration at three plasma powers (OES). Lines indicate the extrapolated gas temperature in the discharge, which is constant for all humidity concentrations (thermocouple). **(b)** Gas temperatures at the end of the discharge channel and in the effluent at various distances from the capillary end as a function of dissipated plasma power measured using a thermocouple.

The dependence of the discharge temperature on the dissipated plasma power is shown in figure 4.3 (b). There, an increase in the discharge temperature with increasing plasma power can be observed. At 1 W plasma power, the discharge tem-

perature is already significantly above room temperature with $(62 \pm 7)\,°C$, while at 12 W an elevated temperature of $(232 \pm 19)\,°C$ is obtained. Since chemical reactions without electron impact are thermally driven, their rate coefficients are strongly dependent on the gas temperature (see chapter 2) and the measured temperatures have to be taken into account when modelling the plasma chemistry of the jet.

In terms of application, the gas temperature at a certain distance from the plasma jet is of interest. In the effluent, the gas temperature still rises linearly with plasma power (see figure 4.3 b), but is lower compared to the gas temperature at the end of the discharge channel. For example, at 6 W plasma power, the gas temperature in the effluent is $(132 \pm 5)\,°C$ and $(104 \pm 5)\,°C$ at distances of 1 mm and 14 mm, respectively. This corresponds to reductions of 11 % and 30 %. The discharge temperature and the temperatures in the effluent at positions of interest (4 mm for LIF measurements and 14 mm for liquid treatments) are listed in table 4.1 for plasma powers of 1 W, 6 W and 12 W.

Table 4.1: Temperature of the discharge $T_{discharge}$ and temperatures in the effluent at 4 mm $T_{4\,mm}$ and 14 mm $T_{14\,mm}$ distance from the capillary end for various dissipated plasma powers P.

P / W	$T_{discharge}$ / °C	$T_{4\,mm}$ / °C	$T_{14\,mm}$ / °C
1	(62 ± 7)	(56 ± 3)	(54 ± 3)
6	(148 ± 14)	(115 ± 5)	(104 ± 5)
12	(232 ± 19)	(195 ± 5)	(172 ± 5)

4.3 Electron dynamics

The following results on PROES measurements were developed in collaboration with Lara Boeddinghaus in the frame of her bachelor's thesis supervised in the course of this dissertation. Some parts of the following section have already been published in her bachelor thesis [190].

Electrons are the main driver of reactions in the plasma. By analysing the emission of excited states from the plasma, information about the excitation by energetic electrons can be gained. Emission spectra of the plasma with and without humidity are shown in figure 4.4. The emission spectrum resembles those typically found in a He plasma, with a few He lines and some lines occurring from species due to impurities from air and water [13, 192–196]. In the spectra of the capillary plasma jet, the He 706 nm line is the most dominant line in both spectra. More He lines can be observed at 501 nm, 587 nm, 667 nm and 728 nm. In the case of no

humidity admixture, the H_α line at 656 nm and OH band emission at 308 nm are visible due to some H_2O impurities in the gas lines. H_2O dissociates into H and OH by electron impact dissociation and both species can be excited afterwards in the plasma. Further, the O line at 777 nm and N_2^+ band emission of the second positive system at 391 nm are present due to air impurities.

By adding humidity to the feed gas, the overall intensity of the emission decreases, but the He 706 nm line is still the dominant line. The OH band emission increases to about 10 % of the He 706 nm line, while the H_α emission stays the same compared to He 706 nm line. The O 777 nm line almost vanishes by adding humidity to the system, while the N_2^+ band emission at 391 nm is still present. The vanishing of the O 777 nm line indicates that either no O is present in the system or that the excitation or emission of O is hindered when humidity is added to the feed gas. Since experiments and simulations of a humidified He plasma jet showed O to be present in a He+H_2O plasma [37], the oxygen emission is likely to be quenched in the He+H_2O plasma.

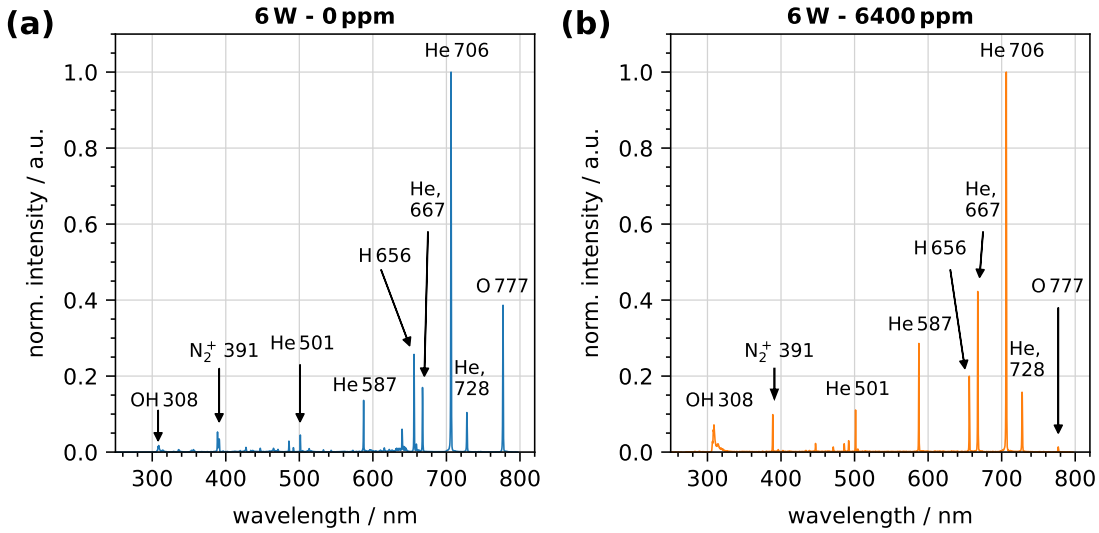

Figure 4.4: OES spectra of the capillary plasma jet at 6 W plasma power and humidity concentrations of **(a)** 0 ppm and **(b)** 6400 ppm. Spectra are normalised to their respective maximum.

The OES measurements presented are not spatially resolved and are time-integrated. To resolve the electron dynamic represented by the emission from excited plasma species spatially and temporally, PROES measurements were performed.

PROES analysis of He. First, the PROES analysis of the He 706 nm is discussed. Since the excitation energy of He $3s^3S^1$ is very high with 22.72 eV (compare table 2.3), its emission pattern tracks high energetic electrons of the plasma. The PROES images of He are shown in figure 4.5 as 2D colourmaps visualising the nor-

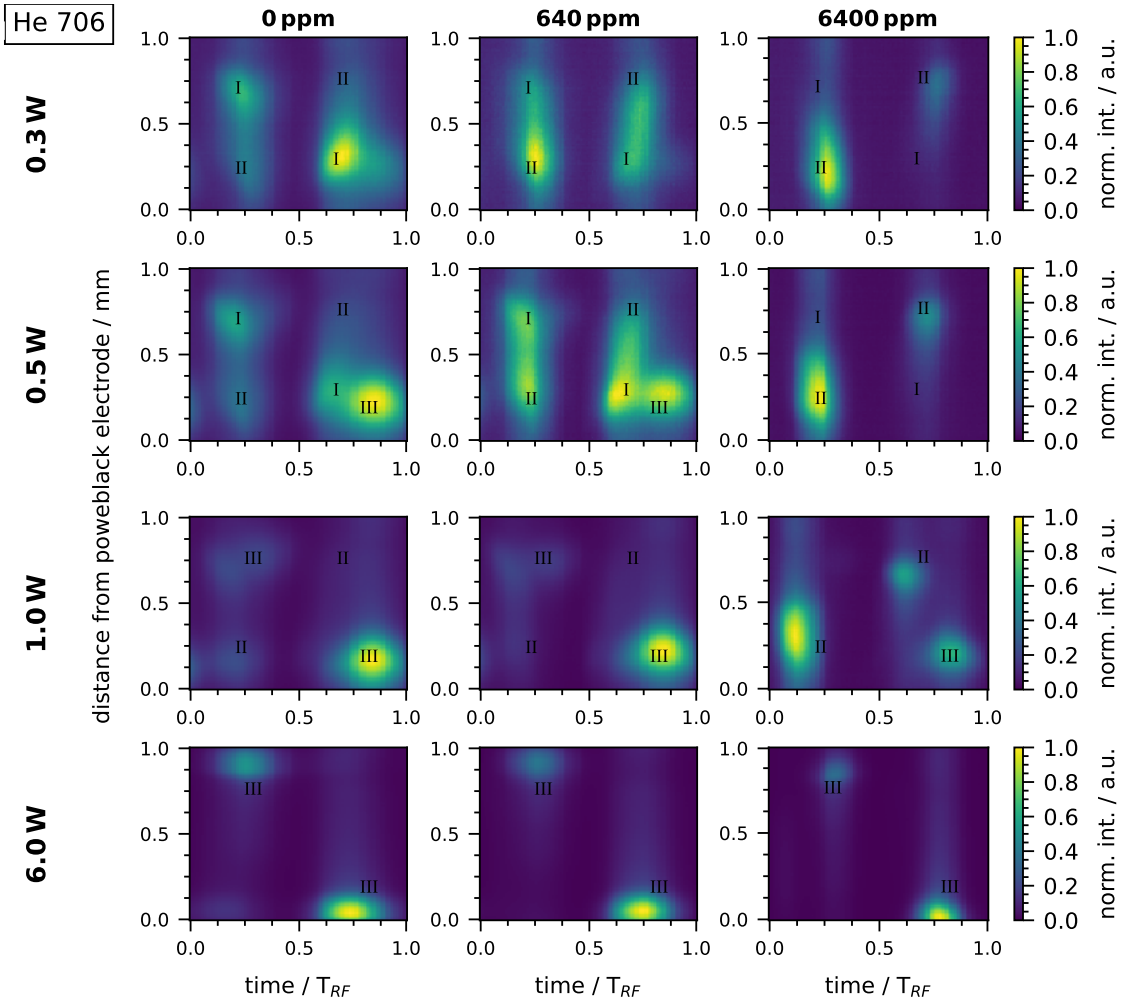

Figure 4.5: PROES images of the He 706 nm line. Plasma was operated at different humidity concentrations to the He feed gas (columns) and different plasma powers (rows). Each image is normalised to its maximum intensity. Emission maxima present in the images are located with I, II and III.

malised intensity between the two electrodes over one complete RF cycle at various plasma powers.

The PROES images of a pure He plasma (0 ppm humidity) are shown in the first column of figure 4.5. At the lowest plasma power of 0.3 W, the emission occurs with two maxima (see maxima I and II in figure 4.5). These two maxima are present at two times within the RF cycle at $0.25\,T_{RF}$ and $0.65\,T_{RF}$ at positions of 0.25 mm and 0.75 mm distance from the powered electrode. Maxima I and II are also visible at 0.5 W but shift to earlier times and a third maximum appears at $0.9\,T_{RF}$ and 0.25 mm from the powered electrode with a higher intensity than maxima I and II. At even higher plasma powers (1 W and 6 W), maxima I and II disappear and only maxima III is present at two positions in time, which shifts to earlier times and closer to the powered electrode as the plasma power increases. These observations described above fit well with the PROES measurements performed

using the COST reference plasma jet [57]. As described in chapter 2, the emission maxima indicate the operation of the APPJ in different modes at different powers. At low plasma powers, the plasma operates in the Ω-mode, characterised by ohmic heating in bulk, and the emission maxima I and II can be attributed to fast electrons accelerated in the expanding and retreating sheaths of the plasma [57, 197, 198]. Maxima III indicate the Penning mode, where high energetic electrons are produced by secondary electron processes such as Penning ionisation in the sheath regions of the plasma [57].

PROES images at 640 ppm and 6400 ppm are additionally shown in figure 4.5 in the second and third column, respectively. At a humidity of 640 ppm, the same pattern at 0.3 W is visible as it was the case without humidity. However, the intensity of the maxima I and II changed, with the maxima II becoming brighter. The change in intensity of the maxima becomes even more pronounced at 6400 ppm humidity as maxima I are barely visible and only maxima II are present in this case. The change in intensity could be because more electrons cannot follow the retreating sheath if H_2O is present, as H_2O molecules are another collision partner for the electrons. By this, the negative space charge region is larger when H_2O is added and the acceleration at the retreating sheath is pronounced, leading to an enhanced intensity of maxima II.

Increasing the plasma power also leads to the appearance of maxima III when H_2O is added to the plasma. At 640 ppm, maxima II begin to appear at 0.5 W as was the case without humidity. However, at 6400 ppm humidity, maxima III begin to occur at a higher plasma power of 1 W. Also in the sheath regions, H_2O molecules act as collision partners and quenchers, resulting in lower electron energies. Thus, higher voltages and higher plasma powers are necessary to provide highly energetic electrons to excite He atoms. At 6 W plasma power, all PROES images are identical, regardless of whether water was added to the feed gas. The high voltage and the high electric field are sufficient to excite the He atoms although a high amount of water molecules acting as quenchers are present in the system.

In addition, the intensity of the maxima I, II and III is not symmetrical in time. For example, the maximum I at $0.65\,T_{RF}$ is brighter than that at $0.25\,T_{RF}$ in the case without humidity admixture and 0.3 W. Assuming homogeneous coupling of the power into the plasma, symmetrical excitation would be assumed. However, slight deviations in the symmetry of the electrode arrangement can lead to an asymmetrical pattern in the excitation [77]. The fact that the addition of humidity to the plasma changes the asymmetry of the excitation pattern suggests that other mechanisms come into play when water is added. To investigate this in detail, a model that takes into account the different excitation processes is necessary for further research.

PROES analysis of reactive species. To investigate the excitation of reactive species, PROES analysis was performed for reactive species involved in the plasma chemistry containing humidity: OH, H and O. The electron impact dissociation of H_2O produces H and OH and an energy of 4 eV is necessary for the dissociation. The excitation of the OH band emission at 308 nm and the H 656 nm line requires less energy (18 eV and 10 eV, respectively) than the excitation of He 706 nm emission (see table 2.3).

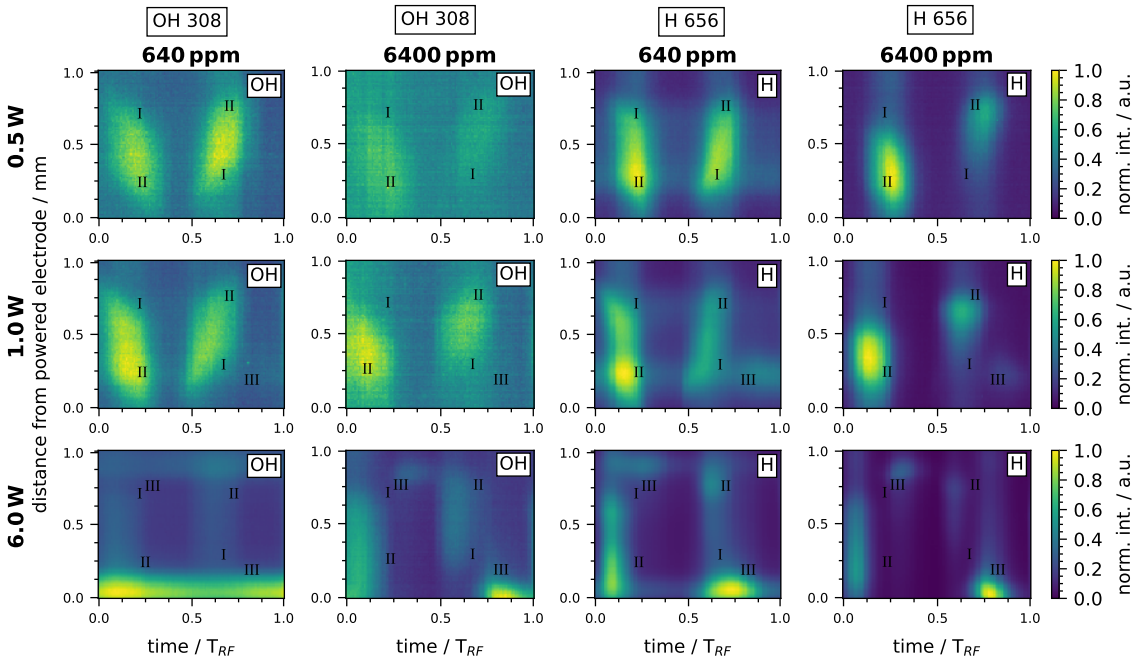

Figure 4.6: PROES images of the OH 308 nm band emission (columns 1 and 2) and the H 656 nm line (columns 3 and 4). Plasma was operated at different humidity concentrations (columns) and plasma powers (rows). Each image is normalised to its maximum intensity and the positions of maxima I, II and III represent the position of the He maxima from PROES images in figure 4.5.

The PROES images of the OH band emission at 308 nm and the H_α line at 656 nm are shown in figure 4.6. Both emission patterns of the two species are identical in position and time, closely linked to the emission of He. For OH and H, maxima I and II are visible at low plasma powers at the same spatial and temporal position as it was the case for He (see labelling in figure 4.6). At 1 W plasma power, maxima I and II are again shifting to earlier times and also maximum III starts to appear, but less intense compared to He. At high plasma power of 6 W, maxima III have fully developed, but maxima II are still visible. This was not the case for He, showing that the reactive species are produced and excited in the sheath region and the bulk at high plasma powers due to their lower excitation energies.

To analyse the excitation of O, two lines were selected: the 777 nm and 844 nm lines, which are the most significant oxygen lines in atmospheric pressure plasmas

[15]. Their PROES images are shown in figure 4.7. The emission from the 844 nm line is barely visible at plasma powers below 1 W. At 1 W maximum II starts to appear at the same spatial and temporal position as was the case for He, OH and H. At 6 W, the emission from O at 844 nm is similar to the emission of OH and H with maxima III being the most dominant and maxima II still present in the plasma bulk. The emission from O at 777 nm line shows a different pattern. Two maxima are present at the temporal position of maxima II. But these two maxima are homogeneously distributed in the spatial direction. With increasing power, the maxima shift to earlier points in time, as it was the case with the maxima II of the other species, and become broader.

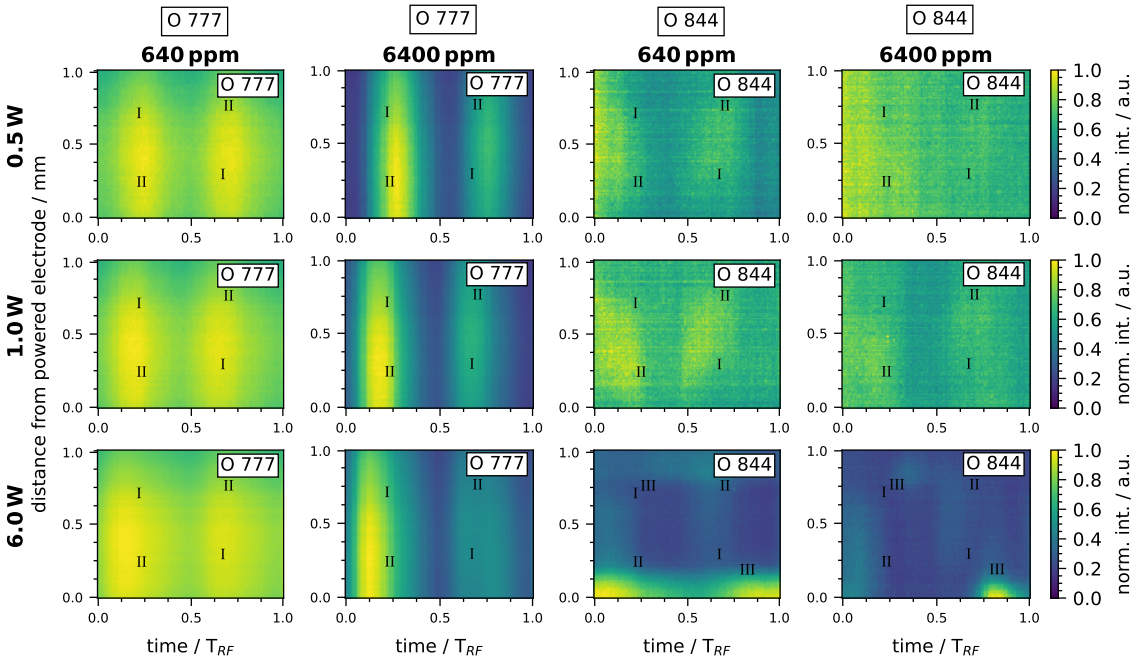

Figure 4.7: PROES images of the O lines at 777 nm (first two columns) and 844 nm (last two columns). Plasma was operated at different humidity concentrations (columns) and plasma powers (rows). Each image is normalised to its maximum intensity and the positions of maxima I, II and III represent the position of the He maxima from PROES images in figure 4.5.

A different emission behaviour of the two O lines was also previously found for measurements with the COST reference plasma jet operated in He+O_2 gas mixture [199]. In their work, the emission from O 777 nm was less modulated over time and broader compared to the lines of He 706 nm and O 844 nm. This behaviour can be explained by the step-wise excitation by the metastable atoms $3s^5S^0 \rightarrow 3p^5P$ (excited state of the 777 nm emission). This excitation has a much larger cross-section compared to the electron impact excitation of $3s^5S^0 \rightarrow 3p^3P$ (excited state of the 844 nm emission) [199, 200]. This can also explain the spatial difference between the two emissions since the excitation of the 777 nm emission might not

only originate from energetic electrons but follow the distribution of metastable atoms. These may be more homogeneously distributed between the two electrodes, while the electrons that excite the $3p^3P$ state of the 844 nm emission are highly localised, as was the case for the emissions of He, OH and H.

All in all, the PROES analysis of the various species provides insights into the excitation of the species within the plasma. The PROES analysis of the capillary plasma jet shows the same excitation pattern as observed for the COST reference plasma jet, indicating identical dynamics of the capillary plasma jet to the COST reference plasma jet. The mode change from Ω- to Penning mode is visible by the emission of the He 706 nm and it is the same for the addition of humidity but higher voltages (higher powers) are needed to achieve the mode change. The emission from reactive species follows the emission of the He line indicating the excitation from high-energetic electrons, predominantly in the sheath regions at high plasma powers. However, some emission of reactive species in the bulk remains at high powers, indicating the excitation of reactive species from lower energetic electrons.

4.4 Detection limit of LIF spectroscopy

The following results on LIF measurements, including the air entrainment presented in the next section, were developed in collaboration with Maike Kai as part of her master's thesis supervised in the course of this dissertation. Some parts of the following section have already been published in her master thesis [191].

OH is the precursor of H_2O_2 and thus, its distribution is of major interest when discussing the H_2O_2 production of the capillary plasma jet. To this end, laser-induced fluorescence spectroscopy was applied in the effluent of the capillary plasma jet. The measured integrated LIF signals in radial (x and y) and axial (z) directions are shown in figure 4.8. The analysis of the spatial distribution of the LIF signal can be used to discuss the detection limit of the LIF spectroscopy. Without determining any potential quenching of the LIF signal, it is not possible to draw conclusions about the distribution of OH. The absence of the LIF signal may indicate either that OH is absent or strong quenching of the excited OH radicals. However, in the regions where no LIF signal is measured, the LIF spectroscopy is limited and no conclusions on the distribution of OH can be made. Thus, the following analysis of the LIF signal provides a basis for the applicability of the LIF diagnostic.

In radial direction (see figure 4.8 a), the maximum LIF signal is detected at the centre of the axes at 0 mm. To the sides, the signal decreases to reach almost zero at ±0.75 mm. Thus, the signal in radial direction is slightly broader compared to the capillary width of 1 mm. Since the signal was measured at an axial distance of

$z = 4\,\mathrm{mm}$, a widening of the gas flow can appear due to friction with the ambient air. Furthermore, the profile of the LIF signal is wider in the x-direction compared to the y-direction. This indicates a slight asymmetry of the transported OH and of the plasma itself. Since the plasma power was high, the plasma operated in Penning mode with a strong appearance of sheath regions near the electrodes [57]. This is a particular feature of the plasma jet used, as the electrodes are only attached on two sides and the rotational symmetry of the system is not given. The electrodes were positioned in the x-direction. Thus, the appearance of the sheaths in front of the electrodes might lead to an asymmetry of the plasma. The trends described are the same at low and high humidity with a higher LIF signal at 640 ppm than 6400 ppm. This aspect is discussed in detail later.

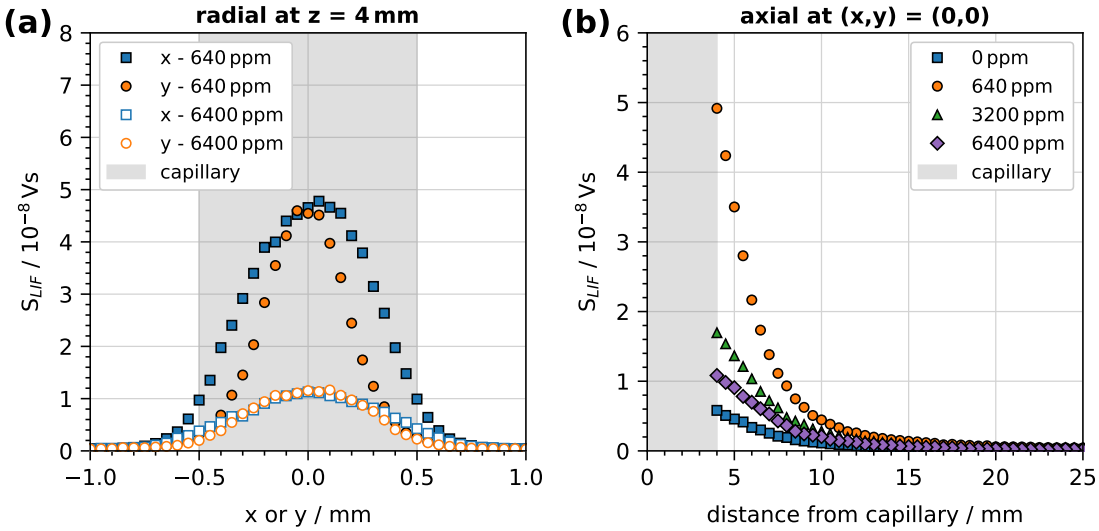

Figure 4.8: LIF signals in **(a)** radial direction at $z = 4\,\mathrm{mm}$ and **(b)** in axial direction at $(x, y) = (0, 0)$. Plasma was operated at 6 W plasma power and various humidity concentrations.

The LIF signal in axial direction, shown in figure 4.8 (b), decreases exponentially with increasing distance. This behaviour is expected since the OH density decreases in axial direction from the plasma jet [127, 131]. At a distance of $z = 20\,\mathrm{mm}$ the LIF signal has almost disappeared. This behaviour is the same for all humidity concentrations shown in the figure and plasma powers (shown in the SI). Thus, the OH radical is only present in the first 2 cm in the effluent or the quenching is too strong at larger distances as the air entrainment increases with increasing distance as described in the next section.

The LIF signal as a function of the distance from the capillary end under pulse modulation of the RF signal is shown in figure 4.9 at duty cycles of 10 % and 50 % and various frequencies. While an exponential decay characterised the unmodulated signals, the LIF signals under pulse modulation, particularly at higher frequencies,

show a peak in their decay. This is true for both duty cycles. The unmodulated mode is characterised by a constant flux of OH radicals in the effluent. Regarding pulse modulation, this view shifts towards "packages" of OH that leave the capillary jet and travel through the effluent. The observed maxima correspond to the OH produced during the plasma-on time and transported by the gas flow into the effluent. The distance where the OH signal peaks occurs at the same distance from the capillary end regardless of duty cycle and frequency as the transport of these OH packages in the effluent is determined by the gas flow rate. This behaviour is similar to the investigations by Schröder et al. of the O density in a self-pulsing APPJ [201]. There, packages of O were observed travelling through the discharge channel with time corresponding to the individual plasma pulses [201]. In our work, no temporal differences in peak position were observed as the trigger of the LIF setup was at the same time spot. The packages of OH show that the production of the short-lived species OH is highly modulated and follows the pulse modulation of the RF signal.

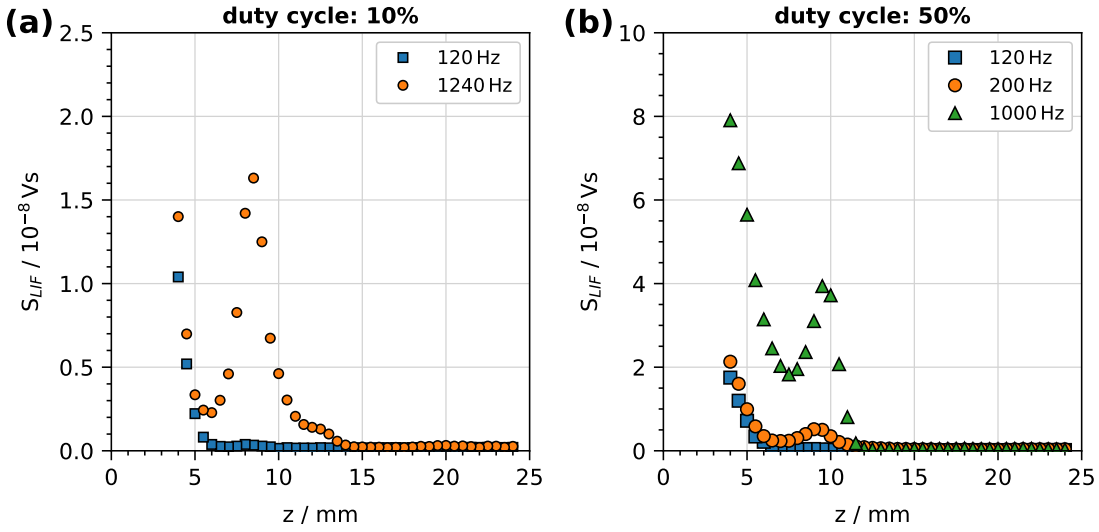

Figure 4.9: LIF signals in axial direction under pulse modulation at various frequencies and a duty cycles of **(a)** 10 % and **(b)** 50 %. Plasma was operated at an unmodulated plasma power of 6 W and a humidity of 6400 ppm.

4.5 Air entrainment

From fitting the temporal decay of the LIF signals in the LIF model, the density of quenchers can be obtained. This indicates the air entrainment into the He gas flow in the effluent. Air entrainment can influence the chemical composition of the effluent and change the composition of the species that arrive at the treated samples. Thus, knowledge about air entrainment is important to discuss its effects on plasma chemistry. The respective figures of the air entrainment (quantified as

He concentration with 100 % corresponding to no air entrainment) are shown in figure 4.10. In the xy-plane at both axial distances, the aforementioned asymmetry between the x-direction and the y-direction can also be seen as the area of 100 % He is slightly broader in the x-direction. This is because the air entrainment was obtained from the measured LIF signals and an asymmetry can also be seen in the analysed data.

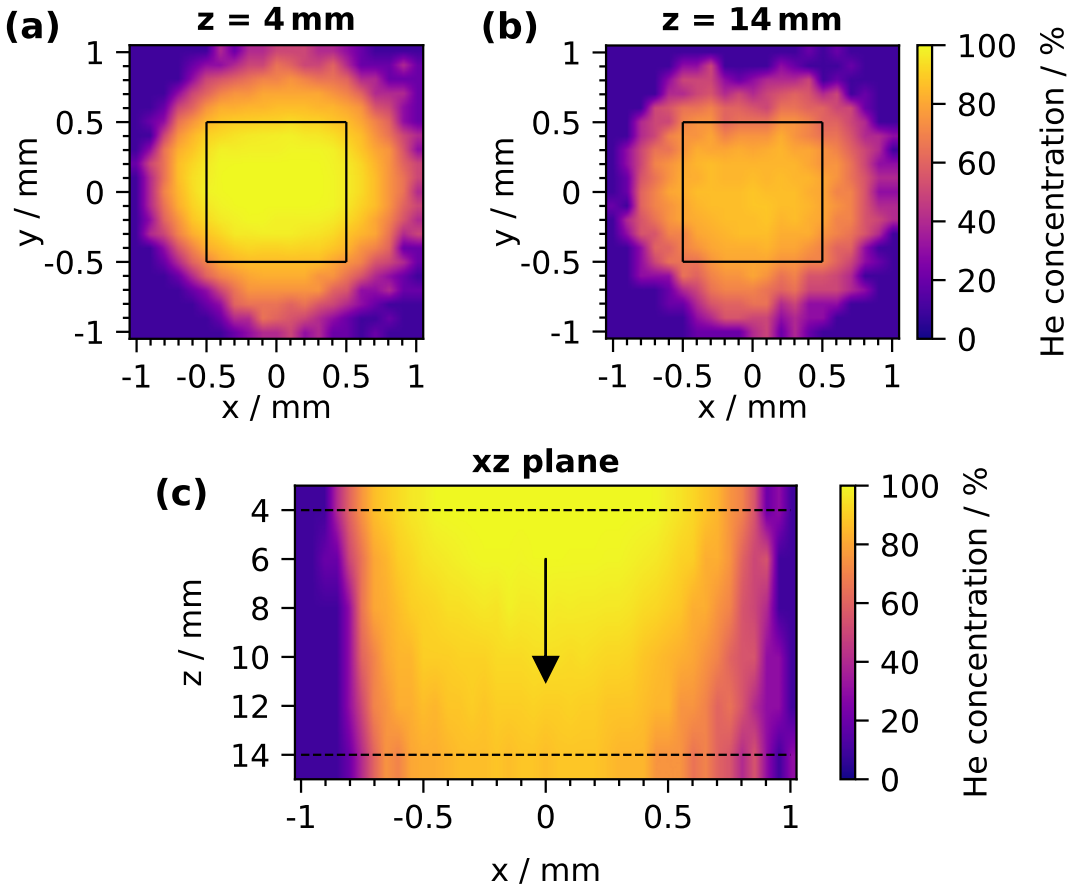

Figure 4.10: Air entrainment. **(a)** xy-plane at $z = 4\,\mathrm{mm}$. **(b)** xy-plane at $z = 14\,\mathrm{mm}$. **(c)** xz-plane. The plasma was operated at 6 W and 640 ppm humidity. The black square in (a) and (b) symbolises the relative position of the capillary at $z = 0\,\mathrm{mm}$. In (c), the capillary was centrally aligned between x positions of $-0.5\,\mathrm{mm}$ to $0.5\,\mathrm{mm}$, the dashed lines represent the positions of the xy-planes and the arrow indicates the gas flow direction.

Further, the respective width in both radial directions remains the same as the distance increases, but the air entrainment is enhanced. At 4 mm distance, the He concentration in the centre is still 100 %, while at 14 mm it is only 87 %. This behaviour can also be seen in the map of air entrainment in the xz-plane in figure 4.10 (c). The shape in the x-direction remains almost the same with increasing distance in the z-direction but the overall air entrainment increases. The air entrainment in

the yz-plane behaves the same due to the rotational symmetry of the gas flow in the effluent (not shown here). The air entrainment into the gas flow has to be considered when treating samples by APPJs at distances larger than 5 mm. The air components will interact in the effluent with the reactive species from the plasma and the chemistry in the effluent might be affected. Thus, the ratio of reactive species reaching the sample is different at different distances. The air entrainment measurements presented here agree well with previously published data of LIF measurements in the effluent of APPJs [49, 133].

4.6 Absolute species densities

The following results on LIF measurements to obtain the OH density in the effluent and FTIR measurements to obtain the H_2O_2 density (including results presented in chapter 6) were developed in collaboration with Maike Kai as part of her master's thesis supervised in the course of this dissertation. Some parts of the following section have already been published in her master thesis [191].

After discussing the distribution of the LIF signal caused by OH in the effluent and the air entrainment into the effluent, the species densities measured in the effluent can be discussed. First, the concentration of H_2O molecules in the effluent is discussed since dissociation of H_2O occurs in the plasma. Then the densities of OH and H_2O_2 and their trends with humidity addition are analysed, followed by an analysis of the measured LIF signal and the obtained OH density. Then the densities of HO_2, H_2 and O_2 are shown under variation of humidity and the effects of plasma power on the density of all species are investigated. At the end of the section, the spatial evolution of the species is described using model results and the effect of pulse modulation on the species densities is investigated.

4.6.1 Consumed water

H_2O is added to the He feed gas and dissociation by electron impact occurs. Thus, the amount of H_2O molecules in the effluent is reduced and H_2O molecules are consumed in the plasma to generate other species. The amount of H_2O molecules in the effluent was measured by mass spectrometry and included in the analysis of the LIF signal. The four-level model described by Verreycken et al. [132] was used to fit the measured LIF signals. The added humidity concentration of the feed gas was set as an input parameter for the model as it determines the density of the H_2O quenchers. During fitting, it was observed that the model always underestimated the measured LIF signal. This indicated that quenching in the model was too high due to a too-high concentration of H_2O molecules. In the plasma, H_2O is

consumed by dissociation processes resulting in a reduced density of H_2O molecules. To overcome this problem, the H_2O density was reduced in the model until the model reproduced the measured LIF signal well. The H_2O concentration used for modelling the LIF measurements is shown in figure 4.11 (a). With increasing plasma power and humidity concentration, more H_2O is dissociated and a more reduced concentration had to be used in the modelling. In the case of 8 W plasma power and 6400 ppm humidity concentration in the feed gas, the model concentration was reduced to 3900 ppm. This corresponds to a reduction by about 40 %.

To verify this approach, the H_2O density in the effluent was measured by mass spectrometry. The measured H_2O density in the effluent is lower than the added humidity to the feed gas as shown in figure 4.11 (b). There, the same trend of more consumed H_2O at higher humidity concentrations and plasma powers is evident. However, the reduction is not as strong as was assumed in the LIF model. At 8 W plasma power and 6400 ppm humidity concentration in the feed gas, the measured H_2O density in the effluent was (5660 ± 50) ppm corresponding to a reduction of only 12 %. Considering the two approaches, namely the fitting of the measured signal with the model and the measurement of the H_2O density, a discrepancy in the values is quite justifiable. This may be due to the absence of additional reactions in the four-level model. Particularly at high humidity conditions, three-body reactions become more significant and can contribute to quenching of OH and thus affect the LIF signal.

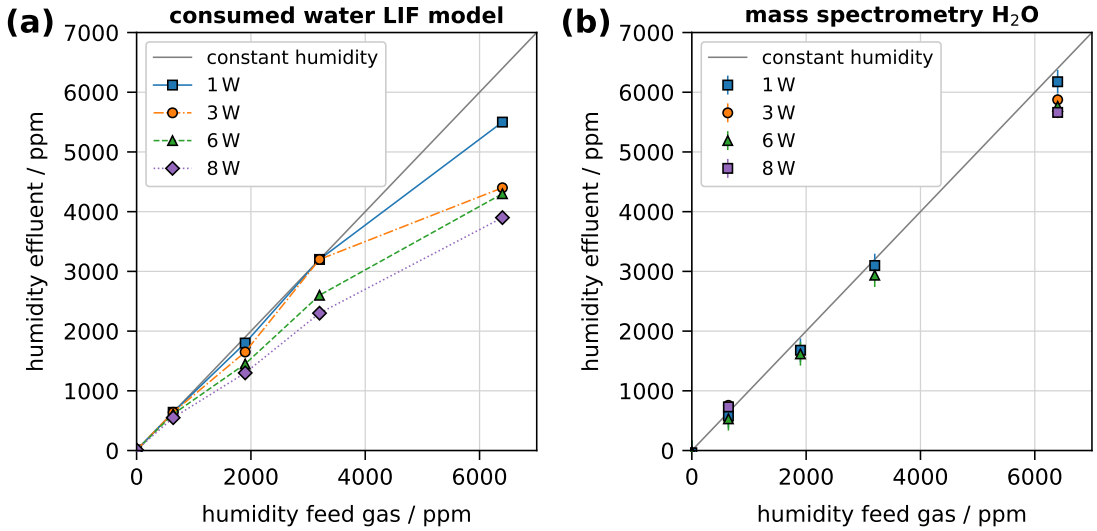

Figure 4.11: **(a)** Humidity concentration in the effluent used for fitting the measured LIF signals as a function of humidity added to the feed gas. **(b)** Measured effluent humidity by mass spectrometry for various humidity concentrations added to the feed gas.

4.6.2 Humidity and plasma power variation

The densities of OH and H_2O_2 as a function of the added humidity are shown in figure 4.12. Without humidity admixture, only small amounts of OH and H_2O_2 are observable. These might originate from impurities present in the gas flow. However, as soon as water is added to the gas flow, the density of both species increases and clear trends can be recognised.

In the case of OH, shown in Figure 4.12 (a), the density increases sharply at a distance of 4 mm from the end of the capillary as soon as water is added to the feed gas. With increasing humidity, the density continues to increase slightly and a maximum density of $2.3 \times 10^{13}\,\mathrm{cm}^{-3}$ is reached. At 14 mm, the density initially increases at 640 ppm, reaches a maximum of $0.96 \times 10^{13}\,\mathrm{cm}^{-3}$ and then decreases. The lower OH density and different trend at larger distances indicate the consumption of the OH radicals in the effluent, for example, to produce H_2O_2: $\mathrm{OH} + \mathrm{OH} + \mathrm{M} \longrightarrow \mathrm{H_2O_2} + \mathrm{M}$. The measured OH densities and trends fit well with previously published works on the OH density in the effluent of the COST reference plasma jet [29, 37, 202], considering the enhanced distance of the measurements by 10 mm due to the distance between plasma and capillary.

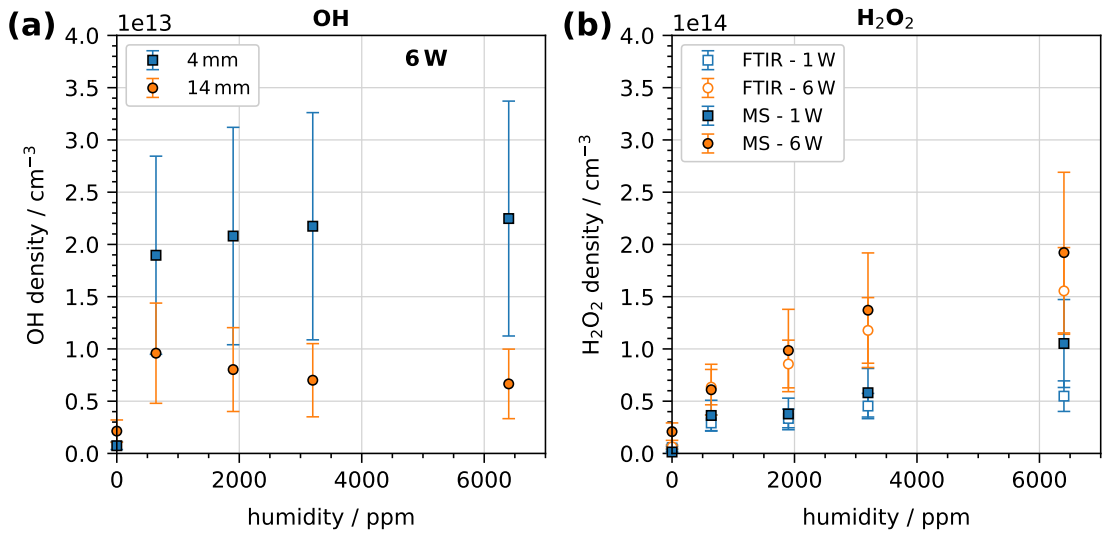

Figure 4.12: (a) OH density at 6 W plasma power as a function of humidity concentration. Densities were measured at distances of $z = 4$ mm and $z = 14$ mm from the capillary end by LIF spectroscopy. **(b)** H_2O_2 density for various humidity concentrations at 1 W and 6 W plasma powers. Densities were measured by FTIR and mass spectrometry.

The H_2O_2 density increases with increasing humidity concentration at 1 W and 6 W plasma power (see figure 4.12 b). Densities of $1.1 \times 10^{14}\,\mathrm{cm}^{-3}$ and $1.9 \times 10^{14}\,\mathrm{cm}^{-3}$ are reached at 6400 ppm and 1 W and 6 W plasma power, respectively. These den-

sities agree with densities obtained for the COST reference plasma jet [29, 34]. The increasing trend with humidity is also consistent with literature [26, 29, 31, 36, 187] and is mainly driven by the enhanced electron impact dissociation of H_2O, forming OH which recombines to H_2O_2 and the H_2O_2 density follows the trend of the OH density in the plasma.

The H_2O_2 density was measured by two techniques: FTIR and mass spectrometry. Both methods show the same trends and absolute densities considering the uncertainties of each method. Thus, the absolute densities in the far-effluent are verified and reliable.

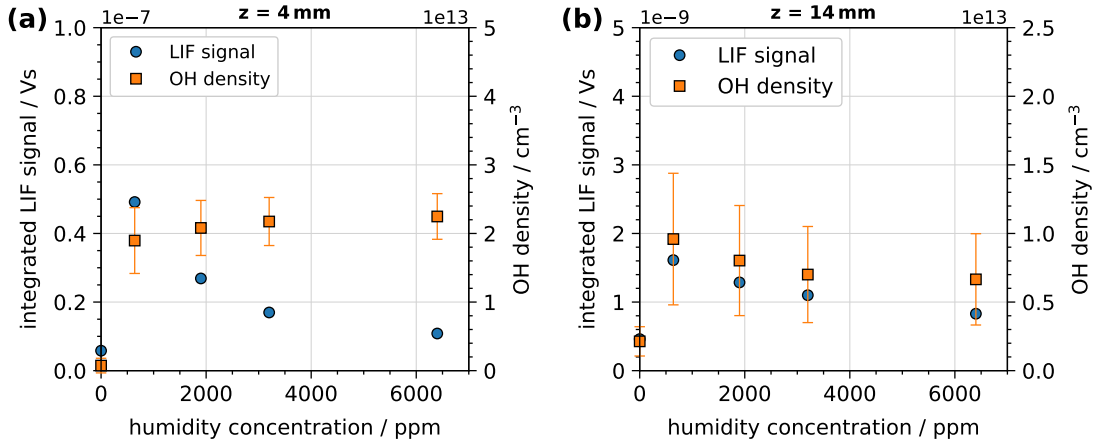

Figure 4.13: Comparison of the measured LIF signal with the corresponding obtained OH density at axial distances of **(a)** $z = 4\,\text{mm}$ and **(b)** $z = 14\,\text{mm}$ in the effluent. Plasma was operated at 6 W.

Important to notice is the different trend of the LIF signal and the obtained OH density. Considering the LIF signal discussed above, the highest signal was obtained at a humidity of 640 ppm at all distances. However, the density of OH at a distance of 4 mm shows a different trend as the maximum OH density occurs at humidity concentrations higher than 640 ppm. The direct comparison is shown in figure 4.13. Close to the capillary at 4 mm (see figure 4.13 a), the LIF signal increases steeply as soon as H_2O is added to the feed gas. The maximum signal is obtained at 640 ppm and with increasing humidity, the signal decreases steadily. In contrast, the OH density shows the same steep increase from 0 ppm to 640 ppm, but levels off at higher humidity concentrations and is almost constant. The different trends can be explained by quenching of OH by H_2O molecules. The measured LIF signal is given by the transition from the excited OH state to the ground state. This process occurs by spontaneous emission or is driven by quenching. The measured LIF signal should originate only from spontaneous emission but is reduced by quenching. In the model to obtain the OH density, quenching by H_2O or N_2 is included and the density is

obtained from the contribution of the spontaneous emission from the excited into the ground state. Thus, the trends are different and from the trends of the LIF signal, the trends of the OH density cannot be directly derived. This aspect becomes less important with increasing distance in the effluent as the trends of the measured LIF signal and the obtained OH density are the same as can be seen in figure 4.13 (b). This might be due to lower gradients in the spatial variation of effluent and atmosphere at larger distances as the air entrainment is stronger at 14 mm as described above. This analysis highlights the challenges of LIF spectroscopy, as the trends of the LIF signal may not reflect the OH distribution and appropriate analysis of the signals is mandatory.

The chemistry of a humidified APPJ consists not only of OH radicals and H_2O_2 molecules but further species are produced and involved in the chemistry. As discussed in chapter 2, further important species are radicals like O, H and HO_2 and long-lived species like O_2 and H_2. The densities of HO_2, H_2 and O_2 measured by mass spectrometry are shown in figure 4.14 with O_2 and H_2 been produced from the reactions of radicals. At low humidity concentrations, HO_2 is barely measurable (see figure 4.14 a). At 6 W plasma power and humidity concentrations higher than 1500 ppm, the HO_2 density reaches values between $0.5 \times 10^{13}\,\mathrm{cm}^{-3}$ and $1 \times 10^{13}\,\mathrm{cm}^{-3}$. At lower plasma power, the HO_2 density is below $0.5 \times 10^{13}\,\mathrm{cm}^{-3}$ but is enhanced at a high humidity concentration of 6400 ppm. In the case of H_2 (see figure 4.14 b), densities of less than $0.1 \times 10^{16}\,\mathrm{cm}^{-3}$ were measured at a plasma power of 1 W. At 6 W, larger H_2 densities can be measured and an increasing trend with humidity can be observed. The maximum density is $7.4 \times 10^{15}\,\mathrm{cm}^{-3}$ and thus, more than one order of magnitude higher compared to HO_2 and H_2O_2.

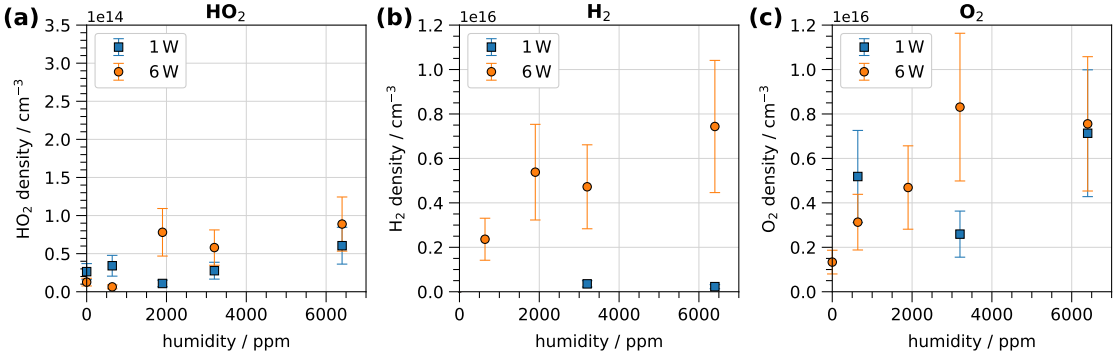

Figure 4.14: Densities of **(a)** HO_2, **(b)** H_2 and **(c)** O_2 as a function of humidity concentration for plasma powers of 1 W and 6 W. Densities were measured by mass spectrometry.

O_2 can also be measured at these high densities reaching almost the same maximum density with $7.5 \times 10^{15}\,\mathrm{cm}^{-3}$ at 6400 ppm humidity and 6 W plasma power (see figure 4.14 c). At 6 W plasma power, an increasing trend with humidity can be

observed where it saturates between 3200 ppm and 6400 ppm. On the other hand, the measured O_2 densities fluctuate and no clear trend can be observed at the lower plasma power of 1 W. This might be due to the low signal-to-noise ratio of the O_2 measurements by mass spectrometry since no shielding of the effluent from the atmosphere was used as described in chapter 3 and fluctuations in the O_2 density measurements by the atmosphere might occur.

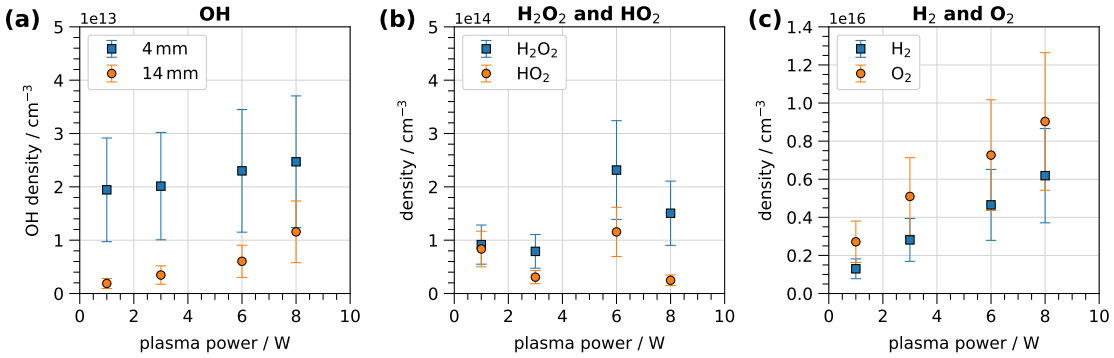

Figure 4.15: Densities as a function of dissipated plasma power. **(a)** OH measured at positions of 4 mm and 14 mm in the effluent by LIF. **(b)** H_2O_2 and HO_2 and **(c)** H_2 and O_2 all measured by mass spectrometry. The plasma was operated at a humidity of 6400 ppm in all cases.

The evolution of the species densities with plasma power in more detail is shown in figure 4.15. The OH density slightly increases with plasma power at both positions in the effluent (see figure 4.15 a). The densities of H_2O_2 and HO_2 are low at powers below 3 W, reach their maximum at 6 W and decrease again at 8 W (see figure 4.15 b). In contrast, H_2 and O_2 show a strong linear increase with plasma power (see figure 4.15 c). The different maximum densities of the species are also visible in the power variation. As already discussed above, H_2 and O_2 have the highest densities in the order of $1 \times 10^{16}\,\mathrm{cm}^{-3}$ followed by H_2O_2 and HO_2 in the order of $2 \times 10^{14}\,\mathrm{cm}^{-3}$ and OH has the lowest density at about $2 \times 10^{13}\,\mathrm{cm}^{-3}$. These trends agree well with modelling results, where H_2 and O_2 were found to have the highest densities at the end of the discharge channel [37].

In conclusion, the final products of a humidified APPJ consist not only of the long-lived species H_2O_2, but also include other molecular species such as H_2 and O_2 with a density of an order of magnitude higher than H_2O_2. This has to be taken into account if humidified APPJs are used for applications where H_2O_2 should be the main product. The other species could interfere with the process or even be harmful to the process.

Mass spectrometry provided the densities of H_2O, H_2O_2, HO_2, H_2 and O_2. To check whether all important long-lived species involved in the water chemistry of

the plasma were measured, a species balance regarding the H- and O species was analysed. For example, from one H_2O molecule, one H_2 molecule can be generated. The equations to calculate the species balance are given by:

$$\mathrm{H-balance} = \frac{n_{H_2O_2} + \frac{1}{2}n_{HO_2} + n_{H_2} + n_{H_2O}}{c_{H_2O}} \tag{4.1}$$

$$\mathrm{O-}\mathit{balance} = \frac{2n_{O_2} + 2n_{H_2O_2} + 2n_{HO_2} + n_{H_2O}}{c_{H_2O}} \tag{4.2}$$

with the measured densities n_j of species j (in ppm) and the inserted humidity concentration c_{H_2O} in the feed gas (in ppm). The corresponding species balances are shown in figure 4.16. At lower humidity concentrations and plasma powers, the balances are not equal to unity. But at these conditions, the overall densities are lower and the impact of the plasma is less. Thus, fluctuations in densities, particularly in the O_2 density from disturbances of the atmosphere, are more pronounced and lead to deviations in the species balance. However, at high humidity concentrations and plasma powers, the species balances are close to unity. This indicates that all relevant long-lived species were measured.

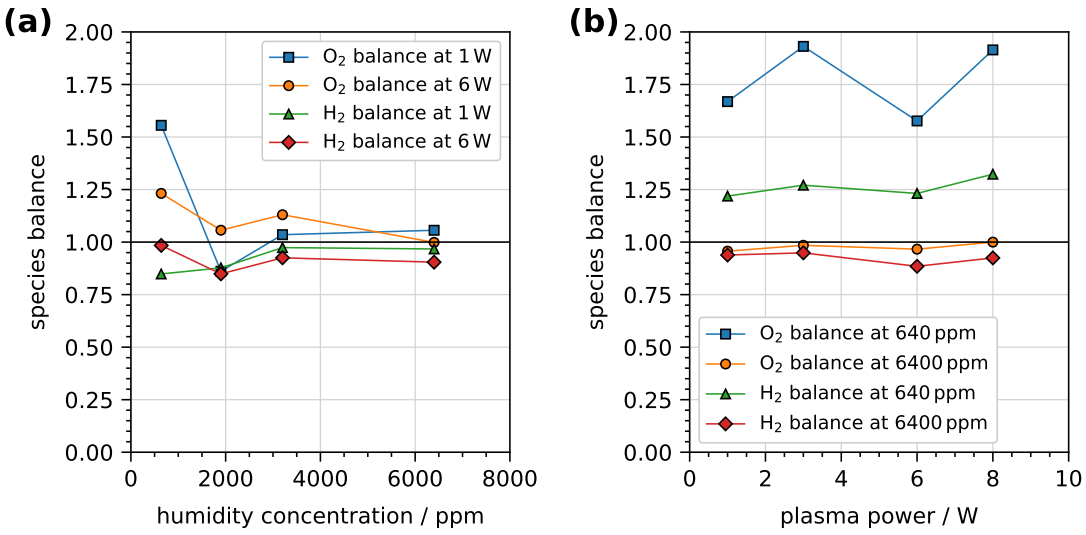

Figure 4.16: Species balances of measured species by mass spectrometry regarding the input humidity. **(a)** Shown as a function of humidity concentration at 1 W and 6 W plasma powers and **(b)** shown as a function of plasma power at 640 ppm and 6400 ppm humidity concentrations.

4.6.3 Chemistry model and species evolution

The water chemistry was explained in detail in chapter 2 and the densities of the most important species were measured in the effluent as presented above. However, the species production in the plasma is still unclear. Thus, a model is necessary

to investigate the species production within the plasma. In a collaborative publication, a pseudo-1D plug flow model was implemented by the Chair of Applied Electrodynamics and Plasma Technology at Ruhr University Bochum to model the chemistry of the capillary plasma jet and to compare it to the measurements [187]. The model results were taken from the publication and are compared to the density measurements in the effluent in figure 4.17. The model was evaluated in the effluent at a distance of 14 mm from the capillary end to be comparable to the LIF and mass spectrometry measurements.

In general, it can be seen that the model and experiment agree quite well. In the case of humidity variation, shown in figure 4.17 (a), all species densities increase with increasing humidity, except for OH where an initial increase followed by a decrease can be observed. The model reproduces these trends well. Furthermore, the relative densities of the species given in the model fit the experiments: The highest densities are found for the molecular species H_2 and O_2, followed by H_2O_2 and HO_2 and the lowest density is attributed to the OH radical. However, the absolute number densities of the model and experiments vary by up to an order of magnitude. Considering the complexity of the measurements and the determination of the reaction coefficients used in the model, as well as the number of reactions involved in the model, the trends agree reasonably well.

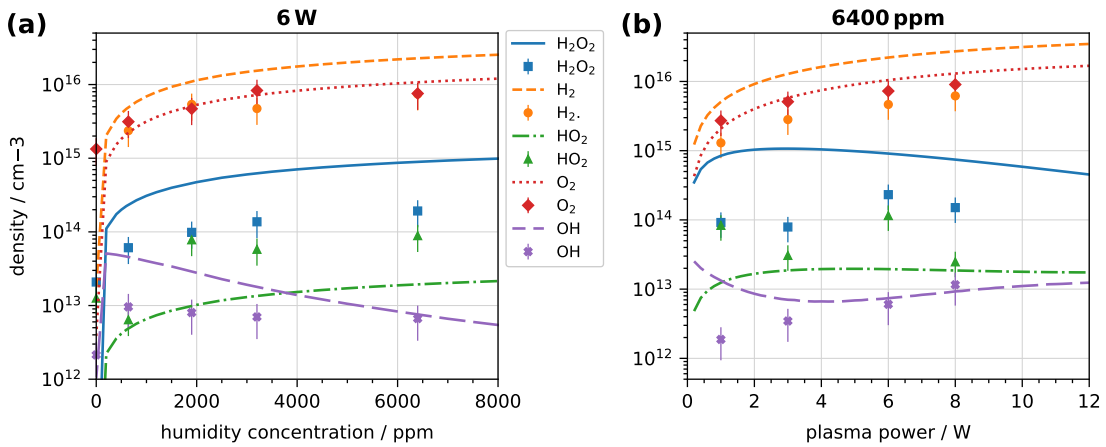

Figure 4.17: Comparison of the species densities from the model (lines) to mass spectrometry measurements (symbols) in the gas phase. **(a)** Densities are shown as a function of humidity admixture at a plasma power of 6 W. **(b)** Densities are shown for plasma powers at a humidity of 6400 ppm. OH density was measured by LIF spectroscopy at a distance of 14 mm from the capillary in the effluent and the densities of the other species were measured by mass spectroscopy. The model densities were also obtained at a position of 14 mm behind the capillary. Model results were taken from a joint publication [187].

The same aspects as described for the humidity variation can also be seen in the comparison of the model and experiments for the power variation shown in figure

4.17 (b). The highest densities are again for H_2 and O_2, followed by H_2O_2 and HO_2 and the lowest is attributed to OH. The trends are also well reproduced as the density of H_2 and O_2 increases with increasing plasma power, H_2O_2 and HO_2 initially increases followed by a decrease at higher plasma powers than 3 W but the trend of OH is slightly off. The model predicts an initial decrease until 4 W and for higher plasma powers the OH density further increases. In the experiments, on the other hand, a linear increase is observable. However, modelling the plasma power variation is more challenging as the plasma power determines plasma parameters such as the electron density and the gas temperature. These parameters were discussed in the beginning of chapter 4 and were used as input parameters for the model during power variation. Possible uncertainties in these measurements are incorporated into the model, so that the model results may deviate from the results of the power variations from the experiments. Nevertheless, the model reproduces the experimental findings very well and from the model, further insights into the chemistry can be obtained. This includes the spatial distribution of the species within the discharge channel, which cannot be measured experimentally as the density measurement could only be carried out in the effluent.

To this end, the model was used to investigate the spatial distribution of species in the discharge channel and the effluent. This is shown in figure 4.18 for the most important species involved in the water chemistry. At both humidity concentrations of 640 ppm and 6400 ppm, the same trends can be observed.

From the electron impact dissociation of H_2O, OH and H are produced. Their densities rise rapidly on the first 1 mm in the plasma channel until both species find an equilibrium of production and consumption and their densities remain the same from 5 mm until the end of the plasma. The consumption of H_2O can be recognised as its density decreases over the entire discharge channel. This is in agreement with the mass spectrometry measurements of H_2O discussed above, where lower densities in the effluent were found compared to the feed gas humidity.

The production of long-lived species starts after the production of H and OH and the densities of H_2O_2, O_2, and H_2 start to increase at about 2 mm. The density of H_2O_2 is quickly established as it stays constant after 10 mm to the end of the plasma zone. Thus, it might be beneficial to shorten the discharge channel to about 10 mm as the H_2O_2 production is fully established after this distance at a gas flow rate of 1 slm. The densities of H_2 and O_2 increase steadily until the end of the discharge channel. This indicates that the production of long-lived species continues throughout the discharge channel from radicals like OH and H. The O density also starts to increase after 2 mm and increases throughout the discharge zone indicating its continuous production. The main production of O occurs from the electron impact dissociation

of O_2 and the recombination of OH: $2\,OH \longrightarrow O + H_2O$ at humidity concentrations of 500 ppm and higher [83]. Since OH is produced instantly in the plasma containing humidity admixtures, its recombination leads to the production of O in the discharge channel. The HO_2 radical shows the lowest densities in the plasma zone and its production starts later at 5 mm. Its density increases then continuously until the end of the discharge zone. As it is mainly produced by OH and H_2O_2 from $OH + H_2O_2 \longrightarrow HO_2 + H_2O$, its continuous increase is reasonable since both species are present in the discharge channel.

In the effluent, different trends of the short-lived radicals and the more stable long-lived species can be observed. The density of H_2O remains constant as the electron impact dissociation stops. The long-lived species H_2O_2, O_2 and H_2 as well as HO_2 remain almost constant on the investigated effluent length of 24 mm. In contrast, the production of radicals like OH, H and O by electron impact dissociation is stopped in the effluent while their consumption continues. Thus, their densities exponentially decrease in the effluent. This was also observed in the experiments presented in this work as the LIF signal of OH decreases exponentially in the effluent and for the O radical density measured by LIF in the effluent of the COST reference plasma jet operated in $He+O_2$ [203]. The production of long-lived species in the effluent is smaller compared to the discharge channel and an increase of the densities of long-lived species is not visible in the effluent.

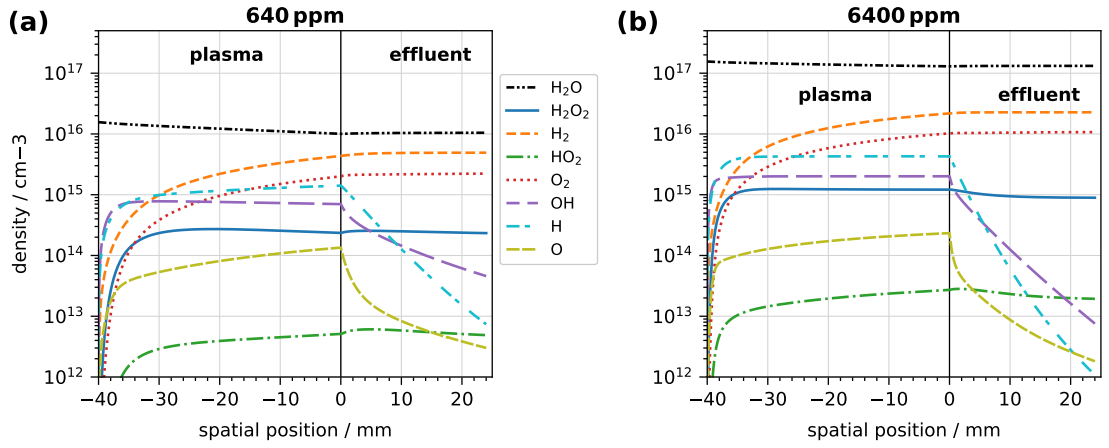

Figure 4.18: Spatial behaviour of the densities of most important species in the chemistry of a humidified plasma for humidity concentrations of **(a)** 640 ppm and **(b)** 6400 ppm. Data were taken from a joint publication [187] and the simulations were performed for a plasma power of 6 W. Negative positions correspond to positions within the plasma.

Furthermore, the model provides insights into the main production and loss reactions for OH and H_2O_2. These are listed in table 4.2. OH is mainly produced by the electron impact dissociation of H_2O. In addition, OH is also produced by H_2O

dissociation by water ions or excited atomic oxygen atoms. Besides H_2O dissociation, the recombination of H and HO_2 also leads to the production of OH. Once OH is produced, it recombines with OH to form H_2O_2 which is the strongest loss process of OH. It also reacts with H to reform H_2O and with O to form O_2. In the case of H_2O_2, it is mainly consumed by OH. Thus, an equilibrium between the production and consumption of H_2O_2 by OH is established within the plasma. Another contribution to the consumption of H_2O_2 is by electron impact dissociation and H is a strong consumption partner of H_2O_2 as both react to either H_2O and OH or H_2 and HO_2.

The analysis of the results from the experiment and model shows that the main species involved in the chemistry of the He+H_2O plasma are: OH, H, O, H_2O_2, HO_2, H_2 and O_2. In the experiments, the radical OH was detected by LIF spectroscopy and the long-lived species H_2O_2 by FTIR and mass spectrometry. The latter was also used to measure HO_2, H_2 and O_2. The analysis of the main production and loss reactions also explains why the species balance of the mass spectrometry measurements was close to unity since the main long-lived species involved in the He+H_2O chemistry were measured.

Table 4.2: The most important production and loss reactions of OH and H_2O_2 in the He+H_2O plasma obtained from model calculations performed in [187].

Production

OH	**H_2O_2**
$e^- + H_2O \longrightarrow OH + H + e^-$	$OH + OH + He \longrightarrow H_2O_2 + He$
$H + HO_2 \longrightarrow OH + OH$	
$H_2O^+ + H_2O \longrightarrow OH + H_3O^+$	
$H_2O + O^* \longrightarrow OH + OH$	

Consumption

OH	**H_2O_2**
$OH + OH + He \longrightarrow H_2O_2 + He$	$OH + H_2O_2 \longrightarrow HO_2 + H_2O$
$OH + OH \longrightarrow O + H_2O$	$e^- + H_2O_2 \longrightarrow OH + OH + e^-$
$He + H + OH \longrightarrow He + H_2O$	$H + H_2O_2 \longrightarrow H_2O + OH$
$OH + O \longrightarrow O_2 + H$	$H + H_2O_2 \longrightarrow H_2 + HO_2$

All in all, the model investigations demonstrated how the production of the species within the plasma is performed. From these results, adaptions of the plasma source

can be made. For example, the production of H_2O_2 is fully established after 20 mm at 1 slm gas flow rate. Thus, the length of the plasma jet could be shortened without a reduction of the produced H_2O_2. Or the gas flow rate could be enhanced by a factor of 2 and the same amount of H_2O_2 might be produced. The latter case is investigated in the plasma-treated liquid discussed in chapter 5.

4.6.4 Species densities under pulse modulation

All density measurements shown above were performed for continuous RF excitation waveforms. Since H_2O_2 is generated by the recombination of OH radicals and also destroyed by OH, modulation of the RF signal might be useful to separate the production of OH and H_2O_2 in the plasma-on case from the destruction of H_2O_2 since the density of OH might be modulated by the pulse modulation. To this end, the density measurements of the most relevant species were also performed for the capillary plasma jet under pulse modulation.

The OH density measurements were performed by LIF 4 mm behind the capillary. The OH density as a function of the number of pulses per residence time is shown in figure 4.19 (a). There, the number of pulses per residence time is given by the product of frequency and residence time of the particles within the plasma as explained in chapter 3. Thus, the number of pulses per residence time resembles a frequency variation. The OH density at a duty cycle of 10 % is a factor of 4 lower compared to the density obtained in the unmodulated case. At 10 % duty cycle, the plasma-off time is too long with more than 10 ms lowering the OH density as it is consumed in the plasma-off time. The OH density at 50 % duty cycle increases with the higher number of pulses and saturates at about 2 pulses. The saturated OH density at 2 pulses and above reaches the value of the unmodulated case. In this case, the plasma-off time is only about 0.2 ms allowing for enhanced production and less consumption of OH delivering equal densities compared to the unmodulated case. This is explained by the production and loss processes of OH. OH is mainly produced by electron impact dissociation of H_2O in the plasma-on time when electrons are present. In the plasma-off phase, the production stops and OH is immediately consumed by chemical reactions. At the high duty cycle and frequencies, the production equals the consumption and the OH density is equal to the unmodulated case.

The density of H_2O_2 under pulse modulation is shown in figure 4.19 (b). Its density is an order of magnitude higher than the OH density. At 10 % duty cycle and low number of pulses, a factor of 10 lower H_2O_2 density compared to the unmodulated case is obtained. However, with an increasing number of pulses, the H_2O_2 density increases to half of the unmodulated value. The rising trend indicates the beginning

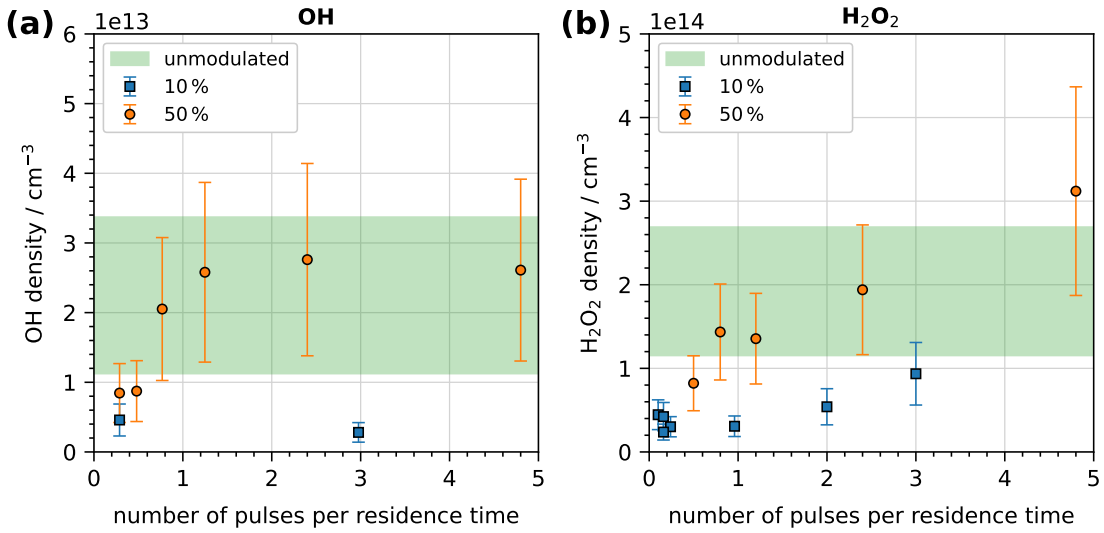

Figure 4.19: **(a)** OH density and **(b)** H_2O_2 density as a function of the number of pulses per residence time under pulse modulation at duty cycles of 10 % or 50 %. Plasma was set to an unmodulated plasma power of 6 W and a humidity concentration of 6400 ppm. The unmodulated case was operated at 6 W and 6400 ppm humidity.

of H_2O_2 production, which is enhanced at 50 % duty cycle. There, the H_2O_2 density is equal to or even higher than the unmodulated density. This indicates that the production of H_2O_2 is fully established when the plasma is modulated at a duty cycle of 50 %. Furthermore, the mean plasma power consumed under pulse modulation is a factor of 10 and 2 lower for duty cycles of 10 % and 50 %, respectively. Thus, pulsing of the RF excitation provides a method to trigger the OH and H_2O_2 production and it can be used to increase the efficiency of the OH and H_2O_2 production. The energy efficiency of the H_2O_2 production is discussed in detail in chapter 5 when the results of species concentration in the plasma-treated liquid under pulse modulation are discussed.

The impact of pulse modulation on HO_2, H_2 and O_2 is shown in figure 4.20 to investigate the effect of pulse modulation on the overall plasma chemistry of the He+H_2O plasma. HO_2 shows the same trend as H_2O_2. Since HO_2 is produced from the reactions of OH and H_2O_2 via $OH + H_2O_2 \longrightarrow H_2O + HO_2$, the same trend indicates that the HO_2 density follows the H_2O_2 density. At a low number of pulses, the HO_2 density is lower compared to the unmodulated case, while at a greater number of pulses, it reaches close to the unmodulated case. Further, at 50 % duty cycle and 4.8 pulses, the HO_2 density under pulse modulation is higher than the unmodulated density as was also the case for H_2O_2. The most remarkable differences between modulated and unmodulated densities can be observed for H_2 and O_2. The H_2 density under pulse modulation barely reaches the unmodulated

density and at 50 % duty cycle, the H_2 density even decreases with increasing the number of pulses per residence time. In contrast, the O_2 density at a low number of pulses per residence time is equal to the unmodulated density while it remarkably increases with the number of pulses per residence time at both duty cycles. At 50 % duty cycle and 4.8 pulses, the H_2 and O_2 densities are 31 % and 470 % of the unmodulated densities, respectively. Thus, there is a three-fold reduction in H_2 density and an almost five-fold increase in O_2 density when applying pulse modulation to the RF He+H_2O plasma. Unfortunately, the model was not suitable for modelling the plasma chemistry under pulse modulation, since longer time scales have to be modelled to adequately account for the on and off times of the plasma. However, a qualitative discussion on the plasma chemistry under pulse modulation is given in the following.

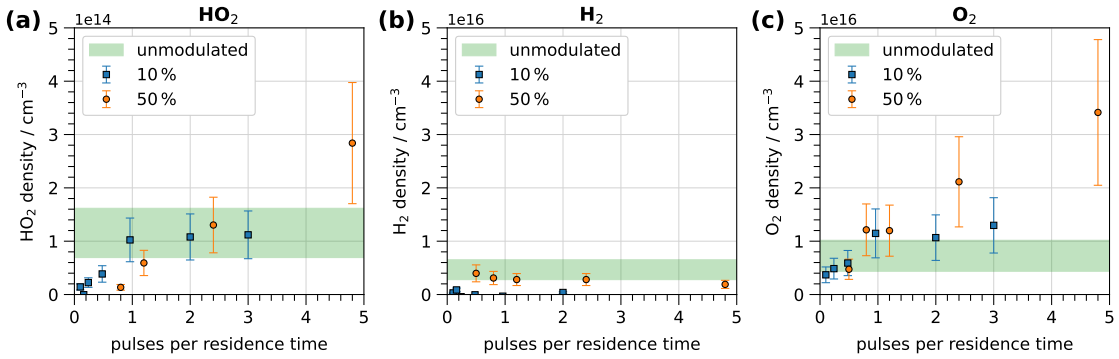

Figure 4.20: **(a)** HO_2 density, **(b)** H_2 density and **(c)** O_2 density as a function of the number of pulses per residence time under pulse modulation at duty cycles of 10 % or 50 %. Plasma was set to an unmodulated plasma power of 6 W and a humidity concentration of 6400 ppm.

Using the low-frequency pulse modulation of the RF excitation, the electron-driven processes can be separated from the neutral chemistry. In the plasma-on phase, electrons are present and the electron impact dissociation of H_2O is performed to produce OH and H. This is the start of the neutral chemistry in the plasma jet as recombination reactions can start. When the voltage is off between the modulation pulses, the production of reactive species from electron impact dissociation is stopped and the radicals will react and their density is lowered while long-lived species can accumulate. This can be seen in the experiments at a duty cycle of 10 % and a high number of pulses where the H_2O_2 density is close to the unmodulated case while the OH density is lower. The trends of a strongly modulated density of reactive species while the long-lived species steadily increase have been modelled previously [204].

In the pulse modulated experiments, the HO_2 density follows again the H_2O_2 as was the case in the unmodulated experiment. H_2 and O_2 showed clearly different

trends as H_2 decreased while O_2 increased. The different trends might indicate that the production of the reactive species H or O are different which leads to different trends in the H_2 and O_2 densities. Or the reactions to produce H_2 and O_2 vary strongly under the pulse modulation. However, from the experimental investigations in this study, no appropriate analysis of this behaviour can be made. A more detailed model of the chemistry and extended measurements of the short-lived species such as H and O of the RF-driven plasma jet under pulse modulation has to be performed. All in all, pulse modulation of the RF signal is a powerful tool to influence the species densities and can be used to set the ratio between short-lived primary species (lower densities indicating a suppressed production) and long-lived secondary species (equal or higher densities indicating an accumulated production).

All measurements under pulse modulation were performed at a humidity concentration of 6400 ppm. The effect of humidity variation on the H_2O_2 concentration under pulse modulation was not investigated. As the spatial profiles of the species within the discharge channel (discussed above) and the main production mechanisms of OH and H_2O_2 are the same at low and high humidity admixtures [37], it is assumed that the humidity variation under pulse modulation of the RF signal does not change and the main focus of the investigation of the power modulation was on the temporal characteristics given by the number of pulses per residence time.

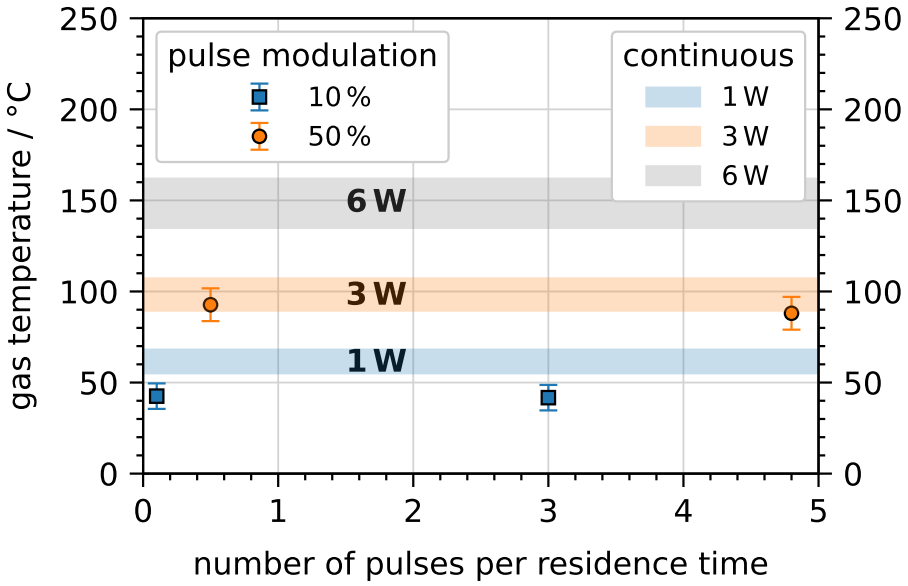

Figure 4.21: Extrapolated gas temperature measured using a thermocouple in the effluent under pulse modulation at duty cycles of 10 % and 50 %. Plasma was set to an unmodulated plasma power of 6 W and a humidity concentration of 6400 ppm. Shaded areas symbolise the gas temperature of the unmodulated case at different plasma powers taken from figure 4.3.

Since the mean plasma power under power modulation is lower, the gas temperature mainly driven by the dissipated plasma power might also be lower. To investigate this, the gas temperature of the plasma under pulse modulation is shown in figure 4.21 for both duty cycles at the minimum and maximum number of pulses per residence time. The 10 % duty cycle shows a lower temperature than the 50 % duty cycle. Furthermore, the temperatures are the same at the minimum and maximum number of pulses, indicating that the pulsing frequency does not affect the temperature in the frequency range investigated. Temperatures of 42 °C and 90 °C are achieved at duty cycles of 10 % and 50 %, respectively. Compared to the unmodulated case (shown as shaded areas in the figure), the temperature at 50 % is the same as measured at 3 W unmodulated plasma power. Under pulse modulation, an unmodulated plasma power of 6 W was set and pulsing at 50 % lowers the energy input by 50 %. Thus, less energy is available for gas heating and it is reasonable that the temperature of the 50 % duty cycle corresponds to the 3 W case. The same is true for the 10 % duty cycle (mean power of 0.6 W) as the measured temperature is lower than the one measured for 1 W unmodulated.

These investigations fit well with literature, where lower gas temperatures were found under pulse modulation [205–207]. Since the H_2O_2 generation at a duty cycle of 50 % is comparable to the unmodulated case, pulse modulation can be advantageous for applications where high gas temperatures are to be avoided. The lower temperatures must also be taken into account when modelling the pulse modulation of the RF excitation.

4.7 Summary gas phase dynamics and chemistry

In summary, the following learnings can be drawn from the investigations presented in this chapter:

- The capillary plasma jet is operable at high humidity admixtures (up to 6400 ppm) and high plasma powers (up to 10 W), enabling a broad application range. The electron density was found to be in the range of $10^{11}\,\mathrm{cm}^{-3}$ to $10^{12}\,\mathrm{cm}^{-3}$, depending on the plasma power and humidity admixture. The gas temperature reaches values up to 250 °C within the discharge and 150 °C in the effluent.
- The PROES analysis provided insights into the excitation of the various species within the plasma. The mode change from Ω- to Penning mode is visible by the emission of the He 706 nm and it is the same for the addition of humidity but higher voltages (higher powers) are needed to achieve the mode change. The emission from reactive species follows the emission of the He line indicating the excitation from high-energetic electrons, predominantly in the sheath regions at high plasma powers. However, some emission of reactive species in the bulk remains at high powers, indicating the excitation of reactive species from lower energetic electrons.
- Analysis of the LIF signal revealed insights into the air entrainment into the effluent, which is about 20 % at a distance of 14 mm from the capillary end.
- The consumption of H_2O was found in the LIF model and experiments leading to the production of reactive species. OH densities in the order of $10^{13}\,\mathrm{cm}^{-3}$, H_2O_2 and HO_2 densities of $10^{14}\,\mathrm{cm}^{-3}$ and H_2 and O_2 densities of $10^{15}\,\mathrm{cm}^{-3}$ were present in the effluent of the capillary plasma jet. The humidity admixture to the He flow and the dissipated plasma power control the production of these species as the densities increase with humidity admixture and plasma power.
- Model results fit well to the measured densities in the effluent and the spatial evolution of the species in the discharge and the effluent was visualised by the model. Differences in the evolution of reactive and more stable species are evident as the densities of reactive species exponentially decay in the effluent while the densities of long-lived species like H_2O_2 stay constant in the first 24 mm in the effluent.
- Pulse modulation of the RF voltage is a powerful tool for influencing species densities. It can be used to accumulate long-lived secondary species while suppressing the formation of short-lived primary species and the energy efficiency of the H_2O_2 production is increased under pulse modulation.

5. Liquid phase dynamics and chemistry

In plasma-driven biocatalysis, enzymes are utilised as catalysts in a liquid environment. The plasma-generated H_2O_2 needs to be dissolved in the liquid for the enzymes to be effective. In addition, plasma species dissolved in liquids are used in various areas such as environmental remediation, materials science and healthcare [38]. Therefore, this chapter focuses on measuring the concentrations of H_2O_2 and OH in the PTL, as well as investigating their distribution within the liquid. Towards the end of the chapter, there is a comparison between the liquid concentrations and the densities of H_2O_2 and OH in the gas phase.

The following results in this and the following chapter on measurements of the H_2O_2 concentration using spectrophotometry and electrochemical sensing were developed in collaboration with Emanuel Jeß in the frame of his bachelor's thesis supervised in the course of this dissertation. Some parts of the following section have already been published in his bachelor thesis [208]. In addition, parts of the results and discussions presented in this chapter have been published in the following papers:

- Steffen Schüttler et al., "Validation of in situ diagnostics for the detection of OH and H_2O_2 in liquids treated by a humid atmospheric pressure plasma jet" *Plasma Process. Polym. 2024;21:e2300079* [165].
- Steffen Schüttler et al., "Production and transport of plasma-generated hydrogen peroxide from gas to liquid" *Phys. Chem. Chem. Phys., 2024,26, 8255-8272* [187].

5.1 H_2O_2 production

At first, the H_2O_2 concentration in the PTL was analysed since its concentration and distribution in the liquid are the most important parameters for plasma-driven biocatalysis. Two methods were used to measure the H_2O_2 concentration: a spectrophotometric approach using the chemical ammonium metavanadate and electrochemical sensing. Since spectrophotometry required the addition of ammonium metavanadate in an acidic environment (pH below 3), this liquid is not comparable to the KPi buffer used in plasma-driven biocatalysis, but this technique can be used in-situ during plasma treatment. Electrochemical sensing was performed in the KPi

buffer but can only be applied ex-situ after treatment. To combine the advantages of both methods, both were applied and the measured concentrations of the two methods were compared. The H_2O_2 concentration in dependence on the humidity concentration and the applied plasma power is shown in figure 5.1. Three main findings can be drawn from this analysis.

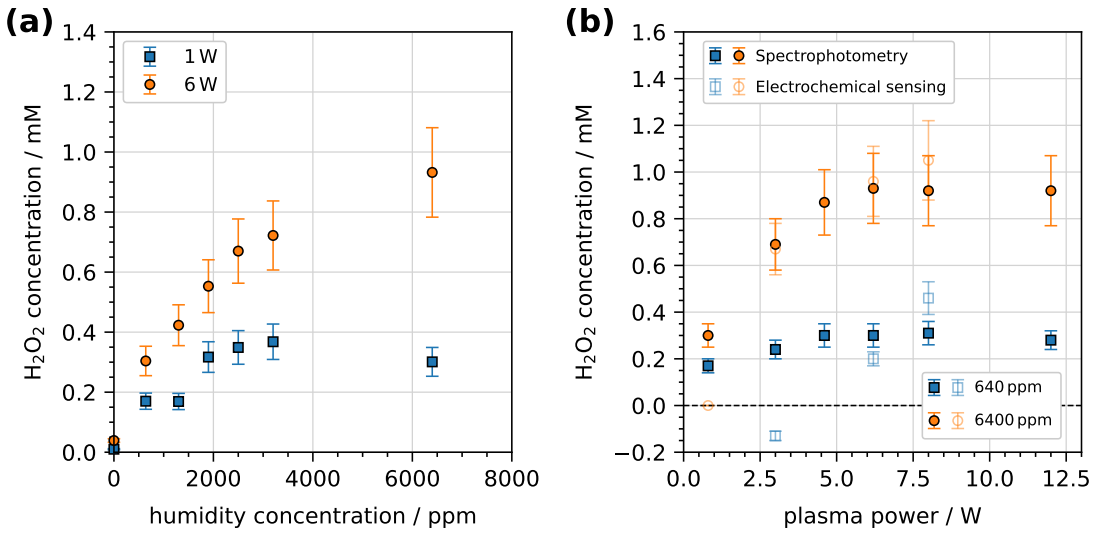

Figure 5.1: H_2O_2 measured in the PTL. **(a)** Effect of the feed gas humidity on the H_2O_2 concentration at 1 W and 6 W plasma powers. **(b)** H_2O_2 concentration as a function of plasma power at humidity concentrations of 640 ppm and 6400 ppm. The comparison of the two liquid diagnostics to measure the H_2O_2 concentration is shown in **(b)**.

First, H_2O_2 steadily increases with increasing humidity concentration (see figure 5.1 a) and increases with plasma power up to 6 W, above which saturation occurs for both humidity concentrations (see figure 5.1 b). These trends are in very good agreement with the H_2O_2 density measurements in the gas phase presented in chapter 4. The aspect that the liquid H_2O_2 concentration shows the same trends as the gas phase H_2O_2 density reveals a direct impact of the gas phase H_2O_2 to the liquid H_2O_2. According to Henry's law, the liquid concentration of a gas hitting a liquid surface is proportional to the partial pressure of the gas. Since H_2O_2 has a high Henry's law solubility constant, it can easily be dissolved in the liquid and its concentration depends on the partial pressure of the gas.

Second, both methods reveal the same H_2O_2 concentrations and trends as can be seen in figure 5.1 (b). At low humidity concentrations and plasma powers, the H_2O_2 concentration is below 0.2 mM and the detection limit of the electrochemical sensors. There, only the spectrophotometric approach provides the required detection limit. The agreement of the two methods is important as two different liquids were used for the treatments of the two methods as explained above. Since both methods show

the same H_2O_2 concentration, the dissolution of H_2O_2 is the same in both liquids and the results by the spectrophotometric approach are also valid for the buffered solution in the plasma-liquid system investigated in this work.

Third, a maximum concentration of 1 mM is achievable at 6 W plasma power and humidity of 6400 ppm. This concentration is worthwhile for plasma-driven biocatalysis. Yayci et al. used the COST reference plasma jet to drive biocatalysis using unspecific peroxygenase (UPO) as enzymes. They found a H_2O_2 production rate of about $0.2\,\mu mol\,min^{-1}$ for the COST reference plasma jet [6]. The capillary plasma jet delivers 1 mM in 5 min to 3 mL liquid volume. This corresponds to a production rate of $0.6\,\mu mol\,min^{-1}$ ($1.2\,mg\,h^{-1}$) and, thus a three-fold higher production than the COST reference plasma jet. Due to the applicability of higher plasma powers applied to the capillary plasma jet, it offers a broader range of parameters and the H_2O_2 production can be enhanced. Yayci et al. stated that "the µAPPJ presents a promising plasma source for plasma-driven biocatalysis" [6], and the use of the capillary plasma jet instead of the COST reference plasma jet even makes the use of plasma jets more promising.

Furthermore, compared to other plasma sources that interact with liquids to produce H_2O_2, which have shown production rates ranging from $57\,\mu g\,h^{-1}$ to $48\,g\,h^{-1}$ [24], the H_2O_2 production rate of the capillary plasma jet falls within the medium range. Nevertheless, the capillary plasma jet provides appropriate H_2O_2 concentrations for plasma-driven biocatalysis and is a non-invasive H_2O_2 source.

5.2 OH distribution

The OH radical is the main species involved in the production and destruction of H_2O_2 and is also measurable by LIF at a distance of $z = 24$ mm from the end of the discharge channel where the liquid surface is positioned during plasma treatment. Thus, it is likely that OH also reaches the liquid surface when liquids are treated by the capillary plasma jet. To investigate this, the impact of OH at the liquid surface was measured using the chemiluminescence (CL) of luminol and the OH concentration in the liquid was measured using the terephthalic acid (TA) dosimeter.

The CL of luminol was used to visualise the distribution of OH. This is shown in figure 5.2 during plasma treatments with various humidity concentrations at plasma powers of 1 W in figure 5.2 (a) and various plasma powers at 640 ppm humidity in figure 5.2 (b). In all images, a clear CL signal is visible at the liquid surface at $z = 0$ mm with a bright spot in the centre at $\Delta x = 0$ mm with the width of 1 mm. The 1 mm width of the bright spot is equal to the width of the capillary and is located at the position where the capillary faces the liquid surface. To the side of

the bright spot, the CL signal becomes weaker. In the centre, the signal extends up to $z = 3\,\text{mm}$ into the liquid but weakens considerably after the first millimetre. At the sides, the signal only extends for less than 2 mm into the liquid. This profile of the CL signal at the liquid surface is visible for all plasma treatments. Some differences in intensity are noticeable by changing the plasma parameters, while the shape remains the same. With increasing humidity, the intensity of the CL signal initially increases, has a maximum at 640 ppm and decreases at higher humidity concentrations. This trend is observed for all plasma powers (CL images for varying humidity at 6 W plasma power are shown in the appendix A.4). Regarding the plasma power, the CL signal increases steadily as the plasma power increases.

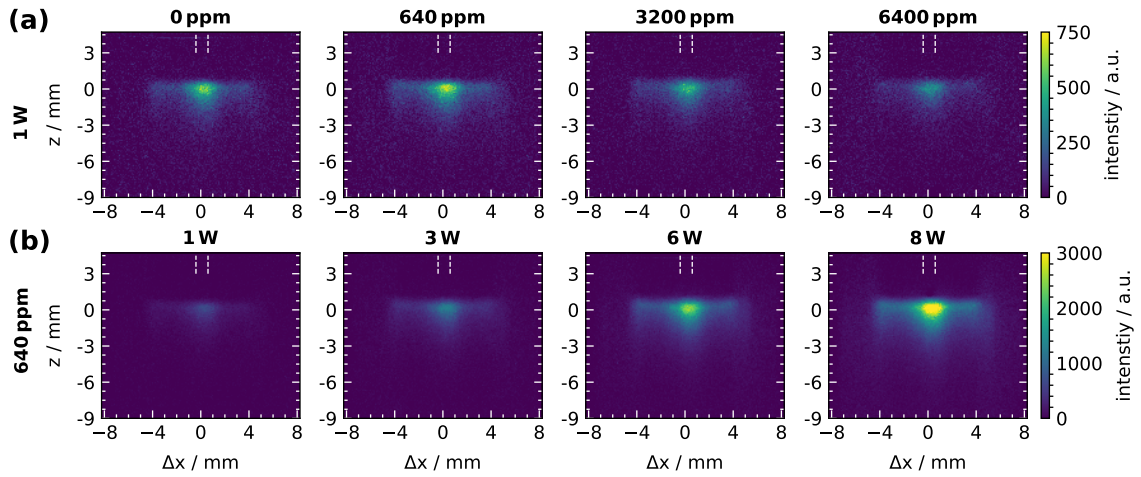

Figure 5.2: CL signals of luminol in the PTL at various plasma parameter. **(a)** Plasma was operated at 1 W plasma power and various humidity concentrations. **(b)** The humidity was kept constant at 640 ppm and the plasma power was varied. At $z = 0\,\text{mm}$ the liquid surface was localised and positive z distances correspond to the gas phase, while negative values are in the liquid phase.

From this analysis, it is clear that the OH radical is mainly present at the liquid surface and does not penetrate deep into the liquid. This agrees well with the description of the penetration depth given in chapter 2: The concentration of radicals like OH, O or HO_2 strongly decays at the liquid interface and barely exceed depths of 100 µm [102–106]. Due to the reactive character of radicals such as OH, the radicals react directly when entering the liquid and reach only micrometres into the liquid. This is also true for reactive species such as O or H. That the CL signal reaches not only a micrometre but a millimetre into the liquid is because the CL signal does not visualise the actual OH distribution but rather its excited state that is linked to the OH distribution. Luminol is excited and its deexcitation is observed. It takes several milliseconds for the deexcitation process and thus the CL signal reaches further into the liquid than the expected penetration depth of OH in liquids.

The CL of luminol is a useful method to visualise the distribution of OH, but it is

not suitable for measuring the absolute concentration of OH in the liquid. To this end, the second method of the TA dosimeter was used. The comparison of the diagnostics is shown in figure 5.3. The observed trends in the intensity of the CL signal are clearly visible: with increasing humidity, the intensity first increases reaches a maximum at about 640 ppm and further decreases, while it steadily increases with plasma power. The measured and corrected HTA concentration, proportional to the OH concentration, shows the same trend. There, an initial increase in concentration with increasing humidity and a subsequent decrease is observed. This trend was also observed in a previous study by measurements of the OH concentration by DMPO spin trap in a PTL [31]. Furthermore, the OH concentration shows a linear increase with increasing plasma power. Thus, both methods agree very well and the same trends for the OH distribution at the liquid surface and the OH concentration measured in the liquid are observable. Two conclusions can be drawn from this: First, the volume-averaged measurement at $z = 8\,\mathrm{mm}$ measured by the TA dosimeter follows the luminol measurements at the liquid surface. The reaction between OH and TA likely occurs at the liquid surface and the reactant HTA is transported deeper into the liquid. Nevertheless, the volume-averaged concentration follows the distribution at the liquid surface. Second, even though O_2^- is the dominant exciter of luminol, its CL at the surface of the PTL shows the same trends as the OH sensitive TA dosimeter. Thus, the CL of luminol visualises the distribution of the OH radical. This supports the conclusions of Shirai et al. stating that the CL luminol can be used to investigate the OH radical in PTL [177].

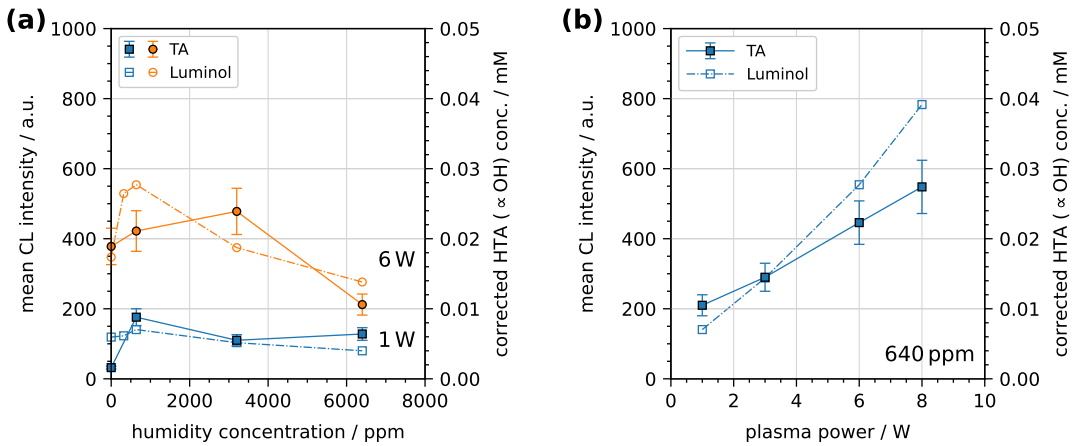

Figure 5.3: Comparison of the CL of luminol (mean CL intensity) with the TA dosimeter (corrected HTA concentration which is proportional to the OH concentration). **(a)** Effect of the feed gas humidity at 1 W and 6 W plasma powers. **(b)** Effect of the plasma power at 640 ppm humidity admixture.

Further, the maximum concentration of the corrected HTA and thus the OH concentration reaches a maximum value of $(0.027 \pm 0.004)\,\mathrm{mM}$. Thus, the accumu-

lated OH concentration measured in the liquid is of the order of 10 µM which is in agreement with previous studies using the COST reference plasma jet [31, 209]. In addition, the OH concentration is two orders of magnitude lower compared to the H_2O_2 measured in the PTL. Since the LIF measurements have shown an exponential decay of OH in the effluent and the distance between plasma and liquid surface was large with $z = 24$ mm, a large amount of OH has already reacted in the effluent and does not reach the liquid surface. The long-lived H_2O_2 is more stable and the achievable concentration in the PTL can be higher.

Regarding plasma-driven biocatalysis, the low OH concentration and its presence only at the liquid surface is useful. Since radicals might harm the enzymes, contact between the two should be avoided. During operation, the enzymes are located at the bottom of the vessel in an area not reached by the OH radicals delivered by the plasma. In contrast, H_2O_2 molecules can be transported through the liquid by convection and diffusion and reach the enzymes so that the catalytic reaction can be performed. The transport of H_2O_2 through the liquid is discussed in detail later.

5.3 Impact of treatment parameters

In the previously described measurements of the OH and H_2O_2 concentrations, the treatment parameters, specifically treatment distance and gas flow rate, were kept constant. However, by varying the treatment parameters, the delivery of the species to the liquid can be affected. Therefore, the effect of the two treatment parameters on the measured OH and H_2O_2 concentration in the PTL was investigated.

First, a variation of the treatment distance was performed and its effect on the OH and H_2O_2 concentration is shown in figure 5.4 (a). In the case of H_2O_2, its concentration decreases slightly with a larger treatment distance. The concentration is lowered by 35 % at $z = 39$ mm distance compared to $z = 14$ mm. The lower H_2O_2 concentration might be due to a modified gas transport rather than due to chemical reactions since H_2O_2 is less affected by reactions in the effluent. A greater treatment distance should lead to enhanced transport to the side as the gas flow diverges with distance [49, 56]. The divergence of the gas flow at these increased distances was visualised by LIF measurements of NO in a horizontal arrangement [49].

In contrast, the OH radical is more affected by a change in treatment distance as visible in figure 5.4 (a). Its concentration shows an exponential decay with increasing distance and at distances larger than $z = 35$ mm, no OH can be measured in the PTL. A longer transport path from the plasma to the liquid enhances the time for chemical reactions in the effluent of the reactive species. This also applies to the OH radical as was also shown by the decay of the LIF signal in the axial direction

from the capillary (see chapter 4). The chemical reactions in the effluent lower the OH density in the gas phase and also the concentration in the liquid. The decay of OH with distance was also observed for the CL signal at various distances between the capillary plasma jet and the liquid surface (shown in the appendix A.5).

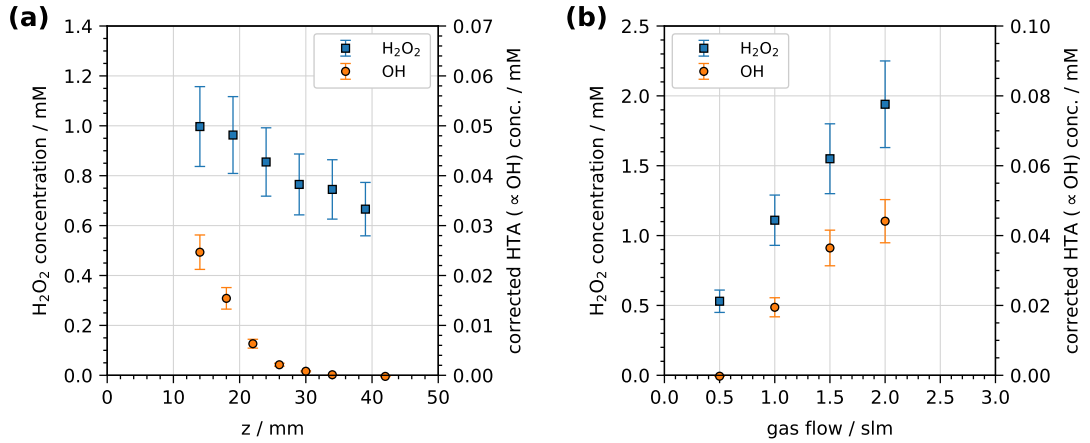

Figure 5.4: Effect of treatment parameters on the concentrations of OH and H_2O_2 measured in the PTL. **(a)** Variation of treatment distance between the capillary and the liquid (total gas flow was constant with 1 slm). **(b)** Variation of gas flow rate (distance between capillary and plasma was kept constant at 14 mm). In both investigations, the plasma was operated at 6 W and 6400 ppm humidity. Please note the different scales for the concentrations of H_2O_2 and OH, as the concentration of H_2O_2 is about two orders of magnitude higher.

Secondly, the gas flow rate was varied at a constant treatment distance and the results are shown in figure 5.4 (b). With increasing gas flow rate, both the OH and H_2O_2 concentrations increase linearly. However, at a gas flow rate of 0.5 slm, no OH can be detected in the liquid. The OH and H_2O_2 concentrations rise linearly from 0.02 mM and 1 mM to 0.04 mM and 2 mM at gas flow rates 1 slm and 2 slm, respectively. Thus, doubling the gas flow rate from 1 slm to 2 slm also doubles the concentrations in the liquid. The increase in H_2O_2 concentration at higher gas flow rates was also previously observed for treatments by the COST reference plasma jet [210].

The vanishing of the OH concentration at 0.5 slm can be explained by the longer time for the transport of OH from the plasma to the liquid as was the case for larger treatment distances. At lower gas flow rates, the gas velocity is slower and thus the transport time of the species in the effluent from the capillary to the liquid surface is enhanced. Reactive OH has more time to react in the effluent and less OH reaches the liquid surface and is dissolved in the liquid. At higher gas flow rates, the transport time is shorter and more OH can reach the liquid surface.

The findings of varying the treatment distance and the gas flow rate indicate

that both parameters can be individually or simultaneously used to reach a higher selectivity towards long-lived species. At larger distances and lower gas flow rates, fewer radicals reach the liquid and are dissolved in the liquid, resulting in a higher selectivity towards long-lived species such H_2O_2. However, both parameters can also be used to enhance the concentrations of dissolved species: At shorter distances and higher gas flow rates, the concentrations of both species are higher.

However, the interaction between the gas flow and the liquid surface at higher gas flow rates is stronger leading to a distortion of the liquid surface. This is shown in figure 5.5 by the CL signals under plasma treatment with various gas flow rates. In all cases, the bright spot at the centre of the liquid surface can be seen, which becomes less pronounced at higher gas flow rates. At low gas flow rates, the liquid surface is calm and the shape is undisturbed. However, starting at 1.5 slm, the liquid surface gets disturbed and a small dip appears in the centre where the gas flow hits the liquid surface. This dip gets even more pronounced at 2 slm and reaches already up to 3 mm into the liquid bulk. This aspect has to be considered in any application because evaporation or even water leaving the treatment vessel has to be avoided.

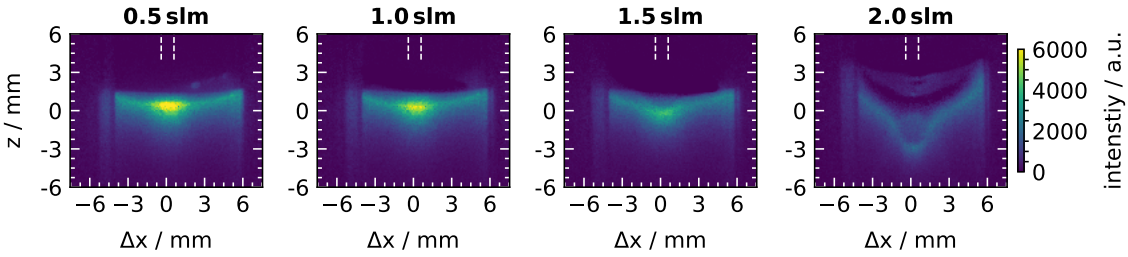

Figure 5.5: CL images at various gas flow rates. Plasma was operated at 6 W and 640 ppm humidity in all cases. At $z = 0$ mm the liquid surface was localised and positive z distances correspond to the gas phase, while negative values are in the liquid phase.

5.4 Species concentration under pulse modulation

Analogue to the measurements of the species densities in the gas phase under pulse modulation of the RF signal, its effect on the species concentrations in the PTL was investigated. Figure 5.6 (a) shows the H_2O_2 and OH concentrations under pulse modulation of the RF excitation. The H_2O_2 concentration is weakly affected by the number of pulses per residence time at a duty cycle of 50 % and reaches a constant value of about 0.7 mM. At the lower duty cycle of 10 %, the H_2O_2 concentration rises with an increasing number of pulses and a concentration of about 0.4 mM is reached at three pulses per residence time. Thus, compared to the unmodulated case, the maximum achievable concentrations under power modulation are 70 % and 40 % lower at duty cycles of 50 % and 10 %, respectively.

In the case of OH, the concentration is below 0.01 mM and fluctuates when the number of pulses for both duty cycles is changed (see figure 5.6 b). The OH concentration under power modulation is about half of the concentration achieved in the non-modulated case, although some of the measured OH concentrations under power modulation reach the same value. However, due to the low concentrations and the fluctuations of the measurements, no clear trends can be detected. It can be stated that the OH radical is suppressed in the liquid under pulse modulation, especially at low duty cycles similar to the analysis of the gas phase densities presented in chapter 4.

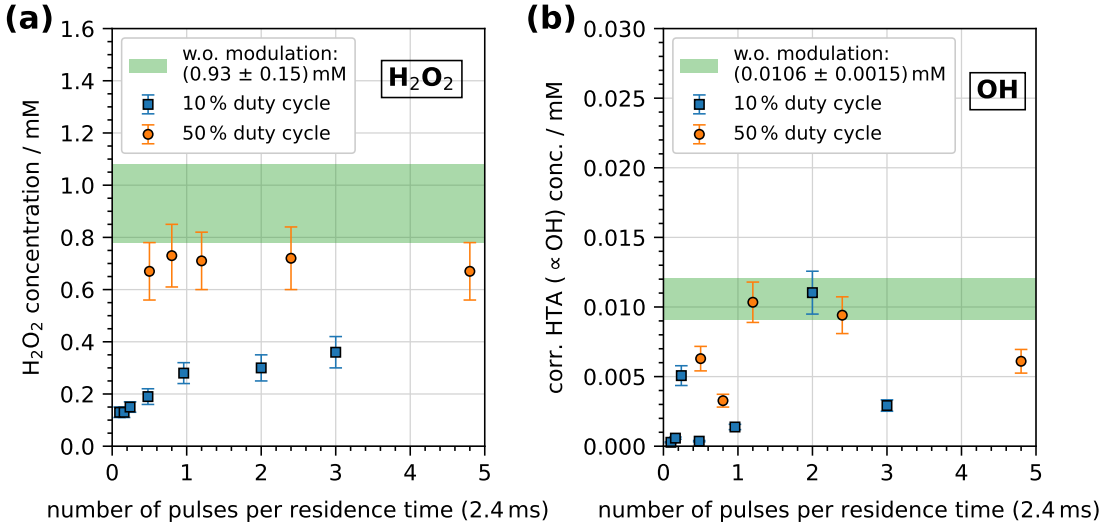

Figure 5.6: Effect of pulse modulation on species concentration in the PTL for **(a)** H_2O_2 and **(b)** OH. Measurements were taken at a humidity of 6400 ppm and an unmodulated plasma power of 6 W with a gas flow rate of 1 slm.

Due to the duty cycle of the modulation pulses, the dissipated plasma power is only half or even one-tenth of the plasma power compared to the unmodulated case. Thus, the energy efficiency of the species production can be enhanced. The energy efficiency η is calculated by:

$$\eta_j = \frac{c_j \, M_j \, V}{P \, T \, F_{DC}} \tag{5.1}$$

with the concentration c_j and molar mass M_j of species j, the treatment volume V and treatment time T, the plasma power P and duty cycle F_{DC}. Some results regarding the energy efficiency of H_2O_2 production are listed in table 5.1 for various number of pulses N_{pulses}. Although the H_2O_2 concentrations at duty cycles of 10 % and 50 % are lower than for the unmodulated case, the energy efficiency is higher. At a duty cycle of 10 %, the maximum energy yield is $(0.73 \pm 0.13)\,\mathrm{g\,kWh^{-1}}$ which is more than three-fold than the unmodulated case with $(0.19 \pm 0.04)\,\mathrm{g\,kWh^{-1}}$. Thus, the low-frequency pulsing of the RF plasma jet can be used to achieve higher energy

efficiencies at lower concentrations. Compared to other plasma sources that interact with liquids to produce H_2O_2, which have shown energy efficiencies ranging from $0.04\,\mathrm{g\,kWh^{-1}}$ to $80\,\mathrm{g\,kWh^{-1}}$ [24], the energy efficiency of H_2O_2 production using the capillary plasma jet falls within the medium range.

Table 5.1: Results of H_2O_2 concentrations $c_{H_2O_2}$ in the PTL under pulse modulation with corresponding energy efficiencies $\eta_{H_2O_2}$ at certain modulation frequencies f_{mod} and duty cycles F_{DC} with the respective number of pulses per residence time N_{pulses}. The row at $F_{DC} = 100\,\%$ corresponds to the results of the unmodulated case. The plasma was operated at 6400 ppm humidity admixture and an unmodulated plasma power of 6 W.

F_{DC} / %	f_{mod} / Hz	N_{pulses}	$c_{H_2O_2}$ / mM	$\eta_{H_2O_2}$ / g kWh^{-1}
10	42	0.1	0.13 ± 0.02	0.27 ± 0.05
	200	0.5	0.19 ± 0.03	0.39 ± 0.07
	400	1	0.28 ± 0.04	0.57 ± 0.09
	1250	3	0.36 ± 0.06	0.73 ± 0.13
50	333	0.8	0.73 ± 0.12	0.30 ± 0.05
	2000	5	0.67 ± 0.11	0.27 ± 0.05
100	-	-	0.93 ± 0.15	0.19 ± 0.04

5.5 Distribution of liquid H_2O_2

Besides the concentration of the species in the liquid, their transport and distribution are important for application purposes. The distribution of OH was already discussed when the results of the CL of luminol were presented. It was found that OH was mainly present at the liquid surface. To investigate the transport of H_2O_2, particle imaging velocimetry (PIV) and UV absorption measurements were performed.

First, the general transport of the liquid was investigated by PIV measurements. PIV measurements of the liquid velocity at gas flow rates from 0.5 slm to 2 slm are shown in figure 5.7. At 1 slm, velocities in the order of $1\,\mathrm{mm\,s^{-1}}$ are visible in the upper 5 mm of the liquid. At depths $z \geq 5\,\mathrm{mm}$, the velocity is reduced. Two vortices can be observed close to the liquid surface. The direction of the vortices goes from the sides of the cuvette towards the centre with an upstream flow in the centre. These reverse vortices have already been observed and investigated by several research groups in experiments [28, 42, 211] and modelling [43, 100, 101, 212]. Convection is responsible for the creation of the vortices. The gas hits the

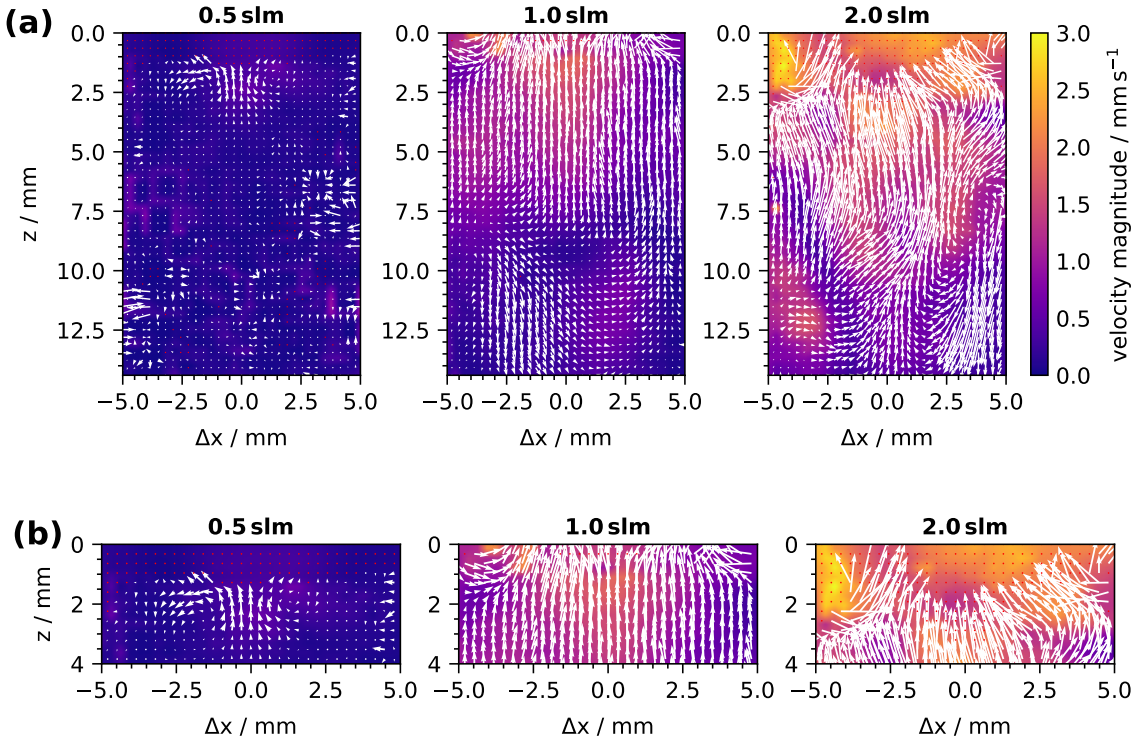

Figure 5.7: **(a)** PIV images of the PTL in UV cuvettes for various gas flow rates. The liquid surface was located at a depth of 0 mm. Measurements were taken at a humidity of 6400 ppm and a plasma power of 6 W. **(b)** Zoom on the liquid surface. The colour bar applies to all images.

liquid surface and travels along the surface in radial direction. Due to friction, the liquid is accelerated to the sides and an induced liquid motion is created.

At higher gas flow rates, here 2 slm, the velocity increases to 3 mm s^{-1} and a strong disturbance at the liquid surface can be observed. At higher gas flow rates, the gas velocity and the momentum transfer from the gas to the liquid are increased. This results in a stronger interaction at the liquid surface and a stronger dip at the point where the gas hits the liquid surface. This was already visible by the dip in the CL signals at 2 slm in figure 5.5 and has been discussed there. Lowering the gas flow rate to 0.5 slm, the movement in the liquid vanished almost completely. Thus, convective transport in the liquid is hindered at low gas flow rates of less than 0.5 slm in the plasma-liquid system investigated.

To visualise the transport of H_2O_2 through the liquid, 2D UV absorption spectroscopy was applied in distilled water. By this technique, H_2O_2 can be separately tracked in the liquid. The temporal absorbance of H_2O_2 in the liquid at various depths in the cuvette is shown in figure 5.8 for the same gas flow rates as investigated by PIV. At a gas flow rate of 1 slm (middle part of the figure), the absorbance increases immediately after the start of the treatment and increases at all depths.

Some fluctuations are visible, which can be attributed to dust particles and impurities in the cuvette.

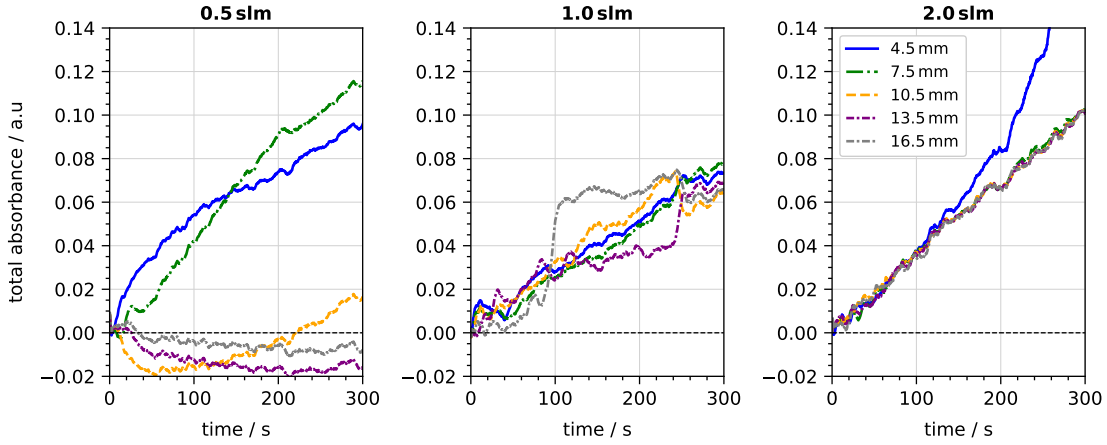

Figure 5.8: Total absorbance of H_2O_2 over treatment time obtained in various depths in the liquid for gas flow rates of 0.5 slm, 1.0 slm and 2.0 slm. Plasma was operated at a humidity of 6400 ppm and a plasma power of 6 W. Distilled water was used as liquid in these measurements. Legend applies to all.

If the gas flow rate is increased to 2 slm, the same trend can be observed, but the increase is faster than in the case of 1 slm. The faster increase is consistent with the enhanced H_2O_2 concentration in the PTL at higher gas flow rates as described above since a higher concentration leads to an enhanced UV absorption. In addition, after about 150 s, the increase in absorption at the lowest depth of 4.5 mm is enhanced. This is due to evaporation, as the evaporation is stronger at higher gas flow rates and thus the measurement is no longer probing the liquid rather than the gas phase. In this case, the reference is no longer correct and the measurement is no longer trustworthy.

The homogeneous distribution of H_2O_2 in the liquid at 1 slm and 2 slm can be attributed to the convective transport discussed above. Convective transport is present at high gas flow rates with velocities in the liquid in the order of several millimetres per second. Thus, the dissolved H_2O_2 is quickly distributed in the liquid and the absorption occurs homogeneously distributed at all depths. However, this behaviour is not true at lower gas flow rates where no convective transport was observed by PIV. The corresponding temporal absorbance at 0.5 slm shows different profiles depending on the measuring depth in the liquid (see the left part in figure 5.8). Close to the liquid surface, the absorption increases immediately. After 50 s the absorption also increases at 7.5 mm. At even greater depths, it takes even longer to see an increase in absorbance. At low depths, the signal is initially negative due to a misalignment of the setup caused by the lowering of the plasma jet and resulting movements of the optical components. However, the increase in absorption

at 10.5 mm after 100 s can still be seen. In this case, the H_2O_2 transport is mainly driven by diffusion as the convection is hindered at a low gas flow rate.

To elaborate the diffusion in more detail, a longer treatment at an even lower gas flow rate of 0.25 slm was performed. The results are shown in figure 5.9 (a) as the mean and standard deviation of three measurements. The same trends can be seen as was the case for 0.5 slm: The absorption first increases at a depth of 4.5 mm after 5 min, then at 7.5 mm after 7 min and even later with increasing depth. Turning off the plasma after 20 min leads to a decrease in absorption at 4.5 mm depths, while at the other depths, the absorption still increases. These trends visualise the diffusion of H_2O_2 through the liquid.

The observed trends fit well with previously published works [161, 213]. Liu et al. studied the distribution of RONS also by UV absorption spectroscopy in a liquid treated with a DBD plasma operated in ambient air without gas flow [161]. Thus no convective transport was present and they found similar timescales of 100 s for a transport path of 5 mm.

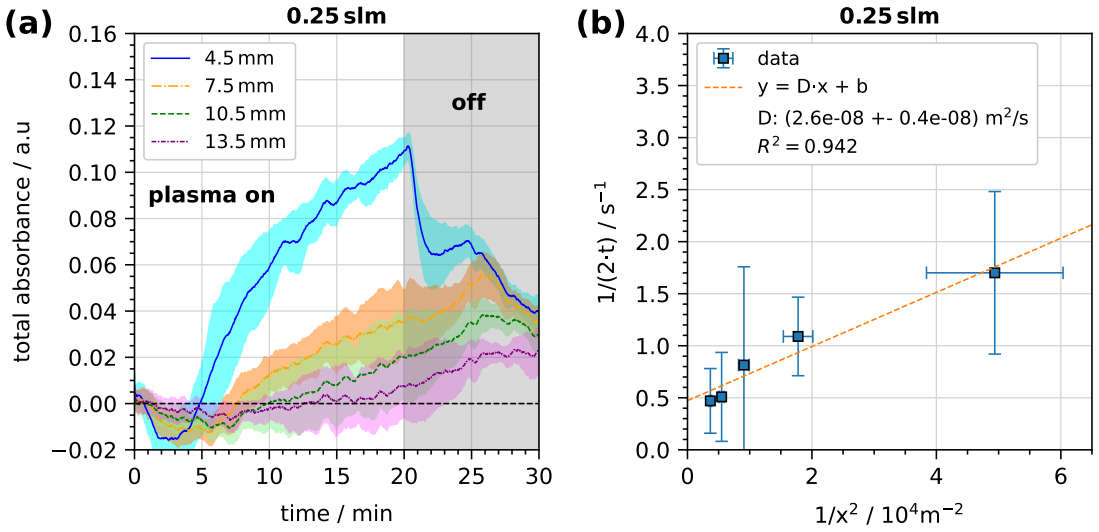

Figure 5.9: **(a)** Total absorbance of H_2O_2 over treatment time obtained in various depths in the liquid for a gas flow rate of 0.25 slm. After 20 min the plasma and gas flow were turned off. Plasma was operated at a humidity of 6400 ppm and a plasma power of 6 W. Distilled water was used as liquid in these measurements. The shaded area shows the standard deviation of three measurements and the solid line represents the mean values. **(b)** Plot of $1/(2t)$ as a function of $1/x^2$ to determine the diffusion coefficient given by the slope of the linear fit.

From the temporal absorption curves at 0.25 slm, an effective diffusion coefficient of H_2O_2 can be obtained experimentally. The diffusion coefficient D can be deter-

mined by the Einstein-Smoluchowski-equation:

$$D = \frac{x^2}{2t} \tag{5.2}$$

with the time t and distance or depth x. Taking the time of the x-axis crossing point t_0 of the absorption curve for the various depths, the diffusion coefficient can be estimated. This is shown in figure 5.9 (b) where $1/(2t_0)$ is plotted as a function of $1/x^2$. A linear increase with a slope of $(2.6 \pm 0.4) \times 10^{-8}\,\mathrm{m^2\,s^{-1}}$ is evident. This slope is equivalent to an effective diffusion coefficient for H_2O_2 in the plasma-treated liquid at 0.25 slm gas flow rate. An intercept b was taken for fitting although in equation 5.2 no intercept is involved. However, the measurements' uncertainties are significant and considering an intercept provided the best fit of the linear relationship. The intercept can be due to further effects such as gravity and convection affecting the transport in the liquid.

In other research works, the H_2O_2 diffusion coefficient in liquids was measured to values in the range of $(1.3 - 2.3)\,10^{-9}\,\mathrm{m^2\,s^{-1}}$[214–217]. The coefficient measured in this work differs from literature values by one order of magnitude. However, considering the uncertainties of the UV absorption measurements and the plasma treatment the discrepancy is quite reasonable. Further effects such as gravity and convection can lead to a higher diffusion coefficient. Following the discussion by Semenov et al., the diffusion coefficient obtained in plasma-treated liquid is an *effective* one taking other effects like gravity or convection into account [44]. Although a small gas flow rate was used and no velocities in the liquid could be detected, small velocities in the range of $\mu\mathrm{m\,s^{-1}}$ can still be present in the liquid. This might contribute to the distribution of H_2O_2 in the liquid and lead to a higher effective diffusion coefficient. This might also explain the presence of the intercept b of the linear fit. Nevertheless, the plasma-liquid system used has proven to be a useful system for investigating the most important transport phenomena in the liquid.

Modelling of transport processes

The experimentally investigated transport phenomena can be evaluated using a simple transport model as described in chapter 3. It uses the experimentally determined effective diffusion coefficient and models the H_2O_2 distribution in the liquid. The transport in the liquid can be described theoretically by the convection-diffusion equation. Assuming radial symmetry, the convection-diffusion equation in axial direction z is given by:

$$\frac{\partial c}{\partial t} + \frac{\partial u_z\, c}{\partial z} = \frac{\partial^2 (D\, c)}{\partial^2 z}, \tag{5.3}$$

with the concentration c in the liquid, u_z the axial velocity in the liquid and D the diffusion coefficient. This differential equation can be solved numerically as described in chapter 3 and the physical principle is as follows. At first, H_2O_2 is delivered from the plasma by a flux $\Gamma_{H_2O_2}$ to the liquid surface from the gas phase and is dissolved in the liquid according to Henry's law. The H_2O_2 flux is given in [molecules $s^{-1}m^{-2}$] and can be calculated by the density of H_2O_2 in the gas phase $n_{H_2O_2}$ derived from the results presented in chapter 4 at the gas flow rate Φ and the area $A = 1\,mm^2$ of the capillary: $\Gamma_{H_2O_2} = n_{H_2O_2} \cdot \Phi/A$. This was set as the boundary condition for the concentration at the liquid surface. After dissolution in the liquid, the concentration gradient is distributed in the liquid according to the convection-diffusion equation. Convection is driven by the mixing of the liquid due to the gas flow, as shown by the PIV measurements, while diffusion is driven by a concentration gradient in the liquid visualised by UV absorption. Taking into account the measured data of the H_2O_2 density, the effective diffusion coefficient and the velocity in the liquid (shown in table 5.2), the experimentally obtained depth profiles of H_2O_2 can be modelled.

Table 5.2: Parameters obtained from experiments and used as input in the convection-diffusion equation to model the depth profiles of H_2O_2 in the PTL. Convection dominates at 2 slm while diffusion is present at 0.25 slm.

Condition	Parameter	Value	Diagnostic
2 slm	u_z	$3\,mm\,s^{-1}$	PIV
	$D_{H_2O_2}$	$2.6 \times 10^{-8}\,m^2\,s^{-1}$	UV absorption
	$\Gamma_{H_2O_2}$	$1.3 \times 10^{22}\,m^{-2}\,s^{-1}$	FTIR
0.25 slm	u_z	$0\,mm\,s^{-1}$	PIV
	$D_{H_2O_2}$	$2.6 \times 10^{-8}\,m^2\,s^{-1}$	UV absorption
	$\Gamma_{H_2O_2}$	$2.1 \times 10^{20}\,m^{-2}\,s^{-1}$	FTIR

The comparison of the model for the convective transport using a liquid velocity of $3\,mm\,s^{-1}$ at 2 slm gas flow rate is shown in figure 5.10 (a). The model fits very well with the experiments as the H_2O_2 concentration in the liquid increases linearly with time at all depths as was the case in the experiments. Thus, the convection-diffusion equation describes the distribution of H_2O_2 in the liquid treated by the plasma jet at high gas flow rates in the convective regime well. Further, the time scale of the H_2O_2 distribution in the liquid is fast and is in the range of seconds. This agrees well with the velocity of $3\,mm\,s^{-1}$ measured in the liquid.

In the case of low gas flow rates and diffusive-driven transport, the convection-diffusion equation can also be used. There, the velocity in the liquid was set to

$0\,\mathrm{mm\,s^{-1}}$ and the equation simplifies to

$$\frac{\partial c}{\partial t} = \frac{\partial^2 (D\,c)}{\partial z^2}\,. \tag{5.4}$$

The modelled depth profiles of H_2O_2 of the diffusion equation are shown in figure 5.10 (b) in comparison to the experiments at depths of 4.5 mm, 7.5 mm and 10.5 mm. Good agreement between the model and the experiments can be observed at all depths. In the first 5 min, the modelled depth profiles begin to increase slowly, while in the experiments the absorption is initially negative due to disturbances in the setup. However, as the modelled profile increases, the experimental profiles also increase and the slope is well described by the model considering the uncertainty range of the experiments. As explained above, the increase is due to the concentration gradient in the liquid with higher concentrations at the liquid surface. At smaller depths (at the liquid surface), the H_2O_2 concentration is higher and the H_2O_2 slowly diffuses to larger depths. After 20 min when the plasma and gas flow are turned off, a discrepancy between the model and the experiment can be seen. In the experiments, the profile immediately starts to decrease while the modelled profile still increases, levels off and slowly decreases.

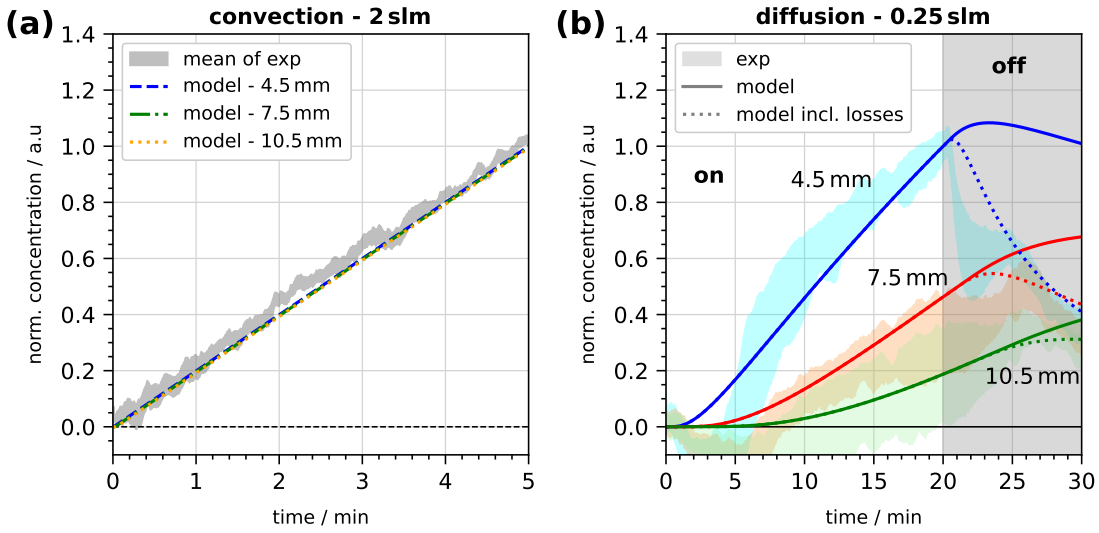

Figure 5.10: **(a)** Model results (lines) of the convective transport in various depths compared to the mean experimental results (shaded area) presented in figure 5.8 (c). **(b)** Model results (lines) of the diffusive transport in various depths in the liquid compared to experimental results (shaded areas) from figure 5.9. The dotted lines represent model results including loss processes (see text). After 20 min the plasma and gas flow in the experiments and the H_2O_2 flux in the model were turned off.

This discrepancy can be attributed to loss mechanisms occurring in the liquid. These can be chemical reactions leading to the destruction of H_2O_2 or evaporation

of H_2O_2 at the liquid surface since the gas flow was turned off and by this, the dynamics at the liquid surface are strongly affected. By including a further loss reaction R_i in the diffusion equation after 20 min when the plasma was turned off

$$\frac{\partial c}{\partial t} = \frac{\partial^2 (D\, c)}{\partial^2 z} - R_i, \tag{5.5}$$

the decrease in the off phase can be better described as shown in figure 5.10 (b). As a loss reaction, the destruction of H_2O_2 by OH present in the liquid was taken with the reaction rate of $2.7 \times 10^4\,\mathrm{m^3\,mol^{-1}\,s^{-1}}$ [106, 218]. The modelled profiles show higher values than the experiments, even when this loss reaction is included. This shows that further loss reactions occur that are not part of the model. However, the model shows qualitatively how the H_2O_2 distribution dynamic in the PTL can be described.

The different concentration profiles of H_2O_2 in the liquid for the convective and diffusive transport can be extracted from the model and are shown for different time steps in figure 5.11. In the case of convective transport, the concentration in the liquid shows a constant concentration profile. This indicates a homogeneous distribution of H_2O_2 as was measured by UV absorption spectroscopy and is derived from the strong mixing of the liquid by the vortices occurring at high gas flow rates. Further, a linear increase in the H_2O_2 concentration can be seen with increasing time. In contrast, the concentration profiles in the diffusive case also show higher values with increasing treatment time, but the individual profiles differ from each other. An exponential decay of the concentration in the liquid can be seen. With increasing time, the H_2O_2 diffuses into the liquid and reaches a depth of 10 mm after 10 min, which is in agreement with the UV absorption measurements of H_2O_2 in the PTL. When the H_2O_2 flux is switched off after 20 min, the H_2O_2 concentration in the liquid is distributed in the complete liquid and the profiles flatten at the surface (depth smaller than 5 mm) and rises in larger depths after 30 min. Adding losses of H_2O_2 at the liquid surface in the model after switching the plasma off, the H_2O_2 concentration at the liquid surface is even more reduced and reaches almost zero and a maximum occurs at about 7.5 mm. This demonstrates the contribution of chemical reactions in the distribution of H_2O_2 in the liquid.

Furthermore, the modelled H_2O_2 profiles agree well with results published in literature where similar trends were observed [102–104, 106]. The concentration profiles are often shown on a logarithmic scale for the depth to visualise the first micrometres of the liquid surface in more detail. This illustration is shown in the appendix A.6 for the results presented in this work. For H_2O_2, the concentration is constant up to a depth of 1 mm. This corresponds to a penetration depth of

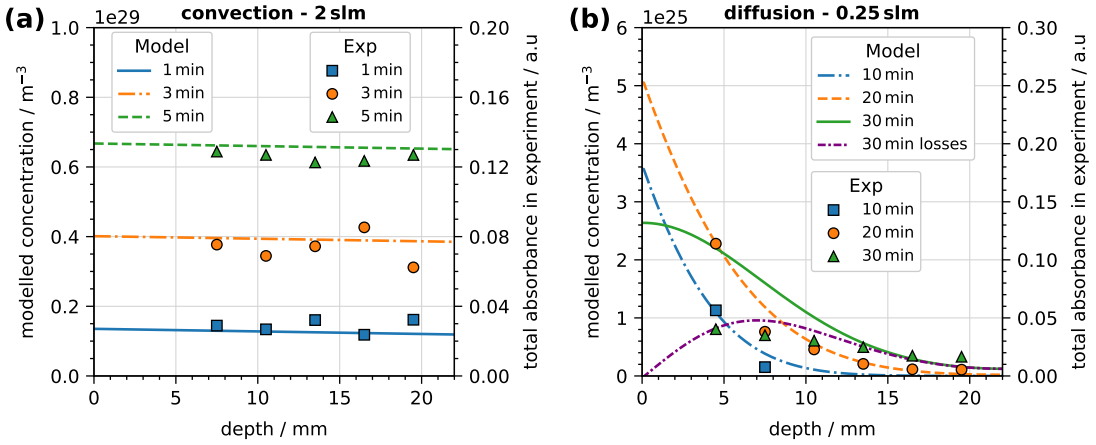

Figure 5.11: H_2O_2 concentration profiles in the liquid for various times obtained from modelling of the convection-diffusion equation (lines). The measured profiles at certain time steps are also shown (symbols). **(a)** Convective transport at 2 slm. **(b)** Diffusive transport at 0.25 slm. After 20 min the H_2O_2 flux in the model was turned off in analogues to the experiments.

millimetres for H_2O_2, which is in agreement with the literature where penetration depths in the millimetre range were reported [102–104, 106].

5.6 H_2O_2 distribution in buffered solution

The liquid measurements presented so far were performed in pure water solutions. However, plasma-driven biocatalysis is conducted in buffered solutions to ensure the stability of the enzymes. To investigate the transport of H_2O_2 in buffered solution, UV absorption was also performed in buffer water mixtures with buffer concentrations of 0 M (pure water), 0.01 M, 0.05 M and 0.1 M (only buffer). The corresponding depth profiles of the UV absorption are shown in figure 5.12. By varying the buffer concentrations, the profiles change from the case of pure water to the case of pure buffer. In the case of pure water, the absorption profiles described above can be identified, with absorption initially increasing at lower depths. In contrast, the pure buffer case shows the same absorption profiles at all depths investigated with a slightly increased absorbance at the lowest depth of 4.5 mm. The cases of 0.01 M and 0.05 M are between the experiments with pure water and only buffer, where the case 0.01 M is more similar to the case with pure water and the case 0.05 M is more similar to the case with pure buffer. Furthermore, the maximum absorbance at the lowest depths decreases with increasing buffer concentration. After 30 min, the average absorbance across all depths is about 0.04 a.u. for all liquids investigated. Since a higher H_2O_2 concentration results in greater absorption, it can be assumed that the H_2O_2 concentration is the same for the water and buffer systems. This

supports the data from the spectrophotometric approach and the electrochemical sensing, where similar concentrations in the different liquids were found.

Compared to the flow analysis of H_2O_2 distribution in water, the "only buffer" case looks similar to the profiles obtained for the convective transport at higher gas flow rates. This might lead to the hypothesis that an increased buffer concentration leads to a more convective behaviour than a diffusive behaviour, although the gas flow rate was kept the same at low values. However, the PIV analysis of the buffered solution did not reveal any differences between the buffered and not buffered solutions (not shown here). Differences in the absorption behaviour of the species in the liquid might also explain the different profiles.

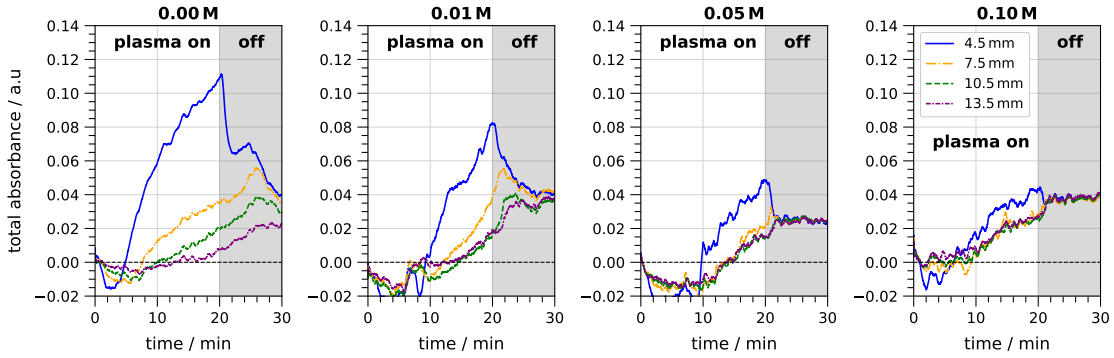

Figure 5.12: Total absorbance of H_2O_2 over treatment time obtained in various depths in the liquid for buffer concentrations in the liquid of 0 M, 0.01 M, 0.05 M and 0.1 M. Plasma was operated at a humidity of 6400 ppm, plasma power of 6 W and gas flow rate of 0.25 slm. Legend applies to all.

It is known that buffers and other liquid solvents can interfere with UV absorption spectroscopy. Buffers have individual UV cut-off wavelengths below which the buffers absorb UV light. Phosphate buffer at pH 7 and a concentration of 0.1 % has a cut-off wavelength of about 200 nm [219], which is suitable for the UV absorption measurements carried out in this work from 230 nm to 270 nm. However, the absorbance of buffers at low UV wavelengths can be greatly increased by the presence of impurities in the liquid [219]. In addition, the solubility of buffer salts can be limited and the salts present in the liquid can interfere with the UV light, causing a shift in the baseline, which is often a problem in chromatographic analyses [220]. It is therefore likely that the KPi buffer interferes with the UV light and leads to a change in UV absorption behaviour over time. The resulting absorption curves are therefore not reliable. Other buffers (citrate, buffer A and PBS-T) and solvents (acetone and dimethyl sulphoxide) were also tested in UV absorbance measurements. The results are not shown here as the other buffers showed the same behaviour as the KPi buffer and the presence of the solvents strongly interfered with the UV absorbance signal. The UV cut-off wavelengths of the solvents are around

300 nm [221], so it is clear that the solvents strongly interfered with the UV light and altered the UV absorption profiles.

To summarise, buffers and other solvents in the liquid interfere with UV light and UV absorption is not reliable in these environments. In contrast, the UV absorption of H_2O_2 could be successfully measured in water.

5.7 Comparing liquid phase to gas phase

To combine the presented measurements regarding the gas phase densities and the liquid concentrations, the trends of gas phase measurements are compared qualitatively to the liquid phase measurements in figure 5.13 for OH and H_2O_2. For both species, a good agreement between the trends regarding the humidity admixture and the dissipated plasma power can be seen. The H_2O_2 concentration and density steadily increase with humidity admixtures and dissipated plasma power, where both level off at plasma powers above 6 W. The maximum H_2O_2 concentration and density are 1 mM and $1.5 \times 10^{14}\,\mathrm{cm}^{-3}$, respectively. In the case of OH, the same trends can be observed as well: the concentration and density initially increase with humidity admixture, reaching a maximum between 640 ppm and 3200 ppm and both decrease at 6400 ppm. With increasing plasma power, the OH concentration and density show a linear increase. The maximum OH concentration and density are 0.025 mM and $1.5 \times 10^{13}\,\mathrm{cm}^{-3}$, respectively.

This good agreement shows that the concentration of the liquid species, both OH and H_2O_2, follow the trends of their gaseous forms. This is in accordance with Henry's law, as the liquid concentration is proportional to the gaseous pressure via Henry's law solubility constant. Thus, as the gas partial density and the partial pressure of the species above the liquid surface increases, the liquid concentration of the respective species also increases.

To compare the gas densities and the liquid concentration quantitatively, calculations have to be performed to transform the gas phase densities into liquid concentrations. In classical calculations, Henry's law is used to convert gas densities into liquid concentrations. In this case, the partial pressure p_i of the species i reaching the liquid is calculated from the species density n_i^{gas} and the ideal gas law $p_i = n_i^{gas}\, k_B\, T$ with the Boltzmann constant k_B and the gas temperature T_{gas}. Using Henry's law solubility constant H_s^{cp} given in table 2.2, the liquid concentration c_i^{liq} can be derived from

$$c_i^{liq} = H_s^{cp}\, n_i^{gas}\, k_B\, T_{gas}. \tag{5.6}$$

Taking the temperature of 400 K obtained from the thermocouple measurements in

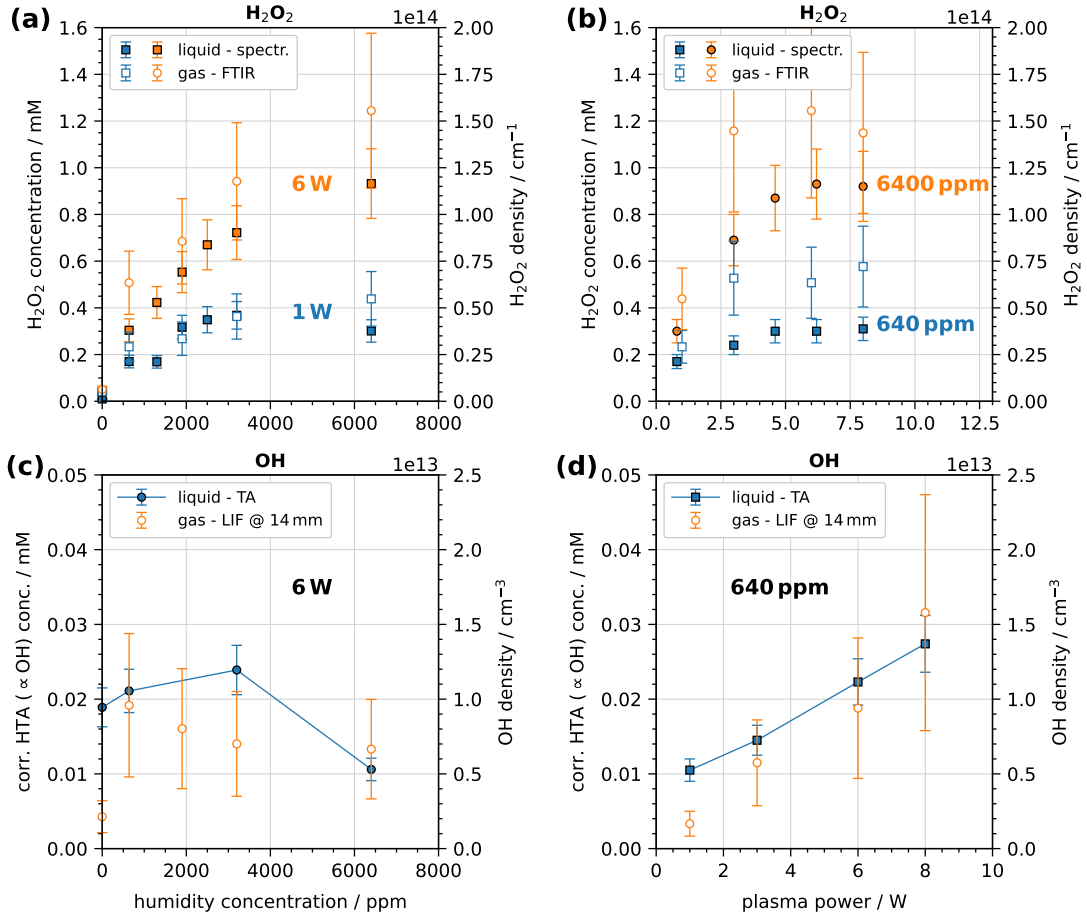

Figure 5.13: Qualitative comparison between the liquid concentrations (left y-axes) and gas phase densities (right y-axes) of **(a)** & **(b)** OH and **(c)**,**(d)** H_2O_2. The trends regarding the **(a)** & **(c)** humidity admixture and **(b)** & **(d)** plasma power can be compared. LIF measurements were performed at a distance of 14 mm from the end of the capillary, which corresponded to the distance set during liquid treatment.

the effluent at a distance of $z = 14\,\mathrm{mm}$ described in chapter 4, the maximum OH and H_2O_2 densities corresponds to concentrations of

$$c_{OH}^{liq}(1.5 \times 10^{19}\,\mathrm{m^{-3}}) = 0.05\,\mathrm{mM}$$
$$c_{\mathrm{H_2O_2}}^{liq}(1.5 \times 10^{20}\,\mathrm{m^{-3}}) = 626\,\mathrm{mM}.$$

Thus, in the case of OH, this value fits quite well to the experimentally obtained concentration of 0.25 mM. However, for H_2O_2, this value is more than two orders of magnitude larger than the maximum measured concentration of 1 mM. H_2O_2 has a large Henry's solubility constant of larger than one. In this case, the liquid concentration at the liquid surface is higher compared to the gaseous density and a thin diffusion boundary layer between the liquid bulk and gas phase is created [44]. This boundary layer has to be considered when transforming the gaseous densities

into liquid concentrations [44]. Then, a more dedicated model has to be solved to account for the boundary layer and to establish an equilibrium distribution of H_2O_2 from the interface into the liquid bulk. This is the case in the liquid measurements as the measured concentration is volume-averaged but not in the model calculations. Thus, the theoretically obtained concentration exceeds the measured concentration. For lower Henry's solubility constants like that for OH, this is not the case. The Henry's solubility constant of OH is lower than one and the formation of a boundary layer is prevented [44] so that the concentrations match.

A simpler approach is just by transforming the H_2O_2 density into a liquid concentration under the assumption that all H_2O_2 molecules enter the liquid phase. This assumption can be justified by the high Henry's law solubility constant describing the high solubility of H_2O_2. This simpler approach describes an equilibrium between the gaseous H_2O_2 density and its concentration in the liquid. The H_2O_2 is delivered to the liquid surface with a density n_i^{gas} at a gas flow rate Φ and an H_2O_2 flux can be calculated. Assuming that all H_2O_2 molecules enter the liquid, the concentration can be derived from the H_2O_2 flux dissolved in the liquid with volume V after treatment time T

$$c_i^{liq} = \frac{n_i^{gas}\,\Phi\,T}{V\,N_A}. \tag{5.7}$$

The Avogadro constant N_A is used to transform the concentration from m^{-3} into molar. With this approach, the achieved concentration is

$$c_{\mathrm{H_2O_2}}^{liq}(1.5 \times 10^{20}\,\mathrm{m}^{-3}) = 0.38\,\mathrm{mM}.$$

This is close to the experimental value of 1 mM and considering the measurement uncertainties of gas and liquid diagnostics, the values fit quite well. This shows that the gaseous densities fit qualitatively and quantitatively well with the liquid concentrations.

5.8 Summary liquid phase dynamics and chemistry

To summarise this chapter, the following lessons have been learned:

- The concentrations of H_2O_2 and OH can be controlled by humidity admixture to the feed gas and the dissipated plasma power. H_2O_2 was measured with concentrations up to a few millimolar, while OH shows lower concentrations in the range of a few tens of micromolar.
- OH does barely reach the liquid bulk and is mainly located at the liquid surface.
- By varying the treatment parameters gas flow rate and distance between plasma and liquid, the concentrations can be enhanced by higher gas flow rates and the selectivity towards H_2O_2 can be improved by larger treatment distances. However, higher gas flow rates are accompanied by strong disturbances at the liquid surface that might negatively influence the application purpose and increasing the treatment distances lowers the concentrations of the species in the liquid.
- Low-frequency pulsing of the RF plasma jet can be used to tune the plasma chemistry and increase the energy efficiency of the H_2O_2 production while reducing the OH concentration.
- The plasma-liquid system in combination with CL of luminol, PIV measurements and UV absorption can be used to investigate transport phenomena in the liquid. OH is mainly located at the liquid surface and does not reach the liquid bulk. At low gas flow rates, the diffusion of H_2O_2 was visible and an effective diffusion coefficient could be estimated. The measured H_2O_2 profiles in the liquid agree well with simple model calculations of the convection-diffusion equation.
- The liquid concentrations of OH and H_2O_2 match their gaseous densities qualitatively in their trends and quantitatively in their values. This is consistent with Henry's law, which describes the solubility of gaseous substances in liquids.

6. Scale-up

All liquid treatments discussed in the previous chapter were performed using a liquid volume of 3 mL. For application purposes, larger liquid volumes are required. For example, in upscaling the plasma-driven biocatalysis, more enzymes are placed in a larger volume of liquid. Therefore, the production of the H_2O_2 of the capillary plasma jet must be increased to achieve appropriate H_2O_2 concentrations in larger liquid volumes. One possibility was tested by increasing the plasma volume. Since the capillary plasma jet is not fixed in size, it is possible to increase the plasma volume. The setup and results of a larger plasma volume are described and discussed in the first section of the chapter. In addition, using He is expensive and is not a sustainable option for large-scale treatments unless a He recycling process is implemented. Therefore, the use of Ar as feed gas was tested and the results are discussed in the second part of the chapter.

6.1 Plasma volume

The capillary plasma jet had a cross-section of 1 mm × 1 mm (smaller capillary, cross-section of 1 mm^2) but it can easily be extended by changing the width of the electrodes and the capillary. This was realised by using a capillary with an inner width of (4.56 ± 0.02) mm and electrodes with a width of 4 mm. The cross-section of the arrangement can be seen in figure 6.1. The different widths of the capillaries and electrodes are due to the larger capillaries being oval in shape rather than square. This improves the stability of the capillary on the centre axis. However, as the distance between the electrodes remains almost the same (inner height of capillary: (0.88 ± 0.02) mm, outer: (1.32 ± 0.02) mm, cross-section: 3.96 mm^2), this does not affect the

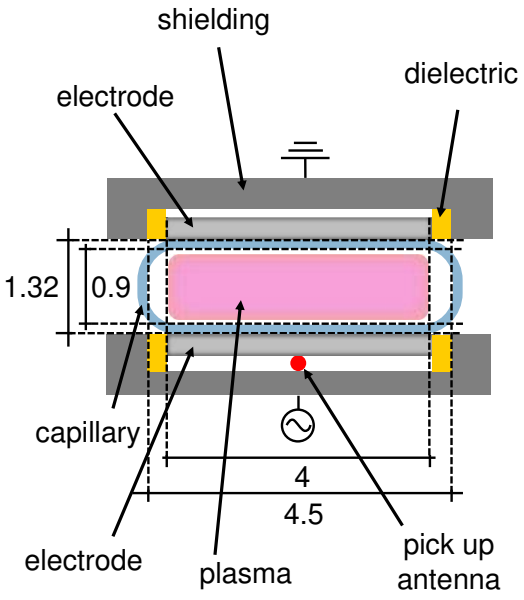

Figure 6.1: Cross-section of the electrode and capillary arrangement for a larger plasma volume. Dimensions in mm.

plasma. The electric field is still similar and the setups with small and wide capillaries can be compared. On the sides of the wide capillary, the electric field could be reduced due to the smaller width of the electrodes, which could affect the plasma performance there. This must be taken into account when comparing the results of the small and wide capillaries.

The comparison of the H_2O_2 production of the capillary plasma jet equipped with the small and wide capillary is shown in figure 6.2. There, a gas flow variation was performed as the gas flow and the capillary cross-section determine the gas velocity, which is different for both capillaries at the same gas flow rate. The gas velocity v_{gas} is given by the gas flow rate Φ at standard conditions divided by the cross-section of the capillary A:

$$v = \frac{\Phi}{A}. \tag{6.1}$$

At the same gas flow rate, the velocity of the gas flowing through the wider capillary is smaller. To obtain a broader range for comparison in the same gas velocity range, the gas flow rate was increased to a total gas flow rate of 4 slm when operating the plasma with the wider capillary. Since the mass flow controllers had a maximum flow rate of 2 slm, the dry and humidified He flows at 2 slm were mixed and a maximum humidity of 3200 ppm was used for the wide capillary. As the measurements with the small capillary were conducted previously to the ones of the wider capillary, the gas flow rate variation for the small capillary was performed at a humidity of 6400 ppm. Lower humidity leads to lower H_2O_2 densities and concentrations, as described in detail in the chapters 4 and 5, whereby the densities and concentrations at 3200 ppm are 80 % lower than at 6400 ppm. Therefore, the results of the gas flow variation of the smaller capillary are corrected by this factor to compare the results of the small and the wide capillary.

Besides the different gas velocities, the interaction area of the effluent and the liquid surface also differs when the width of the capillary is increased. This might change the species transport from the effluent into the liquid as the species can be dissolved at a larger surface area into the liquid and the convective transport might be smaller at a larger capillary width and lower velocities. This aspect has to be taken into account when the results of the liquid treatment are discussed.

First, the H_2O_2 concentration in the PTL is discussed. For both capillaries, a linear increase can be seen in figure 6.2 (a). At the same gas flow rate, the concentration delivered by the plasma operated with the wide capillary is lower. For example, at 2 slm, the concentrations in the liquid are (1.55 ± 0.24) mM and (1.11 ± 0.17) mM for the small and wide capillary, respectively. When transforming the gas flow rate to the gas velocity, the trend shifts as the H_2O_2 concentrations at

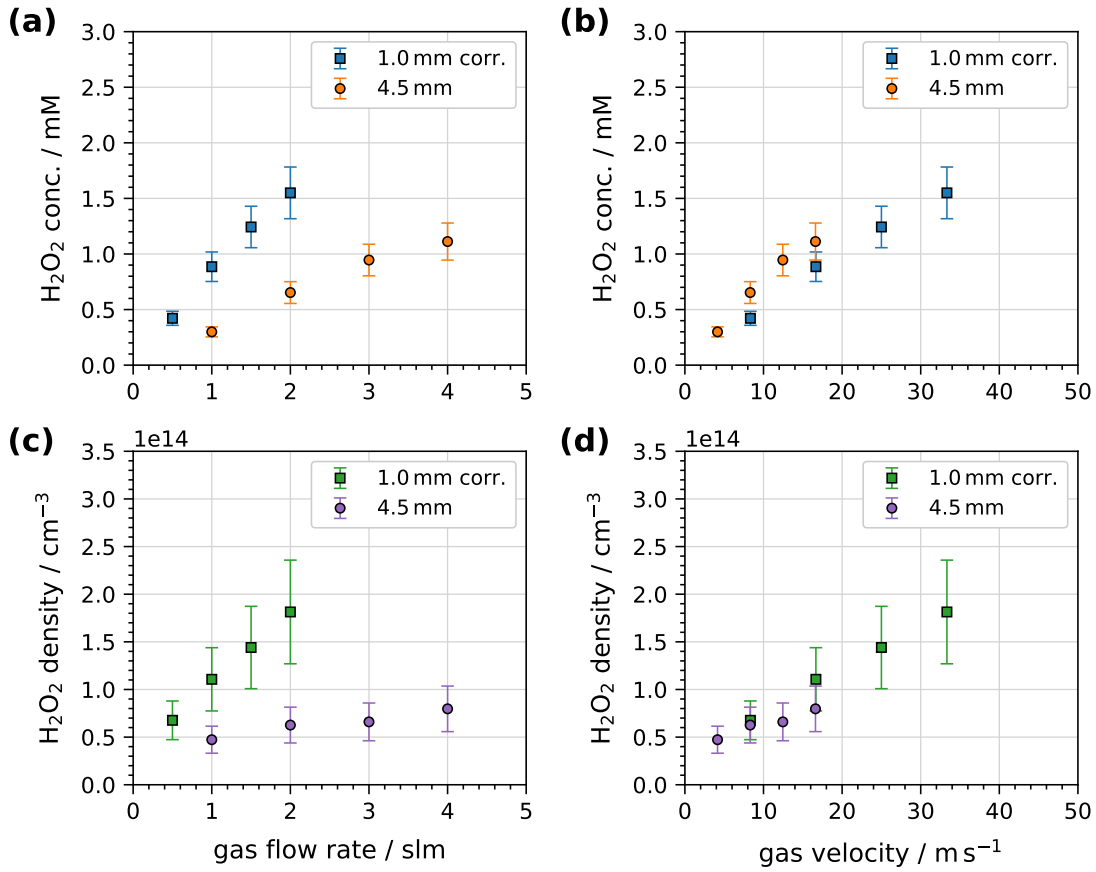

Figure 6.2: **(a)** H_2O_2 concentration as a function of gas flow rate for small (1 mm) and wide (4.5 mm) capillary. **(b)** H_2O_2 concentration as a function of the gas velocity for both capillaries. **(c)** H_2O_2 density as a function of gas flow rate for both capillaries and **(d)** H_2O_2 density as a function of the gas velocity for both capillaries. The measurements were performed with the plasma operated at 6 W plasma power. In the case of the wide capillary, a humidity admixture of 3200 ppm was used while the measurements of the small capillary were conducted with 6400 ppm but the results of the small capillary are corrected by a factor of 80 % to account for the reduced production at lower humidity.

a certain gas velocity are slightly higher for the wider capillary (see figure 6.2 b). Considering the smaller proportion of gas flowing through the plasma in the wide capillary, this trend is counterintuitive as the density and concentrations should be lower.

To investigate this further, the H_2O_2 density was measured by FTIR spectroscopy for both capillaries. The trends of the H_2O_2 density by varying the gas flow rate are the same as observed for the H_2O_2 concentration: with increasing gas flow rate the H_2O_2 density increases and the wider capillary shows a lower density (see figure 6.2 c). In the case of the gas velocity, both capillaries show the same densities at the same gas velocity (see figure 6.2 d). This is in contrast to the liquid measurements where the wider capillary shows higher concentrations. This might indicate that the

species transport into the liquid is different for the two capillaries. As the interaction area is different, also the interaction between the effluent and the liquid might be different. However, the differences regarding the concentrations are small and at a gas velocity of about 16 m s^{-1}, the concentrations agree within the uncertainties.

Overall, it can be stated that the small and wide capillary produce the same amount of H_2O_2 at the same gas velocity (factor of 4.5 higher gas flow rates for the wider capillary). Thus, the scale-up of the plasma volume by widening the capillary at the same height (distance of the electrodes) can be an option to operate at higher gas flow rates at the same production rate to deliver more H_2O_2 to the liquid.

6.2 Ar as feed gas

He as feed gas is promising for atmospheric pressure plasmas, however, it is an expensive gas and non-sustainable due to its limited availability on earth. The He supply will be exhausted by the end of the century under business as usual [222–224]. He recycling could be an option to avoid wasting He, but such setups are expensive and not easy to implement in scientific research facilities. For industrial applications, it might be suitable. An alternative to He might be Ar, which is cheaper and can be extracted from the air. However, using Ar as feed gas in RF-excited atmospheric pressure plasmas has proven to be difficult for ignition and operation [57]. Furthermore, the addition of reactive gases is also more challenging and a sparkle gun is necessary to ignite the plasma. To investigate the H_2O_2 production for Ar as feed gas in the case of the capillary plasma jet used in this work, the H_2O_2 concentration in the PTL was tested when Ar was used as feed gas. For these investigation, the smaller capillary with 1 mm width was used again.

In figure 6.3, the H_2O_2 concentration for various plasma powers at different humidity admixtures to Ar is shown. Since the Ar plasma was barely operable at high humidity admixture, the plasma power had to be higher than 20 W to maintain a stable Ar plasma with high humidity. This was the maximum humidity and plasma power that was operable without damaging the system on short timescales of treatment. The He case at 640 ppm is also shown for comparison.

At 64 ppm, with only 1 % of the Ar flow guided through the bubbler, the minimum plasma power required for operation was 6 W. In this case, only 0.1 mM of H_2O_2 concentration is achievable. Increasing the plasma power to 10 W does not enhance the H_2O_2 production. At a higher humidity of 640 ppm, a concentration of 0.18 mM could be achieved at 10 W plasma power. Compared to He, this is only half of the concentration of the He plasma. At high humidity admixture and plasma power (3200 ppm and 20 W), a concentration of 0.4 mM was measured. However, at these

parameters, particularly at the high plasma power, an Ar plasma was visible in the effluent region. Thus, the plasma is no longer confined between the electrodes and might come into contact with the liquid. This is not practical for applications as the reproducibility of the treatment may not be guaranteed and the higher plasma powers associated with higher gas temperatures could be harmful to the samples.

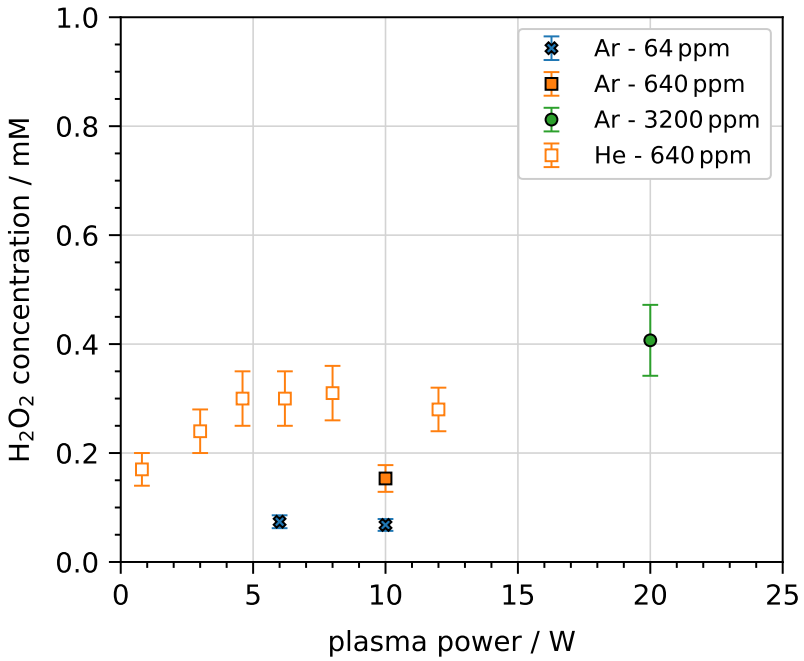

Figure 6.3: Comparison of the H_2O_2 production of the capillary plasma jet operated in Ar or He. The H_2O_2 concentration was measured in the PTL and the plasma was operated at various plasma powers and humidity admixtures. Gas flow and treatment parameters like the distance between the capillary and liquid surface and treatment time were the same for both feed gases.

These results show that an Ar plasma is in general able to produce H_2O_2 and deliver it to the liquid. This is consistent with the literature, where it has been shown that plasmas at atmospheric pressure operated with Ar as feed gas produce H_2O_2 in experimental studies [32, 207] and in modelling studies [108, 225]. The main production mechanism of H_2O_2 in Ar plasmas is also via the recombination of OH in the three body reaction: $OH + OH + M \longrightarrow H_2O_2 + M$. The rate coefficients for the reaction in Ar and He are slightly different. For Ar, the same rate coefficient as for N_2 is assumed in literature [225] with a rate coefficient of $6.9 \times 10^{-31}\,cm^6\,s^{-1}$ [226]. On the other hand, for He a gas efficiency factor of 0.41 is assumed [37] leading to the following reactions and rate coefficients:

$$OH + OH + Ar \longrightarrow H_2O_2 + Ar\,, \quad k = 6.9 \times 10^{-31}\,cm^6\,s^{-1} \tag{6.2}$$

$$OH + OH + He \longrightarrow H_2O_2 + He\,, \quad k = 2.8 \times 10^{-31}\,cm^6\,s^{-1} \tag{6.3}$$

Besides the different rate coefficients, the plasma parameters such as electron density and temperature also differ between Ar and He plasmas as discussed in detail in chapter 2, affecting the electron-driven chemistry of the Ar and He plasmas. Furthermore, the thermal conductivity of the two gases is different which changes the heat transport in the plasmas. The comparison of the gas temperature at the end of the discharge channel is shown in figure 6.4 for the two gases. The Ar plasma shows remarkably higher temperatures. For example, at a plasma power of 6 W, the He plasma has a temperature of 150 °C while the Ar plasma is about 230 °C. Thus, the Ar gas heats up more which also affects the chemistry as the rate coefficients of the neutral chemistry are driven by the gas temperature. Due to the high heat conductivity of He, the energy in the form of heat is transported more efficiently towards the surfaces and the system of the He plasma heats up more. This can be seen at the higher capillary temperature of the He plasma measured at the end of the discharge channel on the outside of the capillary, also shown in figure 6.4. At 8 W plasma power, the capillary under He plasma reaches a temperature of 104 °C whereas under the Ar plasma, it is only 83 °C. This temperature difference might change the overall system's performance.

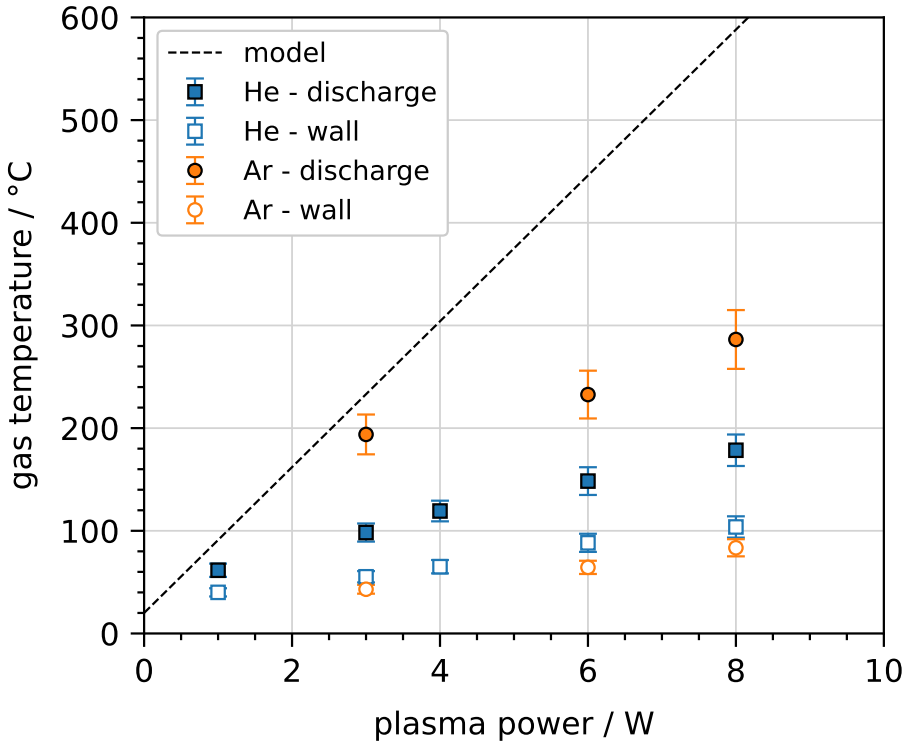

Figure 6.4: Gas temperature extrapolated to the end of the discharge and wall temperature of the capillary at the end of the discharge for both Ar and He as feed gas for various plasma powers. Plasmas were operated at 0 ppm humidity. The dashed line corresponds to the modelled temperature according to equation 6.4.

The change in temperature ΔT can be modelled by gas heating due to the dissipated plasma power. Considering the total plasma power P is consumed for gas heating, ΔT can be calculated from the following equation [15]:

$$P = c_{\text{gas}}\, m_{\text{gas}} \Delta T \frac{p_s \Phi}{k_B T_s}, \tag{6.4}$$

with the specific heat capacity c_{gas} and mass m_{gas} of the feed gas at standard pressure $p_s = 1\,\text{bar}$, temperature $T_s = 300\,\text{K}$, gas flow rate Φ and Boltzmann constant k_B. The product of heat capacity and mass for Ar and He is the same since the heat capacity of Ar is one-tenth that of He but the Ar mass is a factor of ten larger: $c_{\text{He}} \cdot m_{\text{He}} = c_{\text{Ar}} \cdot m_{\text{Ar}}$. Thus, the modelled temperature according to equation 6.4 is the same for Ar and He. The modelled gas temperature is shown as a dashed line in the figure. The measured temperatures are below this threshold, indicating that the measured temperatures are trustworthy. In the case of He, less than half of the plasma power goes into gas heating, and the other part of the plasma power is used for heating the device and the production of chemical products [15]. Since the heat conductivity of Ar is less, more power is consumed for gas heating resulting in a higher temperature of the Ar gas and about half of the power goes into heating of the Ar gas.

All in all, an Ar plasma can produce H_2O_2 and deliver it to the liquid. However, the handling of the plasma is quite challenging and the concentrations are lower, although the main principle of water chemistry is the same. For other plasma sources producing H_2O_2, Ar could be a suitable alternative to He as a feed gas.

6.3 Summary scale-up

The findings from this chapter can be summarized as follows

- A widening of the capillary to extend the plasma volume and the interaction area of effluent and liquid surface was possible. Regarding the comparison at the same gas velocities, the same H_2O_2 production mechanism was found as the concentrations measured in the PTL and the densities in the gas phase were similar.
- The scale-up of the plasma volume by widening the capillary at the same height (distance of the electrodes) can be an option to operate at higher gas flow rates at the same production rate to deliver more H_2O_2 to the liquid and to speed up the process.
- The operation with Ar as feed gas and admixture of H_2O has proven to be difficult. The Ar plasma with high humidity concentrations could only be operated at high plasma powers of more than 10 W accompanied by very high gas temperatures that might be not useable in applications.
- The H_2O_2 production of the capillary plasma jet operated with Ar and 640 ppm humidity was found to be a factor of two lower compared to the He plasma at similar conditions.

7. Tuning plasma chemistry

This chapter deals with two extended applications of the capillary plasma jet that have emerged in the course of this work. First, the effect of additional reactive components such as N_2 and O_2 to the He+H_2O plasma on the production of reactive species was investigated. The cooperation with the B13 project of the CRC 1316 required a gas mixture of He+H_2O+N_2 to produce NH-containing species to generate nanoparticles by the use of micelles in the PTL [14]. In addition, other enzymes are available that consume N-containing species. Thus, investigations on the species produced by the capillary plasma jet in mixtures of He+H_2O+N_2+O_2 are presented in the first sections of the chapter. Secondly, the capillary plasma jet enables a broader application window regarding the excitation mechanisms. Due to the dielectric character of the capillary, high voltages up to 9 kV can be applied and high-voltage pulses with rise times in the order of µs or ns can be used. This enables for example the ignition of the atmospheric pressure plasma in N_2 or air, overcoming the use of expensive and non-sustainable noble gases. Furthermore, the various excitation mechanisms applied to the capillary plasma jet allow the direct comparison of mechanisms in terms of their H_2O_2 production without changing the overall configuration of the plasma source. This provides insights into the efficiency of the various excitation mechanisms. The comparison of high-voltage µs and ns pulses to the RF operation in terms of their H_2O_2 production is shown and discussed in the second section of the chapter.

The following results on investigations of nitrogen fixation of the capillary plasma jet were performed in collaboration with Jannis Kaufmann in the frame of his bachelor's thesis supervised in the course of this dissertation. Some parts of the first section have already been published in his bachelor thesis [227]. Furthermore, the following results on investigations of the µs excitation of the capillary plasma jet were performed in collaboration with Niklas Eichstaedt in the frame of his bachelor's thesis supervised in the course of this dissertation. Some parts of the second section have already been published in his bachelor thesis [228]. In addition, parts of the results and discussions presented in this chapter have been published in the following papers:

- Steffen Schüttler at el., "Nitrogen fixation and H_2O_2 production by an atmospheric pressure plasma jet operated in He–H_2O–N_2–O_2 gas mixture" *Plasma Process. Polym. 21:e2300233 (2024)* [229].

- Steffen Schüttler et al., "Tuning plasma chemistry by various excitation mechanisms for the H_2O_2 production of atmospheric pressure plasma jets" *J. Phys. D: Appl. Phys. 58 025203 (2025)* [230].

7.1 Nitrogen fixation

With a gas mixture of He+H_2O the gas composition is well-defined and the chemistry involves only species of water chemistry. But what happens if air impurities enter the gas composition? Then, also N and O species play a role in the chemistry. Alternatively, N_2 and O_2 can be intentionally added to the gas composition regarding nitrogen fixation, for example, to produce ammonia as a fertilizer [52, 231, 232]. The effects of N_2 and O_2 admixtures on the chemistry of the He+H_2O capillary plasma jet were investigated in terms of this thesis and the results are presented in the following.

Setup and diagnostics

The setup to investigate nitrogen fixation by the capillary plasma jet was the same as presented in chapter 3. Here, the small capillary with a width of 1 mm was utilised. To add N_2 and O_2 simultaneously to the He+H_2O gas flow, the gas supply was extended by two mass flow controllers (Analyt MTC) with maximum gas flow rates of 100 sccm and 1 sccm for N_2 and O_2, respectively. Ignition of the plasma with admixtures of H_2O, N_2 and O_2 was possible. However, the plasma got unstable at too high admixtures and was only operable at high plasma powers of 10 W or more. Maximum admixtures of 3200 ppm humidity, 1 % N_2 and 0.1 % O_2 was chosen at which a stable operation could be guaranteed. The N_2 and O_2 admixtures corresponded to flows of 10 sccm and 1 sccm admixed to the total gas flow of 1 slm.

A 3 mL liquid sample was treated in the same way as described in chapter 3. Thus, the species produced by the capillary plasma jet and transported into the liquid could be investigated when N_2 and O_2 were added to the gas flow. As a liquid sample, the KPi buffer was used. Since the main species that can be produced and be detected in the liquid are H_2O_2, ammonia NH_3, nitrite NO_2^- and nitrate NO_3^- [50, 107, 233, 234], their concentrations were measured by various diagnostics. In the case of NO_x species, only NO_2^- was measured as a proxy.

For the measurements of H_2O_2 in the PTL, the two methods already implemented for the He+H_2O chemistry were used: the spectrophotometric approach utilising ammonium metavandate and the electrochemical sensing. The experimental setup and procedure were the same as described in chapter 3.

The detection of NH_3 in the PTL was based on a fluorimetric approach using o-phythalaldehyde [235]. In this method, NH_3 reacts with o-phythalaldehyde to form a fluorescent product which can be excited by a wavelength of 360 nm and emits light at a wavelength of 450 nm. A commercial "Ammonia Assay Kit" (Sigma-Aldrich, MAK310-1KT) based on this method was utilised. The application protocol of the test kit was explained in the manual and the necessary steps are explained below. A sample of 20 µL of the plasma-treated liquid was extracted after plasma treatment. It was mixed with 180 µL of the working reagent of the kit. The working reagent consisted of 91.8 % buffer, 4.1 % Reagent A and 4.1 % Reagent B. The solution containing the sample and the working reagent was incubated for at least 15 min in the dark at room temperature. Due to the small volume of the liquid sample for detection and the use of the test kit, this method was only applicable ex-situ.

To detect the fluorescence, the final solution was illuminated by a laser-stabilised broadband lamp (Energetiq EQ99X-FC) and the fluorescence signal was measured perpendicular to the light beam by an iCCD camera (Andor iStar, DH334T-18U-E3). In general, the setup is the same as used for the TA dosimeter described in chapter 3 and shown in figure 3.15 (a). Furthermore, a small bandpass filter at 450 nm was positioned in front of the camera to minimise stray light and ensure the observation at the desired wavelength. A calibration was conducted at each measurement day, which was performed by NH_3 standard solutions with concentrations up to 1 mM following the instructions given in the manual of the test kit. The calibration curve showed a linear increase with NH_3 concentration. In post-processing, the measured intensity was integrated and from fitting the calibration curve the NH_3 concentration could be obtained. The measurements were carried out with three consecutive measurements to determine the uncertainty of the method. The mean and standard deviation for each data point are given.

For the detection of the NO_2^- concentration, a spectrophotometric approach was used, based on the use of the Griess reagent method. This method was developed by Griess in 1879 [236] and has been used in numerous applications [237]. For this method, a commercial nitrite assay kit (Sigma Aldrich) was purchased and the protocol of the manual was carried out. NO_2^- reacts with sulfanilamide and the reactant reacts further with naphthylethylenediamine. The final product of the reaction is an azo dye with an absorption maximum at 540 nm. The test kit solution was prepared as described in the manual. 100 µL of the PTL were extracted for analysis. Due to the maximum detection limit of the test kit of 0.1 mM, the sample was diluted by factors of 1, 2, 5, 10, and 20 to prevent saturation and the various dilutions were measured for each treatment. The diluted samples were mixed with 10 µL of Griess Reagent I and afterwards with 10 µL of Griess Reagent II. The

solution was further filled up to 200 µL by adding 80 µL of the buffer. The final solution had to incubate for 10 min in the dark at room temperature. Similar to the NH_3 measurements, this method was performed ex-situ due to the small volume of the liquid sample for detection and the use of the test kit.

The setup to measure the NO_2^- concentration was similar to the one for the spectrophotometry of H_2O_2 using ammonium metavanadate described in chapter 3 and shown in figure 3.12. The light beam from the laser-driven light source (Energetiq EQ99X-FC) was passed through a smaller UV cuvette (200 µL) containing the prepared solutions of samples and test kit. The absorbance was measured using a spectrometer (Avantes Avaspec-ULS 2094x64 TEC-EVO). For each measurement, the background was corrected and a reference of only buffer and test kit was recorded. Calibration of the system was performed with NO_2^- standard solutions with concentrations between 0 mM and 0.1 mM following the instructions given in the manual. Based on three replicates performed for measurements with high dilutions of a factor of 10 and 20, a maximum uncertainty of 0.12 mM was determined. At low dilutions, a maximum uncertainty of 0.024 mM was taken for the measurements.

H_2O_2 diagnostics validation

In chapter 5, a good agreement was found between spectrophotometry and the electrochemical sensor for the detection of H_2O_2 in PTL. However, since in the following experiments N_2 is added to the feed gas, further reactive oxygen and nitrogen species (RONS) can be produced that can affect the diagnostics, so the two methods have to be compared when the plasma is operated in gas mixtures including N_2. This comparison of the measured H_2O_2 concentration at various N_2 admixtures of the two diagnostics is shown in figure 7.1 for plasma conditions of 6 W plasma power, 3200 ppm humidity and no O_2 addition. At 0 % N_2 admixture, both diagnostics reveal the same H_2O_2 concentration considering the uncertainty range. This is in agreement with the results presented in chapter 5 and also the absolute value of about 0.7 mM agrees well with the measurements presented in figure 5.1. Since the measurements presented in this chapter were recorded one year later and the plasma setup and the diagnostics setup were rebuilt, the agreement shows the good reproducibility of the measurements.

Once N_2 is added to the feed gas, the H_2O_2 concentration decreases to about 0.4 mM as shown by both diagnostics. With increasing N_2 content, the H_2O_2 concentration in the case of the electrochemical sensing stays constant but the spectrophotometric approach reveals a continuing decrease until a concentration of 0.1 mM is achieved at an N_2 admixture of 1 %. This indicates a different trend of the H_2O_2 concentration with N_2 admixture by the two methods. In addition, the absolute

values of the spectrophotometry are lower than those of the electrochemical measurement once N_2 is added to the system. This becomes even more pronounced at higher admixture of N_2. Thus, some discrepancies between the two diagnostics exist.

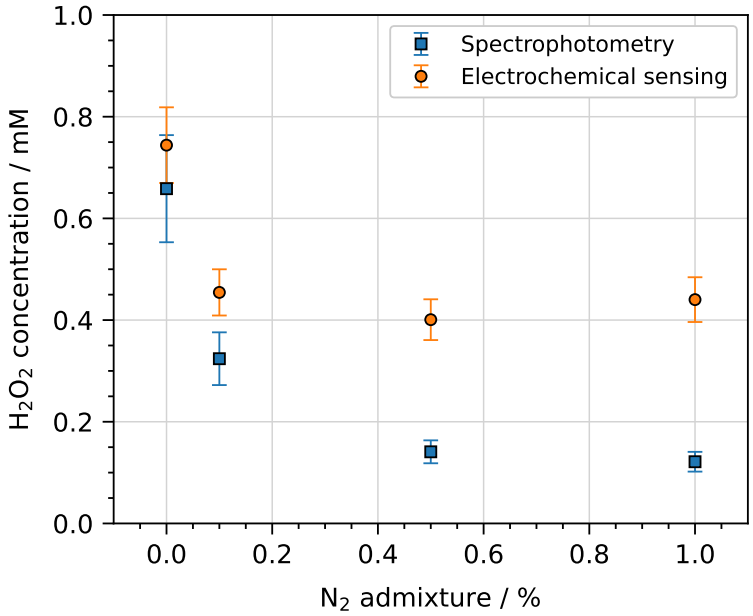

Figure 7.1: Comparison of spectrophotometry and electrochemical sensing for the detection of H_2O_2 in the PTL when N_2 is added to the He flow. Plasma was operated at 6 W plasma power, 3200 ppm humidity and no O_2 addition. The uncertainties were obtained from replicate measurements in the case of He+H_2O plasma, as explained in chapter 3, and do not reflect any interference of spectrophotometry by N-containing species (see discussion in the text).

To discuss the discrepancies, the operating principle of the two diagnostics has to be discussed. The electrochemical sensor is sensitive to H_2O_2 in solutions and detects it directly via electrochemical oxidation and reduction [163, 164]. On the other hand, the spectrophotometric approach utilises ammonium metavanadate as a chemical to form a red-orange-coloured peroxovanadium cation. A previous study has found that this spectrophotometric approach does not interfere with chloride, iron, chlorophenol, and NO_3^- [162]. However, it is known that NO_2^- leads to a decolourisation effect of the peroxovanadate complex [238]. Since a considerable amount of NO_2^- is produced when N_2 is added to the system (results are shown in the following), this decolourisation effect may take place and interfere with the peroxovanadate complex. This was also apparent in the experiments. During plasma treatment, the measured absorption spectra in the liquid became unstable at elevated N_2 admixture. The temporal behaviour of the spectrophotometric approach during plasma treatment with N_2 admixtures is shown in the appendix A.7, where the instability becomes visible.

Thus, the spectrophotometric approach is affected by RONS and the use of the spectrophotometric approach utilising ammonium metavandate is limited. It can only be used for the case of a He+H_2O plasma, where only species involved in the water chemistry are produced such as OH or H_2O_2. When N_2 is added and N-containing species are produced, it is cross-sensitive to species containing N and alternative methods such as electrochemical sensing should be used. Therefore, the following results regarding the H_2O_2 measurements were measured by electrochemical sensing.

Species concentration

The influence of N_2 admixture on the species concentration in the PTL is shown in figure 7.2. There, humidity concentrations of 0 ppm, 640 ppm and 3200 ppm were used and the addition of O_2 is also shown. In the case of H_2O_2, its concentration decreases once a small amount of N_2 is added (see figure 7.2 a). An admixture of only 0.1 % leads to a reduction of around 40 %. This is true for low and high humidity concentrations. The case of 0 ppm was not investigated since the investigation made in chapter 4 and 5 have shown that only a small amount of H_2O_2 is produced without the addition of H_2O. The addition of O_2 to the system leads to an increased H_2O_2 concentration at a humidity of 3200 ppm (see figure 7.2 b). For example, at 0 % N_2, the H_2O_2 concentration increases from 0.75 mM to 0.89 mM which is an increase by 19 %. At a humidity of 640 ppm, H_2O_2 is unaffected by the addition of O_2 to the system. Thus, the O_2 addition can improve the H_2O_2 production at elevated humidity concentrations.

The concentration of NH_3 behaves differently compared to H_2O_2. If no H_2O is added to the gas flow, no NH_3 can be detected regardless of the N_2 admixture (see figure 7.2 c). At a low N_2 admixture of 0.1 %, NH_3 can be barely detected in the liquid. However, at 0.5 % N_2 admixture and above and in combination with humidity in the gas flow, NH_3 can be detected in the liquid and a concentration of 0.2 mM is achieved. When O_2 is added to the gas mixture, the NH_3 concentrations are below 0.1 mM for all N_2 admixtures and humidity concentrations and the NH_3 production is suppressed (see figure 7.2 d).

The third species investigated was NO_2^-. No NO_2^- can be measured in the liquid if no O_2 is added and if either no N_2 or no H_2O is added (see figure 7.2 e). However, NO_2^- concentrations can be measured in the case of no O_2 admixture when N_2 and H_2O are present in the gas flow and a maximum concentration of 1.6 mM can be measured at a humidity of 3200 ppm and an N_2 admixture of 1 %. With increasing N_2 admixture, the NO_2^- concentration increases and a higher humidity concentration leads to higher NO_2^- concentrations. In the case of an O_2 addition, a low NO_2^-

concentration of 0.1 mM can be measured when N_2 is added to the gas flow and the humidity concentration is 0 ppm (see figure 7.2 f). With increasing humidity, the NO_2^- concentration rises remarkably and a maximum value of 1.6 mM is achievable at 3200 ppm humidity, 1 % N_2 and 0.1 % O_2 admixtures. Thus, the same absolute values at the high humidity and N_2 admixtures are obtained as was the case without O_2 admixture. However, at low humidity, the NO_2^- concentration is increased by more than 50 % when O_2 is added to the gas mixture.

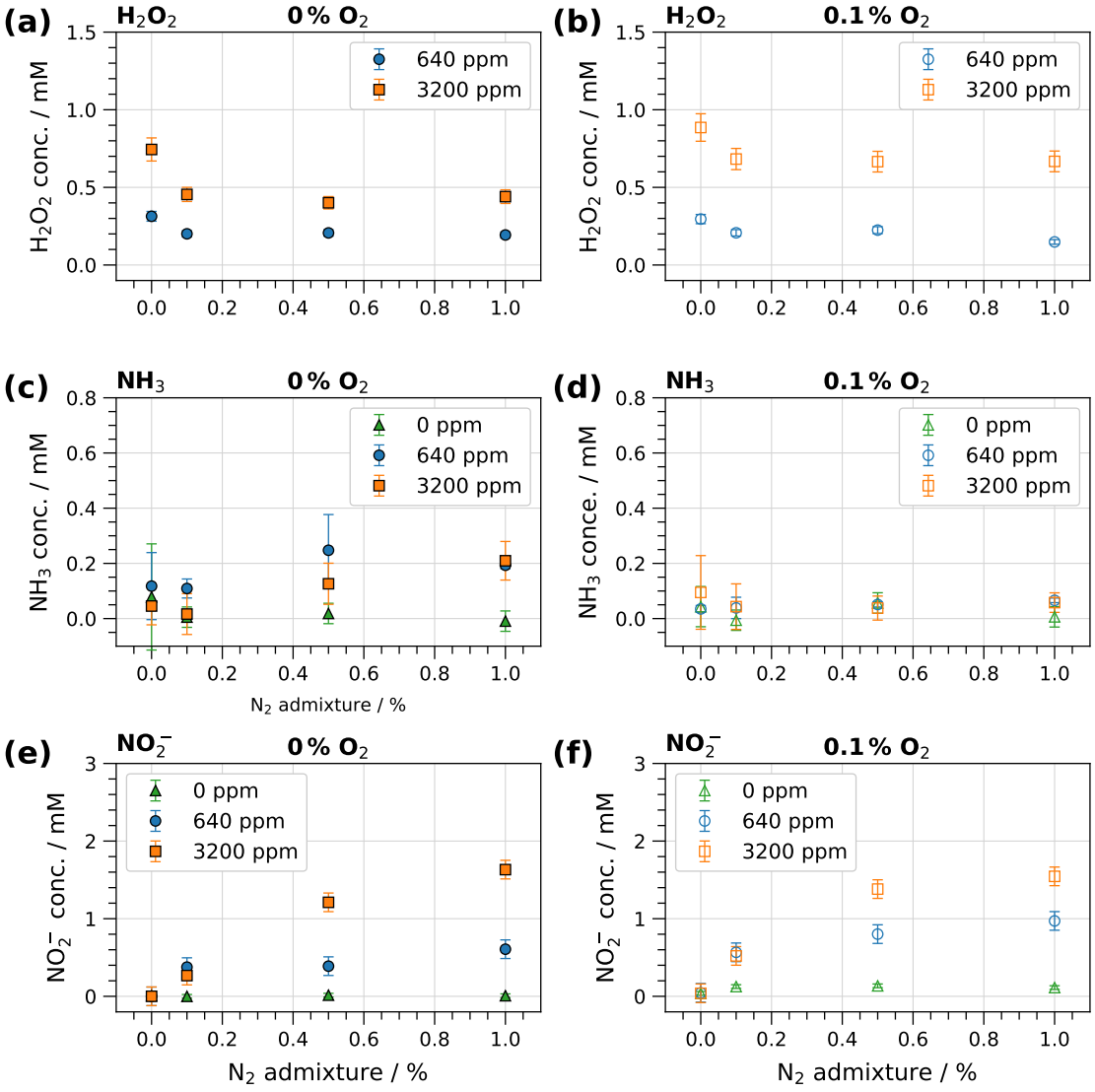

Figure 7.2: Concentrations of **(a)**,**(b)** H_2O_2, **(c)**,**(d)** NH_3 and **(e)**,**(f)** NO_2^- measured in the PTL for various N_2 admixtures at different humidity admixtures. (a),(c),(e): 0 % O_2 admixture; (b),(d),(f): 0.1 % O_2 admixture. All measurements were performed at a plasma power of 6 W.

To discuss the results of the species concentrations regarding the different humidity, N_2 and O_2 admixture, the plasma chemistry with the main production mechanisms of the various species has to be explained. As discussed in chapter 2, H_2O_2 is

produced via the recombination of OH, which itself is produced by electron impact dissociation of H_2O:

$$OH + OH + M \longrightarrow H_2O_2 + M \tag{R 7.1}$$

$$e^- + H_2O \longrightarrow e^- + H + OH\cdot \tag{R 7.2}$$

When N_2 molecules are added to the gas mixture, they will be vibrationally excited and dissociated in the plasma [239, 240]

$$e^- + N_2(g) \longrightarrow e^- + N_2(v), \tag{R 7.3}$$

$$e^- + N_2 \longrightarrow e^- + 2\,N\cdot \tag{R 7.4}$$

N and vibrationally excited $N_2(v)$ react with O or O-containing species to form the nitric oxide radical NO in the Zeldovich mechanism:

$$O + N_2(v) \longrightarrow NO + N, \tag{R 7.5}$$

$$N + O_2(v) \longrightarrow O + NO, \tag{R 7.6}$$

$$N + O \longrightarrow NO \tag{R 7.7}$$

$$N + OH \longrightarrow NO + H\cdot \tag{R 7.8}$$

Since OH is involved in the last reaction, it leads to a loss of the OH radical, which in turn is no longer available for the production of H_2O_2. This might explain the decrease of the H_2O_2 concentration when N_2 is added to the gas mixture, as can be seen in the experiments. Furthermore, when changing the gas admixtures including N-containing species, the species composition and the pH at the liquid surface are changed. The interface of gas and liquid is known to be crucial since the reactive species of the plasma are in contact with the liquid and the dissolution of the species takes place at the interface [38, 43]. Thus, changes in the species composition or pH at the interface influence the solubility and chemistry of the species at the gas-liquid interface [241] and might change the measured H_2O_2 concentration in the liquid.

The main production mechanism of NH_3 involves N and H atoms via the following steps [233, 242]

$$N + H + M \longrightarrow NH + M, \tag{R 7.9}$$

$$NH + H + M \longrightarrow NH_2 + M, \tag{R 7.10}$$

$$NH_2 + H + M \longrightarrow NH_3 + M\cdot \tag{R 7.11}$$

H is present in the plasma when H_2O is added to the plasma due to electron impact dissociation of H_2O. N is produced by the dissociation of N_2. Thus, H_2O and N_2

molecules are required to produce NH_3 and no NH_3 can be produced in the plasma and measured in the PTL without the addition of H_2O or N_2, as can be seen in the experiments. However, the production of NH_3 competes with oxidative pathways of N and H. This explains the decrease in NH_3 concentration when O_2 is added to the system. O_2 is vibrationally excited and dissociated in the plasma

$$e^- + O_2(g) \longrightarrow e^- + O_2(v), \tag{R 7.12}$$

$$e^- + O_2 \longrightarrow e^- + 2\,O\cdot \tag{R 7.13}$$

and O atoms are likely to react with N and H to produce NO and OH [51, 189]

$$N + O + M \longrightarrow NO + M \tag{R 7.14}$$

$$H + O + M \longrightarrow OH + M\cdot \tag{R 7.15}$$

The last reaction leads to an enhanced OH production for a He+H_2O+O_2 gas mixture which can be seen in the experiments as the H_2O_2 concentrations were higher when O_2 was added to the system at high humidity admixture.

Furthermore, the combination of N and O-containing species leads to the production of intermediates of NO_2^-. Since NO_2^- is only present in the liquid phase, its intermediates like NO_2 or HNO_2 are produced in the plasma and dissolved in the liquid where NO_2^- is formed [233]:

$$NO + O_2(g, v) \longrightarrow NO_2 + O, \tag{R 7.16}$$

$$NO + O \longrightarrow NO_2, \tag{R 7.17}$$

$$NO + OH \longrightarrow HNO_2, \tag{R 7.18}$$

$$2\,NO_2(aq) + H_2O \longrightarrow NO_2^- + NO_3^- + 2\,H^+, \tag{R 7.19}$$

$$HNO_2(aq) \longrightarrow NO_2^- + H^+ \tag{R 7.20}$$

with the last two reactions leading to the formation of NO_2^- in the liquid after the solvation of NO_2 and HNO_2. In the first two reactions, NO and dissociated or vibrationally excited O_2 are involved. Thus, the admixtures of N_2 and O_2 are required to generate NO_2. This aspect is evident from the experiments, as the admixture of N_2 and O_2 leads to a low NO_2^- concentration in the plasma-treated liquid. The third reaction can be attributed to the contribution of N_2+H_2O gas mixtures, as this combination leads to the formation of OH and NO as explained above. In the experiments, the NO_2^- concentration was dependent on the humidity concentration and N_2 admixture to the feed gas and increased with both.

The overall chemistry of He+H_2O+N_2+O_2 is very complex and involves over 80 species interacting in over 250 electron-impact reactions and over 1500 heavy particle reactions [186, 225]. The discussion above shows that the trends observed in the experiments can be qualitatively described and analysed considering the main production and loss mechanisms. A detailed model of the plasma chemistry adapted to the setup used can provide further insight into the chemistry and can be used to optimise the plasma chemistry in the case of He+H_2O+N_2+O_2 gas mixtures.

Literature comparison

A comparison of plasma sources used for nitrogen fixation with the results presented in this work is shown in figure 7.4. The plasma sources are very different to each other and different trends regarding nitrogen fixation can be seen. Gorbanev et al. used a gliding arc plasma operated in humidified N_2 feed gas to treat a liquid sample [50], Lamichhane et al. used a kHz plasma jet operated in pure N_2 to treat a liquid [234], and in the work of Toth et al., a coaxial DBD plasma operated in N_2 with the addition of water droplets was used [233]. All studies measured NH_3 concentrations in PTLs extended by other species measurements such as H_2O_2 or NO_2^-.

The measured concentrations in the other studies and the work presented here were in the same range of millimolars. However, the species with the highest production rate differs (see figure 7.4 a). In the case of Gorbanev et al. it was NH_3, Lamichhane et al. found the highest production rate for NO_x including NO, NO_2^- and NO_3^-, although they did not measure H_2O_2, Toth et al. found the highest production rate for NO_3^- and in this work the highest production rate for NO_2^- was found. A possible cause of the different behaviour might be the difference in gas temperature. For example, the gliding arc plasma of Gorbanev et al. has a high-temperature zone of more than 1000 °C [50], while the capillary plasma jet used in this work shows temperatures of only 250 °C in its active plasma zone (see chapter 4). Thus, the plasma chemistry is different in the active plasma phase, and hence the species production might be different. Further analysis of the species production processes of each plasma source is necessary to obtain further insights to explain the differences in more detail.

In terms of gas composition, the biggest difference can be attributed to the main feed gas: The capillary plasma jet operated mainly in He with small admixtures of N_2 while the other plasma sources used N_2 as the main feed gas. The energy yield as well as the conversion rate of nitrogen fixation can be compared between the capillary plasma jet operated in He and the other plasma sources operated in N_2. Due to the use of small N_2 admixtures and comparable concentrations of reactive species in the PTL by the capillary plasma jet, the N_2 conversion rate is almost

four magnitudes higher in the case of the capillary plasma jet used in this work (see figure 7.4 b). However, the energy yield is the same, except for the gliding arc plasma of Gorbanev et al. In their cases, the dissipated plasma power was low with only 0.1 W [50] compared to several watts consumed by the other plasma sources. Nevertheless, although cross-field plasma jets operated by RF excitation in noble gases with small reactive admixtures, like the capillary plasma jet, are not able to operate in pure N_2, a small admixture of N_2 is sufficient to produce a competitive amount of NO_x species and NH_3.

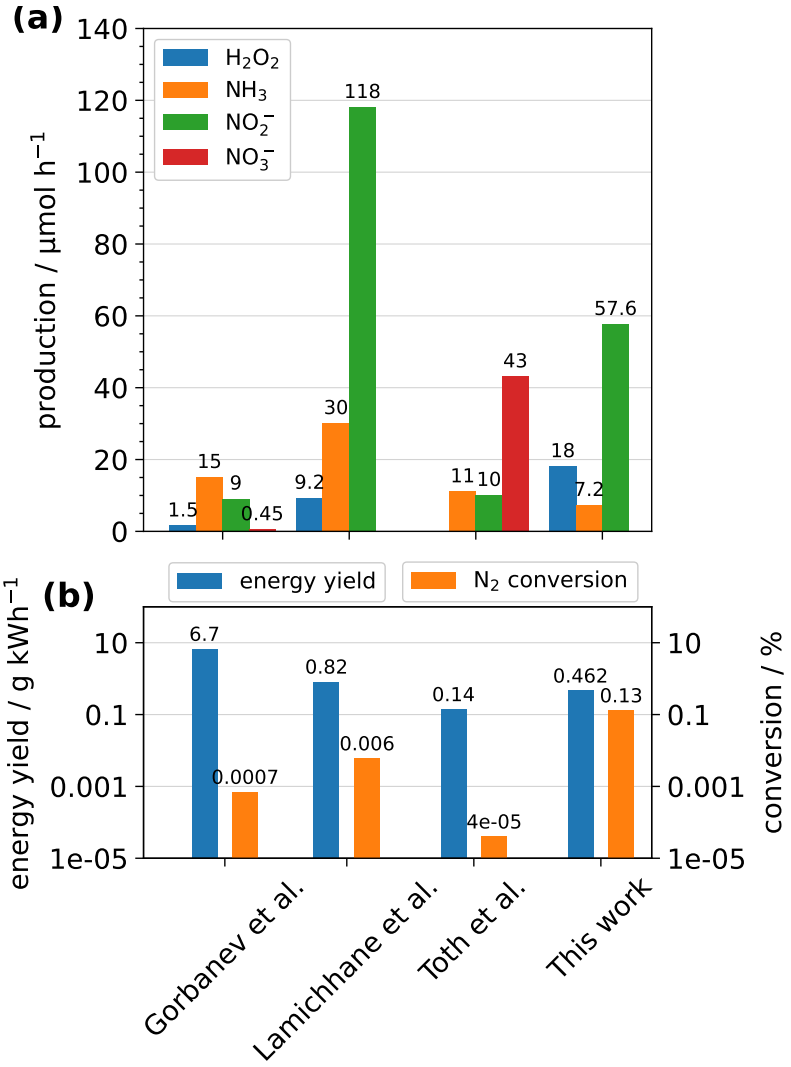

Figure 7.3: Comparison of atmospheric pressure plasmas investigated by Gorbanev et al. [50], Lamichhane et al. [234], Toth et al. [233] and in this work for nitrogen fixation. Lamichhane et al. measured only the combination of NO_x including NO, NO_2^- and NO_3^- by an improved Griess reagent kit [234].
(a) Production rates of H_2O_2, NH_3, NO_2^- and NO_3^-. **(b)** Energy yields and conversion rates of N_2 into NH_3, NO_2^- and NO_3^-. Please note the log scale of the y-axis.

Pulse modulation

The formation of NH_3 and NO_2^- relies on reactions of short-lived species as is the case for the formation of H_2O_2 from the recombination of OH. The pulse modulation of the RF excitation has shown to be a promising tool to suppress the formation of short-lived while accumulating long-lived species when the plasma was operated in a mixture of He and H_2O. The effect of low-frequency pulse modulation on the species concentrations regarding nitrogen fixation was also studied. To this end, the plasma was operated with a gas mixture of 3200 ppm humidity and 1 % N_2 at an unmodulated power of 6 W and liquid treatments were performed. The results are shown in figure 7.4.

The H_2O_2 concentration in dependence of the number of pulses per residence time shows the same behaviour as described for the He+H_2O gas mixture presented in chapter 5: At 50 % duty cycle the concentrations are about half of the value of the unmodulated case and stay constant with the number of pulses while at 10 % duty cycle an accumulation effect can be seen and the H_2O_2 concentration increases with an increasing number of pulses (see figure 7.4 a). For NH_3, shown in figure 7.4 (b), the 50 % duty cycle shows higher concentrations than the 10 % case. In both cases, the concentrations are lower than the unmodulated concentration and fluctuate and no clear trend can be observed. In contrast, the NO_2^- concentration is strongly affected by the pulse modulation. At 50 % duty cycle, the NO_2^- concentration is only half of the unmodulated case and at 10 % it is only one-tenth. Furthermore, no accumulation at the low duty cycle can be observed as was the case for H_2O_2 and the NO_2^- concentration stays constant with an increasing number of pulses at both duty cycles.

This demonstrates that the respective chemistry to produce H_2O_2, NH_3 or NO_2^- behaves differently in the plasma-on and plasma-off phases. In the plasma-on phase, radicals like OH, N and O are generated and the recombination processes to produce long-lived species start. In the plasma-off phase between two pulses, the production of short-lived species vanishes and only the long-lived species are created. If the plasma-off time is set to a considerable time scale, which is the case for the duty cycle of 10 %, an accumulation of H_2O_2 can be observed. Since this is not observed for NO_2^- and H_2O_2 is mainly produced by the recombination of OH, it can be assumed that the OH is less involved in the production of NO_2^-. Otherwise, an accumulation effect of NO_2^- might be observable. Furthermore, the NO_2^- concentration is decreased significantly by the pulse modulation, indicating that the production of the main intermediate NO is suppressed. Since OH is present, as indicated by the high H_2O_2 concentration, either atomic O and N or vibrationally excited O_2(v) and N_2(v) are less generated in the pulse modulation case. The production of NH_3

occurs via N and H in a three-step process. In the plasma-on phase, both atomic species are generated and in the plasma-off phase, these recombine first to form NH and then NH_2 to form NH_3. Since this requires more steps than the production of H_2O_2, more time is required and no accumulation of NH_3 can be observed on the investigated time scales.

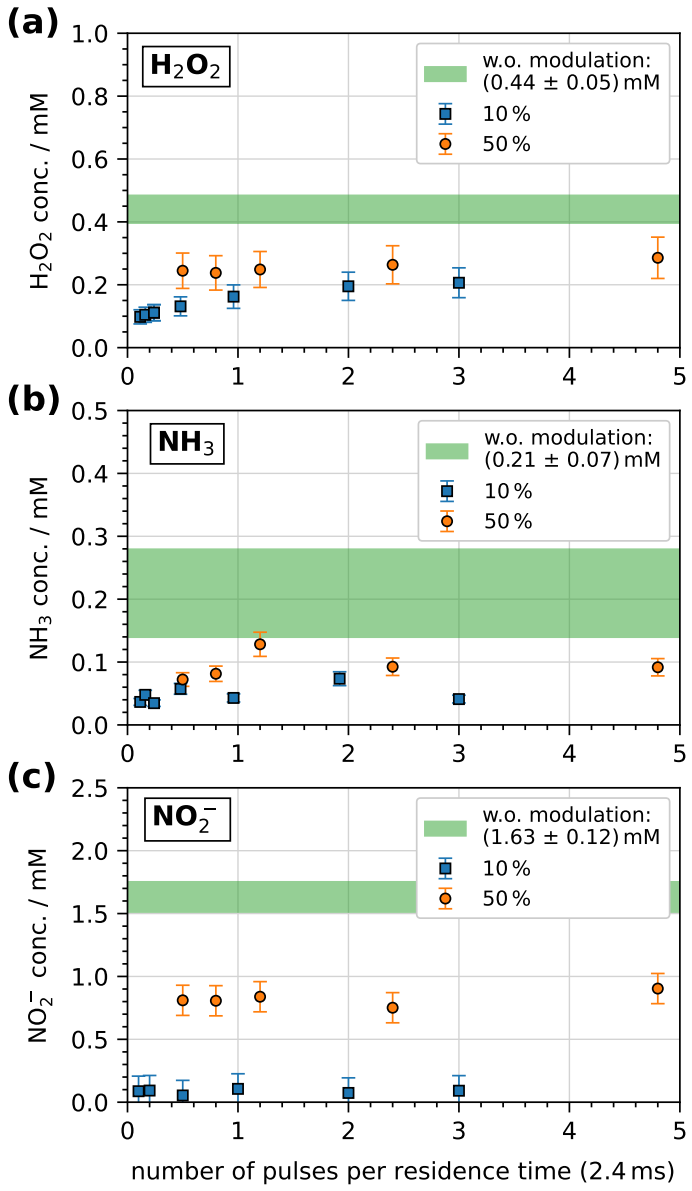

Figure 7.4: Concentrations of **(a)** H_2O_2, **(b)** NH_3, and **(c)** NO_2^- under pulse modulation for various numbers of pulses per residence at duty cycles of 10 % and 50 %. The plasma was set to an unmodulated plasma power of 6 W and the He gas mixture consisted of 1 % N_2 and 3200 ppm humidity. No O_2 admixture was added to the gas mixture.

However, a detailed analysis of the ongoing chemistry under pulse modulation is difficult, as many species and reactions are involved. Which species are more strongly affected by pulse modulation must be further investigated either by experiments or by modelling. Nevertheless, the pulse modulation of the RF excitation can also be used to control the chemistry of the He+H_2O+N_2+O_2 plasma. While in the unmodulated case NO_2^- was the main produced species, it changes under pulse modulation with even H_2O_2 as the main species at a low duty cycle and a high number of pulses. In this case, the production shifted from NO-dominated species to OH-dominated species.

7.2 Various excitation mechanisms

All investigations shown so far in this dissertation were performed using the capillary plasma jet operated with RF excitation. However, due to the dielectric character of the capillary, higher voltages can be applied allowing the capillary plasma jet also to be operated with high voltage pulses with rise times in the order of µs or ns at kHz repetition frequencies. This allows for a broader application range of the capillary plasma jet, as ignition in N_2 or air, for example, requires a higher voltage compared to noble gases. In addition, the use of short ns pulses or slower µs pulses can affect the production of short- and long-lived species due to the different time scales of their production. Using fast ns pulses the production of radicals by electron impact dissociation of molecules like OH is decoupled from neutral chemistry reaction in the period between pulses to produce long-lived species like H_2O_2. The following section deals with various operation modes of the capillary plasma jet such as high voltages with µs or ns rise times compared to RF excitation in their H_2O_2 production.

Setup

The setup used for the operation of the different excitation mechanisms varied slightly from the one described in chapter 3. The same gas supply and RF generator were used as described there and pulsing of the RF waveform was also the same as described in chapter 3. For µs and ns operation, the RF matchbox was removed and two different generators were connected via high-voltage coaxial power cables to the powered electrode. The grounded electrode was connected to the ground of the respective generator. To operate the jet with µs pulses, a homemade amplifier was used. It amplified a low-voltage pulse of a function generator (Tektronix AFG3011) to high-voltage pulses in the order of a few kV with a rise time of a few µs. The ns operation was enabled by another power generator (FID Technology FPG 10), directly connected to the powered and grounded electrodes. The power cable length

was 20 m and in the middle of the cable, a homemade back current shunt (BCS) was placed for power measurements as described below.

Furthermore, the arrangement of the electrodes and the capillary had to be changed to operate at high voltages of up to 9 kV applied during µs and ns operation. Originally, the capillary plasma jet was designed to operate with RF excitation with voltage amplitudes of less than 2 kV. At higher voltages, arcs can occur from the powered to the grounded electrode. These arcs were generated on the sides of the capillary in the atmosphere. This was observed when the first tests with µs operation were conducted. A plasma could barely be ignited and arcs at the side of the capillary occurred. To overcome this problem, an alternative electrode and capillary arrangement was used as shown in figure 7.5. In this case, the powered electrode is only 1 mm wide while the capillary and the grounded electrode had the wider dimension of 4.5 mm and 4 mm, respectively. With this arrangement, the distance at the side from the powered electrode to the grounded electrode was increased and arcing could be prevented at voltages up to 9 kV.

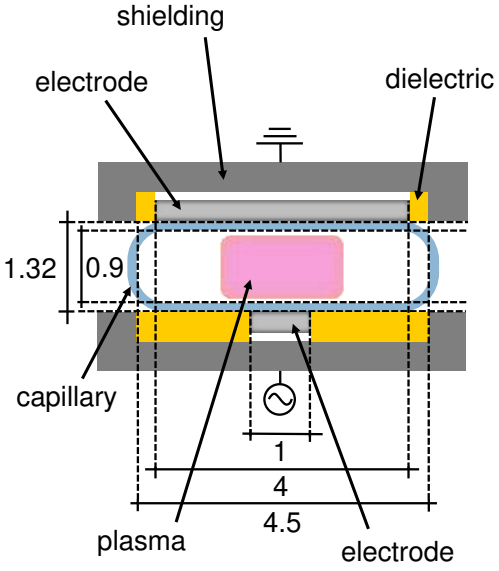

Figure 7.5: Sketch of the electrode and capillary arrangement for the setup under µs and ns operation. For RF operation, the pick-up antenna described in chapter 3 was also used. Dimensions in mm.

In this arrangement, the plasma does not fill the entire cross-section of the capillary. Due to the smaller width of the powered electrode, the plasma is likely to be present only in the direct vicinity of the powered electrode. The plasma emission was analysed with camera images to estimate the expansion of the plasma. The images are shown in the appendix A.8. For the µs and ns operation modes, the width of the plasma is about 3 mm (wider than the powered electrode but smaller than the grounded one). This results in a plasma volume of 67 % of the gas volume. In contrast, the width of the RF plasma is only 2 mm and thus only 44 % of the gas volume. This aspect has to be kept in mind when discussing the results.

Power measurements

To compare the different excitation mechanisms, the dissipated plasma power is one of the most important plasma parameters. The power measurements in the case of

the RF operation were conducted as described in chapter 3. However, the power measurements for the µs and ns operation are different. The main principles of these are described in the following.

In the case of the µs operation, the dissipated power is calculated by the following equation [243, 244]:

$$\bar{P} = \frac{1}{T} \int_0^T U \cdot I \, dt, \tag{7.1}$$

with the applied voltage U, the current I and the time of one excitation cycle T. Conventional voltage and current probes were used to measure the voltage (Tektronix P6015A, 75 MHz) and the current (Tektronix P6021). The voltage probe was connected to the transformer and the current probe was installed around the cable attached to the grounded electrode. An oscilloscope (Teledyne Lecroy HDO6104B, 1 GHz, 10 GS/s) was used to measure the voltage and current signals.

The analysis of the power measurements involved several steps to calculate the dissipated plasma power. At first, the displacement current I_{off} was measured by applying a voltage to the jet without gas flow. In this case, no power could be dissipated and the integral should provide a power of $P = 0$. However, due to the experimental setup, a phase shift ϕ existed between the displacement current and applied voltage, leading to an offset in the measured power. To compensate for the phase shift, I_{off} was shifted in time until $P = 0$ was achieved and the corresponding phase shift ϕ was used for the calibration of the measurements. After igniting the plasma, the measured current was shifted by ϕ and the power could be determined. Reproducing the power measurement showed fluctuations of a few per cent. However, due to the phase shift and the uncertainties of the probe measurements, an uncertainty of 20 % was assumed for the power measurements under µs operation.

The commercial voltage and current probes used for the power measurements of the µs operation are too slow to measure the fast voltage pulse of the ns operation adequately. For example, the voltage probe used under µs operation had a bandwidth of 75 MHz, sufficient for capturing signals with rise times of µs, but not on the ns time scale. Thus, power measurements of fast voltage pulses in the ns range are challenging. To overcome this problem, the back current shunt (BCS) technique was used for power measurement under ns operation [245], which has been implemented in previous studies [246, 247], e.g. to measure the dissipated energy of plasmas in liquids [248, 249] and surface DBDs at atmospheric pressure [250–253].

The BCS was homemade by the Chair of Experimental Physics V at Ruhr University Bochum and consists of 11 resistors of 2.2 Ω resistance placed in parallel in the outer grounded shielding of the coaxial power cable. The total resistance of the BCS was measured to $R_{shunt} = 0.21\,\Omega$. The BCS was mounted in the middle of the 20 m

power cable. The voltage applied to the power cable U is proportional to the current I running through the power cable via the impedance of the cable ($Z = 50\,\Omega$) via Ohm's law: $U = Z \cdot I$. The voltage pulse travels through the cable and is reflected at the electrode as can be seen in figure 7.6 (a). The first voltage pulse i is delivered from the generator and travels to the plasma. Triggering of the oscilloscope was set on this voltage pulse so that it appears at 0 ns. After about 100 ns, a second voltage pulse ii appears that is reflected by the electrode. Further pulses travel through the cable, as shown by pulses iii and iv, also appearing at multiples of 100 ns. Due to interference of the incident and the reflected pulses, these later pulses have distorted shapes. Attempts were made to improve the connection between the cable and the electrode but these reflected pulses could not be avoided. However, since their amplitude is significantly lower than the amplitude of the incident and reflected pulses, pulses iii and iv do not deliver a significant amount of energy into the system and can be neglected.

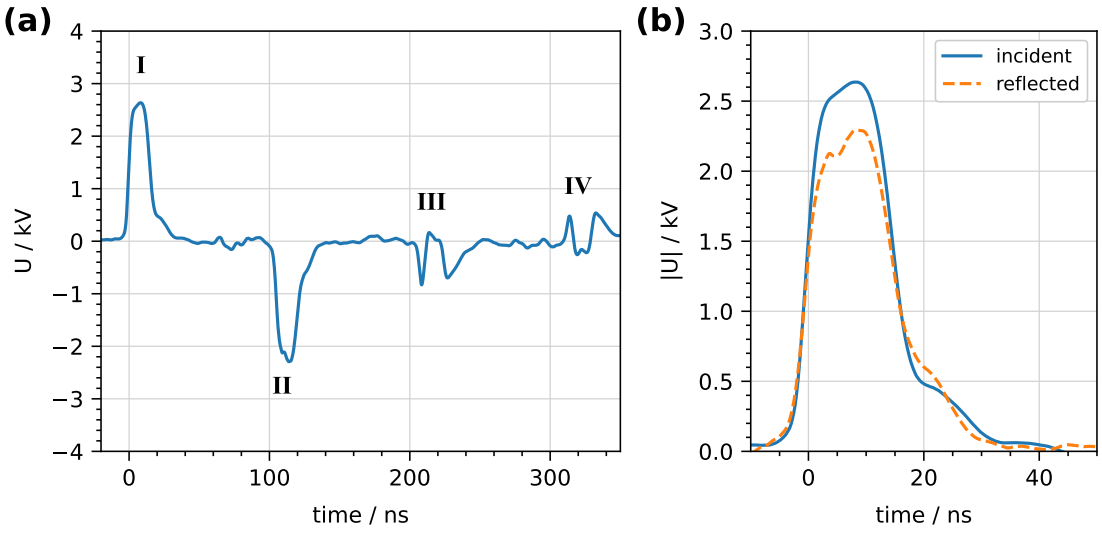

Figure 7.6: (a) Temporal development of the ns voltage pulse. Pulse i comes from the generator and travels to the plasma. Pulse ii is reflected after approx. 100 ns from the system. Further pulses travel through the cable, as shown by pulses iii and iv. These pulses are disturbed by incident and reflected pulses, resulting in distorted shapes. (b) Incident voltage pulse in comparison to shifted and inverted reflected pulse.

The comparison between the incident and reflected voltage pulses is shown in figure 7.6 (b) on the same time scale with absolute voltages of the reflected pulse. It can be observed that the reflected pulse is almost identical in shape but has a lower amplitude than the incident voltage pulse. This difference in amplitude of the incident and reflected pulse is the main idea of the BCS technique. Since the energy of the reflected pulse is lower, the energy difference between the incident and the reflected pulses can be used to determine the energy deposited in the plasma.

The applied voltage to the plasma $U(t)$ is a superposition of the incident U_{inc} and the reflected U_{refl} voltage pulses [252]: $U(t) = U_{inc}(t) + U_{refl}(t)$. To obtain the actual voltage, a calibration of the measured voltage at the oscilloscope U_{osci} has to be performed. A 20 dB attenuator was used at the input of the oscilloscope to avoid disturbances of the signal. The attenuation was experimentally calibrated using a 5 V rectangular voltage pulse, resulting in a correction factor $\gamma = 9.4102$. The actual BCS voltage is then given by $U_{BCS} = \gamma \cdot U_{osci}$. The voltage pulse applied to the electrode and the line current in the power cable are given by:

$$U = Z \cdot I = Z \cdot \frac{\gamma}{R_{shunt}} \cdot U_{osci} \quad , \quad I = \frac{\gamma}{R_{shunt}} \cdot U_{osci} \ . \tag{7.2}$$

To obtain the discharge current from the line current in the power cable, further calculations have to be performed. The line current measured by the BCS is a superposition of the capacitive current of the system and the discharge current of the plasma. The measured line current can be calculated by the voltage difference of the incident and the reflected voltage pulses: $I = I_{discharge} + I_{capacity} = (U_{inc} - U_{refl})/Z$. The capacitive current is given by the difference between the incident and the reflected voltage pulses in the case of no plasma (no He gas flow at low voltage pulses): $I_{capacity} = (U_{inc,off} - U_{refl,off})/Z$. Combining the two equations, the discharge current can be calculated as

$$I_{discharge} = \frac{U_{refl,off} - U_{refl}}{Z} \tag{7.3}$$

under the assumption of the same incident voltage pulse. This was ensured during the measurements by first measuring the signal with the plasma switched off (no gas flow) and then switching on the gas flow and carrying out the measurement with the voltage unchanged. Finally, the dissipated plasma power in the plasma can be calculated via

$$P = U \cdot I = \frac{U^2}{Z} = \frac{U_{osci}^2 \cdot \gamma^2}{R_{shunt}} \tag{7.4}$$

Integration over time of the power provides the energy delivered to the system. This equation is independent of the current as it can be directly calculated from the measured voltage. However, knowledge about the current profile and absolute values is important for comparison of the different operation modes.

To obtain the mean power dissipated in the plasma, the energy of the incident pulse and the reflected pulse have to be calculated. The energy difference between the two results is the energy that is dissipated in the plasma. By multiplying this energy difference ΔE with the repetition frequency f, the mean dissipated plasma power can be obtained:

$$\bar{P} = f \cdot \Delta E = f \cdot \left(\int P_{inc}\, dt - \int P_{refl}\, dt \right) . \tag{7.5}$$

Some of the power is also deposited into the system and not only into the discharge. This was visible as the measured power had an offset when no gas was applied and the power increased linearly with applied voltage. Therefore, the power measurements were also corrected for this offset as shown in the appendix A.9. For the power measurements under ns operation, a relative uncertainty of 20 % was assumed. The fluctuations of the power measurements during the treatment were about 10 %, however, to account for possible uncertainties due to the system (resistance of the resistors, calibration of the attenuation) a higher uncertainty was assumed.

Waveforms and plasma powers

To compare the different excitation mechanisms, extensive power measurements were performed and the results are discussed in the following. First, examples of the applied waveforms under the three operation modes are shown in figure 7.7.

In the µs operation, the voltage reaches peak-to-peak amplitudes of up to 7 kV and three high voltage peaks over time characterise the voltage pulse (see figure 7.7 a) with some smaller oscillations before and after. The trigger signal for the µs operation was set at 0 µs (not shown in the figure). The applied voltage pulse starts about 25 µs after the trigger signal and disappears at 100 µs. The current reaches amplitudes of up to 4 mA and the current waveform consists of two components: the displacement current due to the applied voltage and spikes on the current waveform due to the filamentary character of the plasma in this operation mode. This is a known behaviour for dielectric barrier discharges operating at µs and kHz repetition frequencies [243, 244, 254]. The displacement current follows the derivative of the voltage: With decreasing or increasing voltage, the current is negative or positive, respectively. The spikes correspond to microdischarges (streamers) during the voltage pulse. These are most prominent closely after the maximum and minimum of the voltage.

For RF operation, a sinusoidal voltage was applied at a frequency of 13.56 MHz with one excitation cycle of 74 ns (see figure 7.7 b). The peak-to-peak voltages do not exceed 2 kV and the current is in the order of several mA. Peaks on the current waveform are not visible as was the case under µs operation. The excitation within RF discharges is known to be highly modulated in time and spatially separated between the electrodes as described in detail in chapter 2 and was shown by PROES measurements in chapter 4. In comparison to the µs operation, small microdischarges are not present in RF operation.

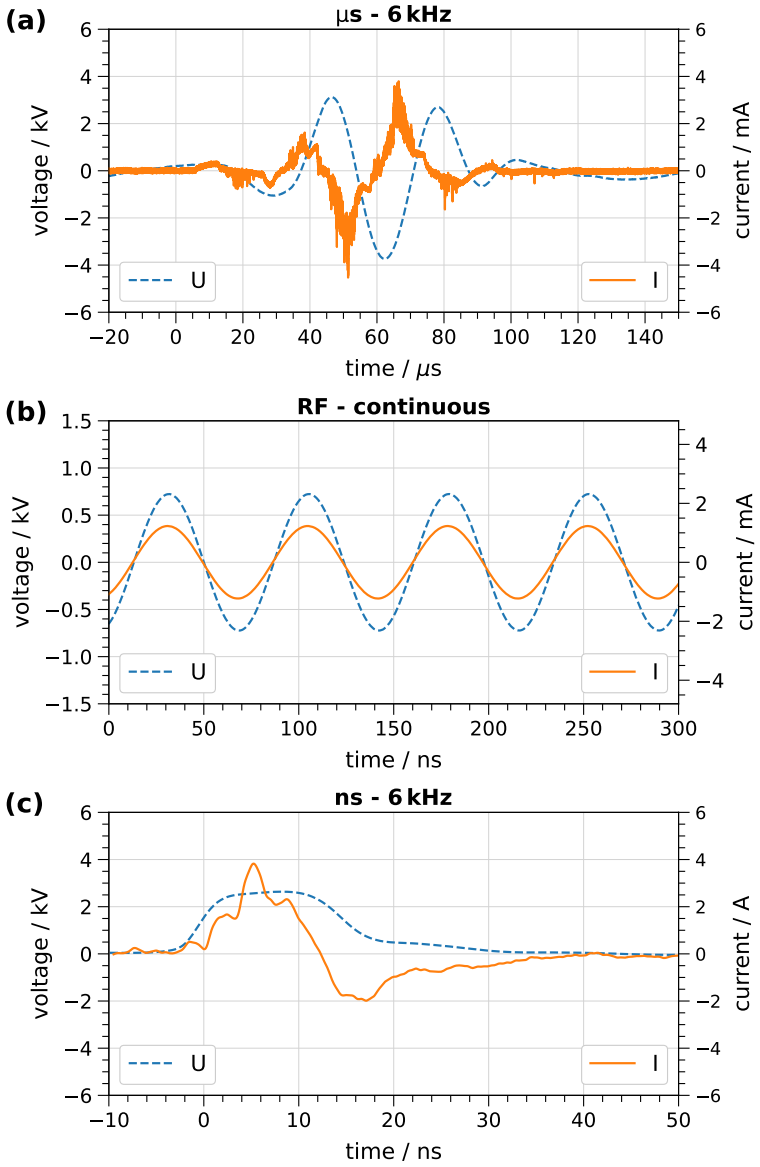

Figure 7.7: Examples of voltage and current waveforms for **(a)** µs operation, **(b)** RF operation and **(c)** ns operation.

The voltage and current curves of the ns operation are shown in figure 7.7 (c). There, the voltage curve is characterised by a fast increase up to several kV amplitudes with rise times of a few ns and the voltage pulse has a width of about 20 ns. In contrast to the µs and RF operations, where currents of mA are achieved, the current in ns operation reaches values of a few A and is predominantly driven by the displacement current of the applied voltage. When the voltage increases, the current shows positive values and with decreasing voltage, the current is negative. Between two pulses, the voltage and the current are zero. Thus, the ns operation is characterised by very short pulses of only 20 ns and a long transition time in between (hundreds of milliseconds).

From the power measurements, the performance of the plasma jet under the three operations can be obtained. The power curves are analysed as dissipated plasma power as a function of applied voltage. The power curves under µs operation are shown in figure 7.8 (a) for various humidity admixtures. The plasma ignition occurs at around 4 kV and with increasing voltage, the dissipated plasma power increases non-linearly. This behaviour was also observed for other DBD-like plasma devices excited with µs pulses [243, 244]. The influence of humidity admixture is minor, as the power curves show the same behaviour for the humidity admixtures investigated, considering the uncertainty of 30 % of the power measurements under µs operation. Plasma powers of up to 2 W at 9 kV voltage can be achieved under µs excitation. Higher voltages could not be applied, since arcing from the powered electrode to the grounded housing occurred in the setup used at higher voltages than 9 kV. Further improvements to the plasma jet design are necessary to enhance the dissipated plasma power even further.

The power curves of the RF operation are shown in figure 7.8 (b). These curves are similar to the ones presented in chapter 4 in figure 4.1. Thus, the different geometry used for the investigations of the different operations does not change the characteristics of the RF plasma. In comparison to the µs operation, the plasma power exceeds 2 W in RF operation and reaches values of up to 10 W at voltages of 1.25 kV and 1.5 kV for humidity admixtures of 0 ppm and 6400 ppm, respectively. The plasma ignites between voltages of 0.4 kV and 0.55 kV depending on the humidity admixture. The dissipated plasma power increases with voltage in two linear regimes. These regimes can be attributed to the Ω- and Penning mode present in RF plasmas at atmospheric pressure as discussed in chapter 2.

In the case of ns operation, the plasma ignites at about 4 kV, which is the same breakdown voltage as under µs operation, and the plasma power shows a steep increase with increasing voltage (see figure 7.8 c). Powers of 1.2 W and 1.5 W at voltages of 5.2 kV can be achieved at humidity admixtures of 0 ppm and 6400 ppm, respectively. This is in contrast to the RF operation, where higher voltages in the case of humidity admixture were required to maintain the same plasma power. This shows a different energy coupling of the µs and ns operation when reactive admixtures are added to the He feed gas, compared to the RF excitation. The RF operation is more sensitive to the addition of reactive species, while the other two are almost comparable if no or additional humidity admixtures are used.

All in all, the three operation modes are different in their performance as the power curves vary for each operation mode. However, comparable plasma powers can be achieved up to 1.5 W. In this regime, the different operation modes can be compared in the sense of their H_2O_2 production. This is discussed in the following.

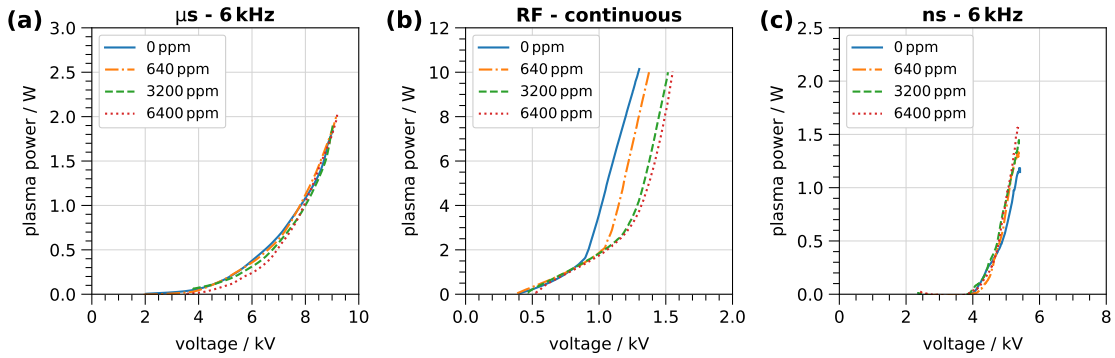

Figure 7.8: Dissipated plasma power as a function of applied voltage (called power curve) for **(a)** µs operation, **(b)** RF operation and **(c)** ns operation. Power curves are shown at various humidity concentrations to the 2 slm He feed gas for all operation modes. Please note the different scales of the x- and y-axes.

H_2O_2 concentration

At first, the H_2O_2 concentration in the liquid was measured for various humidity admixtures for the three operation modes at 0.5 W and 1 W plasma power. The results of the 0.5 W case were similar to the 1 W, therefore only the 1 W case is shown in figure 7.9 (a). For all operation modes, the same trend can be observed. The H_2O_2 concentration increases with increasing humidity admixture. This trend is equal to the behaviour discussed for the H_2O_2 density in the gas phase in chapter 4 and the liquid measurements of the PTL in chapter 5 of the RF plasma jet. Thus, the same discussions are applicable for the µs and the ns operation. The general chemical processes of production and consumption of H_2O_2 in a humidified He plasma are independent of the operation mode: With increasing humidity, more H_2O molecules can be dissociated and more OH is produced followed by enhanced production of H_2O_2. The increase levels off at the highest humidity concentration as the consumption of H_2O_2 by OH also increases and the production and consumption balance.

In contrast, the H_2O_2 concentration differs in value between the operation modes as the RF and ns operation modes provide higher H_2O_2 concentrations than the µs operation. Considering the uncertainties of the measurements, the ns and RF operation provide the same H_2O_2 production. However, the concentrations measured for the µs operation are a factor of two lower than for the ns operation. This might indicate that the faster excitation of the RF and ns operation provides higher H_2O_2 concentrations. However, the humidity variation was only performed at two plasma powers. To compare the trends in absolute H_2O_2 concentrations between the operation modes more precisely, the H_2O_2 concentration was measured for different plasma powers in the range from 0.5 W to 1.5 W at a constant humidity of 6400 ppm.

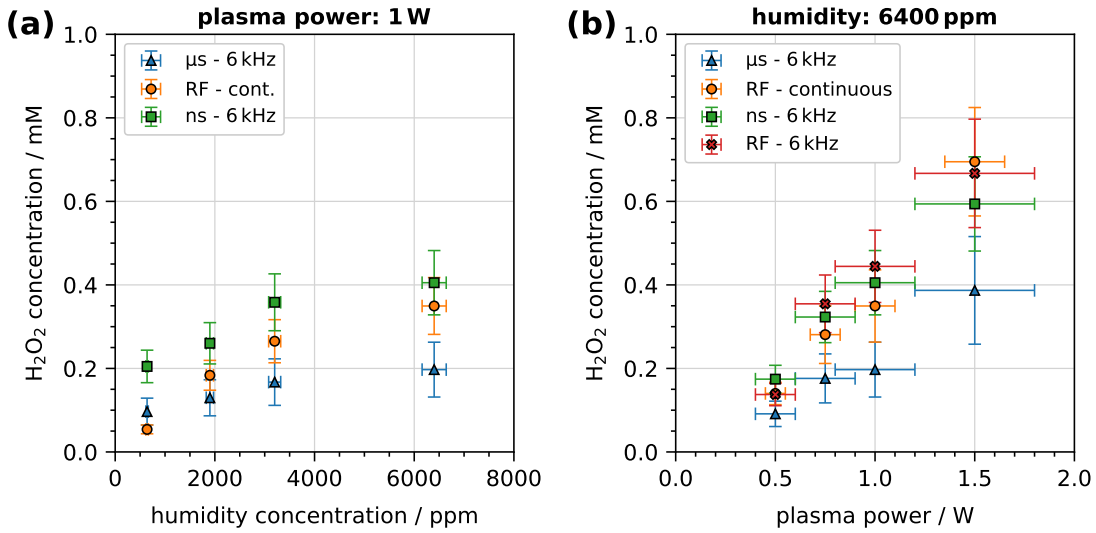

Figure 7.9: H_2O_2 concentration for the three operation modes (RF was driven in continuous and modulated case) as a function of **(a)** humidity admixture at 1 W plasma power and **(b)** dissipated plasma power at 6400 ppm humidity.

This investigation is shown in figure 7.9 (b). Since the three operation modes should be directly compared regarding their H_2O_2 production, the measurements of the RF operation were extended by the pulse modulation of the RF operation with 6 kHz to avoid accumulation effects of H_2O_2 in the liquid. For all operation modes, a linear increase of the H_2O_2 concentration with plasma power can be observed, which is again in agreement with results presented in chapter 4 and 5. Furthermore, the RF and ns operation modes show the same H_2O_2 concentration considering the measurement uncertainties. There, the pulse modulated RF operation shows again the same H_2O_2 concentrations as the unmodulated case similar to the results shown and discussed in chapter 4 and 5. Also in this investigation, the concentrations obtained in µs operation are about 40 to 50 % less compared to RF and ns operation.

To discuss the different H_2O_2 production of the operation modes, the time scales of the electric field driven by the applied voltage and the plasma processes must be discussed. In the ns operation, the fast voltage pulse leads to a fast increase in the electron density and the dissociation of H_2O molecules to produce OH. This dissociation process has a timescale in the range of ns so that the ns operation is sufficient to trigger this process [255]. The slower process of recombination to produce H_2O_2 occurs on the µs to ms range [255]. Since the pulsing is performed with 6 kHz, the time between pulses is 0.17 ms and the recombination processes can be performed between the plasma pulses. Furthermore, as the residence time of the gas in the discharge channel is 2.4 ms, the species within the discharge channel are exposed to several plasma pulses. The same behaviour applies to RF operation in pulse modulation as was discussed in chapter 4. However, in the continuous case

of the RF operation, there is no temporal separation between the production of OH by electron impact dissociation of H_2O and the recombination of OH to form H_2O_2. Thus, the processes are in equilibrium but produce comparable concentrations compared to the RF pulsing mode. The µs operation has the slowest rise time of the voltage and the electric field. In this case, the voltage pulse increases in the order of a few tens of µs. The production of electrons also follows this time period and thus also the production of OH. Consequently, the recombination of OH is delayed and the overall process is slower, which can hinder the production of H_2O_2. In addition, the electric field strength differs as the µs operation requires the highest electric field to operate at 1 W. This high electric field can accelerate the electrons to higher energies leading to destruction mechanisms of H_2O_2 and lowering its production.

Furthermore, the electron density and electron temperature vary between the different operation modes. Both parameters are mainly determined by the reduced electric field. Thus, the change in the electric field due to different excitation processes can also affect the electron density and the temperature. The electron densities for other APPJs were found to be in the order of $10^{11}\,\mathrm{cm}^{-3}$ for µs operation with kHz repetition frequencies [256, 257]. For RF operation, orders of $10^{11} - 10^{12}\,\mathrm{cm}^{-3}$ were found for the electron density [80, 119, 258] and $10^{13} - 10^{14}\,\mathrm{cm}^{-3}$ was found for ns operation [259–262]. The higher electron densities lead to a higher electron impact dissociation of H_2O to produce OH and an intensified production of H_2O_2. However, it has to be further investigated whether these higher electron densities with RF and ns operation compared to µs operation are also present in the plasma jet configuration investigated.

The electron temperature also varies between the different operation modes since the optical emission spectra of the operation modes are quite different. The lines visible in the spectra are an indicator of the electron energy and with this the electron temperature. The optical emission spectra of the three operation modes are shown in figure 7.10. In all spectra, the main lines present in a He+H_2O plasma are present as discussed in chapter 4. The excitation of the RF operation is dominated by the band emission of OH while the emission of the high energetic He line at 706 nm is more pronounced in the µs and ns operation. This might indicate that the mean electron energy is higher in the case of the µs and ns operation than in the RF operation due to the higher applied voltages.

However, finding appropriate literature values of the electron temperature is quite difficult. It was reported that the COST reference plasma jet, comparable to the one used in this work, exhibits electron temperatures below 3 eV [56, 57]. In contrast, ns pulsed plasma jets can have an increased electron temperature of up to 5 eV [260]. Measurement of the electron temperature of the plasma jet investigated in

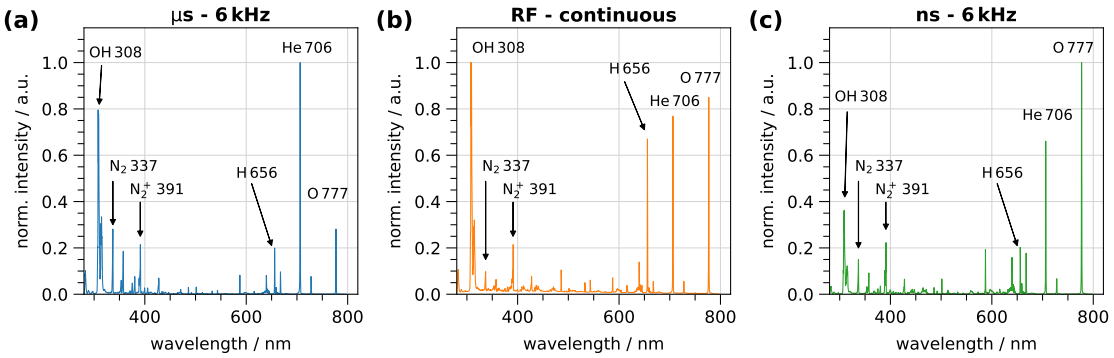

Figure 7.10: OES spectra of the plasma emission of the three operation modes at plasma powers between 0.6 W - 1 W and a humidity admixture of 6400 ppm. **(a)** µs operation, **(b)** RF operation and **(c)** ns operation.

this work under all three operation modes might be an interesting investigation for further research.

For application purposes, the energy yield of H_2O_2 production is of interest, which results from the amount of H_2O_2 produced in relation to the energy used. This was calculated by equation 5.1 as described in chapter 5 and the results are shown in figure 7.11 for the three operation modes. The µs operation shows a constant H_2O_2 yield of about 100 µg kWh^{-1}, while the yield of the RF operation in continuous and modulated cases increases from 100 µg kWh^{-1} to 200 µg kWh^{-1}. The ns operation has a constant H_2O_2 yield of about 150 µg kWh^{-1} for plasma powers higher than 0.5 W and at 0.5 W, the H_2O_2 yield is about 100 µg kWh^{-1} for the ns operation. The increasing trend of the H_2O_2 yield under RF operation might be due to the mode change from Ω-mode to the Penning mode of the RF plasma that occurs between plasma powers of 0.5 W and 1 W as shown and described in chapter 4. In Penning mode, ionisation by metastable becomes more efficient which can also affect the dissociation of H_2O leading to an enhanced production of H_2O_2 and a higher energy efficiency. Whether such mode changes also occur under µs or ns operation has to be further investigated.

Furthermore, when discussing economic efficiency, it is not only the plasma power that is important but also the generator power consumption from the power grid. The consumed generator power was measured using a homemade power meter between the generator and the power plug of the grid. It measures the voltage and current, and the power is calculated by multiplying the two $P = U \cdot I$. The consumed generator power as a function of the plasma power for the three operation modes is shown in figure 7.12 (a). The homemade µs generator consumes the least power from the grid, only 19 W at 1.75 W plasma power. In contrast, the RF generator consumes 60 W and 42 W at 1.5 W plasma power in continuous and pulsed mode,

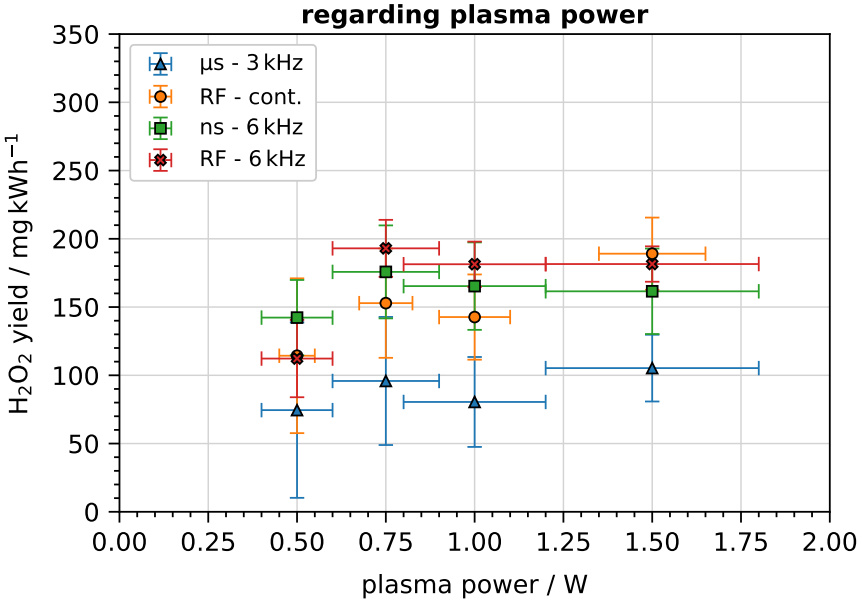

Figure 7.11: H_2O_2 yield calculated from the plasma power for all operation modes. The plasma was operated at 6400 ppm humidity.

respectively. The ns generator consumed the most power with 70 W at 1.5 W plasma power. In addition, the power consumption also varies greatly when the generator is switched on and the plasma is switched off (standby). In standby, the µs generator consumes the least of only 13 W, the RF generator takes 17 W from the grid and the ns generator 38 W. The RF and ns generators were built by companies with additional components like displays and cooling systems. The design of the homemade µs generator is simpler as it consists of only a coil to transform a low applied voltage pulse to a high voltage pulse. Thus, possible differences in the consumed generator power might originate from the design and construction of the generators. Due to the lower consumed generator power of the µs generator, its efficiency of the H_2O_2 production regarding the consumed generator power is enhanced compared to the other generators.

The H_2O_2 yield regarding the consumed generator power of the various operation modes is shown in figure 7.12 (b). There, the trends differ from the ones described regarding the plasma power. The lowest H_2O_2 yield is attributed to the continuous RF operation and the ns operation with a maximum yield of about 4 µg kWh^{-1}. The modulated RF operation reaches 6 µg kWh^{-1} and the µs operation gained the highest yield of 8 µg kWh^{-1} and is thus a factor of two higher than RF or ns operation. For all operation modes, a linear increase in the H_2O_2 yield regarding the consumed generator power with plasma power can be observed. This is because the H_2O_2 concentration increases linearly with plasma power (discussed above) but the consumed plasma power only increases by a few percent when the plasma power

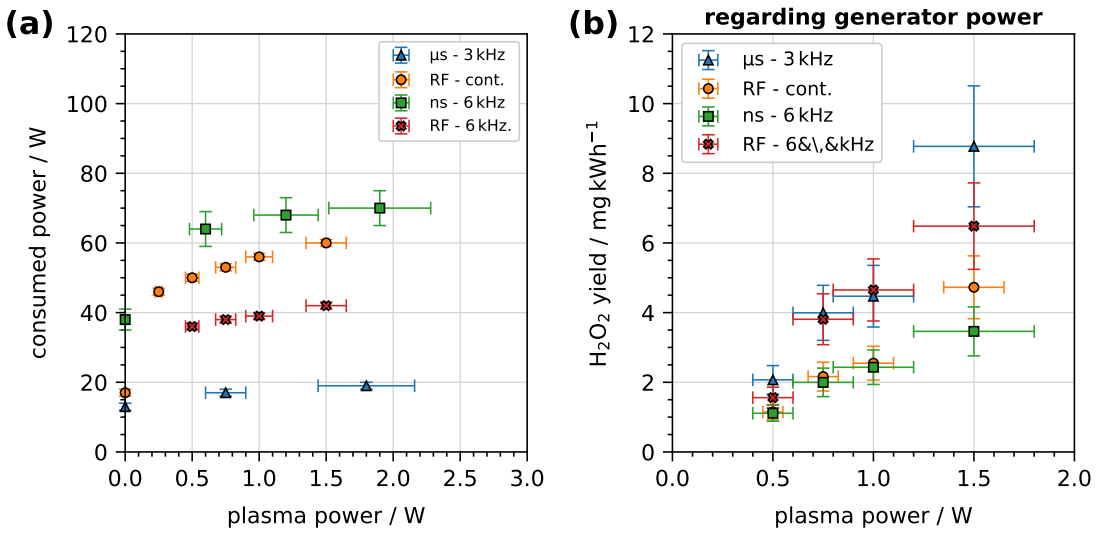

Figure 7.12: **(a)** Consumed generator power for the three operation modes (RF was driven in continuous and modulated mode). At 0 W plasma power, consumed generator power of generator switched on but plasma off was measured. **(b)** H_2O_2 yield regarding the consumed generator power as a function of plasma power. The plasma was operated at 6400 ppm humidity.

increases. Thus, the H_2O_2 concentration determines the evolution of the H_2O_2 yield regarding the consumed generator power and it also increases linearly. Overall, this investigation shows that the choice of the generator is important when discussing the most economically efficient ways to generate reactive species with plasmas. If lower concentrations are applicable, the µs generator might be a good choice as it H_2O_2 yield per kWh from the grid is the highest. Or the generators used for RF and ns excitation should be better matched to the plasma source to reduce the power consumption from the grid.

Frequency variation

Finally, the repetition frequency is an important control parameter as it determines the time between two plasma pulses and with this the time scales of the processes occurring in the plasma. A lower frequency leads to longer plasma-off times while higher frequencies provide more plasma pulses and by this more time for electron-driven processes such as dissociation.

To investigate the impact of the repetition frequency on the systems, the frequency was varied at constant plasma powers in the range of 3 - 6 kHz. These frequencies result in times between pulses of 0.33 ms to 0.17 ms. The H_2O_2 concentration as a function of repetition frequency is shown in figure 7.13. The RF operation was only driven under pulse modulation in this experiment. The same behaviour for all three operation modes can be observed as the H_2O_2 concentration remains the

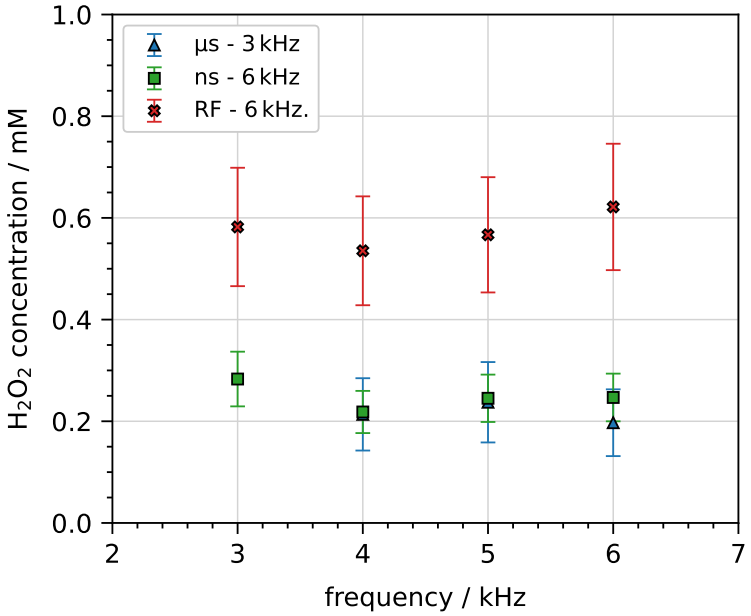

Figure 7.13: H_2O_2 concentration for various repetition frequencies for all operation modes. RF was operated under pulse modulation. All plasmas were operated at a humidity admixture of 6400 ppm. The µs and RF operations were operated at 1 W plasma power and the ns operation was operated at 0.5 W plasma power, which was the maximum achievable plasma power of the ns operation at 3 kHz repetition frequency.

same for the frequencies investigated. This indicates that in the frequency range investigated, the slow recombination process to produce H_2O_2 is fully established. Since it occurs in time scales of µs to ms [255], this behaviour is reasonable. Even higher frequencies could be more beneficial and interesting for analysis as it further reduces the time between the plasma pulses, but the generators were not capable of operating at higher frequencies than 6 kHz.

7.3 Summary tuning plasma chemistry

The following statements can be derived from the investigations made in this chapter:

- The capillary plasma jet operated in a gas mixture of He+H_2O+N_2+O_2 produces a variety of species and concentrations of H_2O_2, NH_3 and NO_2^- can be detected in the PTL.
- H_2O_2 is always presented when H_2O is added, while NH_3^- and NO_2^- are produced in the case of H_2O+N_2 mixtures. NO_2^- is also produced when N_2+O_2 are combined and added to the gas flow without humidity admixture.
- Taking into account the main production mechanisms of the species given in the literature, the experimentally obtained trends can be adequately described.
- Pulse modulation of the RF signal is a powerful tool to control the chemistry and to manipulate the main outcome of the He+H_2O+N_2+O_2 chemistry. At 10 % duty cycle, the production shifts from NO-dominated species to OH-dominated species.
- The capillary plasma can be successfully operated with high-voltage pulses with rise times in the order of µs and ns. There, the H_2O_2 production and energy yield were similar for the ns operation and the RF case (pulse modulated and unmodulated), while the µs operation showed the lowest production rate.
- Regarding the consumed generator power, the µs generator was the most efficient one leading to the highest energy yield of it regarding the consumed generator power from the grid.

8. Conclusion and outlook

In this thesis, an atmospheric pressure plasma jet treating a liquid sample was investigated to understand and optimise the H_2O_2 production and delivery into a liquid sample. A capillary plasma jet was used, acting as a further development of the COST reference plasma jet. It was mainly operated under RF excitation and in humidified He. Several diagnostics were applied in both, the gas and liquid phases.

The plasma performance was analysed by power measurements extended by electrical modelling to obtain information on the electron density and sheath thickness. Gas temperature measurements were performed by thermocouple measurements and optical emission spectroscopy (OES) and phase-resolved optical emission spectroscopy (PROES) was applied to investigate the electron dynamics in the humidified plasma. The densities of gas phase species were measured by laser-induced fluorescence (LIF) for OH, fourier-transform infrared (FTIR) spectroscopy for H_2O_2 and mass spectrometry for H_2O, H_2O_2, HO_2, H_2 and O_2. In the liquid phase, the concentration of H_2O_2 was analysed by a spectrophotometric approach and electrochemical sensing while the OH concentration was measured by the terephthalic acid (TA) dosimeter. The distribution of OH was visualised by the chemiluminescence (CL) of luminol and the distribution of H_2O_2 by UV absorption spectroscopy. In addition, particle imaging velocimetry (PIV) was performed for visualising the convective transport in the plasma-treated liquid (PTL). Furthermore, the influence of low-frequency pulsing of the RF signal on the species production was investigated.

First, the plasma performance of the humidified capillary plasma jet was investigated. It is operable at high humidity admixtures (several thousands of ppm) and high plasma powers (up to 10 W), enabling a broad application range. The electron density was determined by evaluation of an electrical equivalent circuit model with data of voltage and current measurements. The electron density was found to be in the range of $10^{11}\,\mathrm{cm}^{-3}$ to $10^{12}\,\mathrm{cm}^{-3}$, depending on the plasma power and humidity admixture. The gas temperature reaches values up to 250 °C within the discharge and 150 °C in the effluent. The PROES analysis provided insights into the excitation of the various species within the plasma. There, the same behaviour of the capillary plasma jet was observed compared to the COST reference plasma jet. The transition from Ω-mode to Penning mode is indicated by the emission of the He 706 nm line. This change occurs in pure helium plasma and when humidity is added. When humidity is introduced, the transition occurs at higher voltages. The emission from reactive species follows the emission of the He line indicating

the excitation from high-energetic electrons, predominantly in the sheath regions at high plasma powers. However, some emission of reactive species in the bulk remains at high powers, indicating the excitation of reactive species from lower energetic electrons in the bulk. Analysis of the LIF signal revealed insights into the air entrainment into the effluent, which is about 20 % at a distance of 14 mm from the capillary end. Furthermore, the consumption of H_2O was found in the LIF model and mass spectrometer experiments leading to the production of reactive species. The further findings arise from answering the research question.

Research question 1: Can H_2O_2 be generated by the capillary plasma jet? What are the main production and consumption mechanisms of H_2O_2 and what other species are involved in the plasma chemistry? How do plasma parameters such as gas composition and plasma power influence the plasma chemistry?

H_2O_2 could be generated by the capillary plasma jet when operating in humidified He and densities of up to $2 \times 10^{14}\,\mathrm{cm}^{-3}$ could be measured in the effluent of the capillary plasma jet. The main production mechanism of H_2O_2 is by the recombination of OH radicals: $\mathrm{OH} + \mathrm{OH} + \mathrm{M} \longrightarrow \mathrm{H_2O_2} + \mathrm{M}$. OH densities in the order of $10^{13}\,\mathrm{cm}^{-3}$ were found in the effluent. Since OH is also involved in the consumption of H_2O_2 an equilibrium between the production and consumption of H_2O_2 establishes. Further species involved in the plasma chemistry of the He+H_2O are HO_2, H_2 and O_2. The HO_2 density was found to be in the order of $10^{14}\,\mathrm{cm}^{-3}$ and H_2 as well as O_2 densities of up to $8 \times 10^{15}\,\mathrm{cm}^{-3}$ were present in the effluent of the capillary plasma jet. The humidity admixture to the He gas flow and the dissipated plasma power control the production of these species as the densities increase with humidity admixture and plasma power (up to 6 W). Model results fit well to the measured densities in the effluent and the spatial evolution of the species in the discharge and the effluent was visualised by the model. Differences in the evolution of reactive and more stable species are evident as the densities of reactive species exponentially decay in the effluent while the densities of long-lived species like H_2O_2 stay constant on the first 24 mm in the effluent.

Research question 2: How is the transfer of gaseous OH and H_2O_2 to the liquid achieved? What are the physical and chemical processes and how is the species transport conducted within the liquid?

H_2O_2 is measurable in the treated liquid with concentrations up to a few millimolars, while OH shows lower concentrations in the range of a few tens of micromolars. A maximum H_2O_2 concentration of (0.93 ± 0.15) mM at 6400 ppm humidity and 6 W plasma power in 3 mL liquid after 5 min treatment was found. This corresponds to a production rate of $(0.56 \pm 0.09)\,\mu\mathrm{mol\,min}^{-1}$ ($(1.14 \pm 0.19)\,\mathrm{mg\,h}^{-1}$) with an energy yield of $(0.19 \pm 0.04)\,\mathrm{g\,kWh}^{-1}$. OH does barely reach the liquid bulk and is mainly

located at the liquid surface. The OH concentration in the liquid, determined from the corrected HTA concentration, was two orders of magnitudes lower than the H_2O_2 concentration and reached concentrations lower than 0.03 mM. By varying the treatment parameters gas flow rate and distance between plasma and liquid, the concentrations can be enhanced by higher gas flow rates and the selectivity towards H_2O_2 can be improved by larger treatment distances. However, higher gas flow rates come into play with strong disturbances at the liquid surface that might negatively influence the application purpose and increasing the treatment distances lowers the concentrations of the species in the liquid. At low gas flow rates, the diffusion of H_2O_2 was visible and an effective diffusion coefficient could be estimated. The measured H_2O_2 profiles in the liquid agree well with model calculations of the convection-diffusion equation. The liquid concentrations of OH and H_2O_2 match their gaseous densities qualitatively in their trends and quantitatively in their values. This is consistent with Henry's law, which describes the solubility of gaseous species in liquids.

Research question 3: How can pulse modulation of the RF signal be utilised to tune the plasma chemistry? How is pulse modulation affecting the generation of short-lived species like OH and of long-lived species like H_2O_2?

Pulse modulation of the RF voltage is a powerful tool for influencing the species densities and tuning the plasma chemistry. It can accumulate long-lived secondary species while suppressing the formation of short-lived primary species. This is valid in the gas phase as well as in the liquid phase. In the liquid phase, higher energy efficiencies of the H_2O_2 production were found for the pulse modulation of the RF signal, although the concentrations were slightly lower. However, the lower power consumption during pulse modulation leads to a higher energy yield of the production.

Research question 4: How can an increased plasma volume be used for scaling up the H_2O_2 generation? In addition, does the plasma chemistry of H_2O_2 generation and the transfer of the gaseous species into the liquid change when Ar is used as an alternative to He as feed gas?

At the same gas velocities of the gas in the capillary plasma jet with the different plasma volumes, the same H_2O_2 production was found as the concentrations measured in the PTL and the densities in the gas phase were similar. A wider capillary can be used to increase the effluent and liquid surface interaction, but the H_2O_2 production cannot be increased by a larger volume. The operation with Ar as feed gas with admixtures of H_2O has proven to be difficult. The Ar plasma with high humidity concentrations could only be operated at high plasma powers of more than 10 W coming into play with very high gas temperatures that might not be useable

in applications. Furthermore, the H_2O_2 production of the capillary plasma jet operated with Ar and 640 ppm humidity was found to be a factor of two lower compared to the He plasma at similar conditions. Thus, the use of Ar is less efficient for the H_2O_2 production of the capillary plasma jet.

Research question 5: How is nitrogen fixation in the capillary plasma jet achieved when operating in gas mixtures of He+H_2O+N_2+O_2? And what is the efficiency of H_2O_2 generation when the capillary plasma jet is operated with µs or ns pulses instead of RF operation?

The capillary plasma jet operated in a gas mixture of He+H_2O+N_2+O_2 produces a variety of species and concentrations of H_2O_2, NH_3 and NO_2^- can be detected in the PTL. H_2O_2 is always present when H_2O is added, while NH_3^- and NO_2^- are produced in the case of H_2O+N_2 mixtures. NO_2^- is also produced when N_2+O_2 are combined and added to the gas flow without humidity admixture. Also when the plasma is operated in He+H_2O+N_2+O_2 gas mixtures, pulse modulation of the RF signal is a powerful tool to tune the chemistry with the production shifting from NO-dominated species to OH-dominated species. The capillary plasma can be successfully operated with high-voltage pulses with rise times in the order of µs or ns. There, the H_2O_2 production and energy yield were similar for the ns operation compared to the RF case (pulse modulated and unmodulated), while the µs operation showed the lowest production rate. Regarding the consumed generator power, the µs generator was the most efficient one leading to the highest energy yield of H_2O_2 production regarding the consumed generator power from the grid.

8.1 Outlook

The findings within this thesis have shown that the capillary plasma jet is an appropriate H_2O_2 source for supporting biocatalysis. However, all investigations were performed in a small liquid volume of only 3 mL in a standard UV cuvette. Upscaling of this system is difficult as the plasma dimensions under atmospheric pressure are limited. Widening of the plasma volume is a possible option as shown in this dissertation but is also limited. A liquid flow system might be a good option, where the liquid is flowing through a vessel in which the plasma treatment is performed. A first proof-of-principle has been conducted showing that also in the liquid flow system, H_2O_2 is delivered into the liquid and can be measured after the plasma treatment (not shown here). Further developments in this direction have to be carried out to optimise it.

As discussed in chapter 6, the use of He is not a sustainable option. To use humidified air as feed gas would be ideal and the capillary plasma jet operating

with ns pulses can be operated with N_2 or air as feed gas. However, as shown in chapter 7, in addition to H_2O_2, species containing N are also produced when a gas combination of N_2 and H_2O is used. These can be harmful to the enzymes, destroying them and lowering the efficiency of the biocatalysis. Gas recycling of the He can be an option to overcome the problems. However, this requires complex technical improvements and is not suitable for scientific environments but can be for industrial applications.

In addition to biocatalysis involving H_2O_2 consuming enzymes, various enzymes also consume different species, such as NO. Atmospheric pressure plasmas can produce a variety of species under different gas compositions. For example, the production of NO occurs in gas compositions of N_2 and O_2 or noble gases with the admixture of synthetic air [49, 51, 263]. NO is highly reactive. Thus, the transport of NO to the liquid surface and into the liquid bulk is more difficult than for example of H_2O_2. This hinders the performance of the plasma-driven biocatalysis utilising the NO produced by the capillary plasma jet. Experimental investigations have to be carried out to successfully perform the plasma-driven biocatalysis for NO consuming enzymatic reactions.

Investigations of the interaction of species at the liquid interface are crucial for plasma-liquid systems, especially when reactive species like NO are required in the liquid bulk. There is a lack of knowledge regarding the plasma-liquid interactions at the interface. There are a only few diagnostics that have been used to study the interface of plasma-liquid systems so far [40]. For example, laser absorption in a total internal reflection has been used to probe solvated electrons from plasma into a liquid [264] or the use of femtosecond two-photon absorption laser-induced fluorescence (fs-TALIF) of interface-near (above in the gas phase and below in the liquid phase) species was mentioned [265]. These interface diagnostics can be utilised to improve the understanding of plasma-liquid interaction and the delivery of species from atmospheric pressure plasmas into liquids.

8.2 Publication list

The following list provides an overview of the publications published or submitted to peer-reviewed journals during this thesis:

Published

- Steffen Schüttler, Niklas Eichstaedt and Judith Golda, "Tuning plasma chemistry by various excitation mechanisms for the H_2O_2 production of atmospheric pressure plasma jets", *J. Phys. D: Appl. Phys. 58 025203 (2025)*
- Steffen Schüttler, Jannis Kaufmann and Judith Golda, "Nitrogen fixation and H_2O_2 production by an atmospheric pressure plasma jet operated in He–H_{20}–N_2–O_2 gas mixture", *Plasma Process. Polym. 21:e2300233 (2024).*
- Steffen Schüttler, Anna Lena Schöne, Emanuel Jeß, Andrew R. Gibson and Judith Golda, "Production and transport of plasma-generated hydrogen peroxide from gas to liquid" *Phys. Chem. Chem. Phys. 26, 8255-8272 (2024).*
- Steffen Schüttler, Ludwig Jolmes, Emanuel Jeß, Kristina Tschulik and Judith Golda, "Validation of in situ diagnostics for the detection of OH and H_2O_2 in liquids treated by a humid atmospheric pressure plasma jet", *Plasma Process. Polym. 21:e2300079 (2024)*
- Tristan Winzer, David Steuer, Steffen Schüttler, Natascha Blosczyk, Jan Benedikt and Judith Golda, "RF-driven atmospheric-pressure capillary plasma jet in a He/O2 gas mixture: Multi-diagnostic approach to energy transport", *J. Appl. Phys. 132, 183301 (2022).*

Submitted and under review

- Hanna-Friederike Poggemann, Steffen Schüttler, Anna Lena Schöne, Emanuel Jeß, Lars Schücke, Timo Jacob, Andrew R. Gibson, Judith Golda and Christoph Jung, "Transportation behaviour of OH and H_2O_2 in plasma-treated water", Submitted to *Journal of Physics D: Applied Physics* on 22.10.2024.
- Steffen Schüttler, Maike Kai, Emanuel Jeß, Sebastian Burhenn, Laura Chauvet and Judith Golda "Control of the chemistry of a humidified He RF atmospheric pressure plasma jet by pulse modulation", Submitted to *Plasma Sources Science and Technology* on 25.10.2024.

Bibliography

[1] A. Bogaerts et al.: "Challenges in unconventional catalysis". *Catalysis Today* **420** (2023), 114180. DOI: 10.1016/j.cattod.2023.114180.

[2] A. Bogaerts et al.: "The 2020 plasma catalysis roadmap". *Journal of Physics D: Applied Physics* **53**.44 (2020), 443001. DOI: 10.1088/1361-6463/ab9048.

[3] A. Yayci et al.: "Plasma-Driven in Situ Production of Hydrogen Peroxide for Biocatalysis". *ChemSusChem* **13**.8 (2020), 2072–2079. DOI: 10.1002/cssc.201903438.

[4] H. L. Wapshott-Stehli et al.: "Plasma-driven biocatalysis: In situ hydrogen peroxide production with an atmospheric pressure plasma jet increases the performance of OleT $_{JE}$ when compared to adding the same molar amount of hydrogen peroxide in bolus". *Plasma Processes and Polymers* **19**.5 (2022), 2100160. DOI: 10.1002/ppap.202100160.

[5] R. A. Sheldon et al.: "Biocatalysis engineering: the big picture". *Chemical Society Reviews* **46**.10 (2017), 2678–2691. DOI: 10.1039/C6CS00854B.

[6] A. Yayci et al.: "Microscale Atmospheric Pressure Plasma Jet as a Source for Plasma-Driven Biocatalysis". *ChemCatChem* **12**.23 (2020), 5893–5897. DOI: 10.1002/cctc.202001225.

[7] Y. Wang et al.: "Peroxygenases en route to becoming dream catalysts. What are the opportunities and challenges?" *Current Opinion in Chemical Biology* **37** (2017), 1–9. DOI: 10.1016/j.cbpa.2016.10.007.

[8] A. T. Martínez et al.: "Oxidoreductases on their way to industrial biotransformations". *Biotechnology Advances* **35**.6 (2017), 815–831. DOI: 10.1016/j.biotechadv.2017.06.003.

[9] M. Hobisch et al.: "Recent developments in the use of peroxygenases – Exploring their high potential in selective oxyfunctionalisations". *Biotechnology Advances* **51** (2021), 107615. DOI: 10.1016/j.biotechadv.2020.107615.

[10] M. Poraj-Kobielska et al.: "Preparation of human drug metabolites using fungal peroxygenases". *Biochemical Pharmacology* **82**.7 (2011), 789–796. DOI: 10.1016/j.bcp.2011.06.020.

[11] X. Li et al.: "Conformation studies on Burkholderia cenocepacia lipase via resolution of racemic 1-phenylethanol in non-aqueous medium and its process optimization". *Process Biochemistry* **48**.12 (2013), 1905–1913. DOI: 10.1016/j.procbio.2013.09.001.

[12] A. Bozan et al.: "The production of enantiomerically pure 1-phenylethanol by enzymatic kinetic resolution method using response surface methodology". *Turkish Journal of Chemistry* **44**.5 (2020), 1352–1365. DOI: 10.3906/kim-1912-23.

[13] J. Golda et al.: "Concepts and characteristics of the 'COST Reference Microplasma Jet'". *Journal of Physics D: Applied Physics* **49**.8 (2016), 084003. DOI: 10.1088/0022-3727/49/8/084003.

[14] Collaborative Research Centre 1316: *Transient Atmospheric Plasmas - From Plasmas to Liquids to Solids*. Proposal for the Second Funding Period. Ruhr University Bochum, 2022.

[15] T. Winzer et al.: "RF-driven atmospheric-pressure capillary plasma jet in a He/O_2 gas mixture: Multi-diagnostic approach to energy transport". *Journal of Applied Physics* **132**.18 (2022), 183301. DOI: 10.1063/5.0110252.

[16] R. Ciriminna et al.: "Hydrogen Peroxide: A Key Chemical for Today's Sustainable Development". *ChemSusChem* **9**.24 (2016), 3374–3381. DOI: 10.1002/cssc.201600895.

[17] S. Yang et al.: "Toward the Decentralized Electrochemical Production of H_2O_2 : A Focus on the Catalysis". *ACS Catalysis* **8**.5 (2018), 4064–4081. DOI: 10.1021/acscatal.8b00217.

[18] H. Hou et al.: "Production of Hydrogen Peroxide by Photocatalytic Processes". *Angewandte Chemie International Edition* **59**.40 (2020), 17356–17376. DOI: 10.1002/anie.201911609.

[19] Y. Yi et al.: "A review on research progress in the direct synthesis of hydrogen peroxide from hydrogen and oxygen: noble-metal catalytic method, fuel-cell method and plasma method". *Catalysis Science & Technology* **6**.6 (2016), 1593–1610. DOI: 10.1039/C5CY01567G.

[20] J. M. Campos-Martin et al.: "Hydrogen Peroxide Synthesis: An Outlook beyond the Anthraquinone Process". *Angewandte Chemie International Edition* **45**.42 (2006), 6962–6984. DOI: 10.1002/anie.200503779.

[21] S. C. Perry et al.: "Future perspectives for the advancement of electrochemical hydrogen peroxide production". *Current Opinion in Electrochemistry* **30** (2021), 100792. DOI: 10.1016/j.coelec.2021.100792.

[22] A. T. Murray et al.: "Electrosynthesis of Hydrogen Peroxide by Phase-Transfer Catalysis". *Joule* **3**.12 (2019), 2942–2954. DOI: 10.1016/j.joule.2019.09.019.

[23] H. He et al.: "Review and perspectives on carbon-based electrocatalysts for the production of H_2O_2 via two-electron oxygen reduction". *Green Chemistry* **25**.23 (2023), 9501–9542. DOI: 10.1039/D3GC02856A.

[24] B. R. Locke et al.: "Review of the methods to form hydrogen peroxide in electrical discharge plasma with liquid water". *Plasma Sources Science and Technology* **20**.3 (2011), 034006. DOI: 10.1088/0963-0252/20/3/034006.

[25] J. Winter et al.: “Feed gas humidity: a vital parameter affecting a cold atmospheric-pressure plasma jet and plasma-treated human skin cells”. *Journal of Physics D: Applied Physics* **46**.29 (2013), 295401. DOI: 10.1088/0022-3727/46/29/295401.

[26] J. Winter et al.: “Tracking plasma generated H_2O_2 from gas into liquid phase and revealing its dominant impact on human skin cells”. *Journal of Physics D: Applied Physics* **47**.28 (2014), 285401. DOI: 10.1088/0022-3727/47/28/285401.

[27] C. A. Vasko et al.: “Hydrogen Peroxide Production in an Atmospheric Pressure RF Glow Discharge: Comparison of Models and Experiments”. *Plasma Chemistry and Plasma Processing* **34**.5 (2014), 1081–1099. DOI: 10.1007/s11090-014-9559-8.

[28] M. M. Hefny et al.: “Atmospheric plasma generates oxygen atoms as oxidizing species in aqueous solutions”. *Journal of Physics D: Applied Physics* **49**.40 (2016), 404002. DOI: 10.1088/0022-3727/49/40/404002.

[29] G. Willems et al.: “Absolutely calibrated mass spectrometry measurement of reactive and stable plasma chemistry products in the effluent of a He/H_2O atmospheric plasma”. *Journal of Physics D: Applied Physics* **50**.33 (2017), 335204. DOI: 10.1088/1361-6463/aa77ca.

[30] Z. Chen et al.: “Analysis of the production mechanism of H_2O_2 in water treated by helium DC plasma jets”. *Journal of Physics D: Applied Physics* **51**.32 (2018), 325201. DOI: 10.1088/1361-6463/aad0eb.

[31] Y. Gorbanev et al.: “Combining experimental and modelling approaches to study the sources of reactive species induced in water by the COST RF plasma jet”. *Physical Chemistry Chemical Physics* **20**.4 (2018), 2797–2808. DOI: 10.1039/C7CP07616A.

[32] B. Ghimire et al.: “Enhancement of hydrogen peroxide production from an atmospheric pressure argon plasma jet and implications to the antibacterial activity of plasma activated water”. *Plasma Sources Science and Technology* **30**.3 (2021), 035009. DOI: 10.1088/1361-6595/abe0c9.

[33] J. Jiang et al.: “Experimental and modeling studies of the plasma chemistry in a humid Ar radiofrequency atmospheric pressure plasma jet”. *Journal of Physics D: Applied Physics* **55**.22 (2022), 225206. DOI: 10.1088/1361-6463/ac570a.

[34] B. Harris et al.: “The spatial density distribution of H_2O_2 in the effluent of the COST-Jet and the kINPen-sci operated with a humidified helium feed gas”. *Plasma Sources Science and Technology* **32**.11 (2023), 115010. DOI: 10.1088/1361-6595/ad0742.

[35] S.-J. Klose et al.: “The localised density of H_2O_2 in the effluent of a cold atmospheric pressure plasma jet determined by continuous-wave cavity ring-down spectroscopy”. *Frontiers in Physics* **11** (2023), 1221181. DOI: 10.3389/fphy.2023.1221181.

[36] D. X. Liu et al.: “Global model of low-temperature atmospheric-pressure He + H_2O plasmas”. *Plasma Sources Science and Technology* **19**.2 (2010), 025018. DOI: 10.1088/0963-0252/19/2/025018.

[37] S. Schröter et al.: “Chemical kinetics in an atmospheric pressure helium plasma containing humidity”. *Physical Chemistry Chemical Physics* **20**.37 (2018), 24263–24286. DOI: 10.1039/C8CP02473A.

[38] P. J. Bruggeman et al.: “Plasma–liquid interactions: a review and roadmap”. *Plasma Sources Science and Technology* **25**.5 (2016), 053002. DOI: 10.1088/0963-0252/25/5/053002.

[39] Y. Morabit et al.: “A review of the gas and liquid phase interactions in low-temperature plasma jets used for biomedical applications”. *The European Physical Journal D* **75**.1 (2021), 32. DOI: 10.1140/epjd/s10053-020-00004-4.

[40] K. Stapelmann et al.: “Plasma–liquid interactions in the presence of organic matter - A perspective”. *Journal of Applied Physics* **135**.16 (2024), 160901. DOI: 10.1063/5.0203125.

[41] J. Bissonnette-Dulude et al.: “Coupling the COST reference plasma jet to a microfluidic device: a computational study”. *Plasma Sources Science and Technology* (2023). DOI: 10.1088/1361-6595/ad1421.

[42] J. F. M. Van Rens et al.: “Induced Liquid Phase Flow by RF Ar Cold Atmospheric Pressure Plasma Jet”. *IEEE Transactions on Plasma Science* **42**.10 (2014), 2622–2623. DOI: 10.1109/TPS.2014.2328793.

[43] C. C. W. Verlackt et al.: “Transport and accumulation of plasma generated species in aqueous solution”. *Physical Chemistry Chemical Physics* **20**.10 (2018), 6845–6859. DOI: 10.1039/C7CP07593F.

[44] I. L. Semenov et al.: “Modelling of the transport phenomena for an atmospheric-pressure plasma jet in contact with liquid”. *Journal of Physics D: Applied Physics* **52**.31 (2019), 315203. DOI: 10.1088/1361-6463/ab208e.

[45] S. M. Barry et al.: “Cytochrome P450–catalyzed L-tryptophan nitration in thaxtomin phytotoxin biosynthesis”. *Nature Chemical Biology* **8**.10 (2012), 814–816. DOI: 10.1038/nchembio.1048.

[46] F. Yu et al.: “Structural Insights into the Mechanism for Recognizing Substrate of the Cytochrome P450 Enzyme TxtE”. *PLoS ONE* **8**.11 (2013). Ed. by A. Cavalli, e81526. DOI: 10.1371/journal.pone.0081526.

[47] S. C. Dodani et al.: “Structural, Functional, and Spectroscopic Characterization of the Substrate Scope of the Novel Nitrating Cytochrome P450 TxtE”. *ChemBioChem* **15**.15 (2014), 2259–2267. DOI: 10.1002/cbic.201402241.

[48] C. Douat et al.: “Production of nitric/nitrous oxide by an atmospheric pressure plasma jet”. *Plasma Sources Science and Technology* **25**.2 (2016), 025027. DOI: 10.1088/0963-0252/25/2/025027.

[49] P. Preissing et al.: "Three-dimensional density distributions of NO in the effluent of the COST reference microplasma jet operated in $He/N_2/O_2$". *Plasma Sources Science and Technology* **29**.12 (2020), 125001. DOI: 10.1088/1361-6595/abbd86.

[50] Y. Gorbanev et al.: "Nitrogen Fixation with Water Vapor by Nonequilibrium Plasma: toward Sustainable Ammonia Production". *ACS Sustainable Chemistry & Engineering* **8**.7 (2020), 2996–3004. DOI: 10.1021/acssuschemeng.9b07849.

[51] E. Vervloessem et al.: "Sustainable NO_x production from air in pulsed plasma: elucidating the chemistry behind the low energy consumption". *Green Chemistry* **24**.2 (2022), 916–929. DOI: 10.1039/D1GC02762J.

[52] S. Li et al.: "Recent Progress of Plasma-Assisted Nitrogen Fixation Research: A Review". *Processes* **6**.12 (2018), 248. DOI: 10.3390/pr6120248.

[53] I. Adamovich et al.: "The 2022 Plasma Roadmap: low temperature plasma science and technology". *Journal of Physics D: Applied Physics* **55**.37 (2022), 373001. DOI: 10.1088/1361-6463/ac5e1c.

[54] F. F. Chen: *Introduction to Plasma Physics and Controlled Fusion*. Springer International Publishing, 2016. DOI: 10.1007/978-3-319-22309-4.

[55] P. Viegas et al.: "Physics of plasma jets and interaction with surfaces: review on modelling and experiments". *Plasma Sources Science and Technology* **31**.5 (2022), 053001. DOI: 10.1088/1361-6595/ac61a9.

[56] S. Kelly et al.: "Gas and heat dynamics of a micro-scaled atmospheric pressure plasma reference jet". *Journal of Physics D: Applied Physics* **48**.44 (2015), 444002. DOI: 10.1088/0022-3727/48/44/444002.

[57] J. Golda et al.: "Comparison of electron heating and energy loss mechanisms in an RF plasma jet operated in argon and helium". *Plasma Sources Science and Technology* **29**.2 (2020), 025014. DOI: 10.1088/1361-6595/ab6c81.

[58] Y. P. Raizer: *Gas Discharge Physics*. Heidelberg: Springer Berlin, 1991. DOI: 10.1007/978-3-642-61247-3.

[59] H. Conrads et al.: "Plasma generation and plasma sources". *Plasma Sources Science and Technology* **9**.4 (2000), 441–454. DOI: 10.1088/0963-0252/9/4/301.

[60] A. von Keudell et al.: "Foundations of low-temperature plasma physics—an introduction". *Plasma Sources Science and Technology* **26**.11 (2017), 113001. DOI: 10.1088/1361-6595/aa8d4c.

[61] M. A. Lieberman et al.: *Principles of Plasma Discharges and Materials Processing*. 1st ed. Wiley, 2005. DOI: 10.1002/0471724254.

[62] K. H. Becker et al.: "Cluster Issue on Microplasmas". *Journal of Physics D: Applied Physics* **38**.11 (2005). DOI: 10.1088/0022-3727/38/11/E01.

[63] Y. Gorbanev et al.: "Applications of the COST Plasma Jet: More than a Reference Standard". *Plasma* **2**.3 (2019), 316–327. DOI: 10.3390/plasma2030023.

[64] W. M. Haynes, ed.: *CRC Handbook of Chemistry and Physics*. 0th ed. CRC Press, 2014. DOI: 10.1201/b17118.

[65] A. H. Cookson et al.: "Townsend's first ionization coefficient for methane and nitrogen". *British Journal of Applied Physics* **17**.7 (1966), 891–903. DOI: 10.1088/0508-3443/17/7/308.

[66] S. Nijdam et al.: "The physics of streamer discharge phenomena". *Plasma Sources Science and Technology* **29**.10 (2020), 103001. DOI: 10.1088/1361-6595/abaa05.

[67] J. S. Sousa et al.: "Cold atmospheric pressure plasma jets as sources of singlet delta oxygen for biomedical applications". *Journal of Applied Physics* **109**.12 (2011), 123302. DOI: 10.1063/1.3601347.

[68] J.-W. Lackmann et al.: "Inactivation of microbes and macromolecules by atmospheric-pressure plasma jets". *Applied Microbiology and Biotechnology* **98**.14 (2014), 6205–6213. DOI: 10.1007/s00253-014-5781-9.

[69] J. Winter et al.: "Atmospheric pressure plasma jets: an overview of devices and new directions". *Plasma Sources Science and Technology* **24**.6 (2015), 064001. DOI: 10.1088/0963-0252/24/6/064001.

[70] M. Laroussi: "Plasma Medicine: A Brief Introduction". *Plasma* **1**.1 (2018), 47–60. DOI: 10.3390/plasma1010005.

[71] H. Lange et al.: "Vacuum UV Radiation of a Plasma Jet Operated With Rare Gases at Atmospheric Pressure". *IEEE Transactions on Plasma Science* **37**.6 (2009), 859–865. DOI: 10.1109/TPS.2009.2019982.

[72] H. Jablonowski et al.: "Impact of plasma jet vacuum ultraviolet radiation on reactive oxygen species generation in bio-relevant liquids". *Physics of Plasmas* **22**.12 (2015), 122008. DOI: 10.1063/1.4934989.

[73] F. Liu et al.: "Atmospheric plasma VUV photon emission". *Plasma Sources Science and Technology* **29**.6 (2020), 065001. DOI: 10.1088/1361-6595/ab8e4d.

[74] J. Golda et al.: "Vacuum ultraviolet spectroscopy of cold atmospheric pressure plasma jets". *Plasma Processes and Polymers* **17**.6 (2020), 1900216. DOI: 10.1002/ppap.201900216.

[75] D. Popović et al.: "Review on vacuum ultraviolet generation in low-pressure plasmas". *Plasma Processes and Polymers* **18**.9 (2021), 2100061. DOI: 10.1002/ppap.202100061.

[76] T. Gans et al.: "Prospects of Phase Resolved Optical Emission Spectroscopy as a Powerful Diagnostic Tool for RF-Discharges". *Contributions to Plasma Physics* **44**.56 (2004), 523–528. DOI: 10.1002/ctpp.200410074.

[77] L. Bischoff et al.: “Experimental and computational investigations of electron dynamics in micro atmospheric pressure radio-frequency plasma jets operated in He/N_2 mixtures”. *Plasma Sources Science and Technology* **27**.12 (2018), 125009. DOI: 10.1088/1361-6595/aaf35d.

[78] Y. Liu et al.: “Electron heating mode transitions in radio-frequency driven micro atmospheric pressure plasma jets in He/O_2 : a fluid dynamics approach”. *Journal of Physics D: Applied Physics* **54**.27 (2021), 275204. DOI: 10.1088/1361-6463/abf370.

[79] K. McKay et al.: “Excitation frequency effects on atmospheric-pressure helium RF microplasmas: plasma density, electron energy and plasma impedance”. *The European Physical Journal D* **60**.3 (2010), 497–503. DOI: 10.1140/epjd/e2010-00191-7.

[80] J. Golda et al.: “Dissipated electrical power and electron density in an RF atmospheric pressure helium plasma jet”. *Plasma Sources Science and Technology* **28**.9 (2019), 095023. DOI: 10.1088/1361-6595/ab393d.

[81] A. Hurlbatt et al.: “Concepts, Capabilities, and Limitations of Global Models: A Review”. *Plasma Processes and Polymers* **14**.1-2 (2017), 1600138. DOI: 10.1002/ppap.201600138.

[82] S. J. Blanksby et al.: “Bond Dissociation Energies of Organic Molecules”. *Accounts of Chemical Research* **36**.4 (2003), 255–263. DOI: 10.1021/ar020230d.

[83] S. Schröter et al.: “The formation of atomic oxygen and hydrogen in atmospheric pressure plasmas containing humidity: picosecond two-photon absorption laser induced fluorescence and numerical simulations”. *Plasma Sources Science and Technology* **29**.10 (2020), 105001. DOI: 10.1088/1361-6595/abab55.

[84] P. Bruggeman et al.: “Non-thermal plasmas in and in contact with liquids”. *Journal of Physics D: Applied Physics* **42**.5 (2009), 053001. DOI: 10.1088/0022-3727/42/5/053001.

[85] A. Khlyustova et al.: “Important parameters in plasma jets for the production of RONS in liquids for plasma medicine: A brief review”. *Frontiers of Chemical Science and Engineering* **13**.2 (2019), 238–252. DOI: 10.1007/s11705-019-1801-8.

[86] F. Rezaei et al.: “Applications of Plasma-Liquid Systems: A Review”. *Materials* **12**.17 (2019), 2751. DOI: 10.3390/ma12172751.

[87] V. V. Kovačević et al.: “Low-temperature plasmas in contact with liquids—a review of recent progress and challenges”. *Journal of Physics D: Applied Physics* **55**.47 (2022), 473002. DOI: 10.1088/1361-6463/ac8a56.

[88] Y. Gorbanev et al.: “Organic reactions in plasma–liquid systems for environmental applications”. *Plasma Processes and Polymers* (2024), e2400149. DOI: 10.1002/ppap.202400149.

[89] B. R. Locke et al.: "Recent Insights Into Interfacial Transport and Chemical Reactions of Plasma-Generated Species in Liquid". *Plasma Processes and Polymers* (2024), e2400207. DOI: 10.1002/ppap.202400207.

[90] S. Samukawa et al.: "The 2012 Plasma Roadmap". *Journal of Physics D: Applied Physics* **45**.25 (2012), 253001. DOI: 10.1088/0022-3727/45/25/253001.

[91] W. Henry: "III. Experiments on the quantity of gases absorbed by water, at different temperatures, and under different pressures". *Philosophical Transactions of the Royal Society of London* **93** (1803), 29–274. DOI: 10.1098/rstl.1803.0004.

[92] R. Sander: "Compilation of Henry's law constants (version 4.0) for water as solvent". *Atmospheric Chemistry and Physics* **15**.8 (2015), 4399–4981. DOI: 10.5194/acp-15-4399-2015.

[93] R. Sander et al.: "Henry's law constants (IUPAC Recommendations 2021)". *Pure and Applied Chemistry* **94**.1 (2022), 71–85. DOI: 10.1515/pac-2020-0302.

[94] D. W. O'Sullivan et al.: "Henry's Law Constant Determinations for Hydrogen Peroxide, Methyl Hydroperoxide, Hydroxymethyl Hydroperoxide, Ethyl Hydroperoxide, and Peroxyacetic Acid". *The Journal of Physical Chemistry* **100**.8 (1996), 3241–3247. DOI: 10.1021/jp951168n.

[95] J. B. Burkholder et al.: *Chemical Kinetics and Photochemical Data for Use in Atmospheric Studies*. Evaluation No. 19, JPL Publication 19-5, Jet Propulsion Laboratory, Pasadena. 2019. URL: http://jpldataeval.jpl.nasa.gov (visited on 10/14/2024).

[96] D. R. Hanson et al.: "Measurement of hydroxyl and hydroperoxy radical uptake coefficients on water and sulfuric acid surfaces". *The Journal of Physical Chemistry* **96**.12 (1992), 4979–4985. DOI: 10.1021/j100191a046.

[97] Q. Shi et al.: "Uptake of Gas-Phase Ammonia. 1. Uptake by Aqueous Surfaces as a Function of pH". *The Journal of Physical Chemistry A* **103**.44 (1999), 8812–8823. DOI: 10.1021/jp991696p.

[98] J. Y. Park et al.: "Solubility and decomposition kinetics of nitrous acid in aqueous solution". *The Journal of Physical Chemistry* **92**.22 (1988), 6294–6302. DOI: 10.1021/j100333a025.

[99] J. L. Cheung et al.: "Heterogeneous Interactions of NO_2 with Aqueous Surfaces". *The Journal of Physical Chemistry A* **104**.12 (2000), 2655–2662. DOI: 10.1021/jp992929f.

[100] A. Lindsay et al.: "Momentum, heat, and neutral mass transport in convective atmospheric pressure plasma-liquid systems and implications for aqueous targets". *Journal of Physics D: Applied Physics* **48**.42 (2015), 424007. DOI: 10.1088/0022-3727/48/42/424007.

[101] T. Kamidollayev et al.: "Modeling of reactive species interphase transport in plasma jet impinging on water". *Journal of Physics D: Applied Physics* (2023). DOI: 10.1088/1361-6463/acf86a.

[102] Z. C. Liu et al.: "Physicochemical processes in the indirect interaction between surface air plasma and deionized water". *Journal of Physics D: Applied Physics* **48**.49 (2015), 495201. DOI: 10.1088/0022-3727/48/49/495201.

[103] D. X. Liu et al.: "Aqueous reactive species induced by a surface air discharge: Heterogeneous mass transfer and liquid chemistry pathways". *Scientific Reports* **6**.1 (2016), 23737. DOI: 10.1038/srep23737.

[104] J. Jiang et al.: "A new study on the penetration of reactive species in their mass transfer processes in water by increasing the electron energy in plasmas". *Physics of Plasmas* **23**.10 (2016), 103503. DOI: 10.1063/1.4964364.

[105] P. Rumbach et al.: "The penetration and concentration of solvated electrons and hydroxyl radicals at a plasma-liquid interface". *Plasma Sources Science and Technology* **27**.11 (2018), 115013. DOI: 10.1088/1361-6595/aaed07.

[106] K. Ikuse et al.: "Roles of the reaction boundary layer and long diffusion of stable reactive nitrogen species (RNS) in plasma-irradiated water as an oxidizing media — numerical simulation study". *Japanese Journal of Applied Physics* **61**.7 (2022), 076002. DOI: 10.35848/1347-4065/ac7371.

[107] P. Lukes et al.: "Aqueous-phase chemistry and bactericidal effects from an air discharge plasma in contact with water: evidence for the formation of peroxynitrite through a pseudo-second-order post-discharge reaction of H_2O_2 and HNO_2". *Plasma Sources Science and Technology* **23**.1 (2014), 015019. DOI: 10.1088/0963-0252/23/1/015019.

[108] Y. Liu et al.: "Comparison of the transportation of reactive species from He and Ar atmospheric-pressure plasma jets to aqueous solutions". *Journal of Physics D: Applied Physics* (2024). DOI: 10.1088/1361-6463/ad8004.

[109] U. Fantz: "Basics of plasma spectroscopy". *Plasma Sources Science and Technology* **15**.4 (2006), S137–S147. DOI: 10.1088/0963-0252/15/4/S01.

[110] R. Engeln et al.: "Foundations of optical diagnostics in low-temperature plasmas". *Plasma Sources Science and Technology* **29**.6 (2020), 063001. DOI: 10.1088/1361-6595/ab6880.

[111] A. R. Hanna et al.: "Investigating recent developments and applications of optical plasma spectroscopy: A review". *Journal of Vacuum Science & Technology A* **38**.2 (2020), 020806. DOI: 10.1116/1.5141844.

[112] A. Kramida et al.: *NIST Atomic Spectra Database (version 5.11)*. 2023. DOI: https://doi.org/10.18434/T4W30F. URL: https://physics.nist.gov/asd (visited on 05/07/2024).

[113] M. Thiyagarajan et al.: "Optical emission spectroscopic diagnostics of a non-thermal atmospheric pressure helium-oxygen plasma jet for biomedical applications". *Journal of Applied Physics* **113**.23 (2013), 233302. DOI: 10.1063/1.4811339.

[114] P. J. Bruggeman et al.: "Gas temperature determination from rotational lines in non-equilibrium plasmas: a review". *Plasma Sources Science and Technology* **23**.2 (2014), 023001. DOI: 10.1088/0963-0252/23/2/023001.

[115] T. Belmonte et al.: "Theoretical background of optical emission spectroscopy for analysis of atmospheric pressure plasmas". *Plasma Sources Science and Technology* **24**.6 (2015), 064003. DOI: 10.1088/0963-0252/24/6/064003.

[116] P. Bruggeman et al.: "Characterization of a direct dc-excited discharge in water by optical emission spectroscopy". *Plasma Sources Science and Technology* **18**.2 (2009), 025017. DOI: 10.1088/0963-0252/18/2/025017.

[117] S. Y. Moon et al.: "A comparative study of rotational temperatures using diatomic OH, O_2 and $N_2{}^+$ molecular spectra emitted from atmospheric plasmas". *Spectrochimica Acta Part B: Atomic Spectroscopy* **58**.2 (2003), 249–257. DOI: 10.1016/S0584-8547(02)00259-8.

[118] J. Kim et al.: "Optical measurements of gas temperatures in atmospheric pressure RF cold plasmas". *Surface and Coatings Technology* **171**.1-3 (2003), 211–215. DOI: 10.1016/S0257-8972(03)00273-1.

[119] S. Hofmann et al.: "Power dissipation, gas temperatures and electron densities of cold atmospheric pressure helium and argon RF plasma jets". *Plasma Sources Science and Technology* **20**.6 (2011), 065010. DOI: 10.1088/0963-0252/20/6/065010.

[120] N. Srivastava et al.: "Effects of water addition on OH radical generation and plasma properties in an atmospheric argon microwave plasma jet". *Journal of Applied Physics* **110**.5 (2011), 053304. DOI: 10.1063/1.3632970.

[121] J. Luque et al.: "LIFBASE version 2.1.1". *SRI International, Menlo Park, CA* **50** (1999).

[122] P. Bruggeman et al.: "Electronic quenching of OH(A) by water in atmospheric pressure plasmas and its influence on the gas temperature determination by OH(A – X) emission". *Plasma Sources Science and Technology* **19**.1 (2010), 015016. DOI: 10.1088/0963-0252/19/1/015016.

[123] J. Voráč et al.: "Deducing rotational quantum-state distributions from overlapping molecular spectra". *Review of Scientific Instruments* **90**.12 (2019), 123102. DOI: 10.1063/1.5128455.

[124] G. Dilecce et al.: "Laser induced fluorescence in atmospheric pressure discharges". *Plasma Sources Science and Technology* **24**.3 (2015), 034007. DOI: 10.1088/0963-0252/24/3/034007.

[125] G. Dilecce et al.: "Laser diagnostics of high-pressure discharges: laser induced fluorescence detection of OH in He/Ar–H_2O dielectric barrier discharges". *Plasma Physics and Controlled Fusion* **53**.12 (2011), 124006. DOI: 10.1088/0741-3335/53/12/124006.

[126] T. Verreycken et al.: "Time and spatially resolved LIF of OH in a plasma filament in atmospheric pressure He–H_2O". *Journal of Physics D: Applied Physics* **45**.4 (2012), 045205. DOI: 10.1088/0022-3727/45/4/045205.

[127] Y. Morabit et al.: "Turbulence and entrainment in an atmospheric pressure dielectric barrier plasma jet". *Plasma Processes and Polymers* **17**.6 (2020), 1900217. DOI: 10.1002/ppap.201900217.

[128] S. Reuter et al.: "Review on VUV to MIR absorption spectroscopy of atmospheric pressure plasma jets". *Plasma Sources Science and Technology* **24**.5 (2015), 054001. DOI: 10.1088/0963-0252/24/5/054001.

[129] J. Voráč et al.: "Batch processing of overlapping molecular spectra as a tool for spatio-temporal diagnostics of power modulated microwave plasma jet". *Plasma Sources Science and Technology* **26**.2 (2017), 025010. DOI: 10.1088/1361-6595/aa51f0.

[130] J. Voráč et al.: "State-by-state emission spectra fitting for non-equilibrium plasmas: OH spectra of surface barrier discharge at argon/water interface". *Journal of Physics D: Applied Physics* **50**.29 (2017), 294002. DOI: 10.1088/1361-6463/aa7570.

[131] S. Yonemori et al.: "Measurement of OH density and air–helium mixture ratio in an atmospheric-pressure helium plasma jet". *Journal of Physics D: Applied Physics* **45**.22 (2012), 225202. DOI: 10.1088/0022-3727/45/22/225202.

[132] T. Verreycken et al.: "Absolute calibration of OH density in a nanosecond pulsed plasma filament in atmospheric pressure He–H_2O: comparison of independent calibration methods". *Journal of Physics D: Applied Physics* **46**.46 (2013), 464004. DOI: 10.1088/0022-3727/46/46/464004.

[133] J. Cosimi et al.: "Laser-induced fluorescence measurements of spatially resolved OH densities in a helium plasma jet interacting with three different targets in the open air". *Plasma Sources Science and Technology* **32**.6 (2023), 065012. DOI: 10.1088/1361-6595/acdbe6.

[134] W. P. Partridge et al.: "Formulation of a dimensionless overlap fraction to account for spectrally distributed interactions in fluorescence studies". *Applied Optics* **34**.15 (1995), 2645. DOI: 10.1364/AO.34.002645.

[135] N. Sadeghi: "6. Molecular Spectroscopy Techniques Applied for Processing Plasma Diagnostics". *Journal of Plasma and Fusion Research* **80**.9 (2004), 767–776. DOI: 10.1585/jspf.80.767.

[136] V. L. Kasyutich: "Pressure broadening parameters of the hydroxyl radical A $^2\Sigma^+$ (υ'=0) ← X $^2\Pi_{3/2}$ (υ=0) transitions at ca. 308 nm". *The European Physical Journal D* **33**.1 (2005), 29–33. DOI: 10.1140/epjd/e2005-00022-0.

[137] S. C. L. Vervloedt et al.: "Ammonia synthesis by plasma catalysis in an atmospheric RF helium plasma". *Plasma Sources Science and Technology* **33**.4 (2024), 045005. DOI: 10.1088/1361-6595/ad38d6.

[138] S. Yu et al.: "Controlled synthesis of NO in an atmospheric pressure plasma by suppressing NO destruction channels by plasma catalysis". *Journal of Physics D: Applied Physics* **57**.24 (2024), 245203. DOI: 10.1088/1361-6463/ad2ef6.

[139] I. Gordon et al.: "The HITRAN2020 molecular spectroscopic database". *Journal of Quantitative Spectroscopy and Radiative Transfer* **277** (2022), 107949. DOI: 10.1016/j.jqsrt.2021.107949.

[140] B. L. M. Klarenaar et al.: "Time evolution of vibrational temperatures in a CO_2 glow discharge measured with infrared absorption spectroscopy". *Plasma Sources Science and Technology* **26**.11 (2017), 115008. DOI: 10.1088/1361-6595/aa902e.

[141] T. Urbanietz et al.: "Non-equilibrium excitation of CO_2 in an atmospheric pressure helium plasma jet". *Journal of Physics D: Applied Physics* **51**.34 (2018), 345202. DOI: 10.1088/1361-6463/aad4d3.

[142] C. Stewig et al.: "Excitation and dissociation of CO_2 heavily diluted in noble gas atmospheric pressure plasma". *Journal of Physics D: Applied Physics* **53**.12 (2020), 125205. DOI: 10.1088/1361-6463/ab634f.

[143] S. Große-Kreul et al.: "Mass spectrometry of atmospheric pressure plasmas". *Plasma Sources Science and Technology* **24**.4 (2015), 044008. DOI: 10.1088/0963-0252/24/4/044008.

[144] G. Willems et al.: "Mass spectrometry of neutrals and positive ions in He/CO_2 non-equilibrium atmospheric plasma jet". *Plasma Physics and Controlled Fusion* **62**.3 (2020), 034005. DOI: 10.1088/1361-6587/ab6b4c.

[145] D. Ellerweg et al.: "Characterization of the effluent of a He/O_2 microscale atmospheric pressure plasma jet by quantitative molecular beam mass spectrometry". *New Journal of Physics* **12**.1 (2010), 013021. DOI: 10.1088/1367-2630/12/1/013021.

[146] J. Benedikt et al.: "Mass spectrometry of positive ions and neutral species in the effluent of an atmospheric pressure plasma with hexamethyldisiloxane and oxygen". *Journal of Physics D: Applied Physics* **46**.46 (2013), 464017. DOI: 10.1088/0022-3727/46/46/464017.

[147] S. Große-Kreul et al.: "Methods of gas purification and effect on the ion composition in an RF atmospheric pressure plasma jet investigated by mass spectrometry". *EPJ Techniques and Instrumentation* **3**.1 (2016), 6. DOI: 10.1140/epjti/s40485-016-0034-1.

[148] C. Stewig et al.: “Impact of catalysis on n-butane oxidation in an RF atmospheric pressure plasma”. *Plasma Sources Science and Technology* **32**.10 (2023), 105006. DOI: 10.1088/1361-6595/acff17.

[149] J. Benedikt et al.: “Quadrupole mass spectrometry of reactive plasmas”. *Journal of Physics D: Applied Physics* **45**.40 (2012), 403001. DOI: 10.1088/0022-3727/45/40/403001.

[150] J. Benedikt et al.: “Molecular beam sampling system with very high beam-to-background ratio: The rotating skimmer concept”. *Review of Scientific Instruments* **80**.5 (2009), 055107. DOI: 10.1063/1.3133804.

[151] Gert Willems: “Reaction chemistry in non-equilibrium atmospheric pressure plasmas”. PhD thesis. Bochum: Ruhr-University Bochum, 2018.

[152] K. Stephan et al.: “Mass spectrometric determination of partial electron impact ionization cross sections of He, Ne, Ar and Kr from threshold up to 180 eV”. *The Journal of Chemical Physics* **73**.8 (1980), 3763–3778. DOI: 10.1063/1.440606.

[153] H. C. Straub et al.: “Absolute partial and total cross sections for electron-impact ionization of argon from threshold to 1000 eV”. *Physical Review A* **52**.2 (1995), 1115–1124. DOI: 10.1103/PhysRevA.52.1115.

[154] B. G. Lindsay et al.: “5.1 Ionization”. *Interactions of Photons and Electrons with Molecules*. Ed. by Y. Itikawa. Vol. 17C. Series Title: Landolt-Börnstein - Group I Elementary Particles, Nuclei and Atoms. Berlin/Heidelberg: Springer-Verlag, 2003, pp. 5001–5077. DOI: 10.1007/10874891_2.

[155] K. Irikura: *Electron-Impact Cross Section for Ionization and Excitation, NIST Standard Reference Database 107*. 1997. DOI: 10.18434/T4KK5C. URL: http://www.nist.gov/pml/data/ionization/ (visited on 08/14/2024).

[156] H. C. Urey et al.: “The absorption spectrum and decomposition of hydrogen peroxide by light”. *Journal of the American Chemical Society* **51**.5 (1929), 1371–1383. DOI: 10.1021/ja01380a011.

[157] R. B. Holt et al.: “Ultraviolet Absorption Spectrum of Hydrogen Peroxide”. *The Journal of Chemical Physics* **16**.3 (1948), 225–229. DOI: 10.1063/1.1746843.

[158] J.-S. Oh et al.: “In-situ UV Absorption Spectroscopy for Monitoring Transport of Plasma Reactive Species through Agarose as Surrogate for Tissue”. *Journal of Photopolymer Science and Technology* **28**.3 (2015), 439–444. DOI: 10.2494/photopolymer.28.439.

[159] T. R. Brubaker et al.: “Dynamic analysis of reactive oxygen nitrogen species in plasma-activated culture medium by UV absorption spectroscopy”. *Journal of Applied Physics* **122**.21 (2017), 213301. DOI: 10.1063/1.4999256.

[160] J.-S. Oh et al.: “UV–vis spectroscopy study of plasma-activated water: Dependence of the chemical composition on plasma exposure time and treatment distance”. *Japanese Journal of Applied Physics* **57**.1 (2018), 0102B9. DOI: 10.7567/JJAP.57.0102B9.

[161] Z. Liu et al.: “Quantifying the concentration and penetration depth of long-lived RONS in plasma-activated water by UV absorption spectroscopy”. *AIP Advances* **9**.1 (2019), 015014. DOI: 10.1063/1.5037660.

[162] R. Nogueira et al.: “Simple and fast spectrophotometric determination of H2O2 in photo-Fenton reactions using metavanadate”. *Talanta* **66**.1 (2005), 86–91. DOI: 10.1016/j.talanta.2004.10.001.

[163] Y. Matos-Peralta et al.: “Review—Prussian Blue and Its Analogs as Appealing Materials for Electrochemical Sensing and Biosensing”. *Journal of The Electrochemical Society* **167**.3 (2020), 037510. DOI: 10.1149/2.0102003JES.

[164] J. Clausmeyer et al.: “Nanosensors for the detection of hydrogen peroxide”. *Electrochemistry Communications* **40** (2014), 28–30. DOI: 10.1016/j.elecom.2013.12.015.

[165] S. Schüttler et al.: “Validation of in situ diagnostics for the detection of OH and H_2O_2 in liquids treated by a humid atmospheric pressure plasma jet”. *Plasma Processes and Polymers* (2023), e2300079. DOI: 10.1002/ppap.202300079.

[166] J. C. Barreto et al.: “Terephthalic acid: A dosimeter for the detection of hydroxyl radicals in vitro”. *Life Sciences* **56**.4 (1994), PL89–PL96. DOI: 10.1016/0024-3205(94)00925-2.

[167] T. Mason et al.: “Dosimetry in sonochemistry: the use of aqueous terephthalate ion as a fluorescence monitor”. *Ultrasonics Sonochemistry* **1**.2 (1994), S91–S95. DOI: 10.1016/1350-4177(94)90004-3.

[168] B. Myers et al.: “Measuring plasma-generated $^{\cdot}$OH and O atoms in liquid using EPR spectroscopy and the non-selectivity of the HTA assay”. *Journal of Physics D: Applied Physics* **54**.14 (2021), 145202. DOI: 10.1088/1361-6463/abd9a6.

[169] S. Kanazawa et al.: “Application of chemical dosimetry to hydroxyl radical measurement during underwater discharge”. *Journal of Physics: Conference Series* **418** (2013), 012102. DOI: 10.1088/1742-6596/418/1/012102.

[170] T. Charbouillot et al.: “Performance and selectivity of the terephthalic acid probe for OH as a function of temperature, pH and composition of atmospherically relevant aqueous media”. *Journal of Photochemistry and Photobiology A: Chemistry* **222**.1 (2011), 70–76. DOI: 10.1016/j.jphotochem.2011.05.003.

[171] S. Kanazawa et al.: “Observation of OH radicals produced by pulsed discharges on the surface of a liquid”. *Plasma Sources Science and Technology* **20**.3 (2011), 034010. DOI: 10.1088/0963-0252/20/3/034010.

[172] T.-W. Chen et al.: "Analysis of Hydroxyl Radical and Hydrogen Peroxide Generated in Helium-Based Atmospheric-Pressure Plasma Jet and in Different Solutions Treated by Plasma for Bioapplications". *ECS Journal of Solid State Science and Technology* **9**.11 (2020), 115002. DOI: 10.1149/2162-8777/ab9c78.

[173] X. Fang et al.: "OH radical formation by ultrasound in aqueous solutions Part I: the chemistry underlying the terephthalate dosimeter". *Ultrasonics Sonochemistry* **3**.1 (1996), 57–63. DOI: 10.1016/1350-4177(95)00032-1.

[174] C. Lu et al.: "Reactive oxygen species and their chemiluminescence-detection methods". *TrAC Trends in Analytical Chemistry* **25**.10 (2006), 985–995. DOI: 10.1016/j.trac.2006.07.007.

[175] G. Merényi et al.: "Luminol chemiluminescence: Chemistry, excitation, emitter". *Journal of Bioluminescence and Chemiluminescence* **5**.1 (1990), 53–56. DOI: 10.1002/bio.1170050111.

[176] N. Shirai et al.: "Visualization of short-lived reactive species in liquid in contact with atmospheric-pressure plasma by chemiluminescence of luminol". *Applied Physics Express* **11**.2 (2018), 026201. DOI: 10.7567/APEX.11.026201.

[177] N. Shirai et al.: "Correlation between gas-phase OH density and intensity of luminol chemiluminescence in liquid interacting with atmospheric-pressure plasma". *Journal of Physics D: Applied Physics* **52**.39 (2019), 39LT02. DOI: 10.1088/1361-6463/ab2ff2.

[178] A. Liberzon et al.: *OpenPIV/openpiv-python: OpenPIV - Python (v0.22.2) with a new extended search PIV grid option*. 2020. DOI: 10.5281/ZENODO.3930343. URL: https://zenodo.org/record/3930343 (visited on 10/19/2023).

[179] R. J. Adrian: "Twenty years of particle image velocimetry". *Experiments in Fluids* **39**.2 (2005), 159–169. DOI: 10.1007/s00348-005-0991-7.

[180] Y. Ni et al.: "A solar powered handheld plasma source for microbial decontamination applications". *Journal of Physics D: Applied Physics* **49**.35 (2016), 355203. DOI: 10.1088/0022-3727/49/35/355203.

[181] A. Dickenson et al.: "The generation and transport of reactive nitrogen species from a low temperature atmospheric pressure air plasma source". *Physical Chemistry Chemical Physics* **20**.45 (2018), 28499–28510. DOI: 10.1039/C8CP05762A.

[182] S. Mededovic Thagard et al.: "Plasma-based water treatment: development of a general mechanistic model to estimate the treatability of different types of contaminants". *Journal of Physics D: Applied Physics* **50**.1 (2017), 014003. DOI: 10.1088/1361-6463/50/1/014003.

[183] J. Lai et al.: "Understanding Plasma–Liquid Interface Instabilities Using Particle Image Velocimetry and Shadowgraphy Imaging Methods". *IEEE Transactions on Plasma Science* **46**.4 (2018), 875–881. DOI: 10.1109/TPS.2018.2805882.

[184] B. Singh et al.: “Measurement of the flow field induced by a spark plasma using particle image velocimetry”. *Experiments in Fluids* **59**.12 (2018), 179. DOI: 10.1007/s00348-018-2632-y.

[185] S. Park et al.: “Stabilization of liquid instabilities with ionized gas jets”. *Nature* **592**.7852 (2021), 49–53. DOI: 10.1038/s41586-021-03359-9.

[186] A. M. Lietz et al.: “Air plasma treatment of liquid covered tissue: long timescale chemistry”. *Journal of Physics D: Applied Physics* **49**.42 (2016), 425204. DOI: 10.1088/0022-3727/49/42/425204.

[187] S. Schüttler et al.: “Production and transport of plasma-generated hydrogen peroxide from gas to liquid”. *Physical Chemistry Chemical Physics* **26**.10 (2024), 8255–8272. DOI: 10.1039/D3CP04290A.

[188] S. Schröter et al.: “Numerical study of the influence of surface reaction probabilities on reactive species in an rf atmospheric pressure plasma containing humidity”. *Plasma Physics and Controlled Fusion* **60**.1 (2018), 014035. DOI: 10.1088/1361-6587/aa8fe9.

[189] A. Brisset et al.: “Chemical kinetics and density measurements of OH in an atmospheric pressure He + O_2 + H_2O radiofrequency plasma”. *Journal of Physics D: Applied Physics* **54**.28 (2021), 285201. DOI: 10.1088/1361-6463/abefec.

[190] Lara Boeddinghaus: *Diagnostik der Anregungsdynamik in einem Atmosphärendruckplasmajet mittels phasenaufgelöster optischer Emissionsspektroskopie*. Bachelor thesis. Bochum: Ruhr University Bochum, 2023.

[191] Maike Kai: *Diagnostics of Plasma Chemistry in Atmospheric Pressure Plasmas Operated in Humid Feed Gas*. Master thesis. Bochum: Ruhr University Bochum, 2023.

[192] J. Benedikt et al.: “Phase resolved optical emission spectroscopy of coaxial microplasma jet operated with He and Ar”. *The European Physical Journal D* **60**.3 (2010), 539–546. DOI: 10.1140/epjd/e2010-00246-9.

[193] T. Gerling et al.: “Back and forth directed plasma bullets in a helium atmospheric pressure needle-to-plane discharge with oxygen admixtures”. *Plasma Sources Science and Technology* **21**.3 (2012), 034012. DOI: 10.1088/0963-0252/21/3/034012.

[194] L. Chauvet et al.: “Characterization of an asymmetric DBD plasma jet source at atmospheric pressure”. *J. Anal. At. Spectrom.* **29**.11 (2014), 2050–2057. DOI: 10.1039/C4JA00255E.

[195] B. B. Sahu et al.: “Development and characterization of a multi-electrode cold atmospheric pressure DBD plasma jet aiming plasma application”. *Journal of Analytical Atomic Spectrometry* **32**.4 (2017), 782–795. DOI: 10.1039/C6JA00419A.

[196] E. Ilik et al.: “Adding Water Droplets Into Atmospheric Pressure Plasma Jet of Helium”. *IEEE Transactions on Plasma Science* **47**.11 (2019), 5000–5005. DOI: 10.1109/TPS.2019.2948701.

[197] D. W. Liu et al.: "Electron heating in radio-frequency capacitively coupled atmospheric-pressure plasmas". *Applied Physics Letters* **93**.26 (2008), 261503. DOI: 10.1063/1.3058686.

[198] T. Hemke et al.: "Ionization by bulk heating of electrons in capacitive radio frequency atmospheric pressure microplasmas". *Plasma Sources Science and Technology* **22**.1 (2012), 015012. DOI: 10.1088/0963-0252/22/1/015012.

[199] D. Steuer et al.: "State enhanced actinometry in the COST microplasma jet". *Plasma Sources Science and Technology* **31**.10 (2022), 10LT01. DOI: 10.1088/1361-6595/ac90e8.

[200] P. S. Barklem: "Electron-impact excitation of neutral oxygen". *Astronomy & Astrophysics* **462**.2 (2007), 781–788. DOI: 10.1051/0004-6361:20066341.

[201] D. Schröder et al.: "Enhanced oxygen dissociation in a propagating constricted discharge formed in a self-pulsing atmospheric pressure microplasma jet". *Journal of Physics D: Applied Physics* **46**.46 (2013), 464003. DOI: 10.1088/0022-3727/46/46/464003.

[202] J. Benedikt et al.: "Absolute OH and O radical densities in effluent of a He/H_2O micro-scaled atmospheric pressure plasma jet". *Plasma Sources Science and Technology* **25**.4 (2016), 045013. DOI: 10.1088/0963-0252/25/4/045013.

[203] D. Steuer et al.: "2D spatially resolved O atom density profiles in an atmospheric pressure plasma jet: from the active plasma volume to the effluent". *Journal of Physics D: Applied Physics* **54**.35 (2021), 355204. DOI: 10.1088/1361-6463/ac09b9.

[204] S. A. Norberg et al.: "Atmospheric pressure plasma jets onto a reactive water layer over tissue: pulse repetition rate as a control mechanism". *Journal of Physics D: Applied Physics* **52**.1 (2019), 015201. DOI: 10.1088/1361-6463/aae41e.

[205] S. Kelly et al.: "Power modulation in an atmospheric pressure plasma jet". *Plasma Sources Science and Technology* **23**.6 (2014), 065012. DOI: 10.1088/0963-0252/23/6/065012.

[206] Mahreen et al.: "Influence of pulse modulation frequency on helium RF atmospheric pressure plasma jet characteristics". *Contributions to Plasma Physics* **62**.7 (2022). DOI: 10.1002/ctpp.202200007.

[207] S. Kumar Kc et al.: "Influence of duty cycle on the physicochemical characteristics of an AC-driven argon plasma jet and its impact on hydrogen peroxide production and cell viability". *Journal of Physics D: Applied Physics* (2024). DOI: 10.1088/1361-6463/ad5567.

[208] Emanuel Jeß: *Diagnostics of Plasma-Produced Hydrogen Peroxide in Liquids*. Bachelor thesis. Bochum: Ruhr University Bochum, 2022.

[209] B. Myers et al.: “Atomic oxygen density determination in the effluent of the COST reference source using in situ effective lifetime measurements in the presence of a liquid interface”. *Journal of Physics D: Applied Physics* **54**.45 (2021), 455202. DOI: 10.1088/1361-6463/ac1cb5.

[210] D. Feibel et al.: “Gas Flow-Dependent Modification of Plasma Chemistry in µAPP Jet-Generated Cold Atmospheric Plasma and Its Impact on Human Skin Fibroblasts”. *Biomedicines* **11**.5 (2023), 1242. DOI: 10.3390/biomedicines11051242.

[211] V. V. Kovačević et al.: “The effect of liquid target on a nonthermal plasma jet—imaging, electric fields, visualization of gas flow and optical emission spectroscopy”. *Journal of Physics D: Applied Physics* **51**.6 (2018), 065202. DOI: 10.1088/1361-6463/aaa288.

[212] P. Heirman et al.: “Reactivity and stability of plasma-generated oxygen and nitrogen species in buffered water solution: a computational study”. *Physical Chemistry Chemical Physics* **21**.24 (2019), 12881–12894. DOI: 10.1039/C9CP00647H.

[213] K. Oehmigen et al.: “Volume Effects of Atmospheric-Pressure Plasma in Liquids”. *IEEE Transactions on Plasma Science* **39**.11 (2011), 2646–2647. DOI: 10.1109/TPS.2011.2158242.

[214] O. K. Borggaard et al.: “Polarographic Determination of Diffusion Coefficients of Hydrogen Peroxide and Iron Chelates and Rate Constants of Hydroxyl Radical Reactions.” *Acta Chemica Scandinavica* **26** (1972), 3393–3394. DOI: 10.3891/acta.chem.scand.26-3393.

[215] A. J. Elliot et al.: “Estimation of rate constants for near-diffusion-controlled reactions in water at high temperatures”. *Journal of the Chemical Society, Faraday Transactions* **86**.9 (1990), 1539. DOI: 10.1039/ft9908601539.

[216] J. Huang et al.: “Application of a platinum dual-disk microelectrode to measurement of the electron transfer number of dioxygen reduction”. *Journal of Electroanalytical Chemistry* **433**.1-2 (1997), 33–39. DOI: 10.1016/S0022-0728(97)00127-7.

[217] B. Csóka et al.: “Determination of diffusion coefficient in gel and in aqueous solutions using scanning electrochemical microscopy”. *Journal of Biochemical and Biophysical Methods* **61**.1-2 (2004), 57–67. DOI: 10.1016/j.jbbm.2004.03.001.

[218] B. Pastina et al.: “Effect of Molecular Hydrogen on Hydrogen Peroxide in Water Radiolysis”. *The Journal of Physical Chemistry A* **105**.40 (2001), 9316–9322. DOI: 10.1021/jp012245j.

[219] L. R. Snyder et al.: *Practical HPLC Method Development*. 1st ed. Wiley, 1997. DOI: 10.1002/9781118592014.

[220] N. S. Wilson et al.: “Buffers and baselines”. *LC GC NORTH AMERICA* **19**.6 (2001). Publisher: ADVANSTAR, 590–595.

[221] T. J. Bruno et al.: *CRC Handbook of Basic Tables for Chemical Analysis*. 0th ed. CRC Press, 2003. DOI: 10.1201/9781420039917.

[222] W. J. Nuttall et al.: “Stop squandering helium”. *Nature* **485**.7400 (2012), 573–575. DOI: 10.1038/485573a.

[223] S. T. Anderson: “Economics, Helium, and the U.S. Federal Helium Reserve: Summary and Outlook”. *Natural Resources Research* **27**.4 (2018), 455–477. DOI: 10.1007/s11053-017-9359-y.

[224] A. H. Olafsdottir et al.: “Assessing the Past and Future Sustainability of Global Helium Resources, Extraction, Supply and Use, Using the Integrated Assessment Model WORLD7”. *Biophysical Economics and Sustainability* **5**.2 (2020), 6. DOI: 10.1007/s41247-020-00072-5.

[225] W. V. Gaens et al.: “Kinetic modelling for an atmospheric pressure argon plasma jet in humid air”. *Journal of Physics D: Applied Physics* **46**.27 (2013), 275201. DOI: 10.1088/0022-3727/46/27/275201.

[226] R. Atkinson et al.: “Evaluated kinetic and photochemical data for atmospheric chemistry: Volume I - gas phase reactions of O_x, HO_x, NO_x and SO_x species”. *Atmospheric Chemistry and Physics* **4**.6 (2004), 1461–1738. DOI: 10.5194/acp-4-1461-2004.

[227] Jannis Philipp Kaufmann: *Diagnostik von plasmaerzeugten Stickstoffund Sauerstoffspezies in Flüssigkeiten*. Bachelor Thesis. Bochum: Ruhr University Bochum, 2023.

[228] Niklas Eichstaedt: *Untersuchung des Einflusses der Anregungsfrequenz auf die Produktion von plasmaerzeugtem Wasserstoffperoxid*. Bachelor Thesis. Bochum: Ruhr University Bochum, 2024.

[229] S. Schüttler et al.: “Nitrogen fixation and H_2O_2 production by an atmospheric pressure plasma jet operated in He–H_20–N_2–O_2 gas mixtures”. *Plasma Processes and Polymers* (2024), e2300233. DOI: 10.1002/ppap.202300233.

[230] S. Schüttler et al.: “Tuning plasma chemistry by various excitation mechanisms for the H_2O_2 production of atmospheric pressure plasma jets”. *Journal of Physics D: Applied Physics* **58**.2 (2025), 025203. DOI: 10.1088/1361-6463/ad816a.

[231] P. Ranieri et al.: “Plasma agriculture: Review from the perspective of the plant and its ecosystem”. *Plasma Processes and Polymers* **18**.1 (2021), 2000162. DOI: 10.1002/ppap.202000162.

[232] H. Chen et al.: “Review of low-temperature plasma nitrogen fixation technology”. *Waste Disposal & Sustainable Energy* **3**.3 (2021), 201–217. DOI: 10.1007/s42768-021-00074-z.

[233] J. R. Toth et al.: “A Plasma-Water Droplet Reactor for Process-Intensified, Continuous Nitrogen Fixation at Atmospheric Pressure”. *ACS Sustainable Chemistry & Engineering* **8**.39 (2020), 14845–14854. DOI: 10.1021/acssuschemeng.0c04432.

[234] P. Lamichhane et al.: “Low-Temperature Plasma-Assisted Nitrogen Fixation for Corn Plant Growth and Development”. *International Journal of Molecular Sciences* **22**.10 (2021), 5360. DOI: 10.3390/ijms22105360.

[235] M. Roth: “Fluorescence reaction for amino acids”. *Analytical Chemistry* **43**.7 (1971), 880–882. DOI: 10.1021/ac60302a020.

[236] P. Griess: “Bemerkungen zu der Abhandlung der HH. Weselsky und Benedikt ’Ueber einige Azoverbindungen’”. *Ber. Dtsch. Chem. Ges.* **12**.1 (1879), 426–428. DOI: 10.1002/cber.187901201117.

[237] M. Moorcroft: “Detection and determination of nitrate and nitrite: a review”. *Talanta* **54**.5 (2001), 785–803. DOI: 10.1016/S0039-9140(01)00323-X.

[238] M. S. Abdul Galil et al.: “A simple and rapid spectrophotometric method for the determination of nitrite by its decolorizing effect on peroxovanadate complex”. *Spectrochimica Acta Part A: Molecular and Biomolecular Spectroscopy* **67**.1 (2007), 76–82. DOI: 10.1016/j.saa.2006.06.026.

[239] E. Vervloessem et al.: “Plasma-Based N_2 Fixation into NO_x : Insights from Modeling toward Optimum Yields and Energy Costs in a Gliding Arc Plasmatron”. *ACS Sustainable Chemistry & Engineering* **8**.26 (2020), 9711–9720. DOI: 10.1021/acssuschemeng.0c01815.

[240] J. Liu et al.: “Plasma for nitrogen fixation by using N_2 /O_2 mixture: Reaction pathway, energy flow, and plasma reactor”. *Plasma Processes and Polymers* (2023), e2300153. DOI: 10.1002/ppap.202300153.

[241] J. A. Silsby et al.: “The Influence of Gas–Liquid Interfacial Transport Theory on Numerical Modelling of Plasma Activation of Water”. *Plasma Chemistry and Plasma Processing* **41**.5 (2021), 1363–1380. DOI: 10.1007/s11090-021-10182-7.

[242] J. Hong et al.: “Kinetic modelling of NH_3 production in N_2 –H_2 non-equilibrium atmospheric-pressure plasma catalysis”. *Journal of Physics D: Applied Physics* **50**.15 (2017), 154005. DOI: 10.1088/1361-6463/aa6229.

[243] B. Dong et al.: “Experimental study of a DBD surface discharge for the active control of subsonic airflow”. *Journal of Physics D: Applied Physics* **41**.15 (2008), 155201. DOI: 10.1088/0022-3727/41/15/155201.

[244] A. Sobota et al.: “The influence of the geometry and electrical characteristics on the formation of the atmospheric pressure plasma jet”. *Plasma Sources Science and Technology* **23**.2 (2014), 025016. DOI: 10.1088/0963-0252/23/2/025016.

[245] N. B. Anikin et al.: “Study of the oxidation of alkanes in their mixtures with oxygen and air under the action of a pulsed volume nanosecond discharge”. *Plasma Physics Reports* **30**.12 (2004), 1028–1042. DOI: 10.1134/1.1839956.

[246] N. D. Lepikhin et al.: "Fast gas heating and radial distribution of active species in nanosecond capillary discharge in pure nitrogen and N_2:O_2 mixtures". *Plasma Sources Science and Technology* **27**.5 (2018), 055005. DOI: 10.1088/1361-6595/aab74e.

[247] T. L. Chng et al.: "TALIF measurements of atomic nitrogen in the afterglow of a nanosecond capillary discharge". *Plasma Sources Science and Technology* **29**.3 (2020), 035017. DOI: 10.1088/1361-6595/ab6f9c.

[248] Y. Seepersad et al.: "On the electrostrictive mechanism of nanosecond-pulsed breakdown in liquid phase". *Journal of Physics D: Applied Physics* **46**.16 (2013), 162001. DOI: 10.1088/0022-3727/46/16/162001.

[249] K. Grosse et al.: "Nanosecond plasmas in water: ignition, cavitation and plasma parameters". *Plasma Sources Science and Technology* **28**.8 (2019), 085003. DOI: 10.1088/1361-6595/ab26fc.

[250] A. V. Klochko et al.: "Investigation of capillary nanosecond discharges in air at moderate pressure: comparison of experiments and 2D numerical modelling". *Journal of Physics D: Applied Physics* **47**.36 (2014), 365202. DOI: 10.1088/0022-3727/47/36/365202.

[251] G. Correale et al.: "Experimental method to quantify the efficiency of the first two operational stages of nanosecond dielectric barrier discharge plasma actuators". *Journal of Physics D: Applied Physics* **49**.50 (2016), 505201. DOI: 10.1088/0022-3727/49/50/505201.

[252] Y. Zhu et al.: "Nanosecond surface dielectric barrier discharge in atmospheric pressure air: I. measurements and 2D modeling of morphology, propagation and hydrodynamic perturbations". *Plasma Sources Science and Technology* **26**.12 (2017), 125004. DOI: 10.1088/1361-6595/aa9304.

[253] S. A. Shcherbanev et al.: "Effect of plasma-flow coupling on the ignition enhancement with non-equilibrium plasma in a sequential combustor". *Journal of Physics D: Applied Physics* **55**.42 (2022), 425202. DOI: 10.1088/1361-6463/ac82fa.

[254] R. Hosseini Rad et al.: "Enhancement of CO_2 splitting in a coaxial dielectric barrier discharge by pressure increase, packed bed and catalyst addition". *Chemical Engineering Journal* **456** (2023), 141072. DOI: 10.1016/j.cej.2022.141072.

[255] P. Bruggeman et al.: "Atmospheric pressure discharge filaments and microplasmas: physics, chemistry and diagnostics". *Journal of Physics D: Applied Physics* **46**.46 (2013), 464001. DOI: 10.1088/0022-3727/46/46/464001.

[256] Z.-S. Chang et al.: "Diagnosis of gas temperature, electron temperature, and electron density in helium atmospheric pressure plasma jet". *Physics of Plasmas* **19**.7 (2012), 073513. DOI: 10.1063/1.4739060.

[257] G. B. Sretenović et al.: "Electric field measurement in the dielectric tube of helium atmospheric pressure plasma jet". *Journal of Applied Physics* **121**.12 (2017), 123304. DOI: 10.1063/1.4979310.

[258] J. Waskoenig et al.: "Atomic oxygen formation in a radio-frequency driven micro-atmospheric pressure plasma jet". *Plasma Sources Science and Technology* **19**.4 (2010), 045018. DOI: 10.1088/0963-0252/19/4/045018.

[259] S. Hübner et al.: "Electron properties in an atmospheric helium plasma jet determined by Thomson scattering". *Journal of Physics D: Applied Physics* **47**.43 (2014), 432001. DOI: 10.1088/0022-3727/47/43/432001.

[260] C. Jiang et al.: "Electron densities and temperatures of an atmospheric-pressure nanosecond pulsed helium plasma jet in air". *Plasma Sources Science and Technology* **28**.8 (2019), 085009. DOI: 10.1088/1361-6595/ab2182.

[261] M. Hofmans et al.: "Characterization of a kHz atmospheric pressure plasma jet: comparison of discharge propagation parameters in experiments and simulations without target". *Plasma Sources Science and Technology* **29**.3 (2020), 034003. DOI: 10.1088/1361-6595/ab6d49.

[262] F. Wu et al.: "Investigation on the electron density and temperature in a nanosecond pulsed helium plasma jet with Thomson scattering". *Plasma Processes and Polymers* **18**.8 (2021), 2100033. DOI: 10.1002/ppap.202100033.

[263] A. F. H. Van Gessel et al.: "NO production in an RF plasma jet at atmospheric pressure". *Journal of Physics D: Applied Physics* **46**.26 (2013), 265202. DOI: 10.1088/0022-3727/46/26/265202.

[264] P. Rumbach et al.: "The solvation of electrons by an atmospheric-pressure plasma". *Nature Communications* **6**.1 (2015), 7248. DOI: 10.1038/ncomms8248.

[265] A. Dogariu et al.: "Femtosecond TALIF allows imaging atomic oxygen from interfacial plasmas in gas and liquid". **2022** (2022). Conference Name: APS Division of Plasma Physics Meeting Abstracts ADS Bibcode: 2022APS..DPPGP1084D, GP11.084.

[266] P. Linstrom: *NIST Chemistry WebBook, NIST Standard Reference Database 69*. 1997. DOI: 10.18434/T4D303. URL: http://webbook.nist.gov/chemistry/ (visited on 08/07/2024).

[267] D. R. Stull: "Vapor Pressure of Pure Substances. Organic and Inorganic Compounds". *Industrial & Engineering Chemistry* **39**.4 (1947), 517–540. DOI: 10.1021/ie50448a022.

A. Appendix

A.1 Humidity admixture

An ice-cooled bubbler system was used to add water vapour to the feed gas to enrich the gas flow with humidity admixtures. A certain amount of the gas flow was guided through the bubbler to control the humidity. The humidity of the gas flow can be theoretically calculated as follows. The water vapour pressure can be calculated from the Clausius-Clapeyron relation. A solution of the Clausius-Clapeyron relation is the Antoine equation [266]:

$$log_{10}(p_{\mathrm{H_2O}}) = A - \frac{B}{C+T} \tag{A.1}$$

where p is the vapour pressure, T is the temperature (in K) and A, B and C are component-specific constants. The constants for water are $A = 4.6543$, $B = 1435.264$ and $C = -64.848$ taken from [267] and valid in the temperature range of 256 to 373 K. The amount of water vapour in parts per million $c_{\mathrm{H_2O}}$ can then be calculated by the water vapour pressure and the portion of feed gas guided through the bubbler $\Phi_{bubbler}$ compared to the total feed gas flow Φ_{total}:

$$c_{\mathrm{H_2O}} = \frac{\Phi_{bubbler}}{\Phi_{total}} \frac{p_{\mathrm{H_2O}(T)}}{p_0} 10^6 \tag{A.2}$$

with the standard pressure $p_0 = 101\,325$ Pa. The theoretically calculated measured humidity concentration in the feed gas fits well to mass spectrometer measurements as shown by Willems et al. [29]. However, the volume of the bubbler has to be large enough as low volumes (3 mL and less) lead to insufficient bubbling of the feed gas through the bubbler and a short residence time of the gas in contact to the water. Thus, deviations from measured concentrations to the predicted concentrations by the water vapour theory may occur [202]. Since the volume of the bubbler in this work was large enough (100 mL), water vapour theory can be applied to calculate the humidity concentrations of the feed gas.

The bubbler was cooled to maintain reproducible results and to keep the water in the bubbler close to the triple point of water at 0 °C. The cooling process of the bubbler was measured by use of a NiCr-Ni thermocouple type K (B+B Thermo-Technik, ranging from -50°C to 260°C) connected to a two-channel thermometer (Voltcraft). It takes about 1 h to cool down the bubbler and the temperature of

the water in the bubbler was measured to $(1.4 \pm 0.5)\,°C$. A maximum humidity of $(6400 \pm 250)\,ppm$ can be achieved using this temperature. Further, the humidity admixture increases linearly with the fraction of feed gas guided through the bubbler as visible in figure A.1.

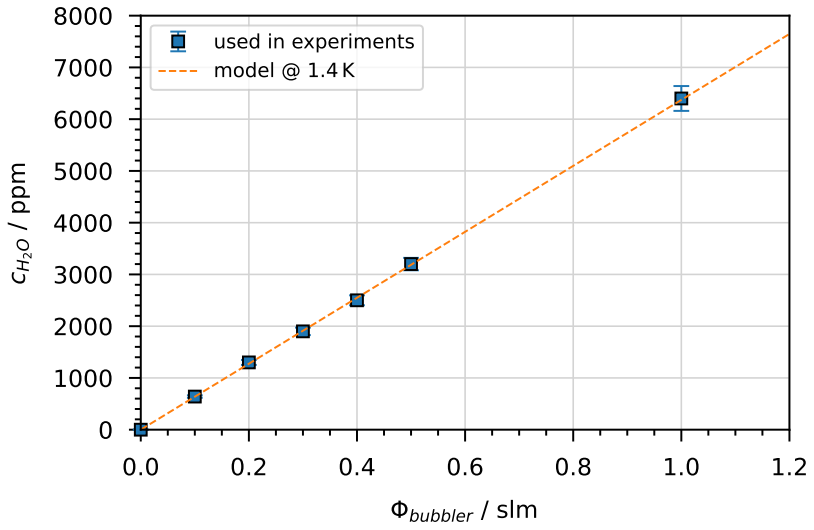

Figure A.1: Humidity concentration in the feed gas for various fractions of feed gas guided through the cooled bubbler. The markers symbolise the parameters used in the experiments and the dashed line shows the behaviours of the water vapour theory calculations.

A.2 Temperature measurements

Calibration curves for the temperature measurements by the thermocouple are shown in figure A.2 (a). For all plasma powers, a linear decrease in the effluent temperature can be seen, with the strongest decrease at 12 W plasma power. The slopes of the calibration curves are $(-0.32 \pm 0.05)\,°C/mm$, $(-1.49 \pm 0.22)\,°C/mm$ and $(-3.08 \pm 0.21)\,°C/mm$ for plasma powers of 1 W, 6 W and 12 W, respectively. The calibration curves were not affected by humidity admixtures to the feed gas (not shown here).

In addition, figure A.2 (b) shows an example of a measured spectrum of the OH band emission at 308 nm together with the fitted spectrum and the corresponding residual. From fitting the spectrum, the rotational temperature can be extracted and used for the determination of the gas temperature of the discharge. As can be seen in the figure, a very good agreement between fitted and measured spectrum could be achieved.

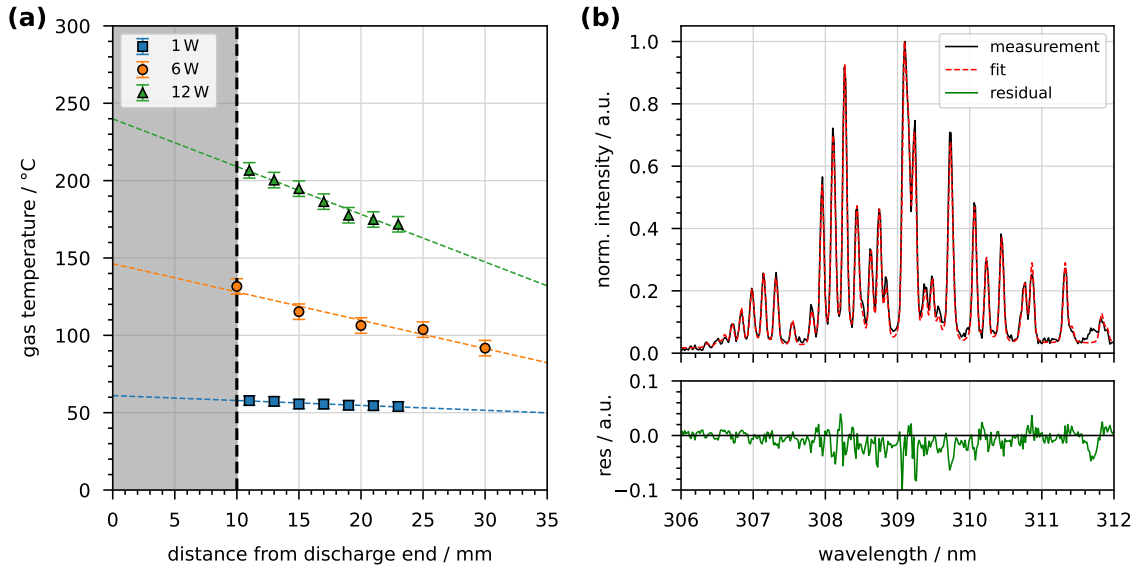

Figure A.2: **(a)** Calibration of the thermocouple measurements. **(b)** Measured and fitted OH band emission with corresponding residual.

A.3 Images of the CL of luminol for correction

Examples of images taken for correction and to detect the CL of luminol are shown in figure A.3. Figure A.3 (a) shows the image of the cuvette containing pure buffer solution without the addition of luminol. Some reflections of the plasma emission at the border of the cuvette and the liquid surface are visible there. Figure A.3 (b) shows the image of the cuvette containing the luminol solution, where the CL is visible at the liquid surface. By subtracting the buffer image from the luminol image, only the CL signal can be obtained, which is shown in figure A.3 (c).

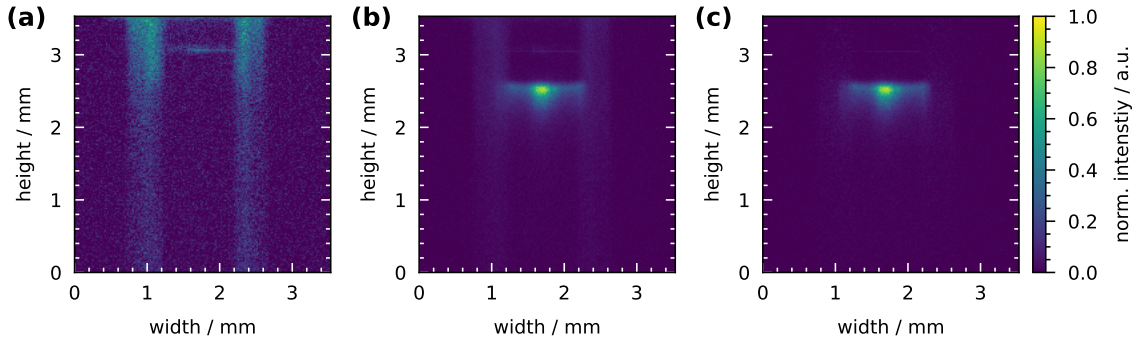

Figure A.3: Images of the CL signal of luminol. Each image is normalised to its respective maximum. **(a)** Image of pure buffer as background. **(b)** Image of the CL of luminol under plasma treatment. **(c)** Corrected CL image by the background.

A.4 Images of luminol under humidity variation at 6 W

The CL signals for humidity variation at 6 W plasma power are shown in figure A.4. The CL signal and the trends are the same as described for 1 W plasma power in chapter 5. In all images, the CL signal is visible at the liquid surface with a bright spot in the centre. The width of the bright spot corresponds to the width of the capillary and is located at the point where the capillary faces the surface of the liquid. With increasing humidity, the intensity of the CL signal initially increases, has a maximum at 640 ppm and decreases at higher humidity concentrations.

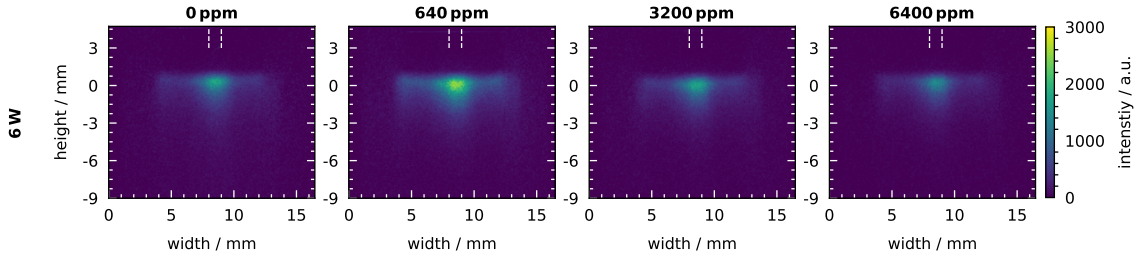

Figure A.4: Images of the CL of luminol at various humidity concentrations at 6 W plasma power. At $z = 0$ mm the liquid surface was localised and positive z distances correspond to the gas phase, while negative values are in the liquid phase.

A.5 Images of luminol under distance variation

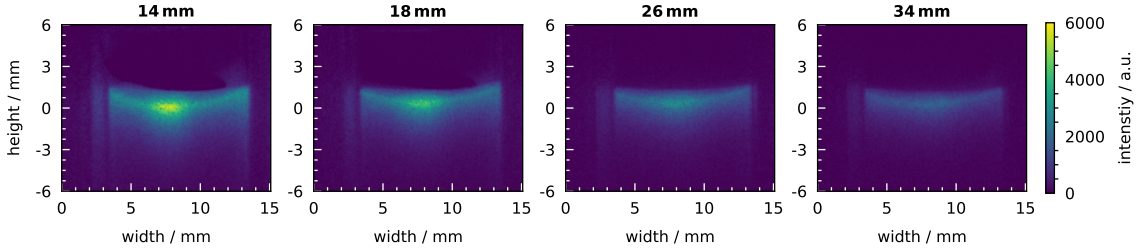

Figure A.5: Images of the CL of luminol at various distances from the capillary end to the liquid surface. Plasma was operated at 1 slm gas flow, 640 ppm humidity and 6 W plasma power. At $z = 0$ mm the liquid surface was localised and positive z distances correspond to the gas phase, while negative values are in the liquid phase.

Figure A.5 shows the CL signal at distances from 14 mm to 34 mm between the capillary plasma jet and liquid surface. With increasing distance, the CL gets weaker and the bright spot in the centre of the liquid vanishes. This indicates a lower density of OH reaching the liquid surface and a broader distribution of OH in the expanding effluent with distance.

A.6 Log scale of modelled H_2O_2 concentration profiles

The concentration profiles of H_2O_2 in the liquid for the convective and diffusive transport extracted from the transport model shown in figure 5.11 are here displayed on a logarithmic scale in figure A.6 for various time steps. In the case of convective transport, the concentration in the liquid shows a constant concentration profile with a slight decrease towards deeper depths than 10 mm. On the other hand, the concentration profiles in the diffusive case also show higher values in time, but the profiles look differently. A linear decay of the concentration in the liquid can be seen on the logarithmic scale at a depth of 0.1 mm and deeper. Close to the liquid surface, the profiles are constant at all time steps. For further details on the profiles, see the discussion in chapter 5.

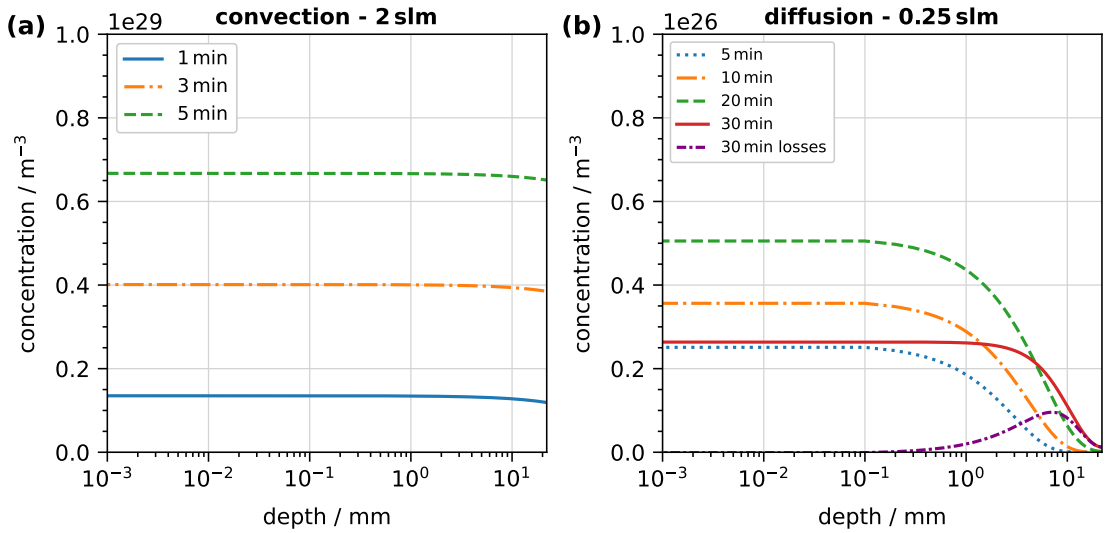

Figure A.6: Logarithmic scale of figure 5.11. **(a)** Convective transport at 2 slm. **(b)** Diffusive transport at 0.25 slm.

A.7 Temporal behaviour of absorbance

To illustrate the disturbances of the spectrophotometric approach when the plasma was operated with N_2 admixtures, the temporal behaviour of the absorbance during plasma treatment is shown in figure A.7. At 0 % N_2 admixture, a linear increase in H_2O_2 admixture can be seen. When N_2 is added to the system, the curves deviate from the linear increase and begin to fluctuate. At the highest addition of 1 % no real trend can be recognised at all.

Ammonium metavanadate used in the spectrophotometric approach reacts with

H_2O_2 to form a red-orange coloured peroxovanadium cation. It is known that nitrite leads to a decolourization of the peroxovanadate complex [238]. Since a considerable amount of NO_2^- is produced when N_2 is added to the gas flow (see chapter 7), this decolourization effect takes place and interferes with the peroxovanadate complex. Thus, the spectrophotometric approach shows unstable absorbance during plasma treatment when operating with N_2 admixtures and it cannot be used in this case. The electrochemical sensing is an alternative to measure the H_2O_2 in PTL when N-containing species are involved.

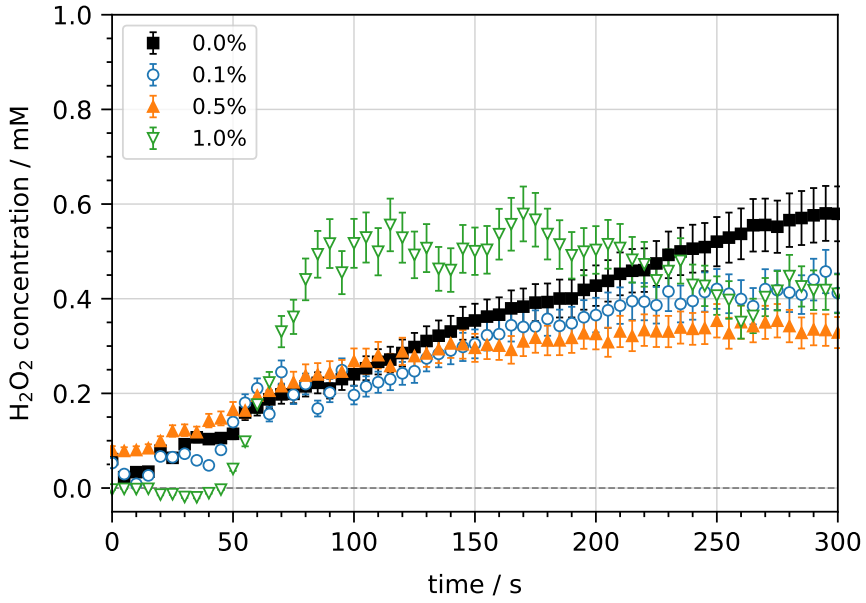

Figure A.7: Temporal behaviour of the absorbance of the spectrophotometric approach at various N_2 admixtures to the feed gas. The plasma was operated at 6 W, 3200 ppm humidity and without O_2 admixtures.

A.8 Determination of plasma volume

Pictures of the plasma emission from the front view of the plasma jet are shown in figure A.8 for the three operation modes. In all cases, the emission of the plasma originates from the centre of the capillary. The µs and ns operations look very similar with a homogeneous emission at a height of 3 mm and a width of about 3 mm. The plasma does not fill the entire capillary and about one-third of the gas does not experience the plasma. The RF operation shows a more patterned structure between the electrodes and has only a width of about 2 mm. Thus, the RF plasma covers only about 50 % of the discharge gap. It is important to note that the emission discussed does not provide any information about the plasma structure in the discharge channel. The measured emission is accumulated over time and the view passes through the discharge channel.

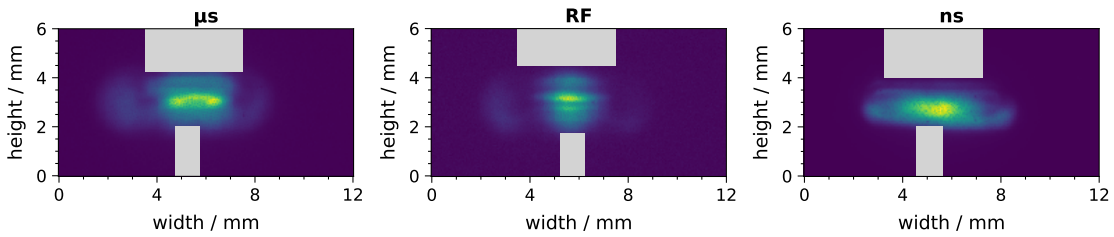

Figure A.8: Pictures of the averaged plasma emission of the three operation modes. Grey bars indicate the positions of the electrodes (wide grounded at the top and small powered at the bottom). Plasmas were operated without humidity admixture. µs operation was performed at 6 kHz and 1.5 W, RF in continuous mode and 1 W and ns with 6 kHz and 0.65 W.

A.9 Correction of power measurements under ns operation

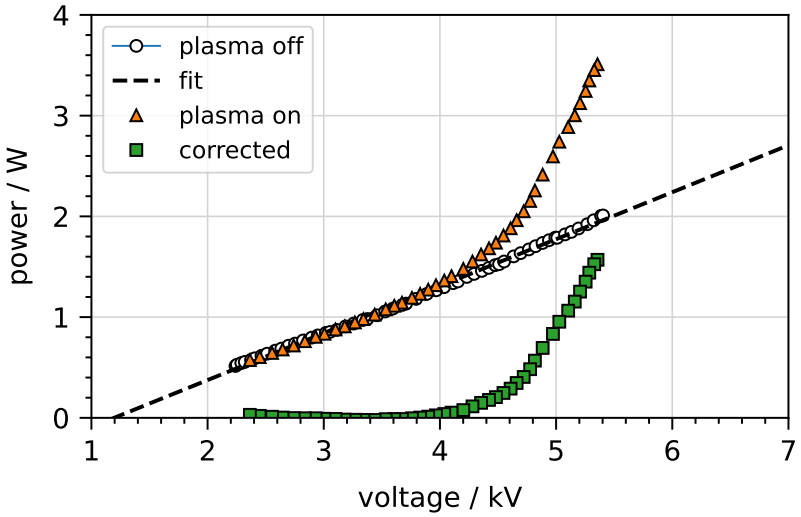

Figure A.9: Correction of power measurements under ns operation. The power curve obtained at a humidity of 6400 ppm (plasma on) was corrected by plasma power measurements without plasma (plasma off). The dashed line corresponds to the linear fit of plasma off data.

Figure A.9 shows the correction of the power measurements under the ns operation. Without a gas flow and applied voltage, the power is not zero but has values between 0.5W to 2 W and increases linearly with voltage. However, when the gas flow is turned, the plasma ignites at about 4 kV. Then, the power increases non-linearly, indicating that a certain amount of the power is deposited into the plasma. This dissipated plasma power can be obtained by subtracting the power delivered into the system with plasma turned off from the power measured with plasma turned on. The power with the plasma turned off was measured when the setup was changed and was used to calibrate the power measurements in ns operation.

Acknowledgements

Abschließend möchte ich mich bei allen Menschen bedanken, die mich sowohl bei der Durchführung und Erstellung dieser Dissertation als auch während meines Studiums unterstützt und begleitet haben:

Zu allererst bedanke ich mich bei **Jun.-Prof. Judith Golda** für die Möglichkeit der Durchführung meiner Dissertation in ihrer Arbeitsgruppe. Ich habe immer deine freundliche, hilfsbereite und offene Betreuung während der Zeit sehr geschätzt. Es hat mir sehr viel Spaß gemacht mit dir über die Ergebnisse zu diskutieren und neue Forschungsmöglichkeiten zu erarbeiten. Vielen Dank!

Ich bedanke mich bei **Prof. Achim von Keudell** für die Übernahme des Zweitgutachtens dieser Dissertation. Zudem möchte ich dir für die tolle Zeit bei EPII danken. Es hat mir sehr viel Freude bereitet Teil deines Teams zu sein. Deine fundierte und ruhige Art und Weise komplexe Themen zu erklären habe ich immer sehr bewundert.

Danke an alle Studierende, die ich im Zuge der Erstellung meiner Dissertation begleiten durfte: **Emanuel Jeß, Maike Kai, Lara Boeddinghaus, Jannis Kaufmann, Niklas Eichstaedt** und **Leonidas Eliakopoulos**. Es war mir eine Freude euch im Labor anzuleiten, mit euch die Ergebnisse zu diskutieren und auch privat viele tolle Gespräche führen zu können.

Danke an **David Steuer** und **Sascha Chur** für die gemeinsame Zeit während des Doktors. Für die zahlreichen Gespräche, die tollen Erfahrungen auf den Konferenzen, die Stadionbesuche und die lustigen Spieleabenden und Dartsspiele.

Meiner ehemaligen Büropartnerin und immer noch besten Freundin **Maike Kai** und meinem aktuellen Büropartner und guten Freund **Elia Jüngling**. Ihr habt die gemeinsame Zeit im Büro unvergesslich gemacht und ich danke euch für die wunderbaren Momente und Gespräche. Elia danke ich noch für die regelmäßigen Dartspiele.

Ich danke allen Mitarbeitenden des Lehrstuhls Experimentalphysik II und der Arbeitsgruppe Plasma Interface Physics. Insbesondere **Dr. Marc Böke** für die Diskussionen in den Meetings und das Korrekturlesen der Dissertation, **Alicia Gonzalez** für ihre organisatorische Arbeit, ohne diese die täglich Arbeit nicht möglich wäre, sowie für die vielen Dartspiele inklusive des Duells auf der Weihnachtsfeier 2023, **Dr. Volker Schulz-von der Gathen** für seine großzügige Hilfsbereitschaft in allen Belangen und **Henrik van Impel** für die freundschaftlichen und tiefgründi-

gen Gespräche sowie die vielen Dartspiele. Ebenso danke ich den ehemaligen Mitarbeitenden **Dr. Sebastian Burhenn** für die gemeinsame Zeit in Meetings, im Labor und auf Konferenzen und **Dr. Laura Chauvet** für ihre Unterstützung bei den Messungen mit dem Massenspektrometer.

Vielen Dank an die Techniker des Lehrstuhls EPII **Björn Redeker, Kai Fiegler, Axel Lang** und **Michael Konkowski** für ihren technischen Support, ohne diesen diese Arbeit nicht möglich gewesen wäre.

Meinen Projektpartnerinnen und -partner aus dem SFB 1316: Vom Lehrstuhl für Angewandte Mikrobiologie an der Ruhr-Universität Bochum danke ich **Prof. Julia Bandow, Dr. Tim Dirks, Sabrina Klopsch** und **Davina Stösser** für die zahlreichen gemeinsamen Stunden im Labor und die Erfahrungen, die ich aus der gemeinsamen Zeit mitnehmen werde. Ebenso habe ich unseren privaten Momente sehr geschätzt. Vom Lehrstuhl für Elektrochemie & Nanoskalige Materialien – Analytische Chemie II der Ruhr-Universität Bochum danke ich **Prof. Kristina Tschulik, Ludwig Jolmes** und **Dr. Gabriel Boitel-Aullen** für die Herstellung und Unterstützung der Elektrochemischen Sensoren. Vom Lehrstuhl für Angewandte Elektrodynamik und Plasmatechnik an der Ruhr-Universität Bochum danke ich **Dr. Andrew Gibson** und **Anna Lena Schöne** für die Zusammenarbeit bei der Modellierung des Plasma-Flüssigkeits-Systems. Vom Institut für Elektrochemie der Universität Ulm danke ich **Dr. Christoph Jung** und **Hanna Poggemann** für die zahlreichen Diskussionen zu der Verteilung der Plasmaspezies in der Flüssigkeit.

Meinen Freunden aus dem Studium danke ich sehr, insbesondere **Maike Kai, Emanuel Jeß, Thilo Romba, Jan Löwer, Jannis Kostrezwa, Mos Nenbangkaeo** und **Johan Wulff**. Ohne euch wäre das Studium nicht so schön geworden, wie es am Ende für mich war.

Ich bedanke mich bei all meinen Freundinnen und Freunden und sowie meiner Familie für ihre Unterstützung und die schönen Momente in meinem Leben. Besonders danken möchte ich mich bei meinem Vater **Werner Schüttler**. Ohne dich wäre ich nicht die Person geworden, die ich heute bin. Danke für deine bedingungslose Unterstützung. Du bist der aufrichtigste und hilfsbereiteste Mensch, den ich kenne und weiß deine Unterstützung über alles zu schätzen. Zudem danke ich meiner Mutter **Claudia Schüttler**. Ich werde dich immer in meinem Herzen behalten.

Ein großer Dank geht an meine Liebe und Verlobte **Vanessa Reder**, die mich wunderbar unterstützt hat in der Erstellung der Dissertation. Ich danke dir für deine großartige Unterstützung in allen schwierigen Momenten und deine aufrichtige Liebe mir gegenüber. Ich bin froh dich an meiner Seite zu wissen und schaue mit großer Freude auf unsere gemeinsame Zukunft. Ich liebe dich von ganzem Herzen!

Steffen Schüttler

PhD Candidate – Ruhr University Bochum

Curriculum Vitae

Name	**Steffen Burkhard Schüttler**
Date of Birth	**27.09.1996**
Place of Birth	**Gelsenkirchen**

Education

since 2021	**PhD student**, *Physics*, Ruhr University Bochum
2018 - 2021	**Master of Science**, *Physics*, Ruhr University Bochum
2015 - 2018	**Bachelor of Science**, *Physics*, Ruhr University Bochum
2014	**Abitur**, Hellweg-Gymnasium Bochum
2006 - 2014	**Secondary School**, Hellweg-Gymnasium Bochum
2002 - 2006	**Primary School**, Grundschule Eppendorf, Bochum

Employment

Since 2021	**Research Assistant**, Plasma Interface Physics, Ruhr University Bochum
2020 - 2021	**Student Assistant**, Chair for Experimental Physics II - Reactive Plasmas, Ruhr University Bochum
2018 - 2019	**Student Assistant**, Chair for Experimental Physics II - Reactive Plasmas, Ruhr University Bochum
2016 - 2018	**Student Assistant**, Chair for Experimental Physics I - Experimental Hadron Physics, Ruhr University Bochum

Activities

July 2024	**Gordon Research Conference**, Andover, USA, Poster Presentation
Feb 2024	**Spring Meeting German Physical Society**, Greifswald, Germany, Invited Oral Presentation
May 2023	**International Symposium on Plasma Chemistry**, Kyoto, Japan, Oral Presentation
June 2022	**International Conference on Plasma Medicine**, Utrecht, Netherlands, Oral Presentation

Scholarship

2020	**Deutschlandstipendium**, German public-private scholarship, RAG Stiftung
2018 - 2019	**Deutschlandstipendium**, German public-private scholarship, Evonik Stiftung

Steinring 9 – 44789 Bochum – Germany
steffen.schuettler@rub.de • *orcid.org/0000-0003-0131-8654*